



CERIA-BASED ANODES WITH COBALT AND COPPER ADDITIONS FOR THE DIRECT UTILISATION OF METHANE IN SOLID OXIDE FUEL CELLS

Bernardo Jordão Moreira Sarruf

Tese de Doutorado apresentada ao Programa de Pós-graduação em Engenharia Metalúrgica e de Materiais, COPPE, da Universidade Federal do Rio de Janeiro, como parte dos requisitos necessários à obtenção do título de Doutor em Engenharia Metalúrgica e de Materiais.

Orientador: Paulo Emílio Valadão de Miranda

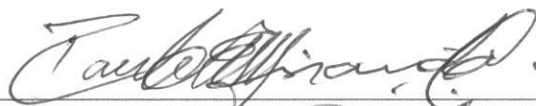
Rio de Janeiro
Fevereiro de 2018

CERIA-BASED ANODES WITH COBALT AND COPPER ADDITIONS FOR
THE DIRECT UTILISATION OF METHANE IN SOLID OXIDE FUEL CELLS

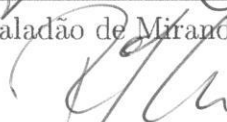
Bernardo Jordão Moreira Sarruf

TESE SUBMETIDA AO CORPO DOCENTE DO INSTITUTO ALBERTO LUIZ
COIMBRA DE PÓS-GRADUAÇÃO E PESQUISA DE ENGENHARIA (COPPE)
DA UNIVERSIDADE FEDERAL DO RIO DE JANEIRO COMO PARTE DOS
REQUISITOS NECESSÁRIOS PARA A OBTENÇÃO DO GRAU DE DOUTOR
EM CIÊNCIAS EM ENGENHARIA METALÚRGICA E DE MATERIAIS.

Examinada por:



Prof. Paulo Emílio Valadao de Miranda, D.Sc.



Prof. Robert Steinberger-Wilckens, Ph.D.



Prof. Nguyen Minh, Ph.D.



Prof. Paula Mendes Jardim, D.Sc.



Dr. Selma Aparecida Venancio, D.Sc.

RIO DE JANEIRO, RJ – BRASIL
FEVEREIRO DE 2018

Sarruf, Bernardo Jordão Moreira

Ceria-based anodes with cobalt and copper additions for the direct utilisation of methane in solid oxide fuel cells/Bernardo Jordão Moreira Sarruf. – Rio de Janeiro: UFRJ/COPPE, 2018.

XVII, 175 p.: il.; 29, 7cm.

Orientador: Paulo Emílio Valadão de Miranda

Tese (doutorado) – UFRJ/COPPE/Programa de Engenharia Metalúrgica e de Materiais, 2018.

Referências Bibliográficas: p. 133 – 166.

1. Solid oxide fuel cells. 2. Electrochemical oxidation. 3. Internal reforming. 4. Coking Resistant. 5. Methane. I. Miranda, Paulo Emílio Valadão de. II. Universidade Federal do Rio de Janeiro, COPPE, Programa de Engenharia Metalúrgica e de Materiais. III. Título.

*“Every person takes the limits of their own
field of vision for the limits of the world.”*

Arthur Schopenhauer
- Studies in Pessimism -

Acknowledgements

Firstly, I would like to thank all my family for the support, my mother Miriam, my father Délcio, my two brothers Guilherme and Délcio, my grandmother Arlene and my wife Monique.

Also, many thanks to my supervisors professors Paulo Emílio Valadão de Miranda and Robert Steinberger-Wilckens for all the support. Special thanks to my second supervisor Dr. Jong-Eun Hong, with whom I have learnt so much, for all his help. In addition, special thanks also to Dr. Selma Aparecida Venâncio for all these years (almost 9) of support and friendship.

Yet, I acknowledge the support of technical staff from both institutions Hydrogen Laboratory of COPPE/UFRJ and Centre for Fuel Cells and Hydrogen Research. In addition, I would like to thank all my friends from both enrolled universities: Alessandro, Gabriella, George, Gustavo, Tatiane, Alberto, Ugo, Rodrigo, Rômulo, Natasha, Patty, Monique, Marlon, Daniel, Kun, Vikrant, Miguel, Lois, Ahmad, Laura, Aimee, James, Geoff, Scott, Fatima, Hal, Alan, Peter, Lina, Anisa, Oliver, Aman and Artur.

Finally, I acknowledge CNPq and CAPES for the scholarships granted, as well as BNDES, EnergiaH Ltda., Oxiteno S.A. and FURNAS S.A. for the financial support to this research.

Resumo da Tese apresentada à COPPE/UFRJ como parte dos requisitos necessários para a obtenção do grau de Doutor em Ciências (D.Sc.)

ANODOS DE CÉRIA COM ADIÇÕES DE COBALTO E COBRE PARA UTILIZAÇÃO DIRETA DO METANO EM PILHAS A COMBUSTÍVEL DE ÓXIDO SÓLIDO

Bernardo Jordão Moreira Sarruf

Fevereiro/2018

Orientador: Paulo Emílio Valadão de Miranda

Programa: Engenharia Metalúrgica e de Materiais

O uso de hidrocarbonetos em pilhas a combustível de óxido sólidos tem se mostrado como uma engenhosa alternativa para tornar a aplicação mais viável facilitando sua penetração no mercado atual e diminuindo o aporte em investimentos infraestruturais. Portanto, o objetivo do presente trabalho foi desenvolver um material com uma matriz de céria e adições de cobalto e cobre para servir como anodo em pilhas a combustível de óxido sólido. O material deve ser capaz de promover a oxidação eletroquímica de hidrocarbonetos como metano.

O eletrocatalisador foi sintetizado em diferentes proporções de cério, cobalto e cobre, foi caracterizado e testado segundo suas propriedades eletroquímicas utilizando-se de difratometria e fluorescência de raios X, análise termogravimétrica, redução a temperatura programada, testes de condutividade elétrica, testes de desempenho e espectroscopia de impedância eletroquímica, quantificação através de cromatografia dos gases produzidos. Por fim, as pilhas operadas foram submetidas à microscopia eletrônica de varredura, análises de espectroscopia Raman e oxidação a temperatura programada para avaliar a presença de eventual carbono proveniente de coqueificação.

As pilhas produzidas se mostraram capazes de operar em temperaturas da ordem de 700-850°C com hidrogênio ou metano como combustíveis. Os testes na pilha pós operada atestaram sua integridade além de confirmarem que quantidades irrisórias de carbono remanesciam em sua estrutura. Portanto, o material de anodo se mostrou promissor para aplicações reais em pilhas a combustível de óxido sólido.

Abstract of Thesis presented to COPPE/UFRJ as a partial fulfillment of the requirements for the degree of Doctor of Science (D.Sc.)

Bernardo Jordão Moreira Sarruf

February/2018

Advisor: Paulo Emílio Valadão de Miranda

Department: Metallurgical and Materials Engineering

The utilisation of hydrocarbons as fuels in solid oxide fuel cells presents as an ingenious alternative for boosting the market widespread of such technology. The main advantage is the lower need of infrastructure investments. Therefore, the objective of this thesis was to develop a ceria-based material with cobalt and copper additions to serve as anode for the electrochemical oxidation of methane.

The electrocatalysts powders were synthesised with different proportion of cerium, cobalt and copper and were then tested and characterised. The characterisation was done by X-ray diffractometry, X-ray fluorescence, thermogravimetric analysis, temperature-programmed reduction, DC-conductivity tests and particle size distribution. The tests consisted in electrochemical performance and impedance, gas chromatography. Post-mortem characterisation was done by scanning electron microscopy and was focused in assessing eventual carbon deposition by Raman spectroscopy and temperature-programmed oxidation.

The produced cells and compositions have shown to be suitable for operating with both hydrogen or methane as fuels in the range of 700-850°C. The post-mortem showed the anode integrity and besides that, no significant carbon was found in the anode post-mortem bulk. Therefore, the anode material has presented itself as a promising alternative for real solid oxide fuel cells applications.

Contents

List of Figures	xi
List of Tables	xiii
List of Abbreviations	xv
List of Symbols	xvi
1 Introduction	1
1.1 Fuel cell - Thermodynamics	2
1.2 Alkaline electrolyte fuel cell - AFC	4
1.3 Polymer electrolyte fuel cell - PEFC	4
1.4 Phosphoric acid electrolyte fuel cell - PAFC	4
1.5 Molten carbonate electrolyte fuel cell - MCFC	5
1.6 Solid oxide fuel cell - SOFC	5
1.6.1 Electrolyte	9
1.6.2 Cathode	12
1.6.3 Anode	16
1.7 Associated Overpotentials	18
1.7.1 Ohmic overpotential	18
1.7.2 Concentration overpotential	19
1.7.3 Activation overpotential	21
1.8 Summary of the chapter and conclusions	24
2 Objectives	26
2.1 Summary of similar works	26
3 Literature review	29
3.1 Reforming processes	29
3.1.1 Methane steam reforming	29
3.1.2 Methane dry reforming	30
3.1.3 Ethanol steam reforming	31

3.2	Oxidation processes	31
3.2.1	Methane oxidation	31
3.2.2	Ethanol oxidation	32
3.3	Carbon deposition	37
3.4	Anode poisoning by sulphur	40
3.5	Types of Anodes	43
3.5.1	Nickel-based anodes	43
3.5.2	Copper-based anodes	47
3.5.3	Perovskite-based anodes	48
3.5.4	Ceria-based anodes	49
3.6	Materials selection - Anodes for carbonaceous fuels	52
3.7	Conclusions	57
4	Materials and methods	58
4.1	Electrocatalyst synthesis	58
4.2	Electrocatalyst characterisation	59
4.2.1	X-ray diffractometry	59
4.2.2	Thermogravimetric analysis	61
4.2.3	X-ray fluorescence	62
4.2.4	Particle size distribution	62
4.2.5	Temperature-programmed reduction	63
4.2.6	Electrical conductivity of the precursor oxides	63
4.3	Cell assembly	64
4.4	Cell testing	65
4.5	Cells <i>post-mortem</i> analysis	68
4.5.1	Raman spectroscopy	68
4.5.2	Scanning electron microscopy	69
4.5.3	Temperature-programmed oxidation	70
5	Electrocatalyst characterisation	72
5.1	X-ray analysis	73
5.2	Thermogravimetric analysis	75
5.3	X-ray fluorescence analysis	78
5.4	Particle size distribution	79
5.5	Temperature-programmed reduction	80
5.6	Electrical conductivity of the precursor oxides	83
5.7	Summary of the chapter and conclusions	84

6	The CeO₂-Co-Cu anode	86
6.1	The buffer layer - phases characterisation	87
6.2	Performance and electrochemical impedance	87
6.3	Performance and GC-coupled analysis	92
6.4	Results comparison and reproducibility	97
6.5	<i>Post-mortem</i> characterisation	99
6.5.1	Raman spectroscopy of the anode surface	99
6.5.2	TPO of the anode bulk	100
6.5.3	SEM of the aged anode cross section	100
6.6	Summary of the chapter and conclusions	108
7	The role of cobalt and copper	110
7.1	X-ray analysis	111
7.2	Thermogravimetric analysis	111
7.3	Electrochemical tests	112
7.4	<i>Post-mortem</i> characterisation	115
7.5	Summary of the chapter and conclusions	116
8	Discussions	118
8.1	Phases formation	118
8.2	Impedance spectroscopy considerations	120
8.3	The buffer layer	121
8.4	Catalytic X Electrocatalytic conversion	123
8.5	Carbon deposition considerations	125
8.6	Final considerations	128
9	Overall Conclusions	130
	Bibliography	133

List of Figures

1.1	Timeline showing how the fuels evolved	1
1.2	Reaction scheme at a single SOFC	6
1.3	Planar SOFC single cells	8
1.4	Fluorite Structure	10
1.5	Ionic conductivity of solid electrolyte materials	12
1.6	Cathode TPB illustration	13
1.7	Perovskite structure	14
1.8	Anode TPB illustration	17
1.9	SOFC standard i-V curve and impedance plot	23
3.1	Carbon deposition phase diagram	38
3.2	Carbon nano fibres formation	39
3.3	Ni-S phase diagram calculated by DFT	40
3.4	Nickel coarsening	44
3.5	Nickel coverage by carbon deposition	44
3.6	Electrolyte cracking	45
3.7	Ni-YSZ and Cu-CeO ₂ -Al ₂ O ₃ comparisons after operation with ethanol	50
3.8	Materials Selection - Bubble chart	54
4.1	Flowchart of the amorphous citrate synthesis	59
4.2	Planes of diffraction - representation of Bragg's Law	59
4.3	Van der Pauw method simplified scheme	64
4.4	Cathode and anode sintering	65
4.5	Pictures of the steps of mounting cell procedure	66
4.6	Raman effect	68
4.7	Electron beam and its interaction with the specimen	69
4.8	Carbon oxidation profile over increasing temperature	71
5.1	X-Ray diffractograms for the starting compositions	73
5.2	Rietveld refinement fitness	76
5.3	Thermogravimetric analysis for the starting compositions	77
5.4	Particle size distribution for the starting compositions	79

5.5	Temperature-programmed reduction for the starting compositions	81
5.6	TPR calculations	82
5.7	Electrical conductivity of oxides	84
6.1	Cell assembly scheme - Bimetallic anode compositions	86
6.2	X-ray analysis of the precursors powders and sintered buffer layer	87
6.3	Electrochemical tests Ce:Co:Cu - 2:1:1, hydrogen as fuel	88
6.4	Electrochemical tests Ce:Co:Cu - 1:2:1, hydrogen as fuel	89
6.5	Electrochemical tests Ce:Co:Cu - 1:1:2, hydrogen as fuel	89
6.6	Electrochemical tests Ce:Co:Cu, methane as fuel	90
6.7	Arrhenius plot for the inverse of total polarisation resistances	91
6.8	Electrochemical GC-coupled tests - cerium-rich	93
6.9	Electrochemical GC-coupled tests - cobalt-rich	94
6.10	Electrochemical GC-coupled tests - copper-rich	95
6.11	Production rates of CO and CO ₂ for all compositions	98
6.12	Raman spectroscopy for the bimetallic compositions	99
6.13	Temperature-programmed oxidation of the cells bulk	101
6.14	SEM imaging over reduced and aged anodes	103
6.15	EDS point composition - identifying the layers	104
6.16	EDX mapping anode cross section - cerium-rich composition	105
6.17	EDX mapping anode cross section - cobalt-rich composition	106
6.18	EDX mapping anode cross section - copper-rich composition	107
7.1	Cells assembly scheme - Monometallic compositions	111
7.2	X-Ray diffractograms for ceria-cobalt and ceria-copper compositions	112
7.3	Thermogravimetric analysis for the monometallic compositions	113
7.4	Electrochemical tests for CeO ₂ -Co ₃ O ₄ anode, hydrogen as fuel	114
7.5	Electrochemical tests for CeO ₂ -CuO anode, hydrogen as fuel	114
7.6	Electrochemical tests CeO ₂ -Co ₃ O ₄ and CeO ₂ -CuO - methane as fuel	115
7.7	Arrhenius plot for total polarisation resistances	115
7.8	Raman spectroscopy for the monometallic compositions	116
8.1	Binary phase diagram CeCoCu possible systems	119
8.2	Bode diagram for the tested cells	121
8.3	Phase diagrams for ZrO ₂ -CeO ₂ -CeO _{1.5} system	122
8.4	Results comparison at 850°C	123
8.5	Raman spectroscopy and carbon deposition	125
8.6	C-O-H ternary phase diagram	126
8.7	OCV for all five compositions	127

List of Tables

3.1	Fuels physical properties	34
3.2	Reactions path of methane and ethanol decomposition.	38
3.3	List of anodes	52
3.4	List of anodes	56
4.1	Plane spacing and lattice parameters relationship	60
4.2	Crystal systems and Bravais lattices	61
5.1	Synthesis of the precursor cerium-rich powder	72
5.2	Synthesis of the precursor cobalt-rich powder	72
5.3	Synthesis of the precursor copper-rich	72
5.4	Rietveld refinement for starting compositions	74
5.5	Oxides lattice parameters according to PDF database	74
5.6	Lattice parameters for the cerium-rich composition	75
5.7	Lattice parameters for the cobalt-rich composition	75
5.8	Lattice parameters for the copper-rich composition	75
5.9	XRF results for the starting compositions	78
5.10	Weight percentages estimated by XRF data	78
5.11	Density of the oxides and metals	78
5.12	Volume percentages for the first compositions	79
5.13	Arrhenius coefficients from conductivity DC test	84
6.1	Linear regression for total polarisation - Bimetallic compositions	91
6.2	Compiled results for the cells tested in Birmingham	92
6.3	Compiled results for the cells tested in Rio de Janeiro	96
7.1	Synthesis precursors $\text{CeO}_2\text{-Co}_3\text{O}_4$	110
7.2	Synthesis precursors of $\text{CeO}_2\text{-CuO}$	110
7.3	Linear regression for total polarisation - Monometallic compositions	116
8.1	Possible paths of methane's reaction and its products	126
8.2	Results from similar work compared to this work	129

9.1	List of materials and specifications sorted alphabetically	167
9.2	List of equipments and manufacturer sorted alphabetically	168
9.3	Equivalences as metals to oxides for each produced composition	169
9.4	Maximum frequencies and real values with hydrogen as fuel	170
9.5	Maximum frequencies and real values with methane as fuel	171
9.6	ECM parameters CeCoCu, with hydrogen fuel	172
9.7	ECM parameters CeCoCu, with methane as fuel at 850 °C	173
9.8	ECM CeO ₂ -Co ₃ O ₄ and CeO ₂ -CuO, hydrogen as fuel.	174
9.9	ECM CeO ₂ -Co ₃ O ₄ and CeO ₂ -CuO, methane as fuel.	175

List of Abbreviations

PEMFC	Polymer electrolyte membrane fuel cell
AFC	Alkaline electrolyte fuel cell
PAFC	Phosphoric acid electrolyte fuel cell
MCFC	Molten carbonate electrolyte fuel cell
SOFC	Solid oxide fuel cell
LT-SOFC	Low temperature solid oxide fuel cell
IT-SOFC	Intermediate temperature solid oxide fuel cell
HT-SOFC	High temperature solid oxide fuel cell
FCVs	Fuel cell vehicles
YSZ	Yttrium-stabilised zirconia
TPB	Three-phase boundary
LSM	Lanthanum strontium-doped manganite
CPOX	Catalytic partial oxidation
DFT	density functional theory
POX	Partial oxidation
AORG	Anode off-gas reaction
CGO	Cerium gadolinium oxide
CZO	Cerium zirconium oxide
TEM	Transmission electron microscopy
GDC	Gadolinium-doped ceria
MIEC	Mixed ionic and electronic conductor
ScSZ	Scandia-stabilised zirconia
XRD	X-ray diffraction
OCV	Open circuit voltage
TGA	Thermogravimetry analysis
XRF	X-ray fluorescence
PSD	Particle size distribution
TPR	Temperature-programmed reduction
EIS	Electrochemical impedance spectroscopy
SEM	Scanning electron microscopy
EDX	Energy-dispersive X-ray spectroscopy
BSE	Back scattered electrons
ECM	Element circuit model
TPR	Temperature-programmed reduction
TPO	Temperature-programmed oxidation
GC	Gas chromatography

List of Symbols

ΔH	Enthalpy
W	Electric work
ΔS	Entropy
T	Temperature
ΔG	Gibbs free energy
η	Reversible efficiency
U_f	Fuel utilisation
\dot{m}_o	Wasted fuel
\dot{m}_T	Total inlet fuel
I	Electric current
\dot{n}_{H_2}	Molar flow in mol.s ⁻¹
F	Faraday's constant
e	Number of electrons generated by reaction mol
P	Electric power
V	Voltage
V_N^o	Nernst standard voltage
R	Ideal gas constant
K	Equilibrium constant
p_j	Partial pressure of the compound "j"
p_0	Standard partial pressure
ν_j	Stoichiometry of the compound "j"
P_p	Pressure of the reaction's product
P_r	Pressure of the reaction's reagent
σ_{ion}	Ionic conductivity
e^-	Electric charge
A	Pre-exponential factor
E	Activation energy
r_i	Ionic radii of each ion on a perovskite
η_{Ohm}	Ohmic overpotential
ρ_i	Ohmic resistivity of the element "i"
l_i	Thickness of the element "i"
R_{col}	Ohmic resistance offered by the current collecting system
ϕ_i	Mass flow of "i"
j_{a_l}	Limiting current density - anode
$p_{H_2}^a$	Hydrogen partial pressure
D_i^{ef}	Effective diffusion coefficient for the electrode "i"

ε	Porosity
ξ	Tortuosity
D_{i-j}	Diffusion contribution by collisions between “i” and “j”
$D_{i,k}$	Knudsen diffusion
r	Average radius of the pores
M_i	Molecular mass
$\sigma_{i,j}$	Average characteristic length for species “i” and “k”
Ω_D	Collision integral
$p_{H_2}^a$	Hydrogen partial pressure at the anode side
$p_{H_2O}^a$	Steam partial pressure at the anode side
j	Actual current density
η_{con}^a	Concentration overpotential - anode
j_{c_l}	Limiting current density - cathode
$p_{O_2}^c$	Oxygen partial pressure at the cathode side
η_{con}^c	Concentration overpotential - cathode
j_0	Exchanging current density
β	Transference coefficient
η_{at}	Activation overpotential
\dot{n}_{CH_4}	Methane’s molar flow
X_{H_2+CO}	Methane conversion yield
M_v	Materials selection index
d'	Distance between two atomic planes
θ	Diffraction angle
n	Order of reflection
λ	X-ray source wavelength
d	Plane spacing
R_c	Corrected electrical resistance
R	Electrical resistance measured at Van der Pauw method
$n_{CH_4(c)}$	Molar amount of converted methane
$n_{CH_4(w)}$	Molar amount of wasted methane
$n_{CH_4(T)}$	Molar amount of total methane inlet
$n_{C_2H_4}$	Molar amount of ethylene
$n_{C_2H_6}$	Molar amount of ethane
n_{CO}	Molar amount of carbon monoxide
n_{CO_2}	Molar amount of carbon dioxide
C_{CH_4}	Conversion percentage of methane
ϕ_{bc}	Methane inlet flow blank test
ϕ_{ic}	Methane inlet flow
$n_{CH_4(b)}$	Molar amount of methane inlet at blank test
ρ_{CH_4}	Density of methane
MM_{CH_4}	Molar mass of methane
$\dot{r}_{CH_4(c)}$	Rate of methane conversion
$h.\nu_0$	Light quantum energy

Chapter 1

Introduction

Considering the history of fuel usage through the development of mankind it is notable the trend on de-carbonisation, or at least the need for it. If we account wood, coal, fossil fuels, natural gas and hydrogen in a timeline respectively, it is clear that the ratio between carbon and hydrogen decreases whereas the specific energy of the fuel increases [1] thus the argument that human society is paving its way into the so called hydrogen era seems to make sense. The average values can be seen in Figure 1.1, that additionally, shows that the chemical nature of fuels become less complex.

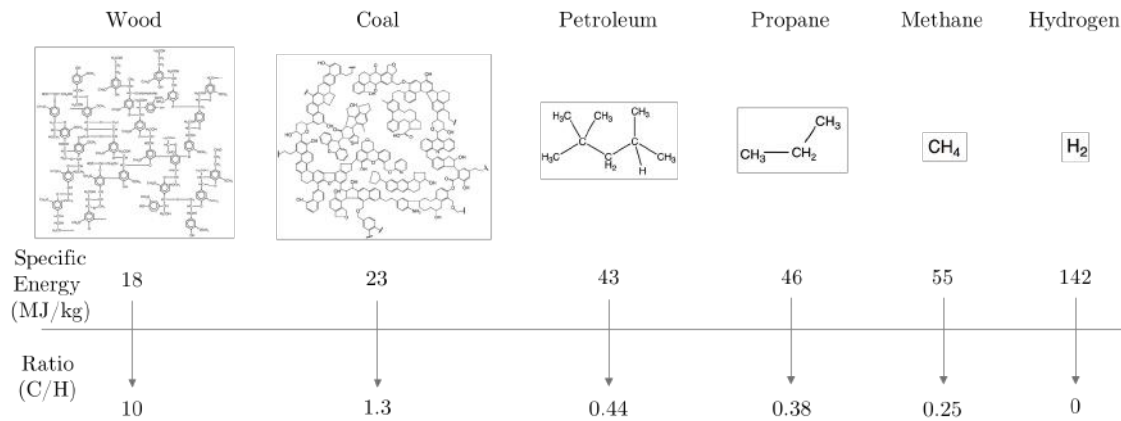


Figure 1.1: Timeline showing how the fuels evolved in terms of C/H and energy density.

Moreover, associated with hydrogen as source of energy, comes the idea of fuel cells. The fuel cell technology is increasingly notable especially by the advances in

fuel cells vehicles related to polymer electrolyte fuel cells (PEFCs). Additionally, in Japan more than 200,000 homes have fuels cell systems for distributed generation of energy.

Fuel cells work by converting a potential chemical energy of a fuel directly into electricity, thus being more efficient than systems that have intermediate steps before delivering power. Fuel cells basically work with a fuel being oxidised in the anode side whilst oxygen is reduced at the cathode side thus delivering an overall reaction that generates electrons, steam and heat.

1.1 Fuel cell - Thermodynamics

Considering an ideal cell, due to the first law of thermodynamics, every reaction Enthalpy (ΔH) is equal to the generated Work (W), in this case electric work, plus Heat (Q), as seen in Equation [1.1](#).

$$\Delta H = W + Q \tag{1.1}$$

According to the second law of thermodynamics [\(1.2\)](#), although the amount of Entropy (ΔS) increases with time if the system remains isolated, the Entropy tends to split until the system reaches thermal equilibrium when interaction with another system occurs.

$$\oint dS = 0 \tag{1.2}$$

In this case, Entropy is compensated by heat transport throughout the system

[2], so that Equation [1.2] can be written as

$$\Delta S = \frac{Q}{T} \quad (1.3)$$

Combining Equations [1.1] and [1.3]

$$W = \Delta H - T.\Delta S \quad (1.4)$$

therefore,

$$W = \Delta G \quad (1.5)$$

The reactions reversible efficiency (η) is given by the ratio between Gibbs free energy (ΔG) and the Enthalpy of the reaction, thus:

$$\eta = \frac{\Delta G}{\Delta H} = \frac{\Delta H - T.\Delta S}{\Delta H} \quad (1.6)$$

Fuel cells present several advantages that outweigh heat engines. **High efficiencies** can be achieved, since no intermediate transformation such as chemical to thermal and then thermal to electric is needed such as in Carnot cycles based system. Fuel cells are **zero or quasi-zero emissions** due to non-hazardous sub-products such as water. In addition, they are **low sound pollution** due to their electrochemical nature and they have **energy co-generation capacity** since the exothermic reactions can produce large amounts of heat [3]. The variety of fuel cells are listed as follows as a function of their electrolyte characteristics.

1.2 Alkaline electrolyte fuel cell - AFC

The electrolyte of this kind of fuel cells is a potassium hydroxide aqueous solution in an asbestos matrix. These fuel cells operate at low temperatures in a range of 50 and 200°C using pure hydrogen as fuel and pure oxygen as oxidizer.

There is no need to use noble metals as catalysts which makes these devices a cheap alternative fuel cell [4]. On the other hand, it needs to operate with high purity gases [3]. R&D for this technology eventually stopped, specially after Nafion creation that could be feasibly used at lower temperatures [5].

1.3 Polymer electrolyte fuel cell - PEFC

This system possesses an electrolyte composed by a proton conducting perfluorinated polymeric membrane. Those membranes have SO_3^- terminal groups that, in the presence of steam, due to an humidified polymeric membrane, link with H_3O^+ conducting the protons generated at the anode.

The performance of such devices depends on their membrane humidification. Although the membrane must be sufficiently humidified to conduct protons, an excess of humidification leads to flooding. The flooding of the membrane impedes the natural flow of the gases. PEFC are considered high efficient devices [6].

As these fuel cells operate at low temperature such as 50-180°C, the maximum temperature allowed in the system will be limited by the water boiling point, thus limiting their efficiency. High pressures are therefore required in order to remove the liquid water reaction products [3].

1.4 Phosphoric acid electrolyte fuel cell - PAFC

Phosphoric acid electrolyte fuel cells use an electrolyte composed by concentrated phosphoric acid dispersed in a silicon carbide matrix. They operate at temperatures around 200°C and use electrodes composed by dispersed platinum particles on a

carbon substrate [7].

They operate with hydrogen as fuel and oxygen as oxidiser and there is no need to use high purity oxygen (CO₂ amounts are acceptable) [3]. However, the use of platinum makes them quite expensive to market widespread.

1.5 Molten carbonate electrolyte fuel cell - MCFC

These devices have an alkaline carbonate electrolyte composed by sodium, potassium as well as lithium operating at high temperatures such as 650°C. Due to the high operating temperature the electrolyte is molten, bringing the need of the utilisation of porous material (alumina) as a support for the electrolyte [8].

One advantage of these fuel cells is that as they operate at high temperatures, the need of using noble metal catalysts is avoided. They operate with hydrogen or methane as fuel and a mixture of O₂ (air) and CO₂ as oxidiser [8].

1.6 Solid oxide fuel cell - SOFC

One of the first solid oxide fuel cell - SOFC - devices was ingeniously proposed in 1930 by BAUR and PREIS [9]. Inspired by the XIXth century Nernst lamp [10-12], they created an apparatus using 15% wt. Yttria-Stabilized Zirconia (YSZ) as electrolyte, an iron based anode and an Fe₃O₄ cathode.

As all fuel cell devices, an SOFC is capable of combining the chemical energy of a given fuel and an oxidiser to convert it directly into electrical power and heat as shown in Figure 1.2. Whilst operating, the main factors that deviate the performance from an ideal behaviour are the ohmic resistance - that generates heat - and the mixture of gases, which prevents fuel utilisation ever reaching its maximum. As SOFCs produces heat it is therefore considered an energy co-generator [2]. The additional heat generated can be used to pressurise steam turbines or simply warm houses.

SOFC single cell operation is given by the ionisation of a fuel (e.g. H₂) at the

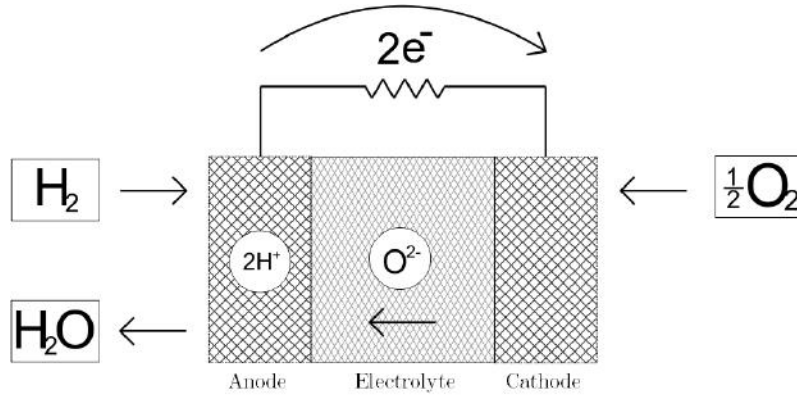


Figure 1.2: Reaction scheme at a single SOFC.

anode side (Equation [1.7](#)); the electrons flow through an external circuit - delivering electrical power - and finally reach the cathode side where the oxidiser (O_2) is reduced (Equation [1.8](#)). After reduction takes place, oxygen ions diffuse through the electrolyte membrane, oxidise the fuel (Equation [1.9](#)) and water is formed as product which, is desorbed away from the anode [\[2, 13, 14\]](#).



Steam concentration increases with fuel utilisation (U_f). Fuel utilisation is denoted by the complementary of the ratio between the amount of fuel that leaves the system without reacting (\dot{m}_o) and the total amount of fuel input (\dot{m}_T), as shown in

Equation [1.10](#).

$$U_f = 1 - \frac{\dot{m}_o}{\dot{m}_T} \quad (1.10)$$

The electric current (I in A) produced is a linear function of the H_2 molar flow reacted (\dot{n}_{H_2} , in $\text{mol}\cdot\text{s}^{-1}$) and the amount of electrons generated by each mol of fuel (e as a discrete non-dimensional unit), as shown in Equation [1.11](#).

$$I = \dot{n}_{H_2} \cdot F \cdot e \quad (1.11)$$

where, F is the Faraday factor (in $\text{s}\cdot\text{A}\cdot\text{mol}^{-1}$). Therefore, as the electric power (P) is equal to the electric work performed by the charge, electric current measurement is a simple way to determine the actual amount of fuel used:

$$P = \dot{n}_{H_2} \cdot W = V \cdot I = \dot{n}_{H_2} \cdot \Delta G \quad (1.12)$$

The Nernst standard potential is given combining Equation [1.12](#) with Equation [1.11](#)

$$V_N^o = \frac{\Delta G^o}{e \cdot F} \quad (1.13)$$

The Gibbs free energy represents the total amount of energy available to generate work. It is a function of the equilibrium constant K which depends on the partial pressures of the reactants.

$$\Delta G = R \cdot T \cdot \ln(K) \quad (1.14)$$

Moreover:

$$K = \prod_j \left(\frac{p_j}{p_0} \right)^{\nu_j} \quad (1.15)$$

in which p_j is the partial pressure of a given compound j , ν_j represents this compound stoichiometry and p_0 is a standardisation of pressure (e.g. 1 bar or 1 Pa, as reference). Merging Equations [1.13](#), [1.14](#) and [1.15](#), the Nernst potential is expressed by Equation [1.16](#) [\[2\]](#), [\[15\]](#).

$$V_N = V_N^o - \frac{R.T}{e.F} \ln \left(\frac{P_p}{P_r} \right) \quad (1.16)$$

SOFC single cells present themselves in a variety of configurations such as planar, tubular or even microtubular [\[2\]](#). Planar cells can also be classified by their support material such as the one of the electrodes or the electrolyte. As the ohmic resistance represents one of the most relevant overpotential for the cells, efforts have been made to fabricate this component the thinnest possible. One of the solutions is to manufacture the cells supported by the anode, which allows the electrolyte to be just a few micrometers thick thus decreasing losses by ohmic resistance [\[16\]](#).

Figures [1.3a](#) and [1.3b](#) represent an electrolyte supported and an anode supported SOFC single cell, respectively.



Figure 1.3: Planar (a) electrolyte-supported and (b) anode-supported SOFC cross-section.

1.6.1 Electrolyte

The electrolyte is usually the responsible to name the fuel cell itself. In SOFCs the electrolyte has the role of transporting oxygen ions through its the lattice vacancies or protons (depending if the SOFC is oxygen or proton conducting) from the cathode side to the anode side. The ion conduction in the oxide electrolyte occurs by a thermally activated process called oxygen vacancy hopping thus taking place if the structure possesses enough oxygen point defects [17, 18].

Therefore a suitable SOFC electrolyte must fulfill some requirements. These structures must be dense so as to impede gas leakage, must be ionic conductors (about 0.1 S.cm^{-1}), electronic insulators ($<10^{-3} \text{ S.cm}^{-1}$), stable whilst submitted to high temperatures and to oxidising/reducing atmospheres, and capable of being produced thin enough to prevent high ohmic losses [2]. Regarding mechanical properties, fracture strength over 400 MPa is common [19].

Fluorite, perovskite based structures, brownmillerite-like phases and pyrochlores have shown to be suitable as state-of-art processes of production are available and they are ionic conductors due to oxygen vacancies present in their crystal structure. Some Bismuth oxides have shown greater ionic conductivities than ceria and zirconia-based fluorites under lower temperatures such as 600°C . However Bismuth Oxides also present considerable electronic conductivities and in addition are expensive alternatives [20, 21].

Fluorite materials used as solid electrolytes

Fluorite materials are known to possess a face centred cubic (fcc) structure of cations and anions occupying its tetrahedral sites as shown in Figure 1.4. Fluorite type materials, specifically Ytria-Stabilised Zirconia, have been used in SOFCs since their beginnings with BAUR and PREIS [9] as the first electrolyte material. Through the years significant improvements were done on such materials aiming to achieve higher ionic conductivities with thinner structures [22, 23].

ZrO_2 , CeO_2 and Bi_2O_3 , are the most used fluorite type materials as SOFC elec-

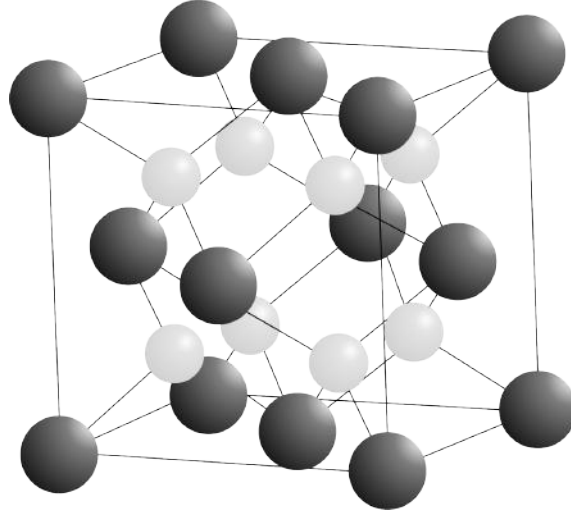


Figure 1.4: Fluorite Structure - A = Darker atoms (cations) and B = Brighter atoms (anions).

trolyte. The Kröger-Vink notation shows (Equation [1.17](#) [\[24\]](#), cations A (Zr^{4+} or Ce^{4+}) host acceptor cations B (Gd^{3+} , Sm^{3+} or Y^{3+}) thus introducing oxygen vacancies.



The concentration of vacancies is a function of the amount of dopant observed on Equations [1.18](#) and [1.19](#).

$$\sigma_{ion} = e^- \cdot n \cdot \mu \quad (1.18)$$

$$\sigma_{ion} = A[V_O^\bullet][1 - V_O^\bullet] \exp\left(\frac{-E}{R.T}\right) \quad (1.19)$$

The e^- represents the electric charge, n the number of ionic vacancies and μ their mobility [\[2\]](#). The deductions expressing the pre-exponential factor A are treated in detail in KILNER [\[25\]](#). Equation [1.19](#) shows that the ionic conduction is a thermally

activated process and depends on the amount of dopant both factors that directly influence on oxygen vacancies density and mobility. However, it may be stated that deliberately raising the dopant amount will increase the oxygen vacancy density. On the other hand, experimental data has confirmed that the ionic conductivity reaches a maximum at a dopant concentration of about 10-20 mol % dopant.

The gradient of oxygen partial pressure between the electrodes is the driving force for electricity production in an SOFC. Therefore it is correct to state that a highly reducing atmospheres at the anode and a highly oxidising one at the cathode should result in higher power densities. Acceptor doped Ceria at high temperatures and low oxygen partial pressures may form oxygen vacancies generating two electrons located on the periphery of Ce^{3+} . This characterises the formation of small polarons that increases electronic conductivity depleting the electrolyte material [26]. Zirconia based materials are found to present lower oxygen partial pressure at temperatures such as 850°C thus showing themselves as more suitable materials for high temperatures than Ceria based ones [27].

The effect of microstructure characteristics such as grain boundaries and grain size interferes directly in total electrical conductivity of polycrystalline electrolyte materials. For instance, the amount of impurities and secondary phase segregations throughout its microstructure causes lattice mismatches that deplete ionic conductivity in regions such as grain boundaries. AC impedance spectroscopy is used to measure and separate intra-grain and grain boundary contributions on ion conducting resistivity [28]. Grain boundary conductivity is known to be 2-3 orders of magnitude lower than intra-grain conductivity [29-31].

Some ionic conductivity curves are presented in Figure 1.5 for various solid electrolyte materials.

Perovskite materials used as solid electrolytes

Some groups have investigated the ABO_3 structures that are found to present ionic conductivity by hopping mechanism [33, 34]. However, it was further suggested that

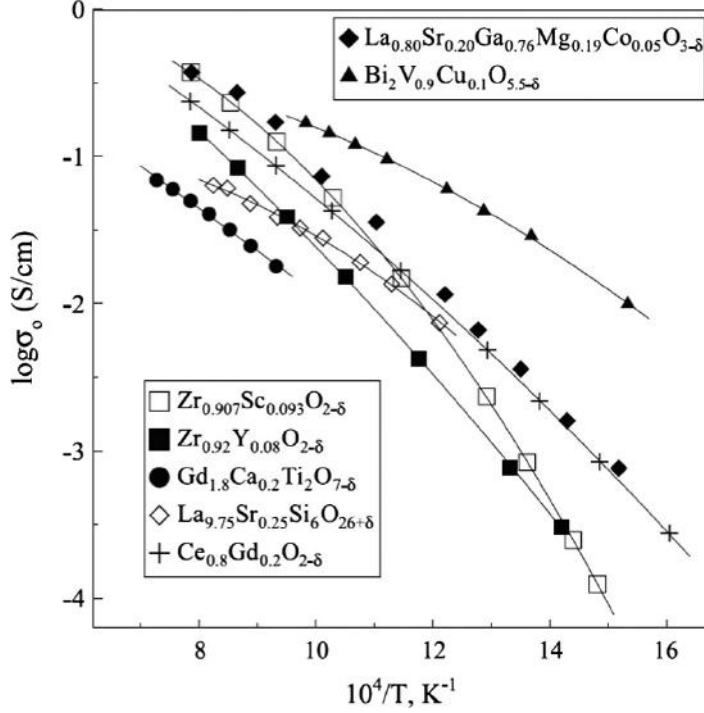


Figure 1.5: Ionic conductivity of solid electrolyte materials. (Reprinted with permission from Elsevier - Ref. [32]).

such perovskite lattices do not allow interstitial diffusion easily, thus presenting high energy barriers [26].

Some Lanthanide-based perovskites have been intensively studied as electrolytes [35–38]. The LnBO_3 can present B as Al, In, Sc and Y that shows great mechanical compatibility and reasonably easy fabrication processes. The greatest concerns are their poor ionic conductivity as well as high p-type electronic conduction in oxidising atmospheres. For that matter, aluminate-type perovskites are being used as protective layers on the anode side of LaGaO_3 electrolytes [39, 40].

1.6.2 Cathode

SOFC cathodes promote the oxygen reduction through their porous channels into bivalent oxygen ions. The reaction occurs promoted by electrons that arrive from the external circuit and are accepted by oxides in the cathode that have the proper activity to absorb oxygen molecules and thus facilitate their reduction by those electrons. Oxygen reduction usually takes place at specific sites called triple phase boundaries - TPB - represented by an interface of cathode oxide material, electrolyte

material and a gaseous oxidiser, such as oxygen. After being reduced, oxygen ions diffuse through the electrolyte to the anode/electrolyte interface.

The existence of the Triple Phase Boundaries - TPB - was first reported in the 1920s. The TPB structure consists of an interface between the ionic conductor (electrolyte material), the electronic conductor (anode or cathode material) and the gas. Concerning cathodes, electrons arrive serving as supply to reduce oxygen molecules inside the electrode channels. These oxygen ions diffuse through the electrolyte material to the anode. This process describes the oxygen reduction in SOFCs cathodes regardless of its microstructure [26], and is depicted in Figure 1.6.

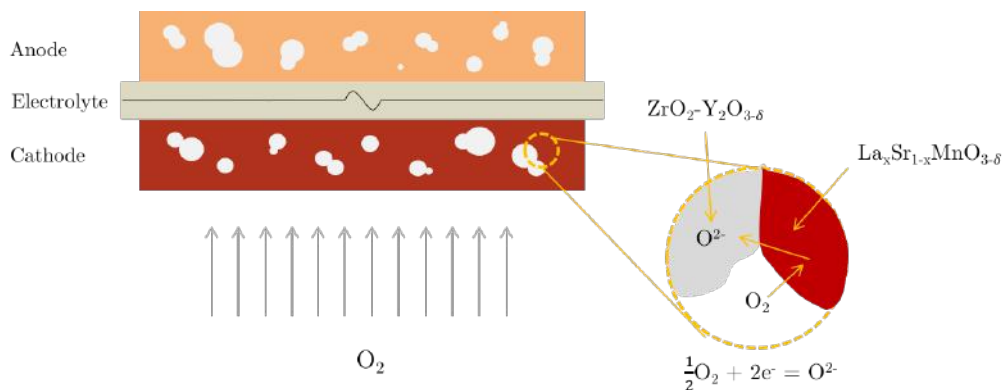


Figure 1.6: Cathode TPB illustration in an LSM/YSZ system.

Thus, for the reactions to occur, cathode materials should be compatible with the electrolyte material. Therefore they must be thermal expansion compatible, possess chemical stability at high temperatures and under oxidising atmospheres, they also must have chemical activity to adsorb oxygen molecules so as to catalyse the reaction, and have high ionic and electronic conductivity. Yet they must be sufficient porous as well as cost effective [41-44]. The first material to be used as cathode in SOFCs was platinum but its high cost made the application infeasible.

Perovskite-based materials have been widely used as SOFC cathode. These materials have shown high activities and stability under the required conditions with reasonable cost effectiveness [45-47].

Perovskite materials used as cathodes

Perovskites are oxides known by possessing larger cations at the *A-sites* with valence n , smaller cations at *B-sites* with valence $(6-n)$ and six O^{2-} ions, as depicted in Figure 1.7. Therefore, those features determine the ABO_3 structure of such materials.

The geometric distribution of a perovskite is given by the Goldschmidt's tolerance factor in Equation 1.20. The tolerance factor determines a range - $1.0 > t_g > 0.75$ - in which the perovskite is stable [2].

$$t_g = \frac{(r_A + r_O)}{\sqrt{2} \cdot (r_B + r_O)}, r_i \text{ are the radii of each ion} \quad (1.20)$$

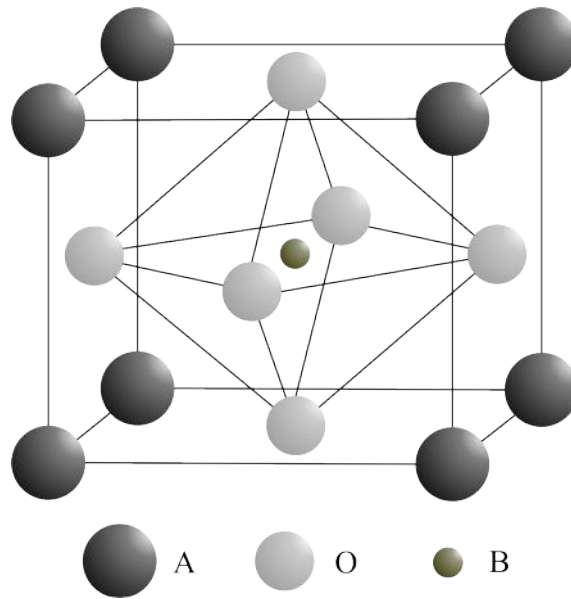
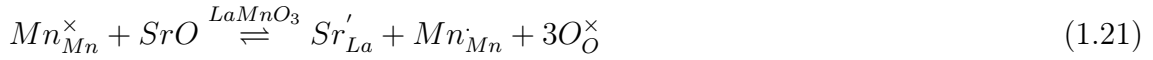


Figure 1.7: Perovskite structure - Larger cations on A-sites and smaller ones at B-site. (Adapted from Ref. [2] and Reprinted with permission from Elsevier).

Although $LaMnO_3$ structures are naturally found as orthorhombic, they suffer a phase transformation into rhombohedral at temperatures such as $600^\circ C$. This phase transformation relies strongly on oxygen partial pressure thus on stoichiometric imbalance. On the other hand, doping $LaMnO_3$ with lower valence cations, causes a deficiency of *A-sites*, increasing the transformation temperature. On materials such as $La_{1-x}Sr_xMnO_{3-\delta}$ - Lanthanum-Strontium doped Manganite (LSM) - the transformation to the cubic structure occurs at $1000^\circ C$ [48-54].

In most cases, undoped perovskites have low ionic conductivity, thus partial substitution of *A-sites* with acceptor cations such as Sr^{2+} , Ca^{2+} or Ba^{2+} or even the reduction of *B-sites* ($\text{B}^{3+} \rightarrow \text{B}^{2+}$) promotes oxygen vacancies which is the requirement for ionic conduction. Although Sr is used as dopant to enhance ionic conductivity, it does not increase the oxygen vacancies but rather oxidises manganese ions thus increasing the electron-hole concentration and improving electrical conductivity [55]. The doping effect is depicted in Equations 1.21 and 1.22.



thus [49]:



For intermediate temperatures - IT-SOFC - materials such as $\text{Ln}_{1-x}\text{Sr}_x\text{Co}_{1-y}\text{Fe}_y\text{O}_{3-\delta}$, (Ln=Lanthanide) appear as a promising choice, showing high electronic and ionic conductivity as well as reasonable catalytic activity to oxygen reduction [56-59].

In addition, the linear behaviour between electrical conductivity and $1/T$ suggests that the small polaron mechanism acts over the charge transfer process [60]. Moreover, the oxygen partial pressure tends to highly influence on electrical conductivity in perovskites. Other than that, lanthanum manganite, as aforementioned, exhibits both excess and deficiency of oxygen depending on oxygen partial pressure.

Therefore, at low oxygen partial pressure manganese is reduced thus positive charge compensates and the perovskite becomes oxygen deficient. On the other hand, at normal SOFC cathode operation conditions (high oxygen partial pressure) the perovskite becomes negatively charged thus with oxygen excess [61].

Manganese oxidation in LSM cathodes could be compensated by both oxygen

interstitials or cation vacancies. However, due to the closed packed perovskite structure the oxidation is most likely to occur by cation vacancies. Studies via neutron diffraction and high resolution microscopy [52, 62, 63] have confirmed this statement. Thus this excess of oxygen in LSM cathodes can be explained in terms of Schottky disorder.

The development of techniques capable of determining the diffusion coefficient as well as the surface exchange coefficient in new cathode materials is very important to incur on the viability of such compounds. For that matter, some works have been carried out some works with O^{16}/O^{18} isotope exchanging giving significant answers about a variety of cathode materials [39, 64].

1.6.3 Anode

The anode is one of the most important structures in an SOFC, being responsible for the fuel oxidation. This reaction takes place at the anode triple phase boundary (TPB) where electrolyte, anode, and gaseous phase meet. The anode TPB is therefore composed of the anode electrocatalytic and electronically conducting phase, the electrolyte phase which is an ionic conductor, and the gaseous fuel. The process of hydrogen oxidation can be written in Kröger-Vink notation as Equation 1.23 [65] showing hydrogen gas being oxidised by oxygen ions transferred by electrolyte material, generating electrical current, water vapour and leaving an oxygen vacancy behind.



Figure 1.8 exemplifies the anode side TPB and the electrochemical reactions that take place.

Several material requirements must be met simultaneously. The anode material must be compatible with the electrolyte material concerning thermal expansion char-

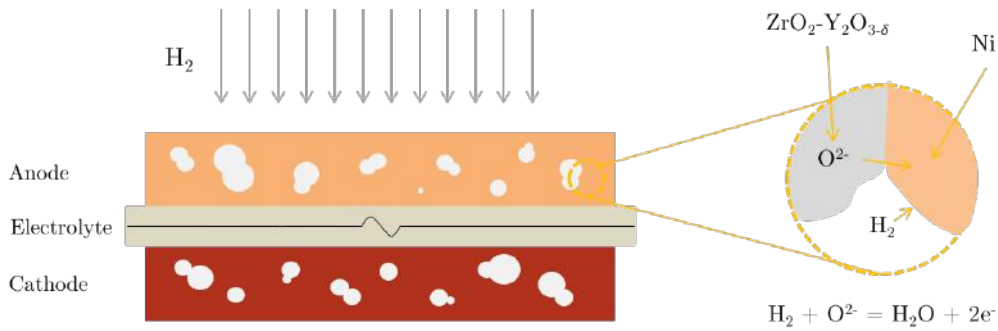


Figure 1.8: Anode TPB illustration in a Ni/YSZ SOFC.

acteristics, it must be chemically stable at high temperatures and under reducing atmospheres, it must possess chemical activity to adsorb the fuel molecules to then catalyse the reaction of oxidation and/or molecule cracking; have high electronic conductivity and a high surface area. Moreover, nowadays it is common that the anode material is required to directly catalyse conversion of hydrocarbon fuels such as natural gas or ethanol, without being affected by carbon formation [2, 26, 65, 66].

Due to all the aforementioned requirements, a careful materials selection has to be made. Inspired by the field of heterogeneous catalysis, noble and transition metals were the first materials to be used as anode electrocatalysts. Initially, platinum was used due to its known great catalytic activity to convert hydrogen. Although platinum works well in the beginning, it starts to lose adhesion with the electrolyte in long-term working conditions [67].

During SOFC development several transition metals such as Ni, Co, Mo, Fe, Mn, and Ru were tested as anode catalysts. Amongst those, Nickel has shown superior electrocatalytic activity [2, 68-70]. Despite having the best activity, metallic nickel presents some incompatibilities such as in thermal expansion coefficient with regards to the electrolyte. So far, the addition of YSZ to the Nickel based material has shown to decrease thermal expansion differences between YSZ and its YSZ/Ni composite cermet [71]. Moreover, due to the incontestable importance of the TPB, YSZ plays two remarkable roles in a composite anode: as ionic conductor it increases the occurrence of TPBs in the anode bulk, thus essential in enhancing electrocatalytic activity, and it offers a ceramic “backbone” to provide pores (gas phase access) and

prevent nickel phase coarsening [72-74] to a certain degree.

1.7 Associated Overpotentials

As already said in Section 1.6, Equation 1.16 shows that the Nernst reversible thermodynamic potential depends on the mixture of gases in reaction. In addition, when the cell is in operation there are overpotentials associated to charge and mass transfer [2].

1.7.1 Ohmic overpotential

All materials, other than superconductors, offer some kind of resistance against electric charge flow. Concerning SOFC, electrodes and current collectors offer some resistance to electron transfer and the electrolyte to ionic charge transfer. These influences can be modelled by Ohm's Law in Equation 1.24.

$$\eta_{Ohm} = (\rho_e \cdot l_e + \rho_c \cdot l_c + \rho_a \cdot l_a + R_{col}) \cdot j \quad (1.24)$$

in which η_{Ohm} represents ohmic polarisation, ρ_e , ρ_c and ρ_a electrolyte, cathode and anode ohmic resistivity, respectively, l_e , l_c and l_a electrolyte, cathode and anode thickness, respectively, R_{col} is the ohmic resistance offered by the current collecting system and j is the current density. However, as the electrolyte contribution is far higher than others, Ohm's Law can be simplified to Equation 1.25.

$$\eta_{Ohm} = \rho_e \cdot l_e \cdot j \quad (1.25)$$

Or

$$\eta_{Ohm} = \eta_0 \cdot \exp\left(\frac{E}{R.T}\right) \cdot l_e \cdot j \quad (1.26)$$

Since the electrical conductivity is the inverse of the resistivity ($\rho = 1/\sigma$) thus Equation [1.27](#) [\[75\]](#):

$$\sigma = \sigma_0 \cdot \exp\left(\frac{-E}{R.T}\right) \quad (1.27)$$

in which σ represents the conductivity, η_0 and σ_0 are pre-exponential factors, and E is the activation energy.

1.7.2 Concentration overpotential

The diffusion of gaseous species through the channels of the electrodes - mass transfer - is a species transfer described by the conservation laws. Therefore, Equation [1.28](#) states that the molar amount of the reagents is proportional to the molar amount the products and consequently proportional to the electric charge generated by the electrochemical reaction by each mol of reaction .

$$|\phi_{H_2}| = |\phi_{H_2O}| = 2|\phi_{O_2}| = \frac{i \cdot N_A}{2 \cdot F} \quad (1.28)$$

in which ϕ_i represent each species i mass flow and N_A is the “Avogadro’s Number” [\[2, 15\]](#).

The mass transport in SOFCs electrodes occurs inside narrow pore channels, indicating high probability of collisions between molecules. Moreover, species may also collide, absorb and desorb to the pores solid walls, as enunciated by Knudsen [\[76\]](#).

Regarding electrode supported cells, it is important to introduce a concept called limiting current density. For instance, considering an anode-supported cell, the anode thickness is much higher than the cathode one, thus as KIM *et al.* [77] stated, Equation 1.29 says that:

$$j_{a_l} = \frac{2Fp_{H_2}^a D_a^{ef}}{RTl_a} \quad (1.29)$$

in which $p_{H_2}^a$ denotes H_2 partial pressure, l_a is the anode thickness and D_a^{ef} is the effective diffusion coefficient for the given binary system - H_2 - H_2O . This coefficient depicts the model sensitivity for the occurrence of particles collisions either between themselves or with pore walls. Therefore, variables such as porosity, tortuosity as well as average pore radius have direct influence on this coefficient as shown in Equations 1.30, 1.31 e 1.32.

$$\frac{1}{D_i^{ef}} = \frac{\xi}{\varepsilon} \left(\frac{1}{D_{i-j}} + \frac{1}{D_{i,k}} \right) \quad (1.30)$$

in which D_i^{ef} is the effective diffusion coefficient for the electrode i , ξ is the electrode tortuosity, ε is the electrode pore fraction, D_{i-j} is the amount of diffusional contribution that is delayed by collisions between molecules and $D_{i,k}$ is the amount of diffusion delayed due to Knudsen's effects.

$$D_{i,k} = \frac{4r}{3} \sqrt{\frac{8RT}{\pi M_i}} \quad (1.31)$$

$$D_{i-j} = 0,00133 \left(\frac{1}{M_i} + \frac{1}{M_j} \right)^{\frac{1}{2}} \frac{T^{\frac{3}{2}}}{P\sigma_{i,j}^2 \Omega_D} \quad (1.32)$$

In which r is the average pore radius, M_i is the molecular mass of species i , M_j

is the molecular mass of species j , $\sigma_{i,j}$ is the average characteristic length and Ω_D is the collision integral. Therefore, anode concentration polarisation can be described as in Equation [1.33](#).

$$\eta_{con}^a = -\frac{RT}{2F} \ln \left(1 - \frac{j}{j_{a_l}} \right) + \frac{RT}{2F} \ln \left(1 + \frac{p_{H_2}^a j}{p_{H_2O}^a j_{a_l}} \right) \quad (1.33)$$

Equation [1.33](#) shows that when $j \rightarrow j_{a_l}$, the overpotential tends to infinite thus the SOFC potential is zero. This is consistent with traditional models stating that in high current densities, concentration polarisation takes place thus compensating the potential of the cell.

Analogously to the anode, a limiting current density to the cathode can be formulated [\[77\]](#).

$$j_{c_l} = \frac{4F p_{O_2}^c D_c^{ef}}{\left(\frac{p-p_{O_2}^c}{p} \right) RT l_c} \quad (1.34)$$

Therefore, the concentration overpotential for the cathode can be written as in Equation [1.35](#).

$$\eta_{con}^c = -\frac{RT}{4F} \ln \left(1 - \frac{j}{j_{c_l}} \right) \quad (1.35)$$

The detailed algebraic procedure for Equations [1.33](#) and [1.35](#) depends on the boundary conditions applied to each particular case. A vast number of studies have been reporting their particular modelling conditions [\[78-80\]](#).

1.7.3 Activation overpotential

The activation overpotential shows a non-linear behaviour at lower current densities but do not increases towards high current densities, in constrast to ohmic

polarisation. Activation behaviour relies essentially on materials properties such as electrical conduction, catalytic activity, morphological characteristics as well as external factors such as temperature and atmosphere [2].

Butler-Volmer's theory formulates a function between activation and morphological factor such as TPB density. This function is illustrated by a term called the exchange current density as seen in Equation 1.36 [79] and denotes the rate at which the electrochemical reaction takes place. Therefore, the higher the TPB density, the higher the rate.

$$j = j_0 \left[\exp\left(\frac{\beta e F \eta_{at}}{RT}\right) - \exp\left(-\frac{(1-\beta)e F \eta_{at}}{RT}\right) \right] \quad (1.36)$$

In which j_0 is the exchange current density and β is the transfer coefficient.

At low current densities, $\left|\frac{\beta e F \eta_{at}}{RT}\right| \ll 1$ and $\left|\frac{(1-\beta)e F \eta_{at}}{RT}\right| \ll 1$, thus the current density can be approximated by Equation 1.37.

$$j \approx j_0 \left| \frac{e F \eta_{at}}{RT} \right| \quad (1.37)$$

Thus, the activation overpotential is given by Equation 1.38.

$$|\eta_{at}| \approx \frac{RT}{e F j_0} j \quad (1.38)$$

On the other hand, at high current densities the overpotential assumes a linear behaviour as described by Tafel's Equation 1.39 [81, 82].

$$\eta_{at} \approx \frac{RT}{e F \beta} \ln(j_0) - \frac{RT}{e F \beta} \ln(j) \quad (1.39)$$

Tafel's Equation 1.39 is a linear function - $a + b \ln(j)$ - in which the exchange

current term denotes the particularities of each system being a thermally activated phenomenon and having a strong dependence on TPB distribution throughout the electrode microstructure. COSTAMAGNA and HONEGGER [83] demonstrate in their work an specific model to exchange current estimative.

Finally, with all cell overpotentials stated, the cell final voltage can be described as a function of current density in Equation 1.40.

$$V(j) = V_N - \eta_{Ohm}(j) - \eta_{con}^a(j) - \eta_{con}^c(j) - \eta_{at}(j) \quad (1.40)$$

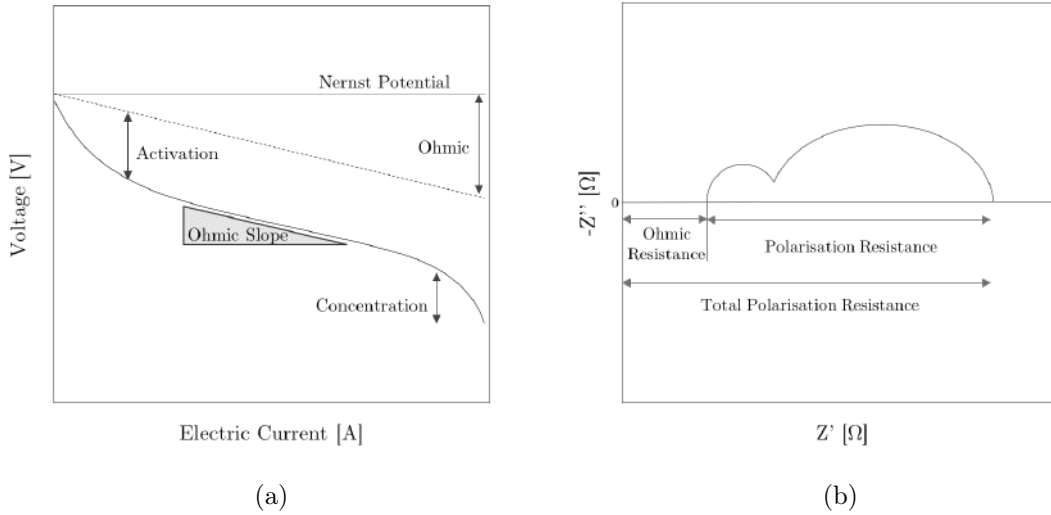


Figure 1.9: SOFC standard (a) I-V curve and (b) impedance plot.

Moreover, the graph in Figure 1.9 depicts Equation 1.40 in which each overpotential contribution is represented. As can be seen, activation losses usually dominates the system at low current densities whereas in the range of practical operation (between 0.8 and 0.5 V) ohmic resistance dominates. At high current densities, concentration overpotential can be experienced as shown in Figure 1.9a.

In terms of impedance, Figure 1.9b presents the Nyquist plot, showing the ohmic resistance represented by the real value that crosses the imaginary axis at zero for the first time. Furthermore, total polarisation is represented by the second time that the real axis crosses the imaginary axis at zero, whereas polarisation (activation plus

concentration) is the difference between them.

1.8 Summary of the chapter and conclusions

Hydrogen-based technologies demand huge transformation of the existent infrastructure for the application to spread in the market [5]. Hydrogen can be produced by several means such as methane steam and dry reforming, gasification of coal, water electrolysis and so on [1]. On the other hand the processes of pre-processing existing fuels to deliver pure hydrogen to a fuel cell is only necessary for the low temperature fuel cells such as PMFC. Considering solid oxide fuel cells (SOFC) that operate at high temperatures (500-900°C), methane decomposition or even electrochemical oxidation can occur within the cell's anode, thus the whole system can be more efficient and less complex to operate.

Furthermore, as SOFC technology starts to leave the first stages of innovation and is targeting towards market spread, biogas direct utilisation could be a feasible alternative of introducing the technology with minor impacts on infrastructure needs. HARDMAN *et al.* [84] make a comparison between Tesla Motors electric cars market strategies against the Fuel Cells Vehicles (FCVs), which are essentially PEFC based. The comparison is valid considering that they are both disruptive innovations and their conclusions show the examples of massive infrastructure investments and how they are crucial for the technology to penetrate the market.

Recently, Nissan Motors have announced their first SOFC based car. The system works basically with a pre-reformer that converts ethanol into syngas ($H_2 + CO$) thus feeding an SOFC stack finally charging a set of batteries. Essentially the car starts with the battery and then keeps running under the fuel cell power. Obviously Nissan objectives are bold whilst using a Solid Oxide Fuel Cell to power a vehicle for the first time and big challenges will be experienced ahead. The complexity of the reformer will be probably one of these challenges. In addition, the reformer will represent more weight and space to be distributed throughout the automobile.

Therefore, a technology capable of using fuels such as ethanol and/or hydrocar-

bons directly in the cells without needing an additional unit such as a reformer, would represent a significant gain towards feasibility. This work aims to develop, optimise and characterise an electrocatalyst to be used as an SOFC anode for direct use of hydrocarbons such as methane. Materials that have been promising for that matter such as cerium oxide [85] and cobalt oxide [86] are to be investigated.

Chapter 2

Objectives

The aim of this thesis work was to develop a ceria-based anode electrocatalyst that could operate directly with carbonaceous fuels. For that matter, the cell is required to mitigate or even suppress coking throughout its microstructure whilst operating with carbonaceous fuels.

As mentioned in the literature review, CeO₂ has shown in many reports to be a promising material for methane internal reforming or even direct usage into SOFCs [87-93]. The addition of copper to ceria-based anodes has been demonstrated to enhance electrical conductivity as well as inhibit coking [93-95]. In addition, adding cobalt to the mixture has shown an increase on catalytic activity [96-98] in the SOFC anode.

2.1 Summary of similar works

FUERTE *et al.* [98] developed a bimetallic anode material composed by cerium, cobalt and copper by the co-precipitation method into an electrolyte Samaria-doped Ceria electrolyte support and an LSM cathode. Their cells were operated in hydrogen, hydrogen mixed with methane and anhydrous methane, respectively, reaching 92, 76 and 13 mW.cm⁻² of maximum power densities at 750°C.

YOO *et al.* [99], on the other hand, used a nickel-based anode with addition of La_{0.2}Sr_{0.8}Ti_{0.98}Co_{0.02}O₃-GDC produced by a solid-state reaction synthesis method

and deposited onto an LSGM electrolyte support. They also operated with hydrogen and methane reaching almost 200 mW.cm^{-2} with methane at 800°C .

ESCUADERO *et al.* [100], produced a bimetallic MoNi-Ce anode by co-precipitation, using an LSGM electrolyte and an LSCF cathode obtaining 360 mW.cm^{-2} whilst operating with pure methane.

FUERTE *et al.* [101] operated their Cu and Cu-Co with CeO_2 anode with hydrogen and hydrogen/methane mixtures. The maximum power densities for the Cu- CeO_2 anode were 64 and 45 mW.cm^{-2} , whereas for the Cu-Co- CeO_2 anode they were 103 and 67 mW.cm^{-2} , for pure hydrogen and hydrogen/methane mixture, respectively. Further work has also been done on ceria-Co-Cu catalysts for direct utilisation of methane or butane [102, 103].

GROSS *et al.* [104] developed a Ce-Cu-YSZ anode with electrodeposited Co with an YSZ electrolyte with an LSM cathode though operating just with hydrogen reaching maximum power density of 120 mW.cm^{-2} at 800°C .

Therefore in the present work, a $\text{CeO}_2\text{-Co}_3\text{O}_4\text{-CuO}$ based catalyst was developed for use in SOFC anode utilising the amorphous citrate method. Different compositions were tested under hydrogen or anhydrous methane as fuels in temperatures ranging from 750 and 850°C . The steps of the project consisted in electrocatalyst productions and characterisation, cells assembly, interface optimisation and characterisation.

The whole work can be summarised into the following steps:

- Electrocatalyst synthesis with different metal concentrations (e.g. Ce:Co:Cu molar proportions of 2:1:1, 1:2:1 and 1:1:2);
- Powder characterisation (X-ray diffraction, thermogravimetry analysis, X-ray fluorescence, particle size distribution, temperature-programmed reduction and DC electrical conductivity tests);
- Cells assembly and electrochemical/impedance testing;
- Synthesis of ceria-metal powders (monometallic) so that the role of each metal

could be understood separately;

- Anode/electrolyte interface improvements;
- Electrochemical testing with hydrogen or methane;
- Cell *post-mortem* characterisation to assess eventual carbon deposition and microstructure evolution.

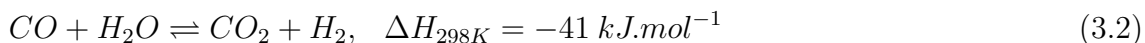
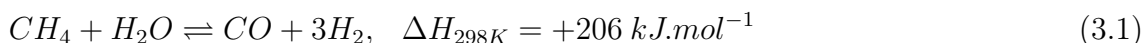
Chapter 3

Literature review

3.1 Reforming processes

3.1.1 Methane steam reforming

The internal reforming processes of hydrocarbons happen to be of high complexity due to a number of parallel reaction paths that can take place. *Methane Steam Reforming* (MSR) is one of the processes most used to produce hydrogen from methane for example, as can be seen in Equation 3.1 [105-107]. This endothermic process is carried out in excess of steam to avoid carbon deposition, followed by the exothermic *Water-Gas Shift Reaction* (WGS), Equation 3.2, to increase the production of hydrogen by adding more water. MSR is generally carried out in reactors filled with nickel catalyst dispersed on an α -Al₂O₃ surface at 900°C.

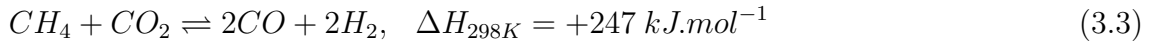


Simulation run with Density Functional Theory suggest that temperatures lower

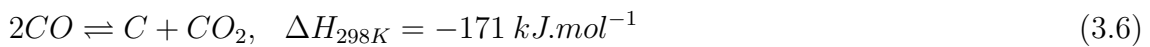
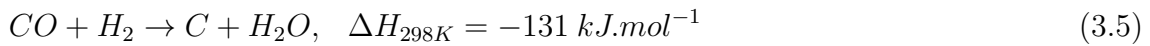
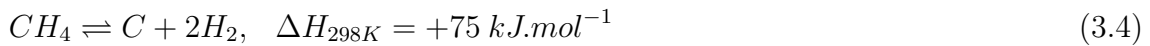
than 500°C should be avoided since the reaction of carbon oxidation becomes rate limited and solid carbon is thus formed [108].

3.1.2 Methane dry reforming

Methane dry reforming (MDR) is also possible in presence of CO₂ as Equation 3.3 states [109]. As can be seen, the methane reforming processes are highly endothermic.

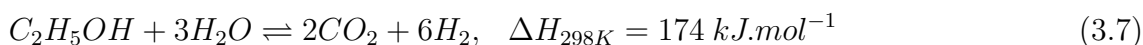


Whilst reforming methane, some paths have to be avoided to suppress carbon deposits over the catalysts. Methane cracking (Equation 3.4) which is its thermal decomposition that produces hydrogen and leaves high concentration of carbon that need to be further oxidised. Carbon monoxide reduction in Equation 3.5 is another reaction that will produce high amounts of carbon in hydrogen-rich atmosphere. Finally the so-called Boudouard reaction in Equation 3.6 also must be avoided.



3.1.3 Ethanol steam reforming

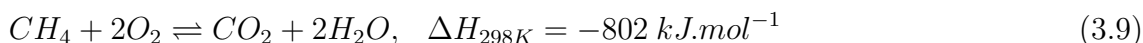
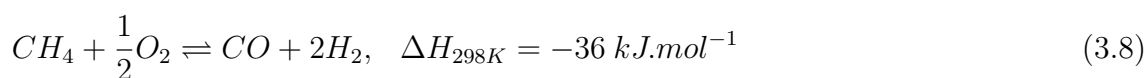
Ethanol steam reforming - ESR - has also been an alternative to hydrogen production [110-112] as stated in Equation 3.7. Note that the enthalpy shown in Equation 3.7 is considered when reactants are all in gas phase. However, if the reactants are liquids the enthalpy increases to 347.4 kJ.mol⁻¹ [113-116].



3.2 Oxidation processes

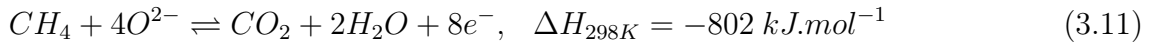
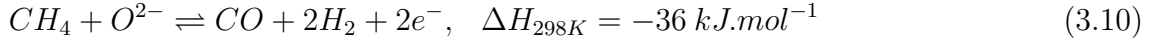
3.2.1 Methane oxidation

Partial oxidation of methane (POM) is another process used to produce syngas and is performed under oxygen flow as shown in Equation 3.8. *Full oxidation of methane* (FOM) shown in Equation 3.9 is a competitive mechanism that produces steam and CO₂ and facilitates reforming. The oxidation has to be run at high temperatures, above 1000°C, however, when using a proper catalyst the process occurs at 700°C. The oxidation is then called *Catalytic Partial Oxidation* - CPOX [107, 117].



Furthermore, due to its electrocatalytical environment, reactions such as *Partial electrochemical oxidation of methane* - PEOM - (Equation 3.10) or even *Full electrochemical oxidation of methane* - FEOM - (Equation 3.11) can take place at anode

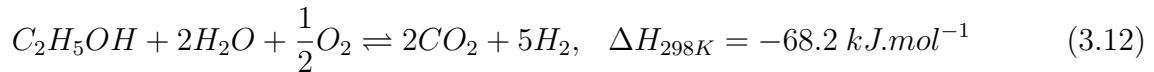
triple phase boundaries (TPB's) sites of an SOFC by influence of the ionic flow of oxygen ions arriving from the electrolyte [118, 119].



Electrochemical oxidation takes place at higher currents, however, hydrocarbon flow must be kept under close control to avoid fuel slip. As SOFCs operate at high temperatures they have the advantage of fuel flexibility due to being able to perform MSR internally. Table 3.1 compares some physical properties of hydrogen, methane and ethanol, considered as SOFC fuels.

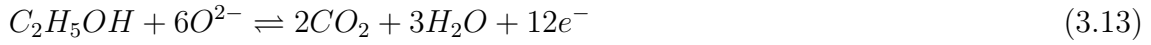
3.2.2 Ethanol oxidation

Catalytic partial oxidation of ethanol - CPOXe - has also been investigated for hydrogen production and is depicted in Equation 3.12. Ethanol's POX reaction works with humidified ethanol and a oxidising agent, generally oxygen.



Full electrochemical oxidation of ethanol (FEOE) is virtually feasible - as in Equation 3.13 - however, given that ethanol decomposition will occur, provided the high temperatures of operation, it can be considered that its sub-products will be

mostly methane, hydrogen, carbon oxides, ethane and ethylene.



Considering the effects of high temperature, when using anhydrous ethanol directly, the products of its decomposition are mainly methane, carbon oxides, hydrogen and undesired C₂ hydrocarbons that can easily crack into carbon rich compounds. Therefore, regarding SOFC operation, the intermediate decomposition of ethane (Equation 3.14) and ethylene (Equation 3.15) are also pathways to be avoided [120].



However, instead of promoting the decomposition of ethane and ethylene, the electrochemical oxidation is also feasible as shown in Equations 3.16 and 3.17 [120].



Concerning C₂ hydrocarbons or alcohols, it has to be taken into account that C-C bonds are easier to break than C-H bonds. Therefore, C-C bond split will probably

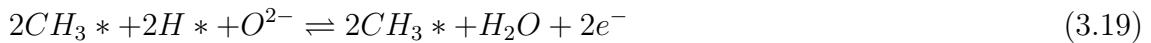
Table 3.1: Fuels physical properties [121].

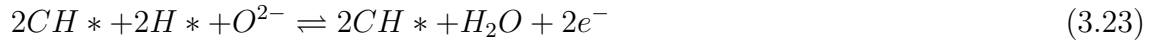
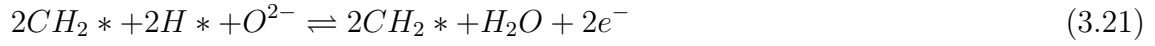
Properties	H ₂	CH ₄	C ₂ H ₅ OH
Molecular Mass (g/mol)	2.01	16.04	46.07
Density (g/l)	0.09	0.72	0.79
Energy Density (kWh/kg)	33.30	13.90	6.61
Melting Point (°C)	-259.20	-184.10	-114.0
Boiling Point (°C)	-252.80	-164.10	78.37
Ignition Temperature (°C)	571.00	632.00	425.00

occurs first, which leads to the conclusion that in C₂ molecules there will be a lot of different radicals within the reaction which makes it very complex to understand. By observing the properties it is noted that methane represents a good choice of fuel especially for being a symmetrical molecule with a decent energy density.

Considering the *Methane Electrochemical Full Oxidation*, the elementary steps that take place before the balanced overall Equation [3.11] are depicted in Equations [3.18] to [3.27]. The denotation “*” means a free catalytic site whereas “X*” means that a certain compound “X” is adsorbed over a catalytic site.

It can be noted that hydrogen bonds splitting and subsequent reaction with oxygen ions occurring when molecules are adsorbed over catalytic sites - Equations [3.18] to [3.24].



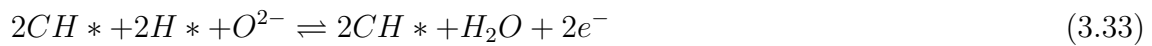
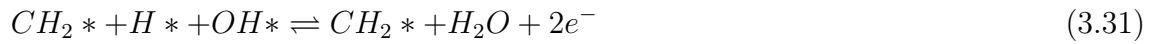


After hydrogen splitting, the electrocatalyst has to provide adequate ability to facilitate carbon oxidation as seen in Equations [3.25](#) to [3.27](#), promoting full oxidation and thus avoiding the deactivation by any remaining carbon over the microstructure.



The same deduction can be held on ethanol's *Full electrochemical oxidation* over-

all reaction in Equation 3.13, through Equations 3.28 to 3.37. The C-H splitting bond is depicted from Equations 3.28 to 3.34.



After C-H splitting and hydrogen oxidation as product, it can be seen the carbon

formation and subsequent removal by oxidation from Equations [3.35](#) to [3.37](#)



3.3 Carbon deposition

One of the main issue of using direct hydrocarbon or carbonaceous fuels into SOFCs fuel stream feeding is carbon bond over the catalyst surface, which deactivates it. CHEN *et al.* [\[122\]](#) were able to theoretically determine the amount of carbon deposited onto a Ni-YSZ catalyst surface by using thermochemical calculations of free energy minimisation. Several syngas compositions were simulated and the results can be confirmed by the C-H-O phase diagram. Table [3.2](#) summarises the reactions explained above, and Figure [3.1](#) shows the ternary phase diagram indicating the carbon deposition area and all reactions listed in Table [3.2](#). The phase analysis clarifies that reactions 8, 9, 12 and 13 are the ones that should be avoided.

Although nickel is a great catalyst to be used in SOFC anodes, it also promotes massive carbon formation when hydrocarbons are being used as fuel. Moreover some other contaminants such as H₂S or HCl can promote the degradation of nickel-based catalysts whilst using hydrocarbons as fuels [\[123, 124\]](#). KIHLMAN *et al.* [\[125\]](#) report that in case of an SOFC system fed with natural gas, the carbon formation highly depends on temperature, feed gas composition and the catalyst that is being used.

Table 3.2: Reactions path of methane and ethanol decomposition.

Case #	Description	Reaction
1	Methane Steam Reforming	$CH_4 + H_2O \rightleftharpoons CO + 3H_2$
2	Methane Dry Reforming	$CH_4 + CO_2 \rightleftharpoons 2CO + 2H_2$
3	Methane Full Oxidation	$CH_4 + 2O_2 \rightleftharpoons CO_2 + 2H_2O$
4	Methane Partial Oxidation	$CH_4 + \frac{1}{2}O_2 \rightleftharpoons CO + 2H_2$
5	Hydrogen Oxidation	$H_2 + \frac{1}{2}O_2 \rightleftharpoons H_2O$
6	Carbon Monoxide Oxidation	$CO + \frac{1}{2}O_2 \rightleftharpoons CO_2$
7	Water-Gas Shift	$CO + H_2O \rightleftharpoons CO_2 + H_2$
8	Methane Cracking	$CH_4 \rightleftharpoons C + 2H_2$
9	Boudouard Reaction	$2CO \rightleftharpoons C + CO_2$
10	Ethanol Steam Reforming	$C_2H_5OH + 3H_2O \rightleftharpoons 2CO_2 + 6H_2$
11	Ethanol Full Oxidation	$C_2H_5OH + 2H_2O + \frac{1}{2}O_2 \rightleftharpoons 2CO_2 + 5H_2$
12	Intermediate Decomposition of Ethane	$C_2H_6 \rightleftharpoons 3H_2 + 2C$
13	Intermediate Decomposition of Ethylene	$C_2H_4 \rightleftharpoons 2H_2 + 2C$

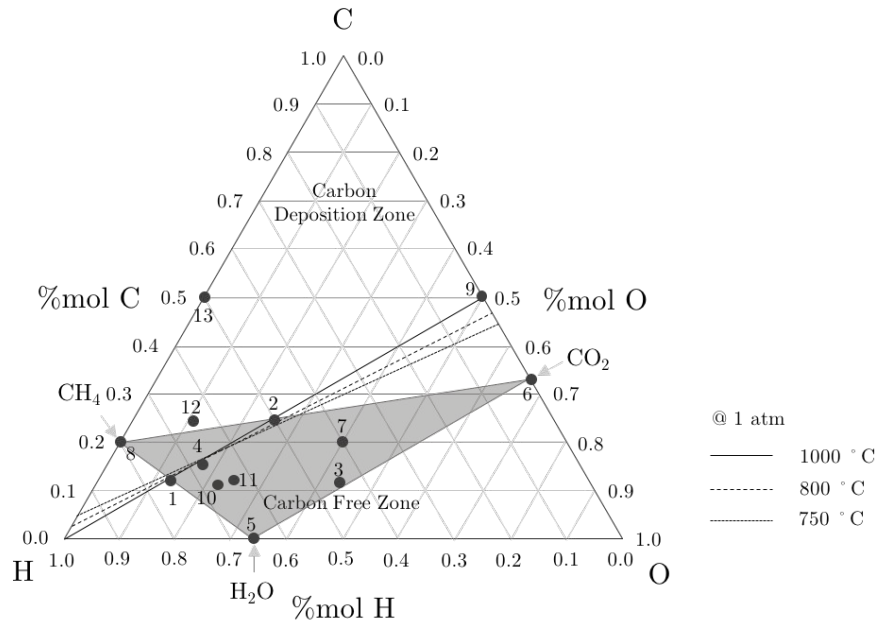


Figure 3.1: C-H-O ternary phase diagram with molar composition for each reaction in Table 3.2. (Adapted and reprinted with permission from Elsevier - Ref. [122])

In addition, at temperatures below 700°C carbon can be formed either from methane decomposition (Equation 3.4) if the steam to carbon ratio (S/C) is low, reduction of carbon monoxide (Equation 3.5), or by the Boudouard reaction (Equation 3.6).

The morphology of the formed carbon depends highly on the operating temperatures and the amount of steam in the fuel composition. KISHIMOTO *et al.* [126] have shown in their work that at a S/C above 2, no carbon formation is observed. On the other hand, ratios below 0.5 has damaged anode microstructure and current collector. Experiments and thermodynamical calculation show that carbon deposition does not occur when using S/C ratios above 1.5 [127-129]. However,

high steam content can cause other problems such as nickel oxidation and issues with water management [130]. ZHAN and BARNETT [131] present an anode with a Ni-YSZ layer covered by Ru-CeO₂ nanoparticles that is able to crack methane. Therefore the product that reaches the anode TPB will be a H₂ and CO rich gas.

Carbon is originally formed in the form of whiskers below 600°C, however, above this temperature pyrolytic carbon may appear [126]. After a few hours of growth, carbon may encapsulate the nickel particles and fill the voids between them. Therefore, carbon may be able to diffuse through the nickel particle bulk and start to grow as nano fibres as seen in Figures 3.2a and 3.2b [132] that will destroy particle structure and delaminate anode layers.

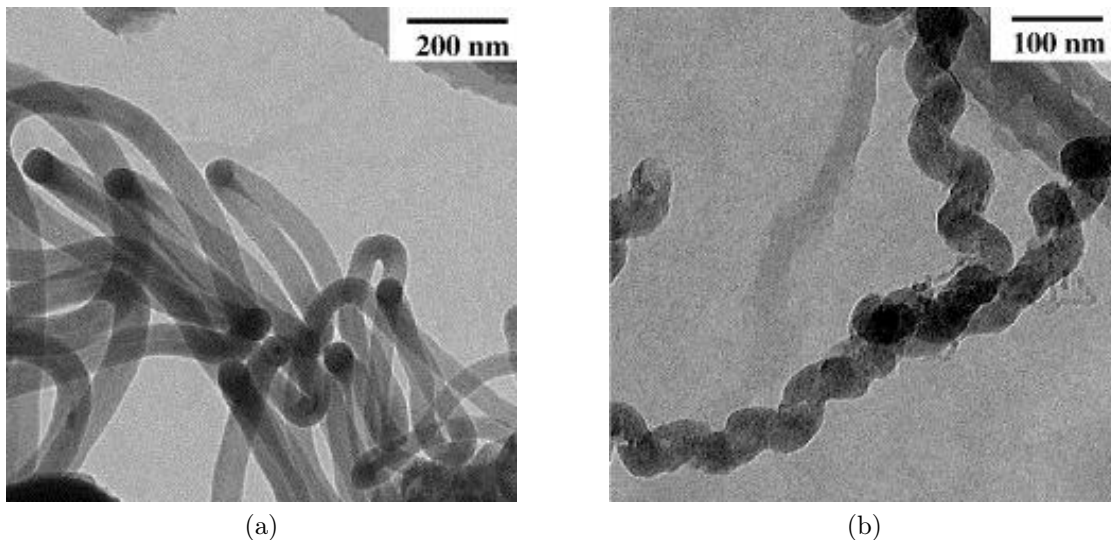


Figure 3.2: (a) and (b) Carbon nano fibres formation. (Reprinted with permission from Elsevier - Ref. [132])

Although thermodynamic calculations ought to be able to predict carbon deposition, real applications show some deviance from theory due to local heterogeneity of gas compositions and operating conditions, thus making experimental validation necessary [133, 134]. Also, it is still an issue to predict the type of carbon formed. Some authors have reported a broad range of conditions which are able to change the type of carbon formed [135, 136].

3.4 Anode poisoning by sulphur

Many H_2S based contaminants present in fuels can easily degrade Ni-based electrocatalysts. Such contaminants chemisorb onto the catalyst surface thus covering and deactivating it [137, 138]. KUROKAWA *et al.* [139] present in their work that CeO_2 added by nitrate aqueous solution can help to mitigate this problem. Yet sulphurous compounds can be formed within the catalyst metal, de-activating it. Formation of Ni_3S_2 is one example when nickel based anodes are concerned. The most significant evidence of sulphur poisoning is the cells voltage drop [140].

The formation of such molecules or intermediate compounds is highly dependent on temperature and $\text{H}_2/\text{H}_2\text{S}$ molar ratio. CHENG *et al.* [141] have calculated the Ni-S phase diagram as shown in Figure 3.3 via Density Functional Theory (DFT).

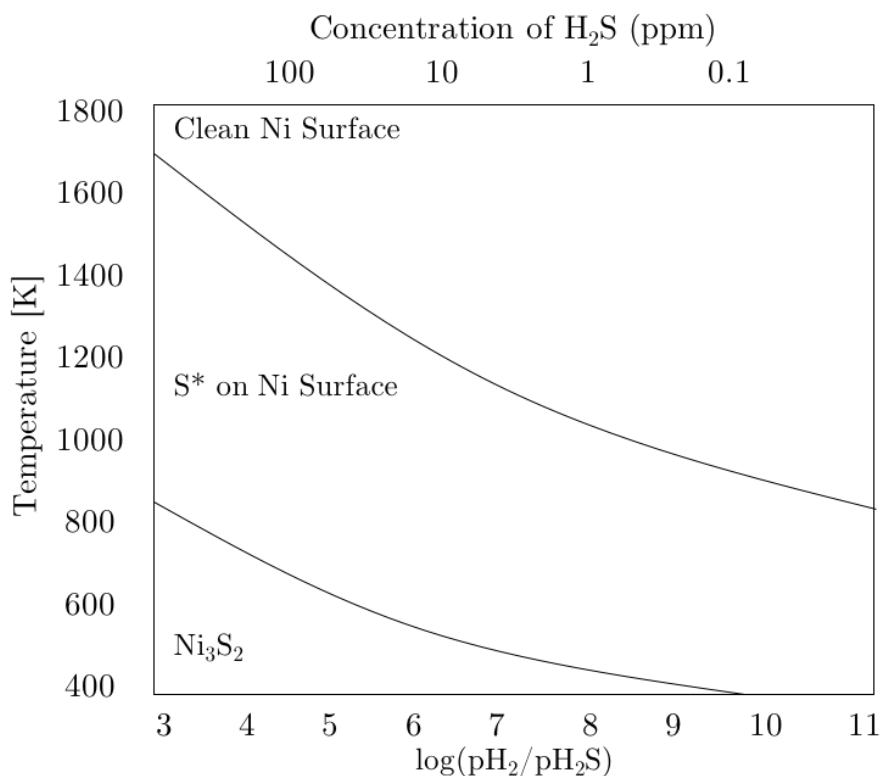
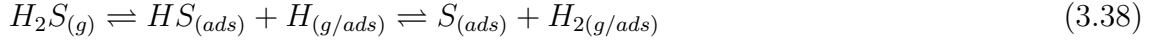


Figure 3.3: Ni-S phase diagram calculated by DFT. (Adapted and reprinted with permission from the Royal Society of Chemistry - Ref. [141])

Sulphur compounds generally interact with the nickel surface in two manners:

chemisorption (Equation [3.38](#)) or sulfidation (Equations [3.39](#)) [\[142\]](#).



At low H₂S concentration and in a range of temperature from 700 to 800°C, Equation [3.38](#) should occur more often, however, at low concentrations, Equations [3.39](#) and [3.40](#), may be dominant, as literature shows [\[105, 143-145\]](#). Also, the electrochemical effect plays a significant role on sulphur poisoning [\[146\]](#). As described in Equation [3.41](#), gaseous H₂S can be split and adsorbed on nickel sites (*) subsequently reacting with oxygen ions (Equation [3.42](#)). Although this electrochemical reaction produces electrons and water, sulphur seems to remain adsorbed on the nickel surface.

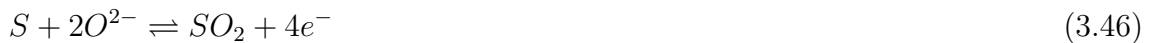


Equations [3.43](#), [3.44](#), [3.45](#), [3.46](#) and [3.47](#) summarise the electrochemical/chemical phenomena that can occur concerning nickel coverage by sulphur compounds [\[147\]](#).

Equation [3.43](#) and [3.44](#) show that the oxidation of H₂S compounds leaves free sulphur dioxide that in spite of producing current might poison the anode material.



On the other hand, Equation [3.45](#), depicting thermal decomposition of H₂S, shows that the products (H₂ and S) are electrochemically oxidised - Equations [3.46](#) and [3.47](#) - also leaving sulphur dioxide.



There is a vast literature about SOFC poisoning by various elements and compounds [\[148-151\]](#). In fact YOKOKAWA *et al.* [\[152\]](#) explains that in addition to fuel impurities, the use of inexpensive raw materials to produce the SOFC may also cause poisoning. SASAKI *et al.* [\[153\]](#), performed a series of electrochemical and thermomechanical experiments to describe nickel catalyst deactivation by sulphur adsorption in relatively low concentrations with chlorine poisoning. It was mainly

observed the sublimation of $\text{NiCl}_{2(g)}$ whilst a partial recovery of cell voltage drop was also distinguished.

3.5 Types of Anodes

3.5.1 Nickel-based anodes

Nickel phase coarsening is the most common phenomenon responsible for decreasing anode TPB length thus increasing cell overpotential [154, 155]. The metallic phase coarsening causes pores to narrow which again decreases the available surface area for reaction. At the same time the growth of the particles reduces the overall available TPB length and gradually interrupts the current flow pathways in the anode. Due to these phenomena, the cermet structure creates a phase dispersion on the ceramic backbone which anchors metallic atoms. Therefore, metal diffusion is reduced thus decreasing the grain growth rate. In addition, the mixture between the electrocatalyst and the ceramic (e.g. YSZ), increases ionic conductivity and the TPB length, and improves electrolyte-anode thermal compatibility [2, 123].

Nickel is an excellent catalyst for hydrogen and methane fuels. Therefore, nickel cermets are the most widely used materials for SOFC anodes. These compounds certainly present one of the best electrochemical performances in long term operation. Nevertheless, Ni-YSZ presents a high carbon activity under typical SOFC operating temperatures and pressures, causing nickel particles to cover with carbon and deactivate. It can be shown from reaction equilibria, that adding the right amount of water to the fuel mixture suppresses this effect [156, 157].

The complexity of controlling the cermet microstructure has been a challenge over the last 10 years of development. Parameters such as porosity, tortuosity, phase continuity, and TPB distribution through the anode bulk are key to minimising cell polarisation [158]. A number of papers have described the complex process of hydrogen oxidation over the Ni-YSZ surface [159, 160]. There are several of papers in the literature concerning long term operation of nickel based SOFC anodes [161]–

[168]. A number of works in the literature state that the required lifetime for state-of-the-art SOFC devices is over 40,000 hours for stationary applications, and over 5,000 hours for transportation application [169-171].

Degradation phenomena could be tied to a series of events such as material transport (coarsening - as aforementioned and depicted in Figure 3.4), deactivation by surface covering as shown in Figure 3.5, and thermomechanic events (stress relief by crack formation) as shown in Figure 3.6 [169, 172].

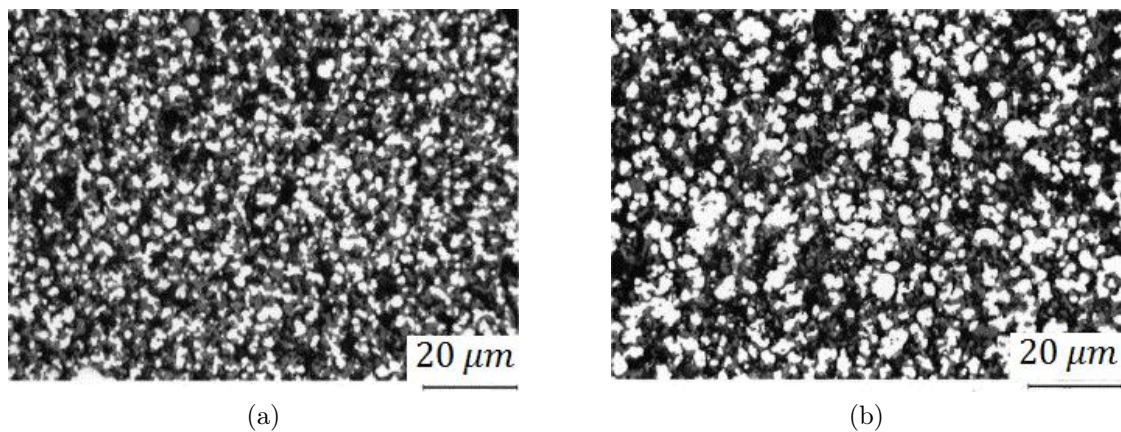


Figure 3.4: (a) Microstructure of anode cermet after reduction and (b) after an exposure for 4000 h in Ar/4% H₂/3% H₂O at 1000°C . (Reprinted with permission from Elsevier - Ref. [163])

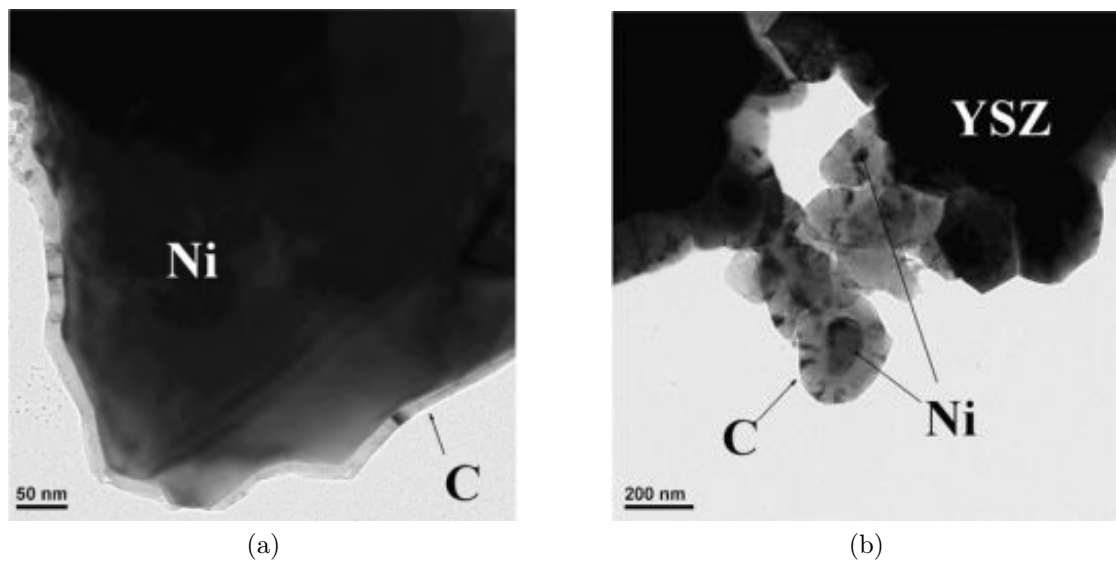


Figure 3.5: (a and b) Transmission electron micrographs of the anode operated with syngas. (Reprinted with permission from Elsevier - Ref. [122])

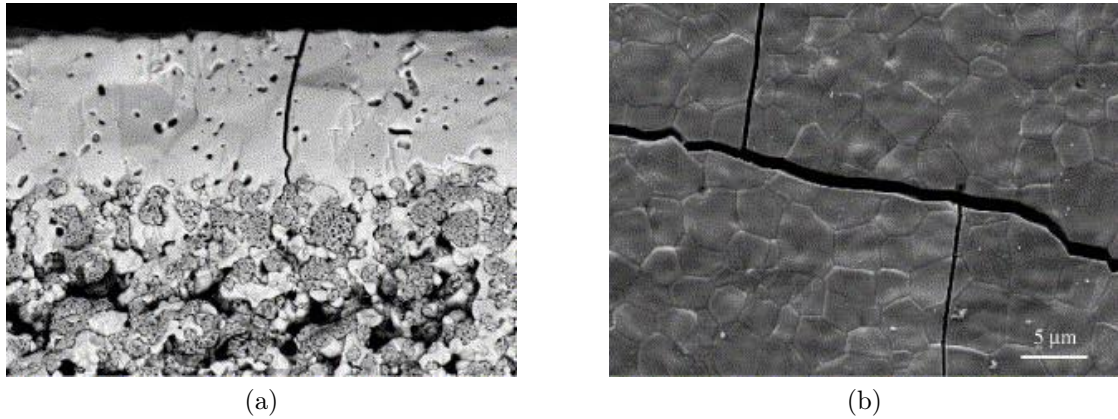


Figure 3.6: Electrolyte cracking (a) cross section and (b) surface. (Reprinted with permission from Elsevier - Ref. [173])

It is very important to determine the proper heat treatment of the electrocatalyst precursor powders so as to avoid sintering shrinkage. Those treatments are denoted powder coarsening and they are applied to control parameters such as powder particle size distribution. It is common to analyse a particle size histogram and realize that its distribution has become narrower or even has turned from a multi-modal to a uni-modal type as the powder was properly calcined. Some studies have been carried out so far regarding the influence of powder coarsening on polarisation effects [154, 174, 175].

PRASAD *et al.* [176] were able to synthesise a Ni-CGO based material by the glycine-nitrate-process which was tested under steam reforming conditions. They observed that the reforming activity decreased whilst in steam rich condition and evidenced, by TEM, that nickel particles had increased drastically in size, from a 5 to 10 nm range to 10 to 20 nm. On the other hand, when steam concentration was kept low, no increase in particle size was experienced thus no decrease on reforming activity. Further work, [177] has demonstrated higher steam reforming activity for a Ni-Ce_{0.75}Zr_{0.25}O₂-based anode. Although the material behaves quite similarly with respect to the amount of steam used, its reforming activity was still higher than that of Ni-CGO.

WU *et al.* [178] operated a modified Ni-YSZ cell with dry methane for over 100 hours with negligible carbon deposition. They reported that the impregnation

with Ag particles, by wet impregnation of an AgNO_3 solution, was able to suppress carbon formation. Their cells were operated at over 500 mW.cm^{-2} of power density with dry methane as fuel.

FARRELL and LINIC [179] compared a Ni-YSZ anode with their Sn/Ni-YSZ catalyst under operation with anhydrous ethanol as fuel for over 20 hours and observed an increase in power density as well as great stability over time. Ni-Sn alloys have also shown to decrease the carbon deposition tendency as compared to monometallic Ni particles.

Furthermore, works in the literature reports Ni-YSZ cermets operating successfully with hydrocarbons when copper particle are incorporated to the microstructure. PARK *et al.* [180] have managed to fabricate a Ni-YSZ anode supported cell by tape casting and introducing copper particles by electroplating. Their cells were able to operate under methane at 700°C resulting in about 240 mW.cm^{-2} of power density, with less carbon deposition than with the Ni-YSZ cells in the same test.

TROSKIALINA *et al.* [181] have presented the work on Ni-YSZ anodes upon Sn infiltration for enhanced durability of cells working on biogas. After 22 hours of operation on biogas the doped cell showed 4.5 times higher performance than the undoped Ni-YSZ benchmark and carbon was not found on the doped cell whereas for the undoped one 0.17 mg/cm^2 was observed by TPO analysis. Even though Sn has a low melting point (231.9°C) the association and calcination over nickel particle surfaces promotes the formation of compounds such as Ni_3Sn , Ni_3Sn_2 and Ni_3Sn_4 . In addition to having higher melting point (from 800 to 1280°C), those alloys are responsible for enhancing the carbon oxidation capacity thus augmenting coking resistance.

Furthermore, there are other works on nickel-based anodes incorporated with various metal loads aiming to suppress coking whilst using carbonaceous fuels. NI-AKOLAS *et al.* [182] report the incorporation of Au and Mo into a Ni-GDC anode. The conclusions were that Au increases the H_2 and CO selectivity of the converted products, the incorporation of Mo does not represent much difference in performance

from the conventional Ni-CGO, however, the association of Au-Mo into Ni-GDC seems to play a synergistic role enhancing the desired selectivity and suppressing coking by a factor of half. Results for SOFC long-term operation with Au-infiltrated cells has also shown to be promising keeping cells voltage as the fuel stream switched from hydrogen to methane and steam [183-185].

Silver has been shown to be a suitable catalyst for CO oxidation thus diminishing the effects of coking. There are works in the literature that report decreasing of coking events by factors of 3 to 4 when Ag and Cu were added to the Ni-YSZ in comparison with cells with addition of Co and Cu [186-189].

3.5.2 Copper-based anodes

Copper has been used in SOFC anodes to enhance electronic conductivity. Yet, since it has a good activity to oxidise carbon, the association of copper with other known catalysts such as ceria has been tested as promising lately [190]. MCINTOSH *et al.* [191] and LU *et al.* [192] report copper's ability to facilitate carbon oxidation and in the mean time enhancing the electronic conductivity of the anode material.

Therefore, copper is used in anodes for direct oxidation of hydrocarbons without too much danger of coking and clogging. Prior carbon films formed between ceria and copper are known to enhance electrical conductivity serving as a bridge for electrons to flow. Cu-CeO₂ anodes have shown to operate better with CO rich fuels than nickel based cermets. Results with syngas and dry H₂ are quite similar regarding Cu-CeO₂ [190] anodes.

Due to copper's low melting point (1086°C) it is not possible to sinter copper-based materials at high temperatures. Thus in case that it needs to be mixed with an electrolyte material such as YSZ it won't be possible to co-sinter them. The solution to this problem are impregnation methods. The impregnation consists basically in incorporating a metal load by adding an aqueous solution of its nitrate onto a porous electrolyte matrix [193, 194]. As the precursor nitrate finds itself solved into water, the resulting metal particles are highly dispersed through the electrolyte porous

microstructure, forming the electrode and through the dispersion showing higher activities. Considering copper, it is common to have an anode matrix such as ceria, both undoped or doped, and impregnate it with copper.

AZZOLINI *et al.* [195] fabricated a tubular anode supported cell in which the anode was composed of a Cu₂O-GDC cermet to be used for intermediate temperatures. They concluded that a single step co-sintering process was successfully performed whilst using sintering aids such as Li₂O that was used to dope the GDC electrolyte.

3.5.3 Perovskite-based anodes

A variety of perovskite and double-perovskite materials are being developed to avoid sulphur poisoning in SOFCs anodes. In addition, as SOFC tend to operate at relatively high temperatures ($> 600^{\circ}\text{C}$), there is a common pursuit on substituting metal catalysts by ceramic oxides thus reducing depletion by coarsening [26, 196].

Perovskites based on chromite and titanate such as $(\text{La}_{1-x}\text{Sr}_x)_{0.9}\text{Cr}_{0.5}\text{Mn}_{0.5}\text{O}_{3-\delta}$ and La-substituted SrTiO₃, respectively, are also being used as anodes in SOFCs. Although their electrical conductivities are not as high as nickel or copper-based anodes, the so called double-perovskite materials such as Sr₂MMoO₆ (M = Mg, Mn, Fe, Co, and Ni) are being investigated, presenting suitable results operating either with hydrogen or methane [196].

Lanthanides-based perovskites such as LaAlO₃ whilst properly doped at B-sites (e.g. by Al) find themselves highly electrical conducting and possess high catalytic activity as well. A-sites strongly influence the oxygen stoichiometry [197, 198]. KIATKITTIPONG *et al.* [199], MOE *et al.* [200, 201], TAGAWA *et al.* [202] discuss all properties related to electrocatalytic oxidation activity, thermal stability and chemical compatibility with the YSZ electrolyte in their work.

SrMoO₃ perovskites have shown one of the greatest electrical conductivities among the oxides whilst doped with trivalent ions such as Cr or Fe on the B-site, thus creating a non-stoichiometry [203, 204]. Therefore high conductivities regarding this type of material [205] such as $10^4 \text{ S}\cdot\text{cm}^{-1}$ can be achieved.

KOLOTYGIN *et al.* [206] evaluated a series of LaCrO_3 , $\text{La}(\text{Ti},\text{Mn})\text{O}_3$ and $\text{Sr}(\text{Nb},\text{Mn})\text{O}_3$ perovskite-based anodes in terms of their electrical conductivity in dependence of oxygen partial pressure, reducibility, and chemical contribution to thermal expansion. Although anode overpotentials were still higher than for Ni-based anodes as shown in their work, important conclusions regarding electrochemical activity and conductivity were drawn.

YOO *et al.* [99] achieved good results using dry methane as fuel directly into their $(\text{La}_{0.2}\text{Sr}_{0.8}\text{Ti}_{0.98}\text{Co}_{0.02}\text{O}_3)\text{-GDC}(\text{Gd}_{0.2}\text{Ce}_{0.8}\text{O}_{2.6})$ anode cells. Maximum power density reached about $197 \text{ mW}\cdot\text{cm}^{-2}$ showing low levels of carbon formation whilst a Ni-GDC control anode had massive coke deposition.

3.5.4 Ceria-based anodes

As a mixed ionic-electronic conductor (MIEC) CeO_2 has shown to be a suitable alternative to be used as anode material in SOFCs. In addition, Ceria also presents a suitable catalytic activity to split C-H bonds and to promote further carbon oxidation being thus adequate to serve as anode material in which the fuel stream is made of carbonaceous gases. Yet ceria has been successfully associated with a variety of other compounds such as copper or cobalt.

Ceria shows reasonable electronic conductivities ($1 \text{ S}\cdot\text{cm}^{-1}$) that can be even increased by adding the previously mentioned metals. Ceria's ionic conductivity can be controlled by properly adding acceptor dopants such as CaO , Y_2O_3 , GdO_3 , and Sm_2O_3 [87-92].

Cu-CeO_2 has been produced successfully by the wet impregnation method. Those anodes have shown high resistance to sulphur poisoning and carbon deposition [207, 208].

YE *et al.* [94] have demonstrated progress on developing Cu-CeO_2 anodes. In their work they have produced a $\text{Cu-CeO}_2\text{-ScSZ}$ anode to run on ethanol at temperatures of 750 and 800°C reaching over $400 \text{ mW}\cdot\text{cm}^{-2}$ of power density. Their cells were able to operate without traces of carbon deposition [94, 95].

VENÂNCIO and MIRANDA [93] synthesised a $\text{CeO}_2\text{-Al}_2\text{O}_3$ based material to be used as functional anode in SOFCs. In further work [209, 210] a comparison was made operating a Ni-YSZ and Cu- $\text{CeO}_2\text{-Al}_2\text{O}_3\text{-YSZ}$ anode directly fuelled by ethanol showing that whilst the former degraded after a few hours of operation, the latter was able to operate for over 200 hours. Results can be seen in Figure 3.7 [210]. CORALLI *et al.* [211], TORRES *et al.* [212] worked on ethanol's balance of plant and have been developing optimising strategies for operational parameters in such plants.

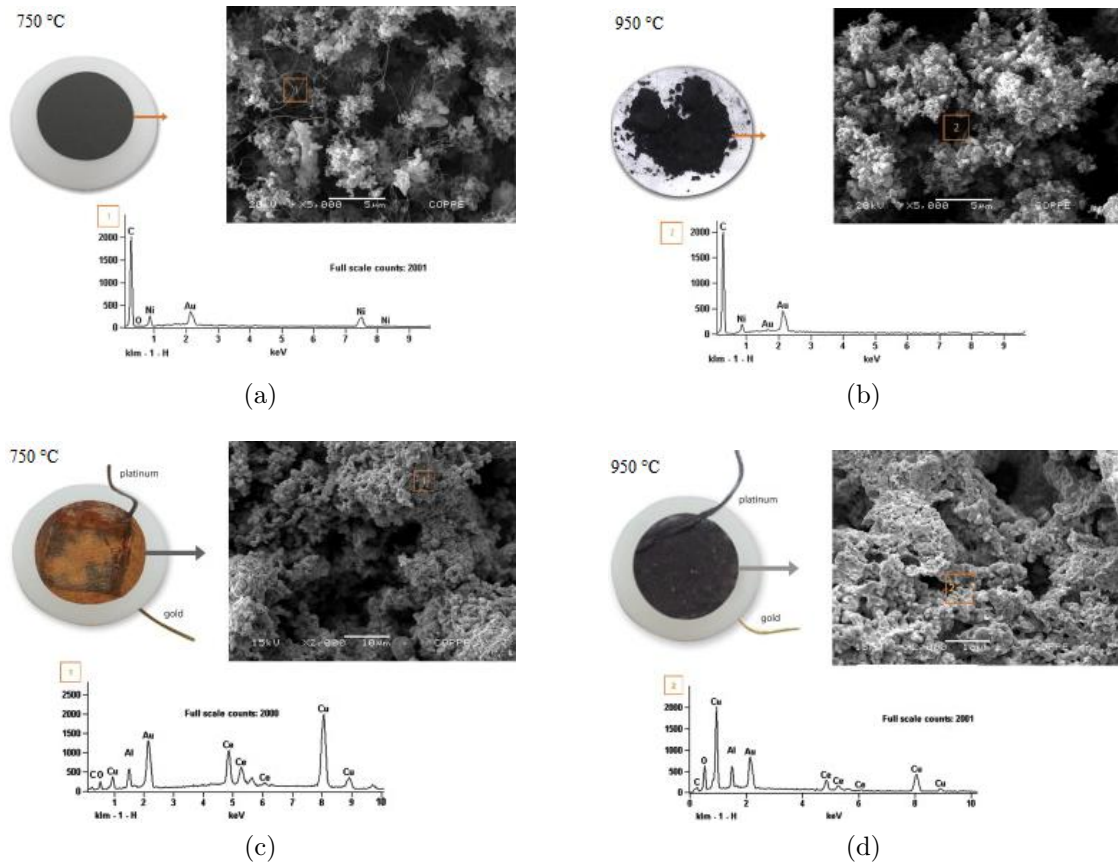


Figure 3.7: Ni-YSZ cell operated with ethanol (a) at 750°C and (b) 950°C - $\text{Cu-CeO}_2\text{-Al}_2\text{O}_3$ cell operated with ethanol (c) at 750°C and (d) at 950°C. (Reprinted with permission from Elsevier - Ref. [210])

Other work has been able to present excellent results by adding cobalt to ceria-based materials to be used as anode for the direct use of methane [96-98]. In such anodes, LEE *et al.* [96] demonstrated the ability of copper to prevent the formation of carbon fibres on the cobalt surface. Cobalt in itself shows high activity to form

carbon, though. The results show that on a sample with the total metal loading composed of cobalt, carbon deposition amounted to over 200% wt. On the other hand, on those samples that possessed 10% wt. of copper and 90% wt. of cobalt, carbon deposition was about 5% wt. [96].

In further work, LEE *et al.* [97] demonstrated that their Cu-Co anode could operate on methane for over 500 hours keeping its electrical potential around 0.6 V with power density over 200 mW.cm⁻². ESCUDERO *et al.* [100] produced a MoNi-Ce anode by co-precipitation synthesis method and ran their LSGM electrolyte supported cell with hydrogen and methane in a range of temperatures from 750 to 850°C. They reported values higher than 350 mW.cm⁻² for maximum power density whilst operating at 850°C with methane. Much effort has been put into cobalt incorporation on a variety of anode materials.

FUERTE *et al.* [98] synthesized a Cu-Co-CeO₂ anode based material by the co-precipitation method obtaining 50 mW.cm⁻² of power at intermediate temperatures (700°C) whilst operating with synthetic biogas (CH₄ = 50-70%, CO₂ = 25-50%, H₂ = 1-5%, N₂ = 0.3-3%). Their SOFCs were tested under a H₂S-rich atmosphere ranging from 300 to 1000 ppm and has shown to perform around 180 mA.cm⁻² over 70 hours. Scanning electron microscopy and energy dispersive spectroscopy were performed unveiling that there was no sign of carbon deposition within the microstructure. GROSS *et al.* [104] produced a Ce-Cu-YSZ anode by impregnation and incorporated cobalt by electrodeposition. Their work presented around 120 mW.cm⁻² at 900°C running with hydrogen as fuel.

In Table 3.3 a variety of SOFCs anodes is listed and sorted by electrical conductivities.

Table 3.3: List of anode materials sorted by conductivity.

Composition	Electrical Conductivity (S.cm ⁻¹)	Operation Temperature (°C)	Carbon Coking	References
La _{0.8} Sr _{0.2} Cr _{0.95} Ru _{0.05} O ₃	0.6 (800°C)	900	No	[213]
La _{1-x} Sr _x Cr _{1-y} Mn _y O ₃	2.4 (950°C)	950	No	[214]
Sr _{0.88} Y _{0.08} TiO ₃	64 (800°C)	900 - 1000	—	[215]
Ni-YSZ	250 (800°C)	750 - 1000	Yes	[216]
SrLaTiO ₂	360 (800°C)	900	No	[157]
Sr ₂ Mg _{2-x} MoO ₆	450 (800°C)	—	—	[217]
Ni-SDC	573 (800°C)	600 - 800	Yes	[216]
Cu-CeO ₂ /Ni-YSZ	600 (800°C)	—	No	[218]
Ni-GDC	1070 (800°C)	600 - 800	Yes	[157] [219]
Cu-CeO ₂	5200 (800°C)	800 - 950	No	[220] [221]
Ni-Cu/SDC	6000 (800°C)	—	Yes	[222]
Cu-GDC	8500 (800°C)	—	No	[223]

3.6 Materials selection - Anodes for carbonaceous fuels

Using a simple approach to justify materials selection through Ohm's law, it can be said that:

$$V = \rho \cdot \frac{L}{A} \cdot I \quad (3.48)$$

or even

$$V = \frac{1}{\sigma} \cdot \frac{L}{A} \cdot I \quad (3.49)$$

Considering electric current represents the amount of charge per second, it follows:

$$I = \frac{Q}{\Delta t} \quad (3.50)$$

Further, assuming Equation [1.11](#),

$$V = \frac{n}{t \cdot \sigma} \cdot \frac{F \cdot e \cdot L}{A} \quad (3.51)$$

In which “ F ” is the *Faraday’s* constant, “ e ” is the number of electrons produced by mol of fuel oxidised, “ L ” is a length in which electrons flow and “ A ” is the cross section area. In order to simplify, $(F \cdot e \cdot L / A)$ can be treated as a single constant “ C ”. Furthermore, considering that n/t will be the amount of electrons available from the electrochemical oxidation of methane and thus a function of its conversion and selectivity to H_2 and CO , n/t may be re-written as:

$$\frac{n}{t} = \dot{n}_{CH_4} \cdot Y_{H_2+CO} \quad (3.52)$$

In which \dot{n}_{CH_4} is the molar flow of methane in time, and Y_{H_2+CO} is the methane conversion yield. The yield is given by the methane conversion percentage times the H_2 and CO selectivity:

$$Y_{H_2+CO} = C_{CH_4} \cdot S_{H_2+CO} \quad (3.53)$$

Thus finally:

$$M_V = C \cdot \frac{\dot{n}_{CH_4} \cdot Y_{H_2+CO}}{\sigma} \quad (3.54)$$

The ratio M_V represents the amount of fuel that has to be available to generate a certain amount of current that a certain material is able to carry, or vice-versa. In other words, it represents the limit between current physical transport and fuel utilisation kinetics. By plotting these contributions in a chart it is possible to select

the materials that provide higher yields of fuel selectivity and suitable electrical conductivity to serve as anode.

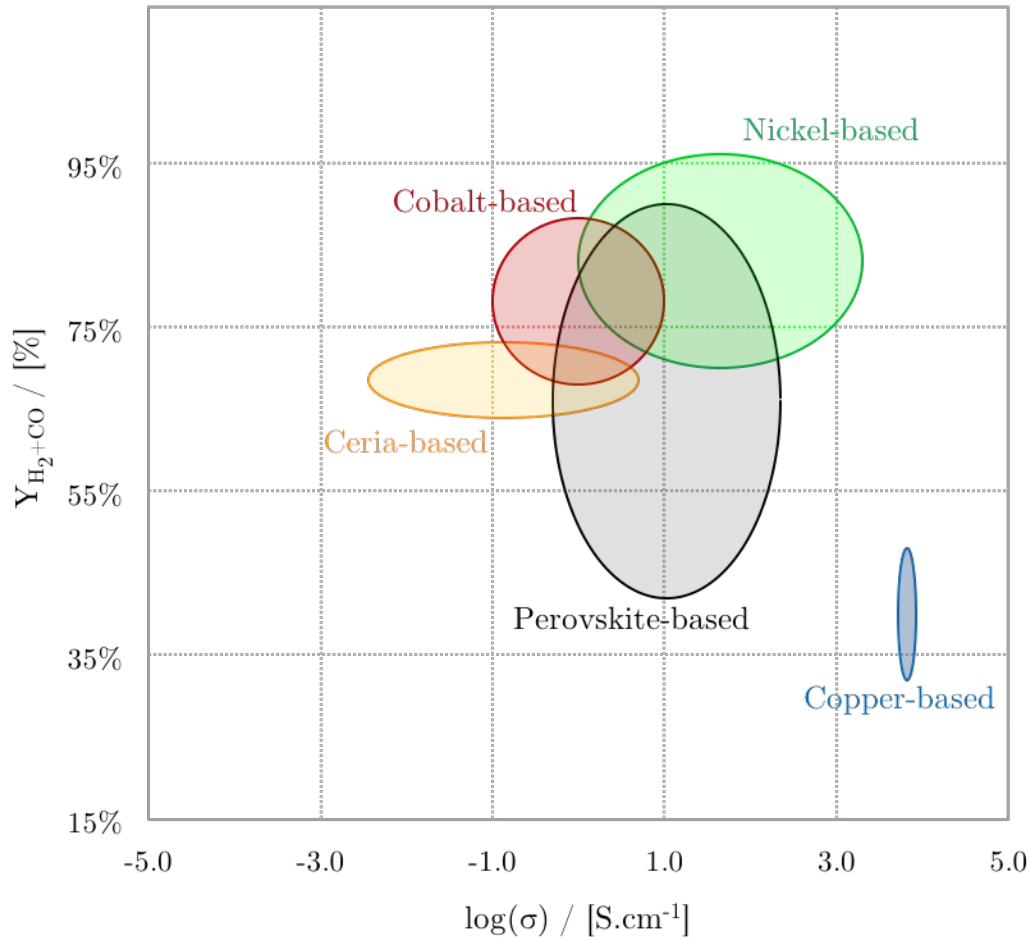


Figure 3.8: Materials Selection - Simplified Bubble chart. (Data to generate the chart is a result of approximate ranges found in the literature. Perovskite-based [26, 206, 224, 225], ceria-based [226–228], nickel-based [26, 222, 229, 230], copper-based [157, 231, 232] and cobalt-based [98, 233].)

Observing the graph in Figure 3.8, conclusions regarding the variables cited might be drawn. For example, although nickel-based anodes seem to be a more suitable choice it has to be taken into account that almost all these types of materials present massive coke formation during direct utilisation of hydrocarbon fuels. The alternatives found in the literature about nickel-based anode operating with carbonaceous fuels are mostly related to reforming or oxidation thereby mixing the fuel with oxidising agents so the carbon can be removed or even avoided [234–239].

Copper-based materials, on the other hand, present the highest conductivity val-

ues though low activity for converting methane being, in general, a poor catalyst. However, the activity of copper-based materials can vary substantially whilst associated with oxides such as ceria. The strategy to avoid carbon deposition in this case lies in the addition of copper that usually forms a thin film over the catalyst that allows carbon to be oxidised easier [240, 241].

Ceria-based materials present great activity for methane conversion, as said, but problems with low conductivity are to be taken into account. Again, the association with materials such as copper have shown that those cermets can be very suitable to be used as electrocatalysts in anodes. For the anodes composed mostly of ceria, the main strategy is to have a catalyst less prone to carbon deposition or that facilitates carbon oxidation by its enhanced oxygen storage capacity [242-246].

Perovskite-based materials, seem to be very promising as anodes for direct use of methane. Those materials present a vast range of conductivity as well as high activity for methane use. Since perovskites are oxygen deficient structures they have the ability of storing/releasing oxygen, which facilitates carbon to be oxidised on the catalyst surface [247-249].

Cobalt-based materials, are also an alternative of high catalysing activity that is sometimes even comparable to nickel-based anodes. However, low conductivities are generally found in the literature specially because these materials are characterised in its oxidised state which hinders the electrical conductivity of them. Cobalt, as a transition metal posses high activity such as nickel and when associated with other rare-earth compounds may form oxygen deficient composites which also is used as strategy to hinder coking [98, 233].

Table 3.4, compiles the information about types of anode materials and their reported fuels in the literature, as well as the strategy used to avoid coking and/or sulphur poisoning. It can be seen that when nickel is used, the main strategy is to perform internal reforming by adding water or carbon dioxide through the fuel stream. For the nickel-free materials the strategies lies in more robust solutions such as the possibility to force carbon oxidation by forcing air into the anode, in

the case of the perovskite materials or even facilitate the electrochemical oxidation of the adsorbed carbon by using oxygen-deficient materials such as ceria or even doped-ceria.

Therefore, with this data compilation one main conclusion is the necessity of developing even more nickel-free materials to serve as adequate anode for SOFC operating with carbonaceous fuels. The more obvious way towards this in our opinion is the natural upgrades that ceria-based materials have been suffering over the last few years provided the incorporation of different second phases such as copper, cobalt, iron, zirconium and especially the alloying with YSZ, GDC and Alumina.

Table 3.4: List of anode by material type and the strategy to avoid microstructure depletion.

Anode Material	Carbon/Sulphur-content fuels reported	Strategy used to avoid coking or sulphur poisoning	References	
Ni-YSZ	Methane, Ethanol, Biogas, Syngas, Methanol	Internal reforming (steam and/or dry)	234 , 236 , 237	
Ni-Cu-YSZ	Methane, Ethanol	Cu-rich facets inhibit carbon growth/ Internal reforming (steam and/or dry)	240 , 250	
Ni-SDC	Methane	Internal reforming/Mixing with hydrogen/ Coking was not suppressed	251	
Nickel-based	Ni-GDC	Methane, Ethanol, Syngas	Internal reforming (steam and/or dry)	252 , 253
	Ni-Sn	Methane, Syngas, Biogas	Modifying the catalytic nature of nickel particle	181
	Ni-Au-Mo	Methane, Syngas, Biogas	Modifying the catalytic nature of nickel particle	182
	Ni-Ag	Methane, Syngas, Biogas	Modifying the catalytic nature of nickel particle	186 , 189
	$\text{La}_{0.8}\text{Sr}_{0.2}\text{Cr}_{0.98}\text{V}_{0.02}\text{O}_{3-\delta}$	Methane, Propane	Delay the kinetics of carbon formation/ Air at the anode side to oxidise carbon	254
	$\text{La}_x\text{Sr}_{1-x}\text{TiO}_3$	Syngas/Sulphur-content hydrogen	Resistance to sulphur poisoning	255 , 256
	$\text{La}_{1-x}\text{Sr}_x\text{VO}_3$	Natural Gas/Sulphur-content hydrogen	Resistance to sulphur poisoning	257
Perovskite-based	$\text{SrMo}_{1-x}\text{Ga}_x\text{O}_{3-\delta}$	Methane	Facilitates carbon oxidation due to its oxygen-deficient structure	258
	$\text{LaAl}_{0.5}\text{Mn}_{0.5}\text{O}_3$	Methane	Facilitates carbon oxidation	120
	$\text{La}_{1-x}\text{Sr}_x\text{Cr}_{1-y}\text{Mn}_y\text{O}_3$	Sulphur-content hydrogen	Resistance to sulphur poisoning	214
	$\text{Sr}_2\text{FeNb}_{0.2}\text{Mo}_{0.8}\text{O}_{6-\delta}$	Methane	Easily reoxidised when air is inputted	247
	$\text{Ce}_{0.75}\text{Zr}_{0.25}\text{O}_2$	Methane, Ethanol	Facilitates carbon oxidation	120
	$\text{Ce}_{1-x}\text{Ca}_x\text{O}_{2-\delta}$	Methane	Facilitates carbon oxidation	259
	Cu-CeO_2	Methane, Ethanol	Facilitates carbon oxidation	94
Ceria-based	$\text{Cu-Fe-Ce}_{0.9}\text{Gd}_{0.1}\text{O}_{2-\delta}$	Methane	Facilitates carbon oxidation	221
	$\text{Cu-CeO}_2/\text{Al}_2\text{O}_3$	Methane, Ethanol	Facilitates carbon oxidation	120 , 260
	$\text{Co-Cu-CeO}_2\text{-YSZ}$	Carbon monoxide	Facilitates carbon oxidation	101
	$\text{Co}_3\text{O}_4\text{-CeO}_2\text{-CuO}$	Methane	Facilitates carbon oxidation	101
	Cu-YSZ	Methane, Ethanol	Facilitates carbon oxidation	261 , 262
Copper-based	Cu-CGO	Methane, Ethanol	Facilitates carbon oxidation	263

3.7 Conclusions

Today the state-of-the-art of SOFC operational viability and market introduction relies on materials capable of using complex fuels such as methane or ethanol by the simplest way such as direct utilisation, being able to eliminate all costly and time consuming pre-reforming steps. Moreover, the abundance of methane-rich gases, such as natural gas as well as biogases, on offer is another factor that plays in favour of such efforts to these new materials developments.

As could be seen throughout this work, the ways towards feasibility of SOFCs lie over the fact that they have to be able to operate with abundant fuels such as carbonaceous sources of hydrogen. For that to happen, the requirement of avoiding or even suppressing carbon deposition has be met. The nickel-based materials have always showed to suit as the best catalyst for hydrogen and even for methane and the possible solutions for decreasing carbon deposition in such cases seems to be in the internal reforming aided by steam and carbon dioxide within the fuel stream.

Technically, ceria-based cermets or perovskite-based anodes seem to be playing very well the role of direct carbonaceous fuels electrocatalyst, presenting reasonable results concerning power density values, and facilitating further carbon oxidation. Further oxides association such as ceria and metals (Cu, Co, Ni) are also promising.

Chapter 4

Materials and methods

4.1 Electrocatalyst synthesis

The synthesis of the ceramic powders was performed via the amorphous citrate method. Roughly, the process consists in dissolving the nitrates of each precursor metal into de-ionised water and stabilising its metallic ions with proper amounts of citric acid.

After that, the citrate-nitrate solutions are mixed all together and NH_4OH is added to the solution to neutralise its pH. The solution is then kept at 80°C and under magnetic stirring producing a gel. Still under stirring, the temperature is increased to 90°C to eliminate part of the volatiles. Finally, the synthesis product is kept under atmospheric air at 200°C during 6 hours to produce the synthesis ashes.

Cerium (III) nitrate hexahydrate (MT-02), Cobalt (III) nitrate hexahydrate (MT-04), and Copper (II) nitrate trihydrate (MT-05) were used as precursors. In addition, Citric acid monohydrate (MT-03) was used. The pH was stabilized by adding ammonium hydroxide (MT-01) whilst measured by a pH meter (EQ-06), and kept under magnetic stirring (EQ-04), whilst the temperature was monitored by a thermometer (EQ-15).

The whole process is depicted by the flowchart in Figure [4.1](#). Once the ashes

¹Each material and equipment listed in the present work is detailed at the Appendix I and sorted alphabetically in Tables [9.1](#) and [9.2](#), with reference codes MT-XX and EQ-XX respectively.

were formed they were pulverised in an agate mortar with a pestle and then stored in a glass recipient in the as-synthesised condition.

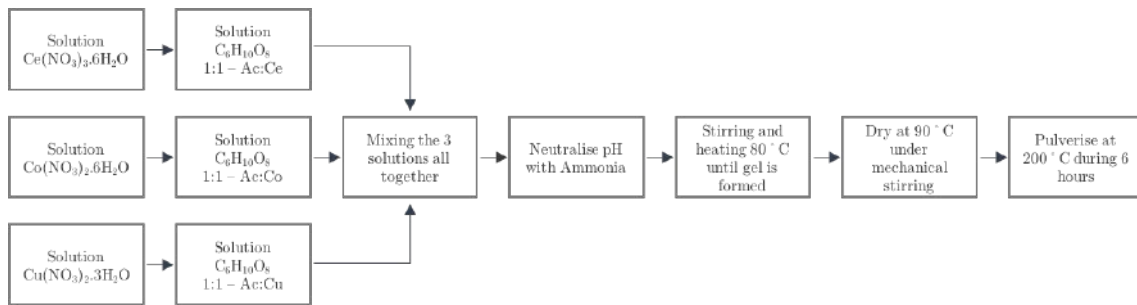


Figure 4.1: Flowchart of the amorphous citrate synthesis.

4.2 Electrocatalyst characterisation

4.2.1 X-ray diffractometry

The intensity of diffracted X-rays is counted by an X-ray detector as a function of diffraction angle. Since the X-ray source emits a beam of known wavelength, the counting satisfies Bragg's Law (Equation 4.1) [264]. In Figure 4.2 the planes of diffraction are represented.

$$2 \cdot d' \cdot \sin \theta = n \cdot \lambda \quad (4.1)$$

in which d' is the distance between atomic planes, θ is the diffraction angle, n is the order of reflection and λ is the wavelength of the X-ray source.

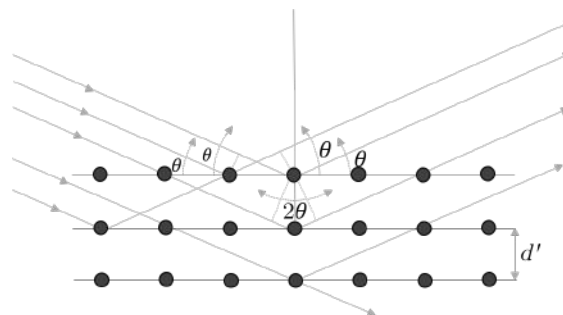


Figure 4.2: Planes of diffraction - representation of Bragg's Law.

Therefore, it is very common to have the representation of Bragg's law in terms of plane spacing d rather than d' in which $d = d'/n$ that originates Equation [4.2](#). Moreover, considering the Miller index (h, k, l) , a relationship with plane spacing can be established taking into account the space group of a given crystal. Table [4.1](#) shows the lattice parameters calculation for seven crystal systems.

$$2.d.\sin\theta = \lambda \tag{4.2}$$

Table 4.1: Plane spacing relationship with lattice parameters for each crystal system.

Cubic	$\frac{1}{d^2} = \frac{h^2+k^2+l^2}{a^2}$
Tetragonal	$\frac{1}{d^2} = \frac{h^2+k^2}{a^2} + \frac{l^2}{c^2}$
Hexagonal	$\frac{1}{d^2} = \frac{h^2+hk^2+k^2}{a^2} + \frac{l^2}{c^2}$
Trigonal	$\frac{1}{d^2} = \frac{(h^2+k^2+l^2)\sin^2\alpha+2(hk+kl+hl)(\cos^2\alpha-\cos\alpha)}{a^2(1-3\cos^2\alpha+2\cos^3\alpha)}$
Orthorhombic	$\frac{1}{d^2} = \frac{h^2}{a^2} + \frac{k^2}{b^2} + \frac{l^2}{c^2}$
Monoclinic	$\frac{1}{d^2} = \frac{1}{\sin^2\beta} \left(\frac{h^2}{a^2} + \frac{k^2\sin^2\beta}{b^2} + \frac{l^2}{c^2} - \frac{2hlc\cos\beta}{ac} \right)$
Triclinic	$\frac{1}{d^2} = \frac{[b^2c^2\sin^2\alpha h^2+a^2c^2\sin^2\beta k^2+a^2b^2\sin^2\gamma l^2+2abc^2(\cos\alpha\cos\beta-\cos\gamma)hk+2a^2bc(\cos\beta\cos\gamma-\cos\alpha)kl+2ab^2c(\cos\gamma\cos\alpha-\cos\beta)hl]}{V^2}$ in which V is the volume of a unit cell.

Crystallography studies have their origin in the observation of symmetrical mineral structures such as quartz, fluorite, pyrite, and corundum. Considering seven crystal systems consisting of 14 Bravais lattices, 32 point groups on the basis of eight symmetry elements, screw and glide reflection axis, the structures can be sorted into 230 space groups. The unit cell geometry, the Bravais lattices and their respective representation symbol for each crystal system are shown in Table [4.2](#).

Taking into account the basic crystallography of the compounds and the experimental data extracted from X-ray analysis it is possible to stochastically calculate the lattice length and angle by adjusting peak shape and width as well as peak relative scale. This technique is called the Rietveld refinement [\[265\]](#).

XRD analysis in this work was performed with a Bruker D8 diffractometer (EQ-17). The 2θ range was 10-90°, varying each 0.02°. Monochromatic radiation $\text{CuK}\alpha$

Table 4.2: Crystal systems and Bravais lattices.

System	Axial lengths and angles	Bravais lattice	Symbol
Cubic	$a = b = c$, $\alpha = \beta = \gamma = 90^\circ$	Simple	P
		Body-centered	I
		Face-centered	F
Tetragonal	$a = b \neq c$, $\alpha = \beta = \gamma = 90^\circ$	Simple	P
		Body-centered	I
Hexagonal	$a = b \neq c$, $\alpha = \beta = 90^\circ$, $\gamma = 120^\circ$	Simple	P
Trigonal	$a = b = c$, $\alpha = \beta = \gamma \neq 90^\circ$	Simple	R
Orthorhombic	$a \neq b \neq c$, $\alpha = \beta = \gamma = 90^\circ$	Simple	P
		Body-centered	I
		Base-centered	C
Monoclinic	$a \neq b \neq c$, $\alpha \neq \gamma = 90^\circ \neq \beta$	Face-centered	F
		Simple	P
		Base-centered	C
Triclinic	$a \neq b \neq c$, $\alpha \neq \beta \neq \gamma \neq 90^\circ$	Simple	P

= 0.15418 nm with acceleration voltage of 40 kV and 30 mA current was used. XRD was applied to all the produced powders both on their as-synthesised and heat treated state, aiming to compare them and observe phase formation and crystallisation. Rietveld refinement was performed over the raw data using FullProf[®] Suite software [266] to confirm the powder composition and calculate lattice parameters. The background was described by a linear interpolation of pre-determined points with refinable heights.

4.2.2 Thermogravimetric analysis

Thermogravimetric analysis - TGA - is a technique that consists of a continuous record of mass changes of samples, whilst temperature is changed. The measurements are made by a thermobalance. The graph produced is called a thermogram or pyrolysis curve [267]

TGA analysis was taken over the synthesised powders in order to determine the temperature of volatiles and nitrates evaporation as well as eventual oxides

decomposition. A NETZSCH TG 209 F1 (EQ-14) was used ranging between room temperature and 900°C with 10 °C.min⁻¹ heating rate and 30 minutes dwelling at 900°C in air.

4.2.3 X-ray fluorescence

When a material is exposed to high energy X-rays or γ -rays it emits secondary X-rays (or fluorescent X-rays). Basically, when excited with enough energy to promote atom ionisation, electrons are expelled from inner layers thus forcing electrons from higher orbitals to take the spot of those at lower orbitals. This process releases energy (photons of characteristic wavelength) that is then quantified by the spectrometer. The counting of these emissions indicates statistically the chemical elements in the sample [268, 269].

X-ray fluorescence was taken in a Bruker S8 Tiger XRF Spectrometer (EQ-19) over pelletised powder samples which were pressed within 2 ton pressure within a 13 mm diameter die after being mixed with wax in a mass ratio of 5:1 for powder to wax. XRF scanning was done during a 18 minutes scan.

4.2.4 Particle size distribution

For measuring the particle size distribution (PSD) of the powders a Mastersizer 2000 by Malvern (EQ-05) was used and the technique consists in measuring a laser scattering occurring whilst the dispersed particles pass through a window.

Samples were prepared by dispersion of around 50 mg of powder in approximately 15 mL of de-ionised water. The solutions were sonicated for 30 minutes. Then each solution was added to the equipment stirrer gradually until approximately 15% of obscuration was achieved. The analysis was carried out in a stirring speed of 1,700 rpm.

4.2.5 Temperature-programmed reduction

Temperature-programmed reduction or TPR is a technique commonly used to determine if an oxide catalyst has the ability of being reduced in hydrogen-rich atmosphere at given temperatures. Therefore, it is a powerful technique to compare different materials giving their ability to absorb hydrogen.

Once the catalyst sample is placed inside the U-tube quartz reactor, the temperature is increased and controlled. A hydrogen containing mixture, such as hydrogen-nitrogen or hydrogen-argon is flowed over the sample whilst the outlet gas is monitored by a thermal conductivity detector (TCD) or a mass spectrometer [270].

TPR was performed on each produced powder using a Quantachrome ChemBET Pulsar TPR/TPD equipment (EQ-08) that ranged from room temperature to 900°C, stepping 5 °C.min⁻¹ over approximately 20 mg of powder in a quartz reactor. The gas mixture consisted of 5% H₂ and balanced N₂.

4.2.6 Electrical conductivity of the precursor oxides

Electrical conductivity tests were carried out on pellets. For pelletising, approximately 1 g of each powder type was uni-axially pressed in a 20 mm diameter cylindrical die, under 2.5 tons of charge, thus causing a stress of 19.5 MPa. After pressed, the pellets were sintered in air at 1000°C for 2 hours.

For electrical measurements, the Van der Pauw method was used in which four silver probes were pasted onto equidistant points of the pellet thickness axis as shown in the scheme of Figure 4.3. Voltage was measured whilst a given charge was applied throughout the inverse diagonal probes as depicted in Figure 4.3. The resistance results were corrected (R_c) using the Van der Pauw geometry correction in Equation 4.3 [271, 272].

$$R_c = \frac{\pi \cdot d}{\ln(2)} \cdot R \quad (4.3)$$

in which R_c is the corrected resistance, d is the pellet diameter and R is the measured resistance.

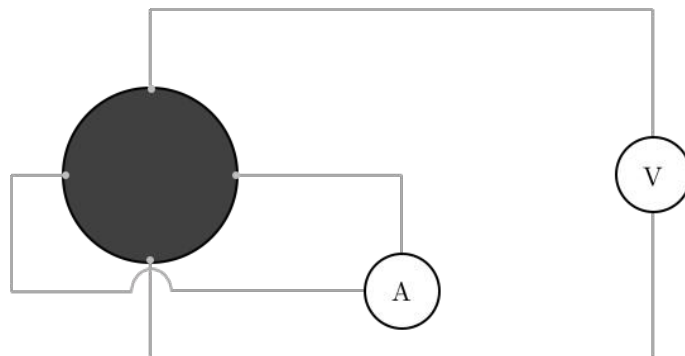


Figure 4.3: Van der Pauw method simplified scheme.

4.3 Cell assembly

To assemble the cells their anode electrocatalysts were heat treated at 800°C for 2 hours in air after they were synthesised. The anode inks were prepared by mixing 30% in mass of powder with balanced Terpeneol-based vehicle (MT-13). After mixing it mechanically, the paste was roll milled for at least 10 minutes. The cathode ink was prepared identically, using Strontium-doped Lanthanum Manganite - LSM - (MT-11) commercial powder.

A buffer layer composed by 50% wt. of the electrolyte material ($\text{Sc}_{0.10}\text{Ce}_{0.01}\text{SZr}$) MT-07 and 50% wt. of CeO_2 was developed. The main idea was to enhance thermal compatibility and anode anchorage over the electrolyte surface by using a mix of anode/electrolyte components. The buffer layer ink was produced by roll milling the electrolyte and CeO_2 ensemble all together. This layer was then deposited by screen printing onto 150 μm thick Scandium and Cerium doped Zirconia - ScCeSZ (MT-06) electrolyte button supports and sintered at 1300°C for 2 hours.

The cathode layer was screen printed onto the other side of the electrolyte and dried at room temperature in air for 30 minutes for the ink to accommodate over the electrolyte surface homogeneously. Then the cathode was sintered at 1100°C with 5 °C.min⁻¹ during 2 hours as shown in Figure [4.4a](#). Analogously, the anode was

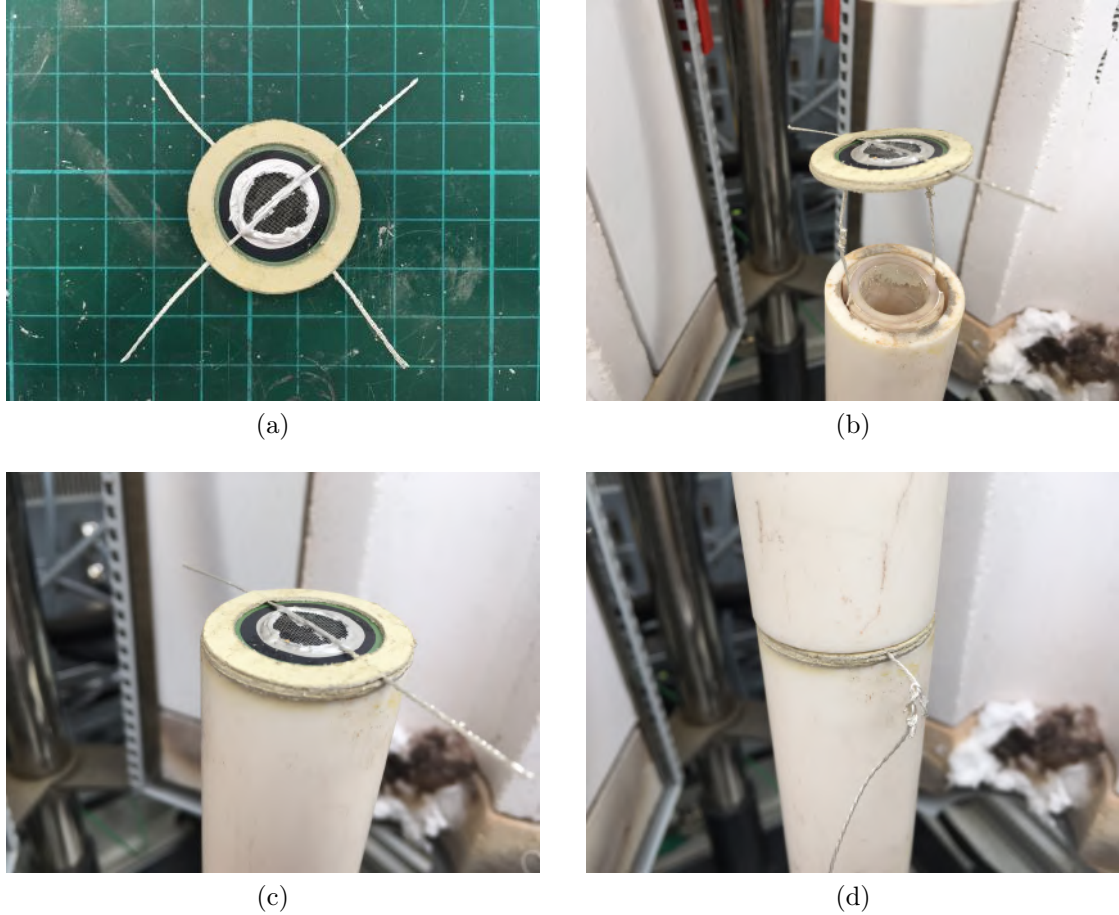


Figure 4.5: Cell testing (a) sealing material over the each electrode, (b) connecting anode silver wires, (c) placing the cell over the alumina tube and (d) resting the upper tube over the cathode side and connecting the cathode silver wires.

for methane as fuel at 850°C. Electrochemical impedance spectroscopy was taken from 1 MHz to 50 mHz around open circuit voltage with 10 mA of current amplitude.

For the second set of cells, hydrogen was used as fuel from 700 to 800°C and the tests with methane were done from 775 to 825°C. Gas chromatograph injections were done for tests run with methane. For each cell, the gas products at the outlet were analysed in galvanostatic mode at 0, 10, 20 and 30 mA at 775, 800 and 825°C, respectively. For each injection the molar amount of unconverted methane ($n_{CH_4(u)}$), ethylene ($n_{C_2H_4}$), ethane ($n_{C_2H_6}$), carbon monoxide (n_{CO}), and carbon dioxide (n_{CO_2}) were measured.

Therefore the molar amount of methane converted ($n_{CH_4(c)}$) is the molar sum of

all products except the unconverted methane according to Equation [4.4](#).

$$n_{CH_4(c)} = n_{CO} + n_{CO_2} + 2(n_{C_2H_6} + n_{C_2H_4}) \quad (4.4)$$

The conversion (C_{CH_4}) is thus given by the converted methane over the total inlet methane ($n_{CH_4(T)}$) as in Equations [4.5](#) and [4.6](#):

$$n_{CH_4(T)} = n_{CH_4(c)} + n_{CH_4(u)} \quad (4.5)$$

$$C_{CH_4} = \frac{n_{CH_4(c)}}{n_{CH_4(T)}} \quad (4.6)$$

The molar amounts of each product are therefore determined analytically. The amounts of CO and CO₂ produced under electric charge are normalised by the subtraction from the CO and CO₂ generated at OCV thus assuming that it is generated by eventual mixture with oxygen.

The chromatograph's inlet flow in volume per time unit (ϕ_{ic}) in Equation [4.7](#) is determined with a blank test. This test is performed by injecting a known flow of methane directly into the chromatograph (ϕ_{bc}) and by measuring the molar amount ($n_{CH_4(b)}$). Therefore, the amount measured over the known inlet flow is associated with the known molar amount measured at each test.

Finally, using the percentage of methane converted (C_{CH_4}) the rate of conversion in mol.s⁻¹ can be estimated using Equation [4.8](#).

$$\phi_{ic} = \frac{n_{CH_4(T)}}{n_{CH_4(b)}} \cdot \phi_{bc} \quad (4.7)$$

$$\dot{r}_{CH_4(c)} = \phi_{ic} \cdot C_{CH_4} \cdot \frac{\rho_{CH_4}}{MM_{CH_4}} \quad (4.8)$$

From Equation [4.8](#), $\dot{r}_{CH_4(c)}$ is the rate of methane conversion (in mol.s⁻¹), ρ_{CH_4} is the density of methane (6.56×10⁻⁴ g.mL⁻¹) and MM_{CH_4} its molar mass (16.04 g.mol⁻¹). The same accounting was done for CO and CO₂ rates.

4.5 Cells *post-mortem* analysis

4.5.1 Raman spectroscopy

A light quantum ($h \cdot \nu_0$) hits a particle generating an elastic scatter, know as *Rayleigh scatter*, with higher probability. However, the vibrational effects which molecules are submitted to when excited, generate an inelastic scatter of lower probability, known as the *Raman scatter*. This scattering phenomenon emits a quantum of $h \cdot \nu_0 \pm h \cdot \nu_s$. Since most molecules at room temperature are in their ground state, when excited by a quantum source ($h \cdot \nu_0$) a quantum of energy of $h \cdot \nu_0 - h \cdot \nu_s$ leaves the molecule. This is known as Raman process [\[276\]](#). The effect is illustrated in Figure [4.6](#).

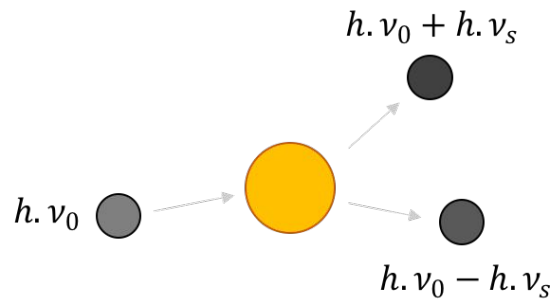


Figure 4.6: Raman effect.

In this work, after cell operation, Raman spectroscopy was taken over their surface with a 633 nm wavelength laser in a Renishaw inVia Raman microscope (EQ-09). Samples were scanned at several spots (at least three) from 3200 to 100 cm⁻¹ within 20 seconds acquisition time and 1% of the laser total power.

4.5.2 Scanning electron microscopy

The image formation in scanning electron microscopy (SEM) depends on the interaction between the electron beam source and the material. The interactions can be either elastic or inelastic.

The elastic effect occurs when the electrons from the incident beam find an atomic nuclei or even electrons with similar energy from outer shells of the specimen atoms. Elastic scattering usually present low energy loss and wide angles of deflection. Furthermore, when the scattering angle is higher than 90° , the electrons are called backscattered (BSE).

On the other hand, when the incident beam transfers substantial energy to the atoms of the sample, the event is called inelastic scattering. The amount of energy released during inelastic scattering is totally dependent on the electron-atoms binding energy. Therefore, when ionisation occurs due to electron excitations it promotes a phenomenon called secondary electron (SE) emission. Those interactions aforesaid are the main processes used to image the sample [277].

In addition, many other interactions such as Auger electrons, characteristic X-rays as well as cathodoluminescence are generated. In Figure 4.7, it can be seen the interaction of the electron beam with the sample can be seen, representing the different depths at which the aforementioned phenomena occur [277].

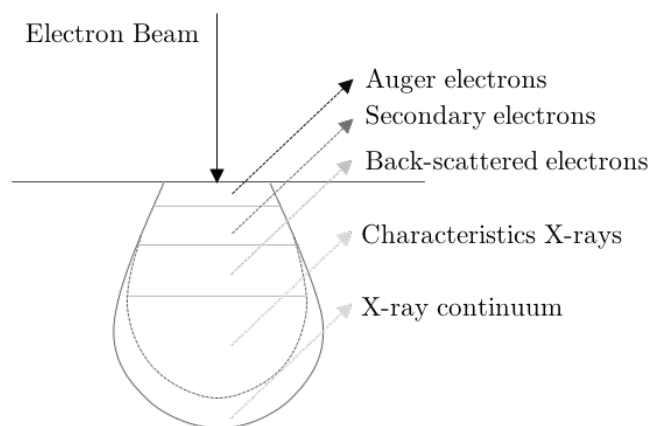


Figure 4.7: Electron beam and its interaction with the specimen.

Usually, BSE occurs when the electrons leave the sample with energies greater

than 50 eV and are very useful to image topography as well as differentiate atomic number. If the specimen's atom has a high atomic number, for instance, more electrons will be backscattered thus producing higher signals. Therefore, if different atoms are present, they will appear with different grey levels. Moreover, SEs are classified as low-energy electrons (3-5 eV) and are very useful and widely used to image the surface of the specimen [277].

Anode surfaces were submitted to scanning electron microscopy (SEM) to check for microstructure morphology and conditions. SEM was performed using a JEOL JSM-6460LV (EQ-12), with acceleration voltages ranging from 15 to 20 kV on a backscattering electrons (BSE) detector. In addition energy dispersive X-ray spectroscopy (EDX) was used to determine phase distribution.

Due to the cells low active area plus the fact that current collectors are placed over the surface with silver paste thus damaging the anode when removed, the imaging was not done over the actual operated cells but with reduced and aged anodes. For the ageing procedure, the anodes, previously screen-printed onto the electrolyte, were placed in an alumina reactor tube and kept at 800°C whilst a reducing atmosphere (15 mL.min⁻¹ H₂ + 15 mL.min⁻¹ N₂) filled the tube for over 50 hours.

4.5.3 Temperature-programmed oxidation

Temperature-programmed oxidation or TPO was used to assess carbon deposition on the *post-mortem* cells. TPO works by introducing an oxygen-rich atmosphere that oxidises eventual carbon deposits forming carbon oxides.

To perform TPO, a quartz reactor, previously cleaned by oxygen flushed at 800°C, was used to place the operated anode sample. After placing the quartz tube inside the furnace, 20 % vol. oxygen in balanced nitrogen was opened. The outlet gas was injected into a gas chromatograph from 200 to 850°C in which the molar amounts of CO and CO₂ were measured each 50°C step.

Before measuring TPO with the *post-mortem* samples, a validation test was done

using graphite powder and the results of carbon oxidation can be seen in Figure 4.8 that shows the graphitic carbon being eliminated as CO and CO₂ mainly from 550 to 800°C as expected [278].

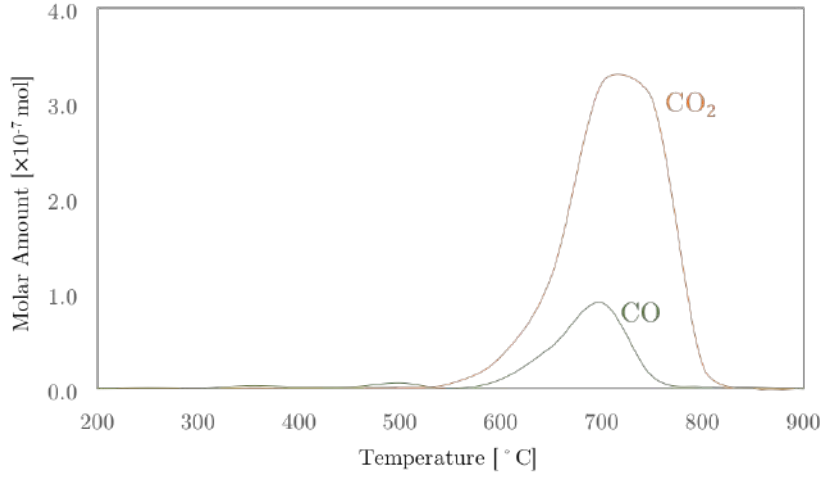
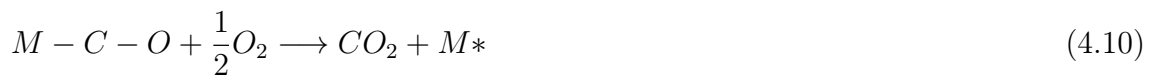


Figure 4.8: Carbon oxidation profile over increasing temperature.

The tests with carbon black were done in pair and thus 2 procedures were run with different amounts of graphite and the average results were then considered in order to validate the setup. As comparison effect, eventual carbon deposits over anode cells is oxidised in a different manner. Since carbon is adsorbed at the catalytic sites of the anode, the oxidation does not take place as CO but mainly CO₂ in two basic steps described in Equations 4.9 and 4.10 in which M represents a generic metallic site in catalysis. Therefore, if high amounts of CO are being observed, it means that significant amounts of carbon are being deposited through the anode bulk [275].



Chapter 5

Electrocatalyst characterisation

For the three bimetallic compositions produced, the following amounts of nitrates, water, citric acid and ammonium hydroxide used are shown in Tables [5.1](#), [5.2](#) and [5.3](#).

Table 5.1: Synthesis of the precursor cerium-rich powder.

Ce:Co:Cu - 2:1:1	Nitrate Solution		Citric Acid Solution		NH ₄ OH [mL]
	Salt [g]	DI Water [mL]	Citric Acid [g]	DI Water [mL]	
Ce(NO ₃) ₃ .6H ₂ O	21.5582	12.3190	9.5434	4.9673	27.00
Co(NO ₂) ₃ .6H ₂ O	7.2275	5.3936	4.7717	2.4836	
Cu(NO ₃) ₂ .3H ₂ O	5.9906	4.3410	4.7717	2.4836	

Table 5.2: Synthesis of the precursor cobalt-rich powder.

Ce:Co:Cu - 1:2:1	Nitrate Solution		Citric Acid Solution		NH ₄ OH [mL]
	Salt [g]	DI Water [mL]	Citric Acid [g]	DI Water [mL]	
Ce(NO ₃) ₃ .6H ₂ O	13.5016	7.7152	5.9769	3.111	33.00
Co(NO ₂) ₃ .6H ₂ O	18.1050	13.5110	11.9530	6.2220	
Cu(NO ₃) ₂ .3H ₂ O	7.5036	5.4374	5.9769	3.1110	

Table 5.3: Synthesis of the precursor copper-rich powder.

Ce:Co:Cu - 1:1:2	Nitrate Solution		Citric Acid Solution		NH ₄ OH [mL]
	Salt [g]	DI Water [mL]	Citric Acid [g]	DI Water [mL]	
Ce(NO ₃) ₃ .6H ₂ O	13.3143	7.6082	5.8940	3.0678	33.00
Co(NO ₂) ₃ .6H ₂ O	8.9273	6.6622	5.8940	3.0678	
Cu(NO ₃) ₂ .3H ₂ O	14.7980	10.7240	11.7880	6.1356	

To simplify the powders produced will be named cerium-rich, cobalt-rich and

copper-rich for the molar ratios of Ce:Co:Cu 2:1:1, 1:2:1 and 1:1:2, respectively from here onwards.

5.1 X-ray analysis

XRD analysis results are shown in Figure 5.1 in which the red-dashed lines are the diffractograms of each electrocatalyst right after synthesis and the black continuous lines are the patterns for the powders heat treated at 800°C during 2 hours.

The XRD results indicated the formation of CeO_2 , Co_3O_4 and CuO rather than solid solutions. Solid solutions between CeO_2 and Cu are not common [279], however the phase diagram of CeO_2 -CoO shows that cobalt has a certain solubility into ceria's lattice [280]. The least state of copper oxidation (Cu_2O) can also be spotted but for the as-synthesised copper-rich powder.

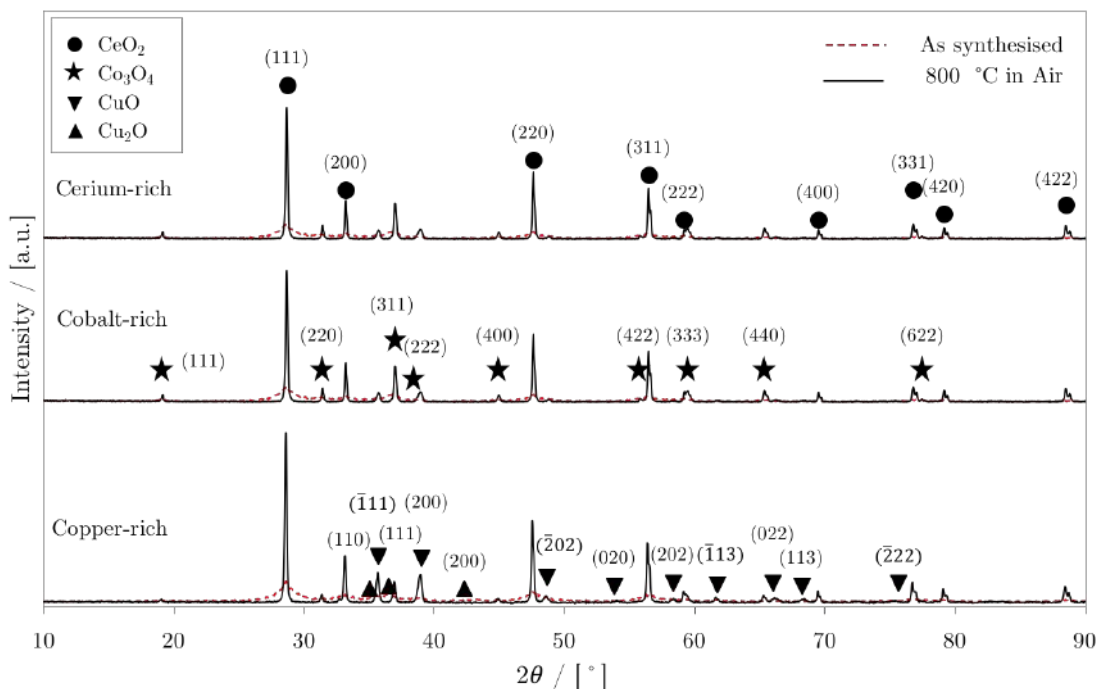


Figure 5.1: X-Ray diffractograms for cerium-rich, cobalt-rich and copper-rich compositions.

Rietveld refinement was performed according to space groups, atomic coordinates, lattice parameters and symmetry found in PDF-03-065-2975, PDF-00-042-1467 and PDF-04-007-1375 for CeO_2 , Co_3O_4 and CuO respectively. The refined

results for composition estimation can be seen in Table 5.4. According to the aforementioned PDF Cards, the lattice parameters are shown in Table 5.5.

Table 5.4: Rietveld refinement for cerium-rich, cobalt-rich and cobalt-rich compositions.

Ce:Co:Cu - 50:25:25 % mol					
Oxide	Weight (%)	Metal	Weight (%)	Molar (%)	Discrepancy (%)
CeO ₂	69.10	Ce	70.37	50.93	0.93
Co ₃ O ₄	15.50	Co	14.24	24.50	0.50
CuO	15.41	Cu	15.40	24.57	0.43
Ce:Co:Cu - 25:50:25 % mol					
Oxide	Weight (%)	Metal	Weight (%)	Molar (%)	Discrepancy (%)
CeO ₂	39.93	Ce	41.70	23.60	1.40
Co ₃ O ₄	39.28	Co	36.99	49.79	0.21
CuO	20.80	Cu	21.31	26.60	1.60
Ce:Co:Cu - 25:25:50 % mol					
Oxide	Weight (%)	Metal	Weight (%)	Molar (%)	Discrepancy (%)
CeO ₂	43.35	Ce	44.47	26.18	1.18
Co ₃ O ₄	18.47	Co	17.09	23.92	1.08
CuO	38.18	Cu	38.43	49.90	0.10

Table 5.5: Oxides lattice parameters according to PDF database.

PDF Cards	a [nm]	b [nm]	c [nm]	α (°)	β (°)	γ (°)
PDF-03-065-2975 (CeO ₂)	0.5411	0.5411	0.5411	90.00	90.00	90.00
PDF-00-042-1467 (Co ₃ O ₄)	0.8084	0.8084	0.8084	90.00	90.00	90.00
PDF-04-007-1375 (CuO)	0.4684	0.3423	0.5129	90.00	99.54	90.00

In tables 5.6, 5.7 and 5.8 the lattice parameters calculated for each composition, respectively, can be seen. By the PDF cards mentioned it is taken that CeO₂ has the cubic structure of Fluorite with symmetry space group $Fm\bar{3}m$, Co₃O₄ is a cubic Spinel with space group $Fd\bar{3}m$ and CuO has the monoclinic Tenorite structure from space group C 2/c.

The quality of the fitted data can be observed in Figures 5.2a, 5.2b and 5.2c in which the red dots represent the experimental data, the black line is the fitted calculated model and the blue line is the difference between the experimental data and the fitted one. In addition, inserted in the graphs are the R-factors and the “goodness of fitness” χ^2 .

Table 5.6: Lattice parameters calculated by Rietveld refinement - cerium-rich.

Oxide	Lattice parameters for the cerium-rich composition					
	a [nm]	b [nm]	c [nm]	α [°]	β [°]	γ [°]
CeO ₂	0.5409(5)	0.5409(5)	0.5409(5)	90.00	90.00	90.00
Co ₃ O ₄	0.8074(6)	0.8074(6)	0.8074(6)	90.00	90.00	90.00
CuO	0.4696(4)	0.3408(0)	0.5127(5)	90.00	99.66	90.00

Table 5.7: Lattice parameters calculated by Rietveld refinement - cobalt-rich.

Oxide	Lattice parameters for the cobalt-rich composition					
	a [nm]	b [nm]	c [nm]	α [°]	β [°]	γ [°]
CeO ₂	0.5411(4)	0.5411(4)	0.5411(4)	90.00	90.00	90.00
Co ₃ O ₄	0.8079(0)	0.8079(0)	0.8079(0)	90.00	90.00	90.00
CuO	0.4698(4)	0.3410(5)	0.5132(1)	90.00	99.60	90.00

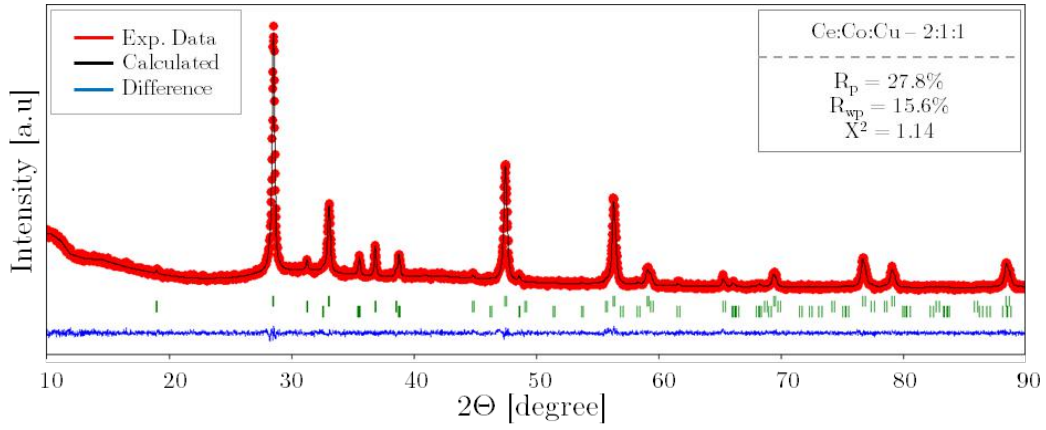
Table 5.8: Lattice parameters calculated by Rietveld refinement - copper-rich.

Oxide	Lattice parameters for the copper-rich composition					
	a [nm]	b [nm]	c [nm]	α [°]	β [°]	γ [°]
CeO ₂	0.5410(7)	0.5410(7)	0.5410(7)	90.00	90.00	90.00
Co ₃ O ₄	0.8077(5)	0.8077(5)	0.8077(5)	90.00	90.00	90.00
CuO	0.4696(5)	0.3410(1)	0.5130(0)	90.00	99.62	90.00

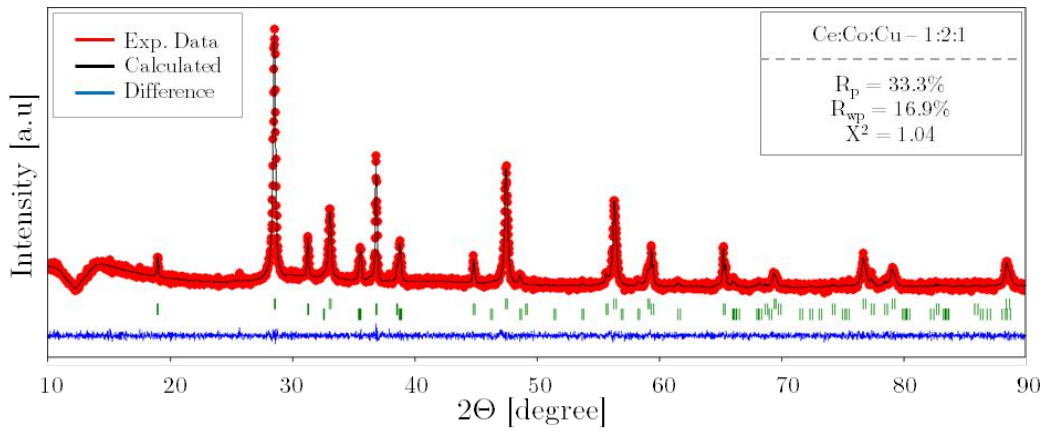
5.2 Thermogravimetric analysis

The TGA results are shown in Figure 5.3. The results show two bigger mass losses for each TGA graph in which the first one is between 25 and 450°C and the second one between 840 and 900°C. For the cerium-rich composition the losses are around 5.77 and 0.86% respectively. For the cobalt-rich composition, the losses are 5.44 and 2.41% respectively. Finally, for the copper-rich composition, results are 5.32 and 1.05%.

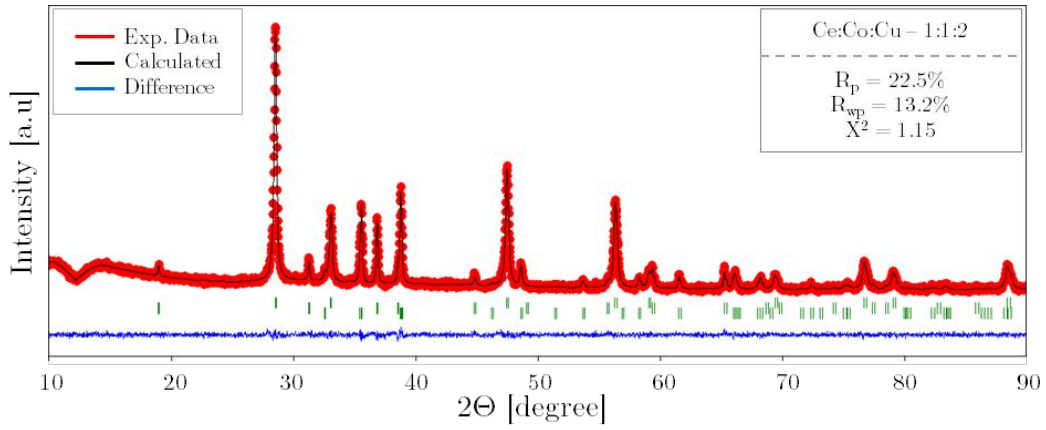
The first loss is associated with volatiles evaporation such as water and remaining nitrate compounds originated from the synthesis process. It is known that Co₃O₄ decomposes to CoO at 920°C according to Equation 5.1, thus the second loss can be definitely linked to this decomposition [281-283] and it can be noticed because



(a)



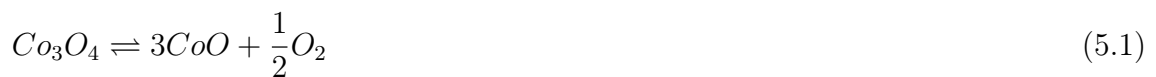
(b)

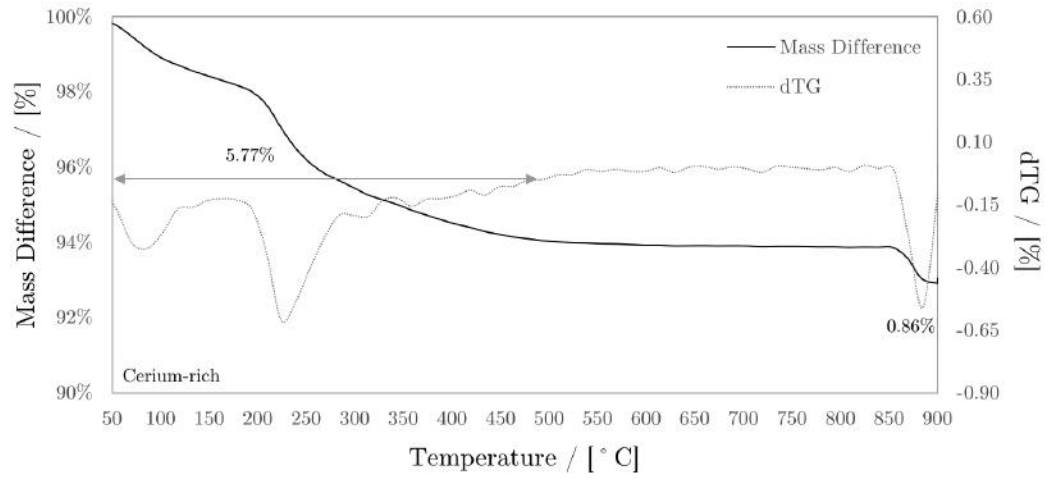


(c)

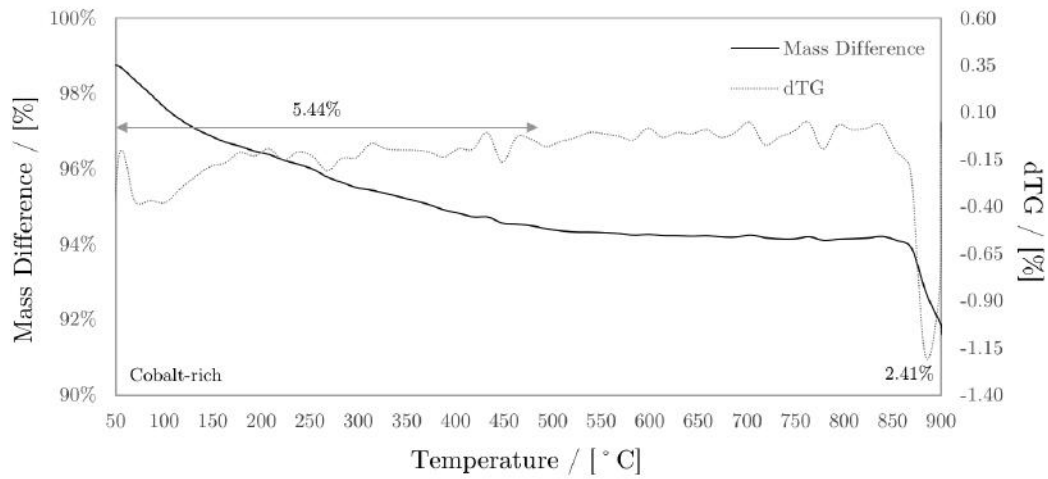
Figure 5.2: Rietveld refinement fitness, R-factors and goodness of fit for (a) cerium-rich (b) cobalt-rich and (c) copper-rich composition.

it is higher in the second composition (cobalt-rich) than the others.

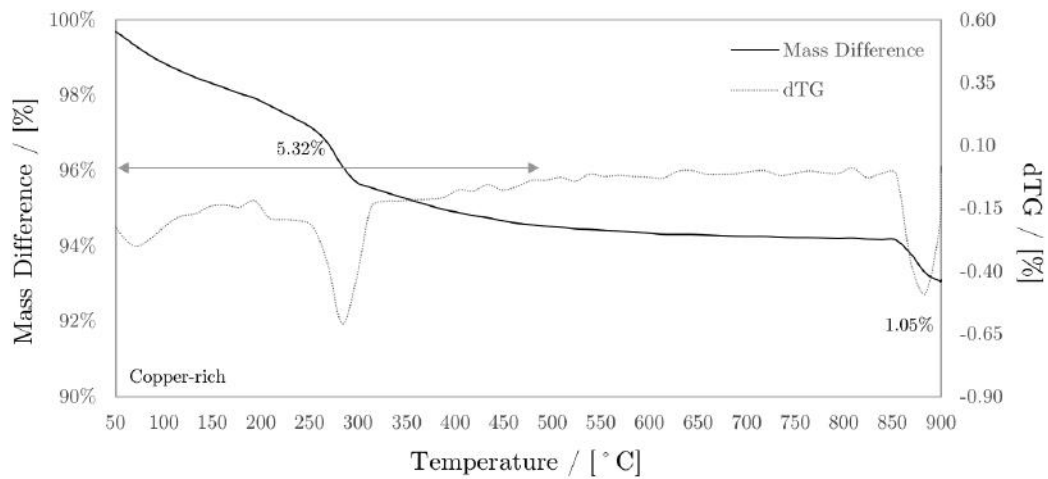




(a)



(b)



(c)

Figure 5.3: Thermogravimetric analysis for the (a) cerium-rich (b) cobalt-rich and (c) copper-rich compositions.

5.3 X-ray fluorescence analysis

The compilation of XRF results can be seen in Table 5.9. Once more it shows fair accordance with the synthesis design, especially when taking into account the counting error which is provided by the equipment manufacturer for each compound given their sensibility to fluorescence.

Table 5.9: XRF results for cerium-rich, cobalt-rich and copper-rich compositions.

Element	Molar		
	50:25:25 %	25:50:25 %	25:25:50 %
Ce	52.86 ± 0.64 %	28.31 ± 0.71 %	28.09 ± 0.71 %
Co	23.43 ± 0.61 %	48.11 ± 0.33 %	24.33 ± 0.45 %
Cu	23.71 ± 0.50 %	23.58 ± 0.44 %	47.58 ± 0.29 %

Using the XRF results in Table 5.9, it is possible to estimate the weight percentages of the oxides before and after reduction as shown in Table 5.10.

Table 5.10: Weight percentages estimated by XRF data.

Compositions	Precursors wt. %			Reduced wt. %		
	CeO ₂	Co ₃ O ₄	CuO	CeO ₂	Co	Cu
2:1:1	68.44	15.76	15.81	73.88	12.49	13.63
1:2:1	43.26	38.20	18.55	50.23	32.57	17.21
1:1:2	43.07	19.38	37.56	49.33	16.30	34.37

Furthermore, dividing the weights calculated in Table 5.10 by the density of each compound shown in Table 5.11 the volume fraction of each phase is estimated in Table 5.12. In addition, considering that ceria will probably not be completely reduced it is possible to calculate the increase in porosity due to cobalt and copper oxide reduction.

Table 5.11: Density of the oxides and metals.

Compounds	CeO ₂	Co ₃ O ₄	CuO	Co	Cu
Density (g.cm ⁻³)	7.65	6.11	6.31	8.90	8.96

For a matter of comparison with literature, Table 9.3 of the Appendix I presents the equivalences of percentages in mol and mass for the metals and their oxides.

Table 5.12: Volume percentages estimated from weight percentages and densities in Tables 5.10 and 5.11 respectively.

Compositions	Oxides vol. (%)			Reduced vol. (%)			Porosity Increase (%)
	CeO ₂	Co ₃ O ₄	CuO	CeO ₂	Co	Cu	
2:1:1	63.76	18.38	17.85	63.76	11.82	12.82	11.60
1:2:1	38.09	42.11	19.80	38.09	32.57	17.09	12.25
1:1:2	38.16	21.50	40.34	38.16	16.21	33.95	11.68

5.4 Particle size distribution

The particle size distribution for each powder sample is shown in Figure 5.4. As can be observed, the distributions are similar between each other and mainly in bi-modal shape, apart from the Cerium-rich composition. The particle sizes in 10% of the distribution (D_{10}) were 2.43, 1.78 and 2.40 μm , whereas the D_{50} were 8.90, 4.20 and 10.43 μm and finally the D_{90} were 39.85, 25.82 and 32.37 μm concerning the cerium, cobalt and copper-rich compositions respectively.

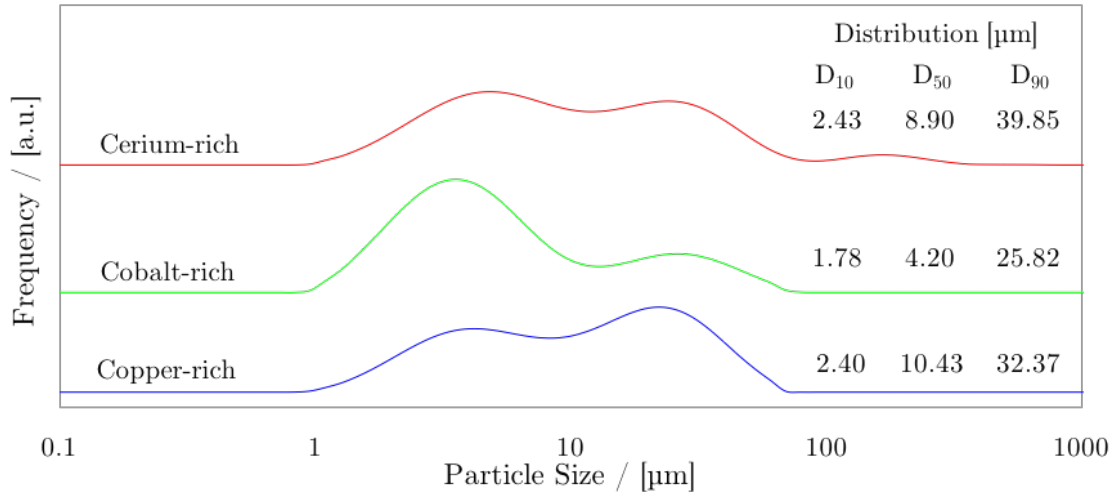


Figure 5.4: Particle size distribution for cerium-rich, cobalt-rich and copper-rich compositions.

It has to be pointed out that the synthesis method used is supposed to produce nanoscale or submicroscale powder. However, as seen, the distribution presented particle size as micrometric, which can be explained by the agglomeration of the powder after being stored. Yet, when the suspension is produced with each powder, the particles are supposed to deagglomerate due the action of the dispersant present

in the vehicle. Therefore, the PSD analysis performed with the Malvern instrument in aqueous media does not represent the real application in SOFC but the response of agglomeration for each powder when stored.

Nevertheless, what can be said about the results of PSD is that all distributions were homogeneous for each material given that they all have similar nature and density and all three compositions had a similar range of particle sizes mainly with bi-modal normal distribution.

5.5 Temperature-programmed reduction

The results of TPR are shown in Figure 5.5. Since each powder is composed by a mixture of oxides, the peaks of hydrogen consumption are overlapped. The reduction of copper oxide as isolated phase takes place between 150 and 500°C according to Equations 5.2 and 5.3 [284-286].



The cobalt oxide, analogously to copper oxide, reduces in two steps. The first reducing reaction occurs according to Equation 5.4 around 300°C for the cobalt oxide as isolated phase whereas total reduction will take place around 500°C as depicted in Equation 5.5 [281, 287].





Regarding cerium oxide, the reduction process is defined by the peaks at higher temperatures. The reduction of CeO_2 will occur partially turning Ce^{4+} into Ce^{3+} as shown in Equation 5.6. Cerium oxide's reduction will turn the lattice oxygen deficient, thus enhancing the electrical conductivity. Moreover, the cerium oxide reduction process takes place in two well defined steps. Firstly, the surface-capping oxygen anions attached to Ce^{4+} surface with an octahedral coordination will react with hydrogen at temperatures such as 500 to 650°C. Then, finally, oxygen from ceria's bulk structure will be released at temperatures above 750°C [284, 285, 288].

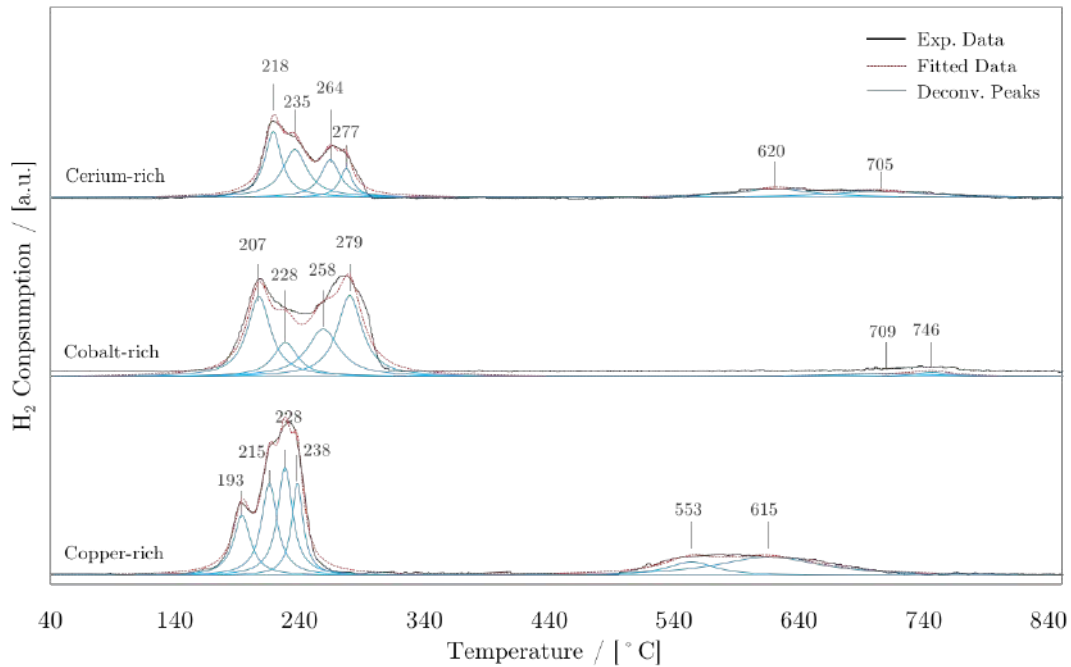


Figure 5.5: Temperature-programmed reduction for the cerium-rich, cobalt-rich and copper-rich compositions with their peaks deconvoluted.

In agreement with the aforesaid, the last two peaks can be assigned to cerium

oxide, specifically to its surface and bulk reduction, respectively, whereas the four previous peaks are assigned to copper and cobalt oxide full reduction.

After a blank test in which pure nitrogen was inserted into the reactor until steady state and then switched to the mixture (5% of hydrogen in balanced nitrogen), the reactor total volume was estimated at 50 mL. Since the mixture achieved the steady state after 75 seconds and the input gas was 40 mL.min⁻¹ in which 2 mL.min⁻¹ (5%) was hydrogen, 2.50 mL of hydrogen occupied the reactor when it was full. The relative signals were then calculated in comparison with the signal assigned to the full reactor and the consumption of hydrogen was then estimated in volume. The consumption of hydrogen during the whole experiment was 1.67, 2.10 and 7.84 mL for cerium, cobalt and copper-rich compositions, respectively.

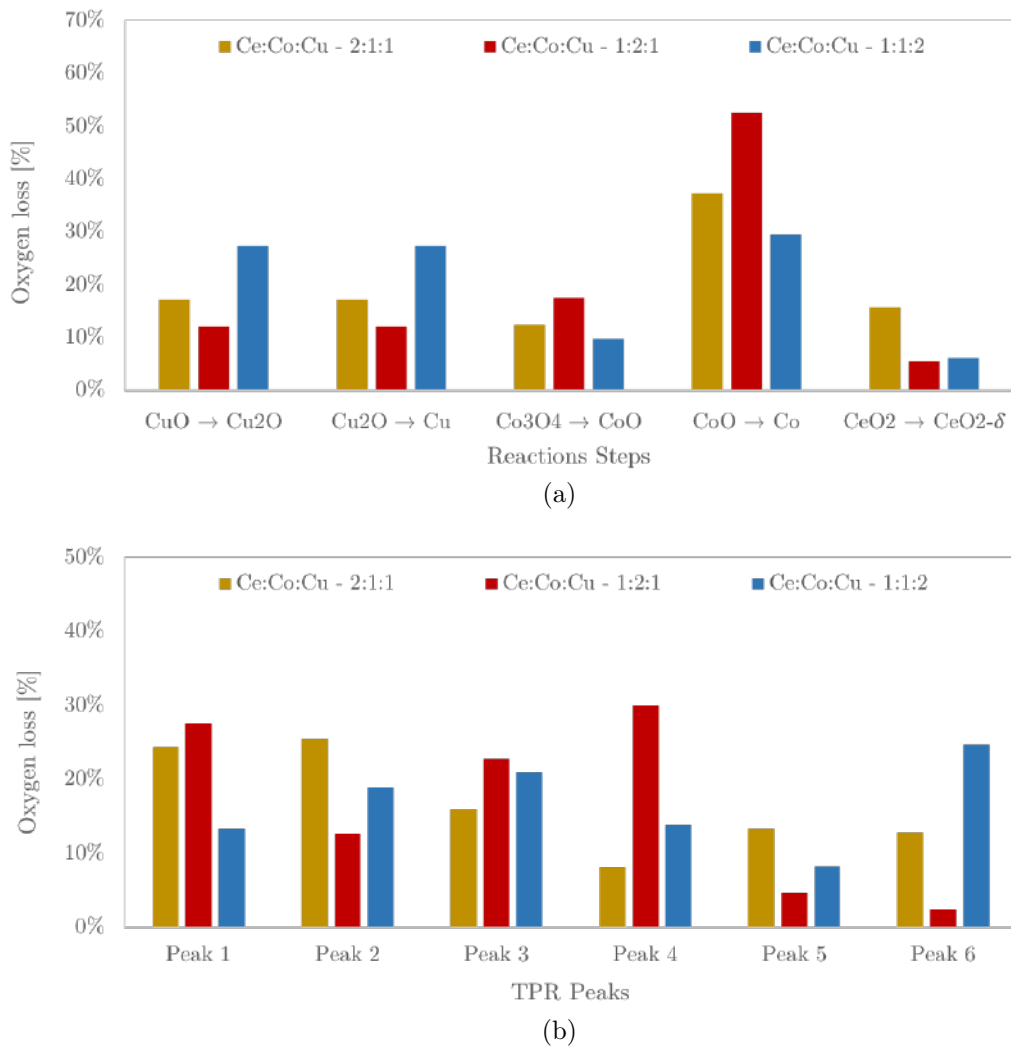


Figure 5.6: TPR Calculations (a) theoretical oxygen loss at each reaction step (b) oxygen loss related at each reduction peak obtained after deconvolution.

Considering the density of H₂ as 0.087 g.L⁻¹, the mass of hydrogen consumed by each composition was 0.14, 0.18 and 0.67 mg. These values can be normalised by mass, considering it was used 21.0, 22.3 and 21.6 mg of each electrocatalyst and thus hydrogen was absorbed in rates of 0.47, 0.56 and 2.16 mL.min⁻¹ per gram of each electrocatalyst. In Figures 5.6a and 5.6b the theoretical calculations of oxygen mass percentage lost at each reaction step are represented (Equations 5.2 to 5.6) and the percentage of oxygen related to each peak area determined after deconvolution.

It is notable in Figure 5.6a that the reactions of copper and cobalt oxides reduction represents those with higher potential of hydrogen absorption. Yet, in Figure 5.6b it can be observed that for the cobalt-rich composition there is a high potential of hydrogen consumption indicated by peaks 1 and 4, whereas for the copper-rich, peaks 2 and 3 are higher. Finally, the peaks 5 and 6 are most likely related to cerium oxide reduction. Although the copper-rich composition possesses a high value of hydrogen absorption at peak 6, this might be related to the fact that part of the copper oxide reduction can take place at higher temperatures such as 500 or even 660 °C [284-286, 289].

5.6 Electrical conductivity of the precursor oxides

The Arrhenius plot of the DC conductivity test is shown in Figure 5.7 from which linear and angular coefficients can be extracted to estimate the activation energy according to Equation 5.7. The results of the oxides conductivities are consistent with the compositions presented, which shows increasing in conductivity with increasing metal load in the oxides composition.

$$\ln(\sigma) = \ln(\sigma_0) - \frac{E}{R} \cdot \frac{1}{T} \quad (5.7)$$

Table 5.13 presents the equations for each composition and their respective coefficients from which activation energy (E) is calculated and shown. The interesting

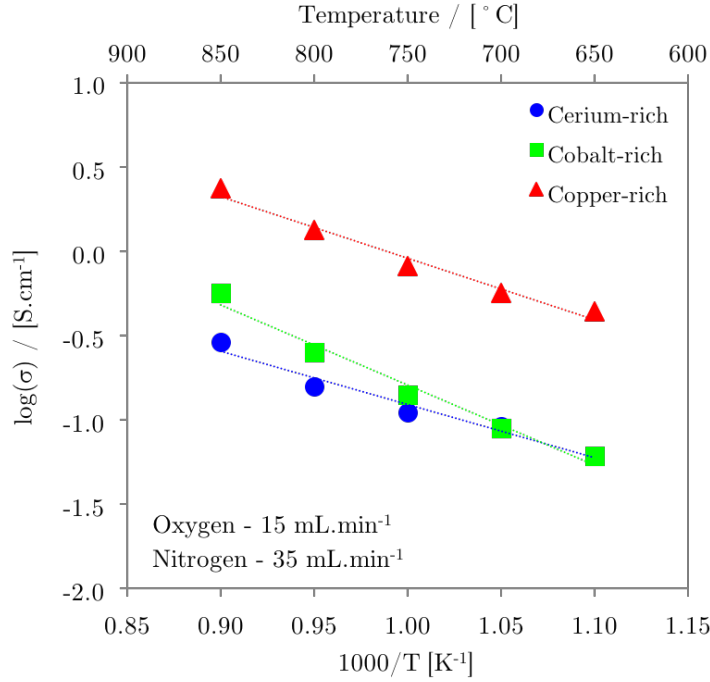


Figure 5.7: Electrical conductivity of oxides for cerium-rich, cobalt-rich and copper-rich compositions.

result that can be observed is that the cerium-rich composition has the lowest activation energy, followed by the copper-rich one. Therefore, the former is the one which has conductivity less affected by temperature followed by the latter, whereas the cobalt-rich composition is the most influenced by it. Yet, the addition of copper plays an important role on increasing electrical conductivity, as expected.

Table 5.13: Arrhenius coefficients from conductivity DC test.

Composition	Equation	R ²	σ ₀ [S.cm ⁻¹]	-E/R	E [kJ.mol ⁻¹]
Ce:Co:Cu - 2:1:1	-7.4951x + 5.2683	0.9472	5.2683	-7.4951	62.31
Ce:Co:Cu - 1:2:1	-11.2410x + 9.2174	0.9561	9.2174	-11.241	93.46
Ce:Co:Cu - 1:1:2	-8.6178x + 8.3740	0.9558	8.3740	-8.6178	71.65

5.7 Summary of the chapter and conclusions

Regarding the powder characterisation in the present chapter, it was confirmed by XRD and XRF analysis that the desired compositions were successfully produced by the amorphous citrate method. Rietveld refinement confirmed once more the com-

positions whilst lattice parameters showed fair accordance with the PDF database.

The phases discussion has shown that in oxidising conditions and at room temperature the isolated oxides are most likely to occur, whereas at high temperatures and reducing atmosphere Co and Cu will probably be reduced over CeO_{2-x} surface.

TGA analysis shows 800°C as a suitable temperature for the powders to be treated after the synthesis process, confirming that all volatiles were eliminated and phases formed but still avoiding the unnecessary decomposition of cobalt oxide. Particle size distribution confirmed that even after treatment, the powders size were still at a micro-scale.

TPR analysis pointed out that the metallic-rich compositions (cobalt and copper) have the highest ability to absorb hydrogen until full oxidation as expected. The confirmation of the oxides reducibility indicates the ability of these metals to absorb hydrogen and shows that they might be catalytically active, especially by the fact of having semi-filled orbitals in the 3d electronic layer. Moreover, cerium oxide has confirmed its two stage of oxidation, first the surface and then the bulk. Ceria's partial oxidation might leave oxygen vacancies which increases the ionic conductivity thus augmenting TPB length.

DC conductivity tests revealed that copper plays an important role on increasing electrical conductivity of the electrocatalyst. In addition, cobalt-rich catalysts conductivity seems to be slightly more sensitive to temperature changes.

Chapter 6

The CeO₂-Co-Cu anode

The thermal compatibilities between anode and electrolyte must be taken into account for the development of a suitable anode configuration, as already said. The thermal coefficient of cerium oxide is reported to be around $12 \times 10^{-6} \text{ K}^{-1}$ [290, 291], whereas for cobalt oxide spinel (Co₃O₄) such coefficient is up to $6 \times 10^{-6} \text{ K}^{-1}$ [292, 293], and finally for copper oxide it is $5 \times 10^{-6} \text{ K}^{-1}$ [294]. However, zirconia-based ceramics are known to have thermal coefficients around $13\text{-}14 \times 10^{-6} \text{ K}^{-1}$ [295]. In addition, accounting for the fact that in reducing atmospheres those oxides will be as metal phases, the mismatch between them and the electrolyte will be even more critical. For that matter, an interface buffer layer was developed to serve as interface material between electrolyte and actual anode as the cell design depicted in Figure 6.1.

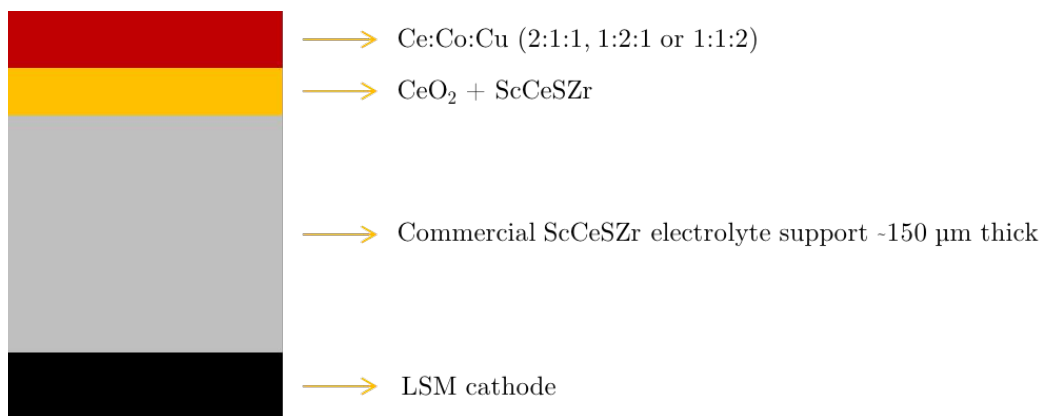


Figure 6.1: Cell assembly scheme - Bimetallic anode compositions.

6.1 The buffer layer - phases characterisation

XRD analysis was done over the powders CeO_2 and $\text{Sc}_{0.10}\text{Ce}_{0.01}\text{SZr}$ and compared to the buffer layer mixture that was previously sintered. The diffractograms are shown in Figure 6.2. The two first XRD patterns from bottom to top represent the peaks of the precursors whereas the last pattern shows isolated phases of CeO_2 and $\text{Sc}_{0.10}\text{Ce}_{0.01}\text{SZr}$ as well as $\text{Zr}_x\text{Ce}_{1-x}\text{O}_{2-\delta}$. Slight displacements of the peaks of the buffer layer can be observed, meaning that an intermediate solid solution (e.g. $\text{Zr}_x\text{Ce}_{1-x}\text{O}_{2-\delta}$) was formed [296, 297]. In this case “x” is most likely to be in the range from 0.25 to 0.50.

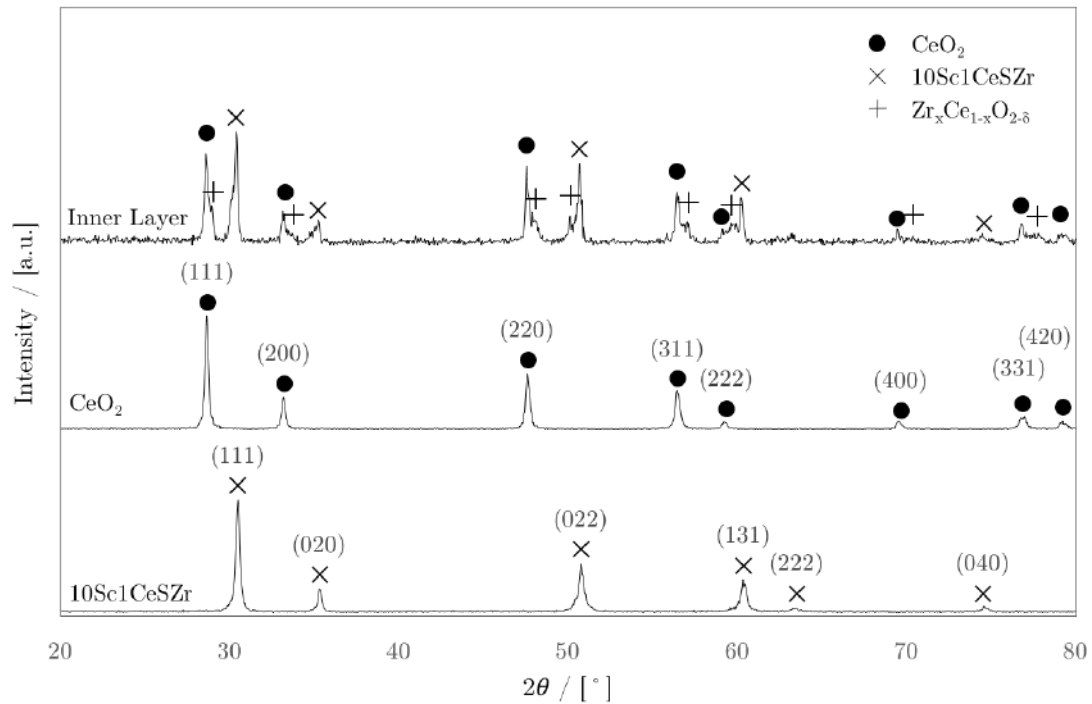


Figure 6.2: X-ray analysis of the precursors powders and sintered buffer layer.

6.2 Performance and electrochemical impedance

The results of performance and impedance spectra for the cerium-rich composition under hydrogen as fuel are shown in Figures 6.3a and 6.3b respectively. The maximum power densities for this cell were 176, 273 and 363 $\text{mW}\cdot\text{cm}^{-2}$ at 750, 800 and

850°C, respectively. The OCVs were 1.02, 1.01, 1.00 V for the lowest to the highest temperature. The ohmic resistances were 0.27, 0.20 and 0.15 $\Omega\cdot\text{cm}^2$, whereas total polarisation were 1.27, 0.77 and 0.52 $\Omega\cdot\text{cm}^2$ ($R_2 + R_3$ from Table 9.6 of Appendix II) for the same range of temperatures.

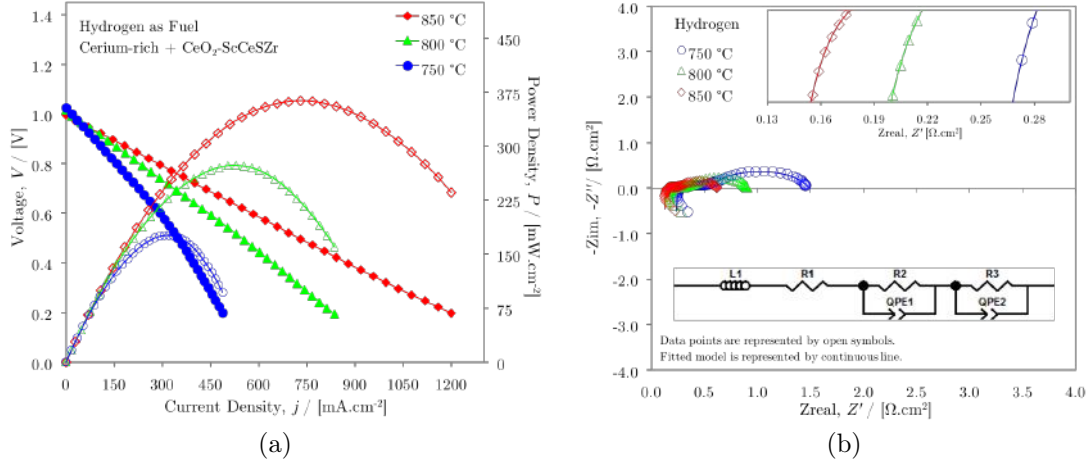


Figure 6.3: Electrochemical performance for the Ce:Co:Cu - 2:1:1 composition from 750 to 850°C (a) i-V plots and (b) impedance spectroscopy with hydrogen as fuel.

The results for the cobalt-rich bimetallic composition are shown in Figures 6.4a and 6.4b for hydrogen as fuel in which maximum power densities were 152, 261 and 485 $\text{mW}\cdot\text{cm}^{-2}$ whereas OCVs were 1.18, 1.17 and 1.16 V at 750, 800 and 850°C. The ohmic resistances were 0.42, 0.24, 0.20 $\Omega\cdot\text{cm}^2$. Total polarisation could be detected after the ECM was fitted for each case. Although the behaviour at lower frequencies could not be precisely predicted because the last arc seemed not to reach its maximum, the same ECM was used as for the other two compositions assuming that the assembly of each cell was similar. Therefore, total polarisation for this cell was 2.95, 1.99 and 1.43 $\Omega\cdot\text{cm}^2$ at 750, 800 and 850°C, respectively.

Figures 6.5a and 6.5b show electrochemical performance and impedance spectra for the copper-rich composition. The maximum power densities for this test under hydrogen were 136, 235 and 327 $\text{mW}\cdot\text{cm}^{-2}$ and OCVs were 1.10, 1.09, 1.07 V at 750, 800 and 850°C. Ohmic resistance was 0.37, 0.28 and 0.22 $\Omega\cdot\text{cm}^2$. Even though the impedance spectra are not indicating where the imaginary axis crosses the real axis in this case, it is notable that its derivative is negative at low frequencies, therefore the

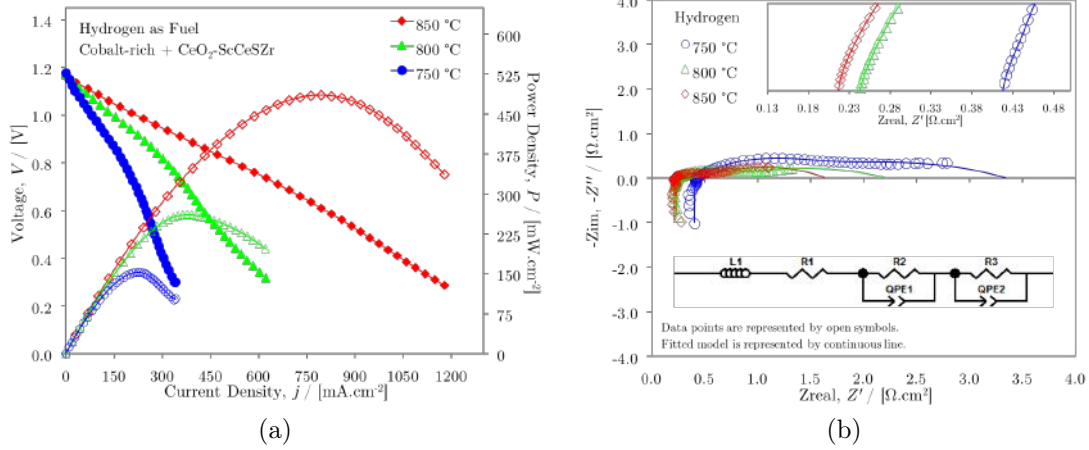


Figure 6.4: Electrochemical performance for the Ce:Co:Cu - 1:2:1 composition at 850°C (a) i-V plots and (b) impedance spectroscopy with hydrogen as fuel.

total polarisation can be estimated as around 2.44, 1.24 and 0.81 $\Omega \cdot \text{cm}^2$ respectively at 750, 800 and 850°C.

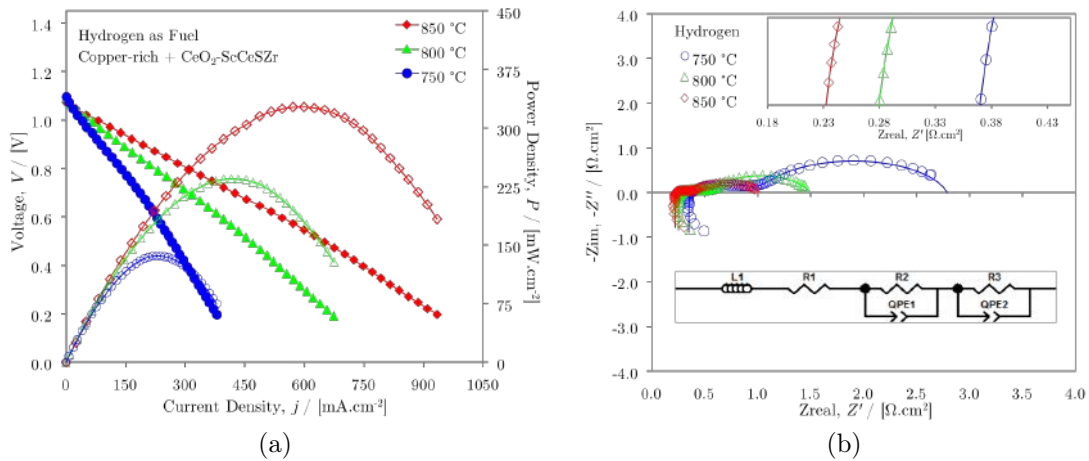


Figure 6.5: Electrochemical performance for the Ce:Co:Cu - 1:1:2 composition from 750 to 850°C (a) i-V plots and (b) impedance spectroscopy with hydrogen as fuel.

The results for the tests run with methane as fuel are presented in Figure 6.6a for electrochemical performance and in Figure 6.6b for impedance spectroscopy. The maximum power densities at 850°C with methane as fuel were 103, 416 and 35 $\text{mW} \cdot \text{cm}^{-2}$ whereas OCVs were 0.90, 1.24 and 0.90 V for cerium, cobalt and copper-rich compositions, respectively. Yet the ohmic resistances observed from Figure 6.6b were 0.15, 0.22 and 0.26 $\Omega \cdot \text{cm}^2$ for cerium, cobalt and copper-rich compositions respectively.

The estimated total polarisation was 1.20, 11.86 and 2.05 $\Omega\cdot\text{cm}^2$. The first element (R1) represented on the ECM refers to ohmic resistance whereas the other two subsequent resistances, coupled with the constant charge capacitive effect, are assigned to the impedance arcs. For the detailed parameters of fitted ECMs, refer to Tables 9.6, 9.7 in the Appendix II. The maximum frequency points are also presented in Tables 9.4 and 9.5 in the Appendix II for hydrogen and methane as fuels, respectively.

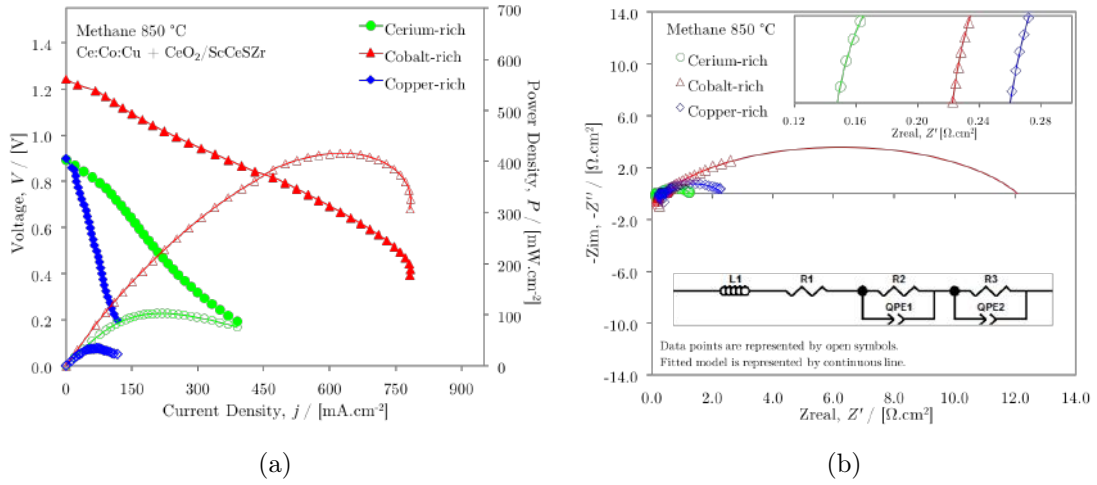


Figure 6.6: Electrochemical performance for Ce:Co:Cu compositions at 850°C (a) i-V plots and (b) impedance spectroscopy with direct methane as fuel at 850°C.

Considering the total polarisation resistances for the three compositions in hydrogen at various temperatures, an Arrhenius plot is shown in Figure 6.7. The inverse of the total polarisation resistance, is plotted according to Equation 6.1.

$$\ln\left(\frac{1}{R_p}\right) = \ln\left(\frac{1}{R_0}\right) - \frac{E}{R} \cdot \frac{1}{T} \quad (6.1)$$

The total polarisation herein presented is related to the full cell, however, since the cathode and the electrolyte were not changed from cell to cell, it can be assumed that the differences between each cell is related to anode characteristics. Therefore the activation energy is proportional to anode ability to adsorb and dissociate hydrogen molecules as well as its diffusion and charge transfer through the TPB regions.

In Table 6.1 the linear coefficients and slopes are represented. In summary, the energy consumed is a sum of electrical and mass transfer processes as well as catalytic activity. This can explain why the slope is higher for the copper-rich composition even if its conductivity is higher. Cobalt is expected to enhance catalytic activity whereas cerium oxide provides higher microstructure stability in terms of coarsening. Table 6.2 compiles the results for the tests performed at the University of Birmingham.

Table 6.1: Linear regression for total polarisation - Bimetallic compositions.

Composition	Equation	R ²	1/R ₀ [Ω ⁻¹ .cm ⁻²]	-E/R	E [kJ.mol ⁻¹]
Ce:Co:Cu - 2:1:1	-10.270x + 9.8108	0.9982	9.8108	-10.270	85.38
Ce:Co:Cu - 1:2:1	-8.3243x + 7.0600	0.9995	7.0600	-8.3243	69.21
Ce:Co:Cu - 1:1:2	-12.704x + 11.5580	0.9893	11.5580	-12.704	105.62

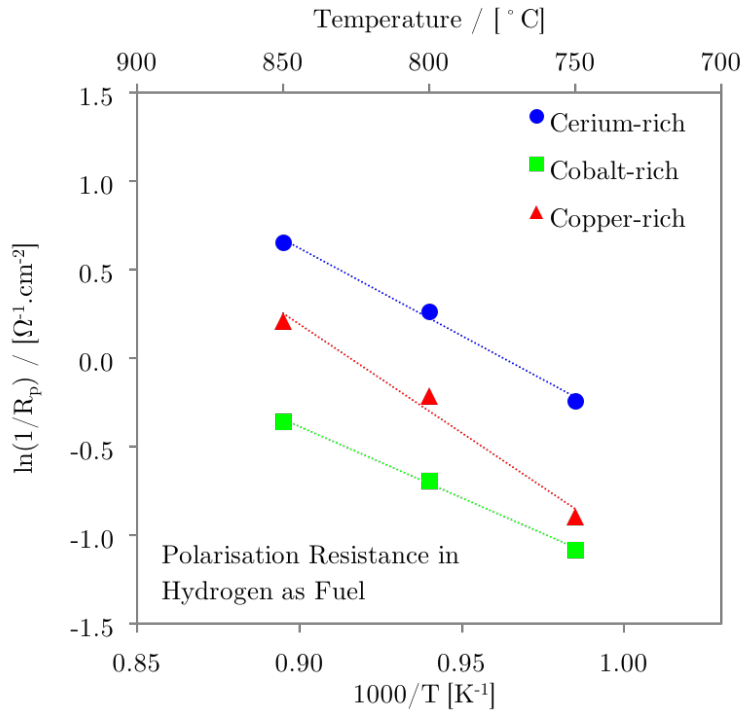


Figure 6.7: Arrhenius plot for the inverse of the total polarisation resistances of cells in hydrogen as fuel.

Table 6.2: Compiled results for the cells tested at the University Birmingham

Composition	Fuels	Temperature [°C]	OCV [V]	Max. P. D.* [mW.cm ⁻²]	@ 0.7 V [mA.cm ⁻²]	Ohmic Res. [Ω.cm ⁻²]	Total Pol. [Ω.cm ⁻²]
Cerium-rich	Hydrogen	750	1.02	176	226	0.27	1.27
		800	1.01	273	344	0.20	0.77
		850	1.00	363	436	0.15	0.52
	Methane	850	0.90	103	125	0.15	1.20
Cobalt-rich	Hydrogen	750	1.18	152	217	0.42	2.95
		800	1.17	261	377	0.24	1.99
		850	1.16	485	660	0.20	1.43
	Methane	850	1.24	416	600	0.22	11.86
Copper-rich	Hydrogen	750	1.10	136	187	0.37	2.44
		800	1.09	235	316	0.28	1.24
		850	1.07	327	425	0.22	0.81
	Methane	850	0.90	35	40	0.26	2.05

*P.D. = Power Density

6.3 Performance and GC-coupled analysis

The tests in the present section were performed in order to obtain reproducibility for the three Ce:Co:Cu compositions in a different test rig set up. In addition, the tests were run with the outlet anode gas coupled to a GC, as described in Section 4.4. The main objective was to determine the amounts of CO and CO₂ as products of electrochemical oxidation, thus identifying which reaction path each catalyst composition is most likely to promote.

Figures 6.8a and 6.8b show the results of electrochemical performance as well as the GC analysis of the anode products at the outlet gas for cerium-rich composition in Figure 6.8c. Maximum power densities for the cerium-rich composition in hydrogen were 100, 190 and 290 mW.cm⁻² at 700, 750 and 800°C whereas in methane 108, 150 and 205 mW.cm⁻² at 775, 800 and 825°C, respectively.

At 775°C CO production increases with higher charges indicating partial electrochemical oxidation whereas CO₂ amount remains unaltered. However at 800°C, under 10 and 20 mA, the CO amount increased whereas in 30 mA full oxidation seems to take place as CO₂ production increases. Finally, at 825°C the CO amount decreases with increasing charge whereas CO₂ increases. Therefore, full electrochemical oxidation seems to be favoured for this composition when temperature is above 800°C.

In addition, the amount of C₂ hydrocarbons for cerium-rich results remains al-

most unaltered indicating that these products are generated by the thermal decomposition of methane. The average of C_2 selectivity was 7 % with 0.41 % standard deviation considering all cases tested for the cerium-rich composition.

Figures 6.9a, 6.9b and 6.9c present the results of electrochemical performance both in hydrogen and methane as fuels at different temperatures as well as the GC analysis of the anode products at the outlet gas for cobalt-rich composition. From Figures 6.9a and 6.9b maximum power densities with hydrogen were 300, 460 and 560 $mW.cm^{-2}$ at 700, 750 and 800°C whereas for methane 160, 210 and 260 $mW.cm^{-2}$ at 775, 800 and 825°C, respectively.

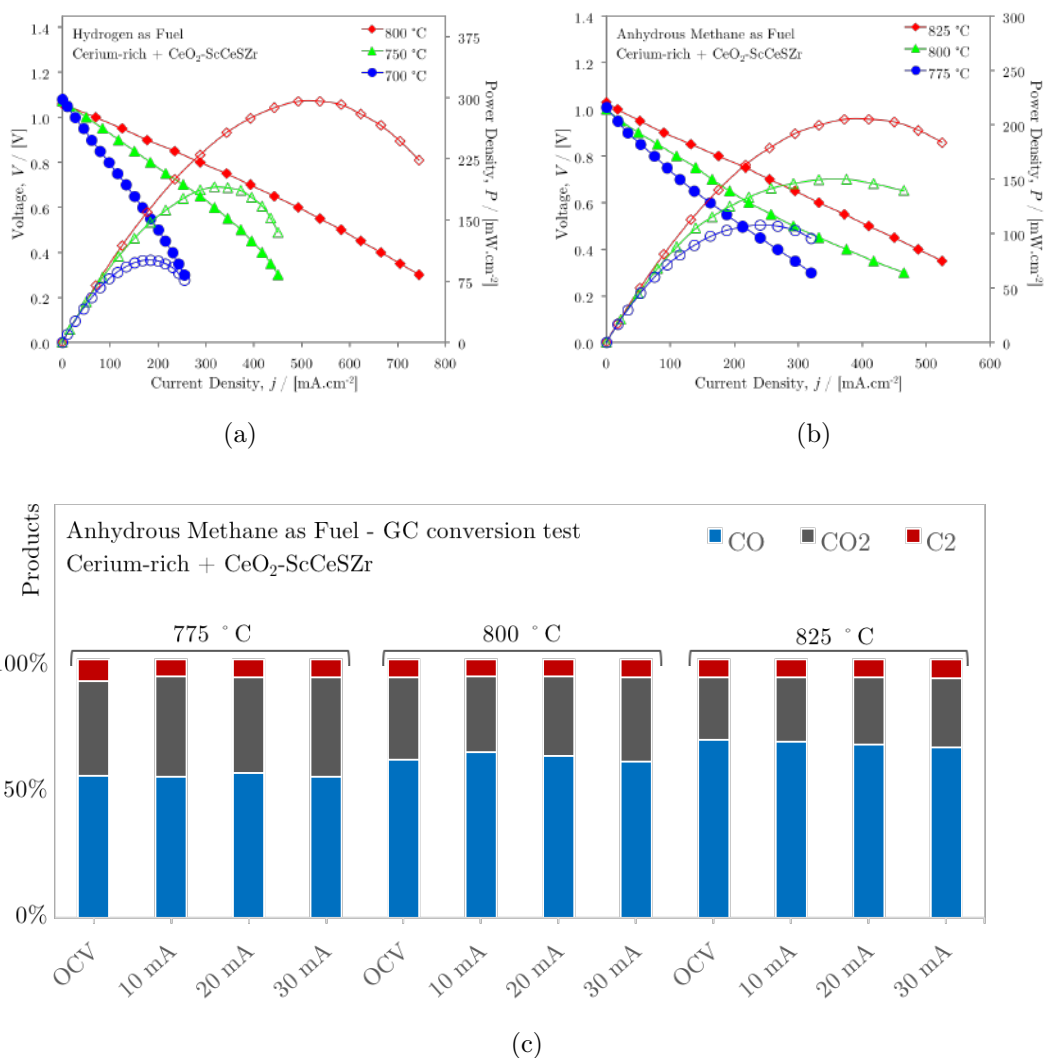


Figure 6.8: Electrochemical tests - cerium-rich with (a) hydrogen and (b) methane as fuel and (c) molar amount of products at different temperatures and loads conditions.

Figure 6.9c indicates that at 775°C the reaction path seems to be displaced

towards full oxidation rather than partial oxidation since the amount of CO_2 increases from 10 to 30 mA. The same seems to occur at 800°C . On the other hand, at 825°C as current increases, CO amount increases with current, thus indicating reaction's displacement towards partial oxidation.

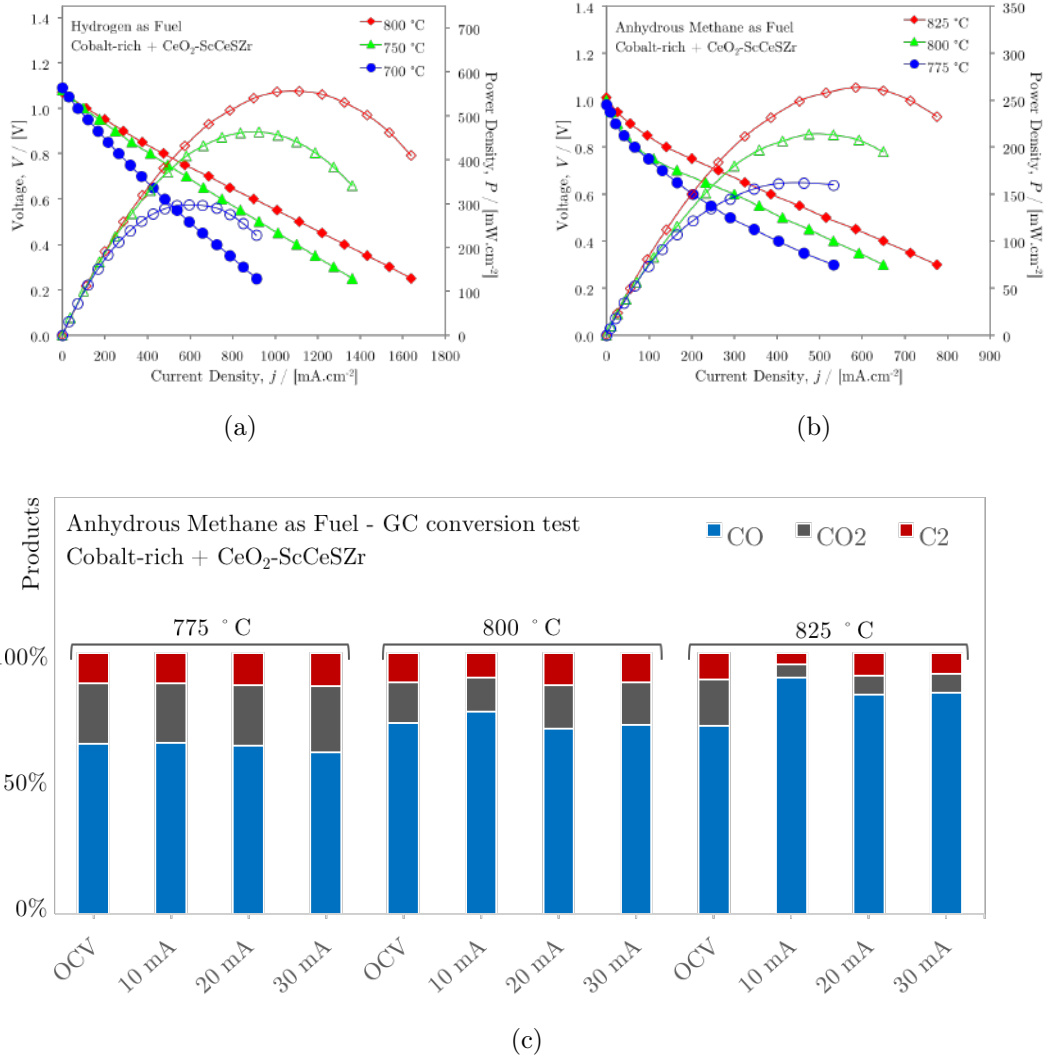


Figure 6.9: Electrochemical tests - cobalt-rich with (a) hydrogen and (b) methane as fuel and (c) molar amount of products at different temperatures and loads conditions.

Regarding the C_2 production for the cobalt-rich anode, the selectivity is 11 % with standard deviation of 1.1 % for cases at 775 and 800°C indicating thermal decomposition within these conditions. On the other hand, at 825°C the selectivity to C_2 decreases by half at 10 mA when comparing with OCV at the same temperature. As CO amounts increase drastically at this temperature, this might be another proof of electrochemical reaction since the amounts of thermal decomposition prod-

ucts become smaller to give place to CO production.

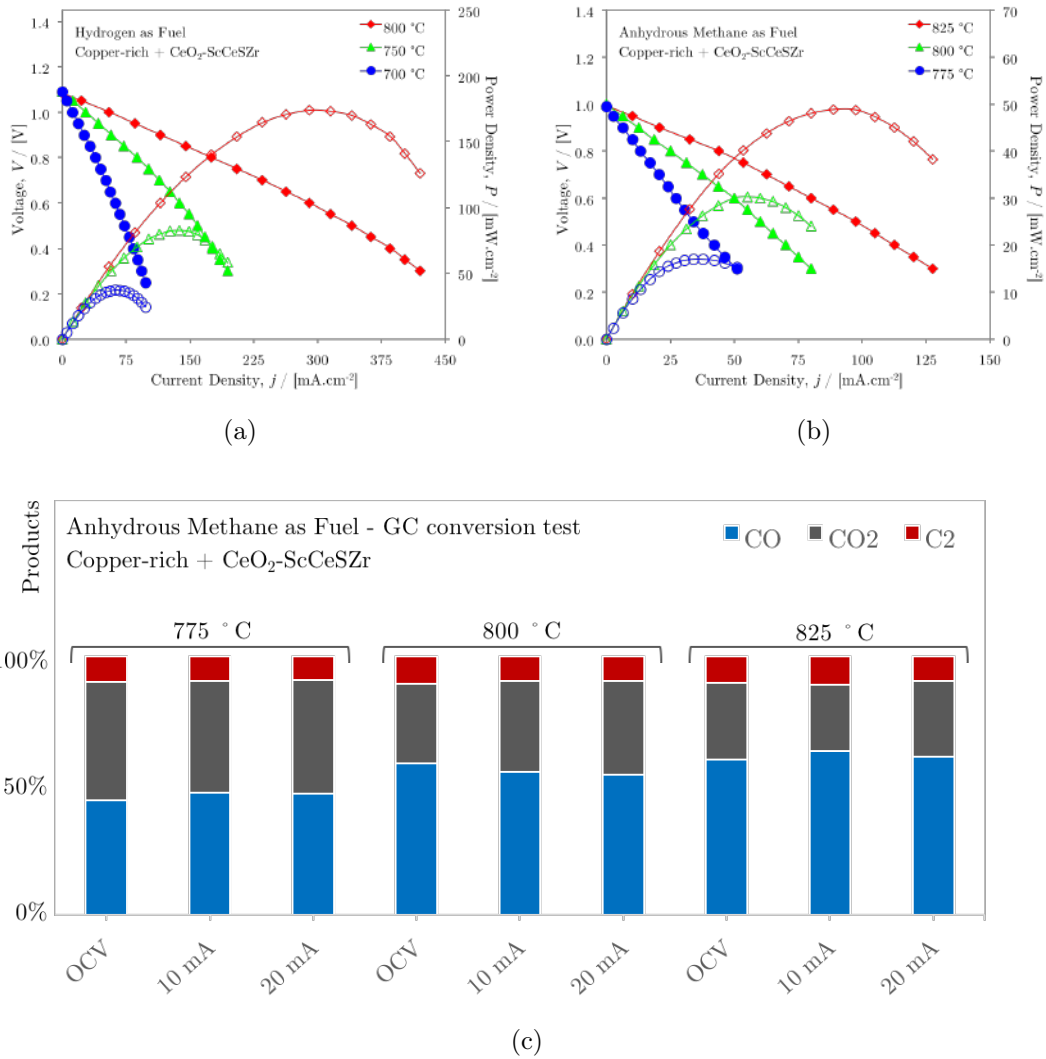


Figure 6.10: Electrochemical tests - copper-rich with (a) hydrogen and (b) methane as fuel and (c) molar amount of products at different temperatures and loads conditions.

Figure 6.10 show the results for electrochemical performance both in hydrogen or methane as fuels for the copper-rich composition, as well as the reaction products at the anode outlet gas. Maximum power densities in hydrogen were 37, 83 and 174 mW.cm⁻² whereas in methane 17, 30, 49 mW.cm⁻² at 775, 800 and 825°C, respectively.

Figure 6.10c shows that at 775°C the production of CO increases with current whereas CO₂ decreases, indicating partial oxidation, the same occurs at 825°C. However, at 800°C the reaction path seems to be displaced towards full oxidation,

Table 6.3: Compiled results for the cells tested at Federal University of Rio de Janeiro.

Composition	Fuels	Temperature [°C]	OCV [V]	Max. P. D. [mW.cm ⁻²]	@ 0.7 V [mA.cm ⁻²]
Cerium-rich	Hydrogen	700	1.08	100	133
		750	1.07	190	253
		800	1.06	290	393
	Methane	775	1.01	108	115
		800	1.00	150	165
		825	1.03	205	255
Cobalt-rich	Hydrogen	700	1.09	300	370
		750	1.08	460	583
		800	1.07	560	688
	Methane	775	0.98	160	130
		800	1.00	210	165
		825	1.01	260	263
Copper-rich	Hydrogen	700	1.09	37	51
		750	1.09	83	114
		800	1.08	174	235
	Methane	775	0.99	17	21
		800	1.00	30	38
		825	0.99	49	63

since the CO₂ amount increases. Tests at 30 mA were not performed since the voltage of the cell was very low at this current.

In addition, the selectivity to C₂ hydrocarbons does not seem to change significantly within different conditions indicating that the production is again due to thermal cleavage rather than electrochemical. The average selectivity to C₂ hydrocarbons was 9.9% with a standard deviation of 0.5%. In table 6.3 are compiled the results for the tests performed at the Federal University of Rio de Janeiro.

The rates of CO and CO₂ were calculated for each case as explained in Section 4.4 and then plotted against electric current for each operation temperature in Figure 6.11.

Figures 6.11a and 6.11b show the rate of CO and CO₂ measured for the cerium-rich composition. In Figure 6.11a, the production of CO at various temperatures remains almost unaltered as current increases, suggesting the effect of electrochemical partial oxidation (EPO) was not being sensed in this case whereas the CO₂ rate

- Figure 6.11b - slightly increases for all temperatures with current, suggesting small shares of electrochemical full oxidation (EFO).

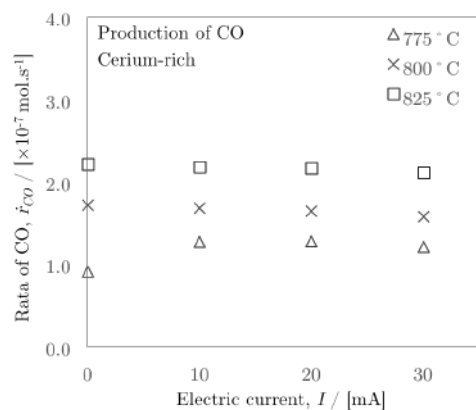
For the cobalt-rich composition, CO production seems to increase with increasing current especially at 825°C. At 775 and 800°C the differences are small, but still increasing with current as can be seen in Figure 6.11c. Yet CO₂ rate also increases with current suggesting activity of EFO as seen in Figure 6.11d. Additionally, it has to be pointed out that the rates for this composition are twice as big than for the cerium-rich one.

For the copper-rich composition the production rates also increase, but slightly. However, it is the composition that shows the most well-defined trend of increasing carbon oxides production with drawn current. The copper-rich composition results are represented in Figure 6.11e and 6.11f.

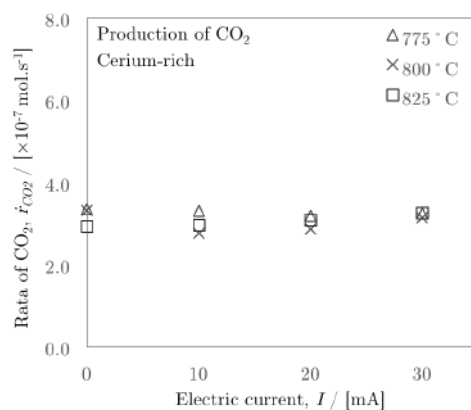
6.4 Results comparison and reproducibility

The results taken in both places can be compared using Tables 6.2 and 6.3. For the cerium-rich composition, the reproducibility can be noted from the tests with hydrogen that show results very close for each cell. In addition, the trend of each temperature changing makes sense, since power increases at a homogeneous rate with increasing temperature. However, results with methane differ drastically amongst them, since they are comparable with a difference of 75°C.

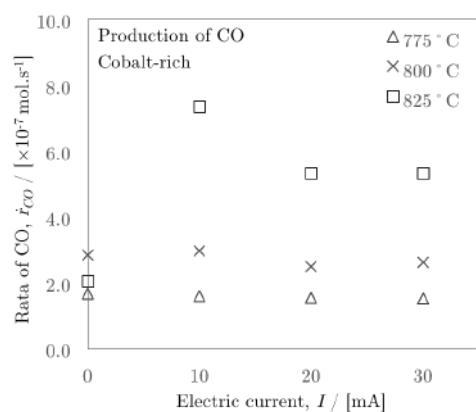
Regarding the cobalt-rich composition, even though results differ greatly in hydrogen the power-temperature trend is kept similar for both cells. Moreover, results with methane for these cells follow similar trends despite the difference on the absolute values. Copper-rich cells, despite having the worst results, they were reasonably compatible both in hydrogen and methane, showing reasonable reproducibility. The results comparison makes obvious that the cobalt-rich composition behaves the best in all tests, indicating that cobalt seems indeed to play an important role for the methane processing reactions.



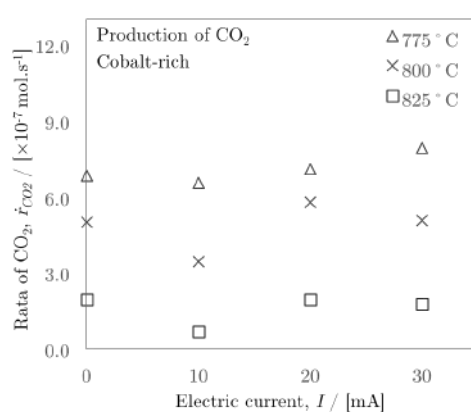
(a)



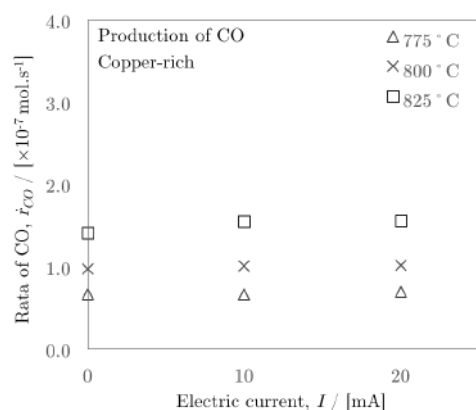
(b)



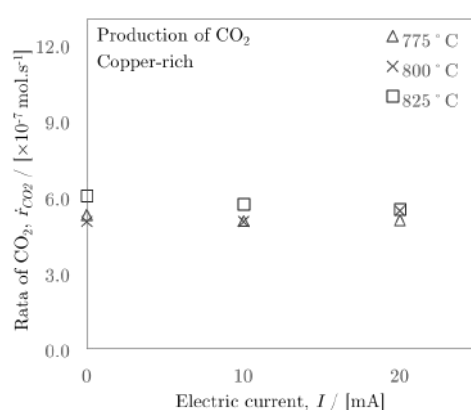
(c)



(d)



(e)



(f)

Figure 6.11: Production rates of (a) carbon monoxide and (b) carbon dioxide for cerium-rich composition, (c) carbon monoxide and (d) carbon dioxide for cobalt-rich composition, (e) carbon monoxide and (f) carbon dioxide for copper-rich composition.

6.5 *Post-mortem* characterisation

6.5.1 Raman spectroscopy of the anode surface

Raman spectra in Figure 6.12 show peaks located at 196, 482, 523, 621 and 691 cm^{-1} that are related to Co_3O_4 [298-301], 286 and 347 cm^{-1} to CuO [302] and 462 cm^{-1} to CeO_2 [303]. The peak at 550 cm^{-1} is assigned to Cu_2O [304].

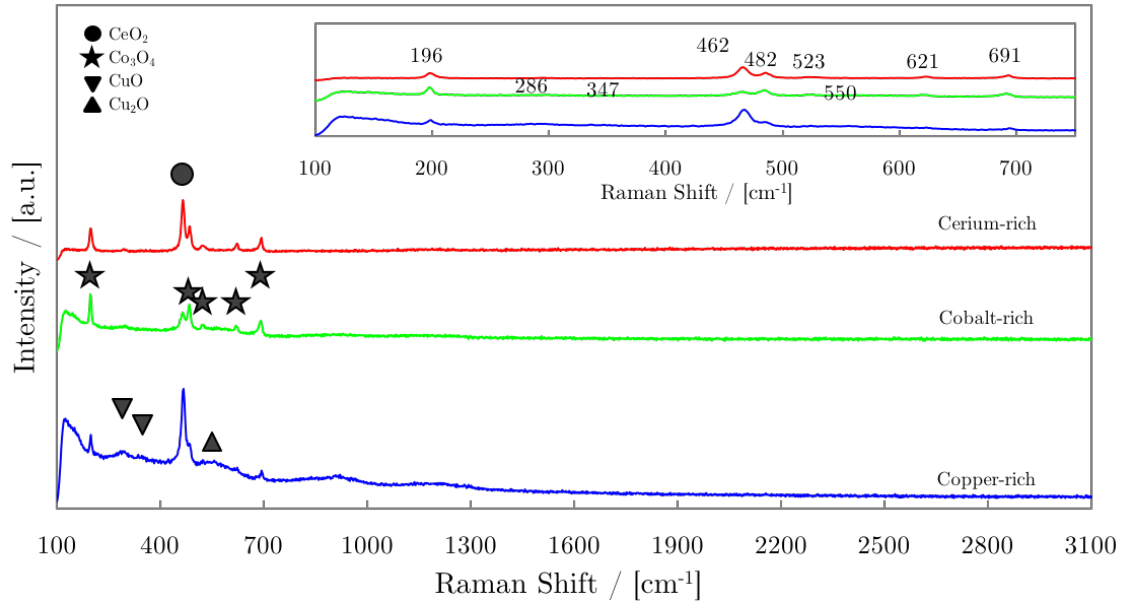


Figure 6.12: Raman spectroscopy for the bimetallic compositions of post-operated anode cells.

The ceria peak at 462 cm^{-1} can be assigned to the Ce F_{2g} mode due to symmetrical stretching of the O-Ce-O vibrational unit in octahedral coordination [305, 306]. The absence of a fluorite-type structure at 600 cm^{-1} suggests that solid solutions were most likely not formed [304] which corroborates with previous X-ray discussion. In addition, broadening and shifting of the Ce F_{2g} band indicates that ceria's particle size might be changed [304].

The Raman peaks of crystalline Co_3O_4 are related to E_g (482 cm^{-1}), F_{2g} (523 and 621 cm^{-1}) and A_{1g} (691 cm^{-1}) modes [281, 307, 308]. Therefore, this confirms that cobalt oxide is present only in its highest state of oxidation (Co_3O_4) even after the cell being operated showing that this oxide kept its oxi-redox capacity.

The peaks at 286 and 347 cm^{-1} of CuO can be assigned to the A_g and B_g vibra-

tional modes respectively [309]. Although peak locations are slightly different from literature (298 and 345 cm^{-1} [310]), this can be due to size effects.

6.5.2 TPO of the anode bulk

The graph in Figure 6.13 shows the TPO profiles for a sample of approximately 1.26 mg of graphite powder and the Ce:Co:Cu anodes after being operated with direct methane for over at least 10 hours. The GC coupled to the outlet gas that flowed through each sample was able to detect the absolute amounts of CO and CO₂ as products of carbon oxidation over a temperature range of 150 to 850°C.

The graph represents the molar amounts in comparison to the baseline test with carbon black. The sum of the products of oxidation for each composition was recorded and compared to the graphite mass previously known. The amounts of carbon oxidised from the anodes were estimated as 0.29, 0.29 and 0.25 mg for cerium-rich, cobalt-rich and copper-rich, respectively. Taking into account the anode average volume it can be said that the carbon deposits were in the order of 0.19, 0.19 and 0.16 $\text{g}\cdot\text{cm}^{-3}$ which represents less than 3% wt. of the anode in all three cases.

Long-term tests were not object of study in this work, but so far it can be said that the anode material ceria-cobalt/copper-based has shown to be resistant to coking, considering that a state of the art nickel-based anode would be completely destroyed after a couple of hours of operation with direct anhydrous methane [93, 210, 311, 312]. In addition, carbon oxidation shown in the profiles occurred in small mass/volume ratio and peaks shape identified in the GC chromatogram were not sharp and well-defined and therefore very sensitive to integration errors, again confirming that the molar amount formed was almost negligible.

6.5.3 SEM of the aged anode cross section

Scanning electron microscopy images are shown for each aged anode cross section in Figure 6.14. The images show clearly the distinction between the three layers,

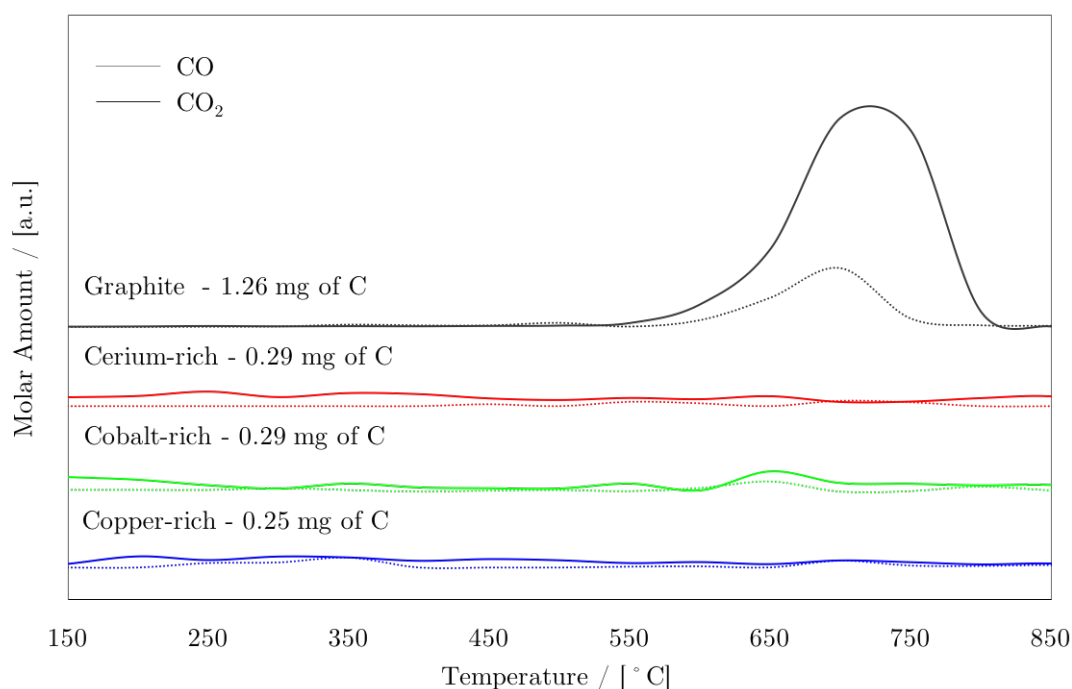


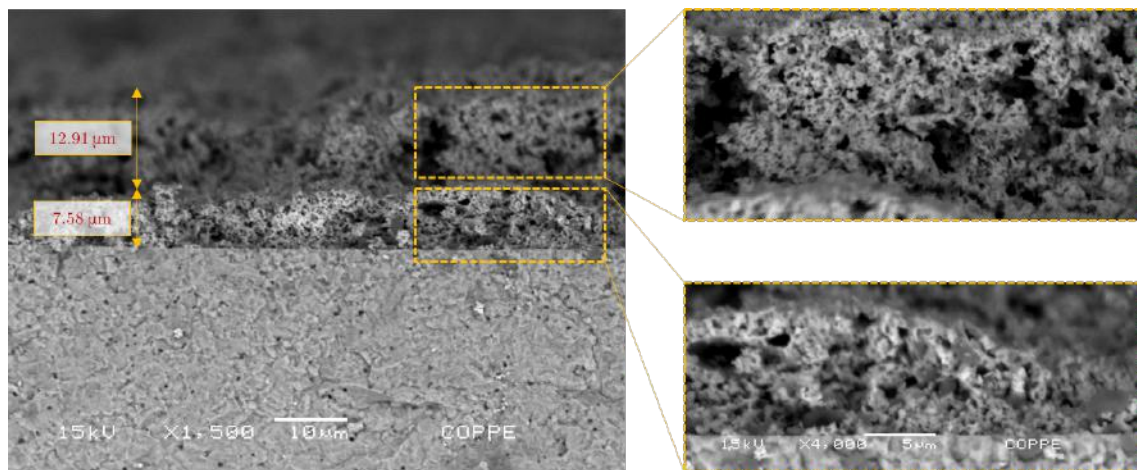
Figure 6.13: Temperature-programmed oxidation of the cells bulk after operation.

the electrolyte at the bottom supporting the thin buffer layer and finally the anode layer on top of it.

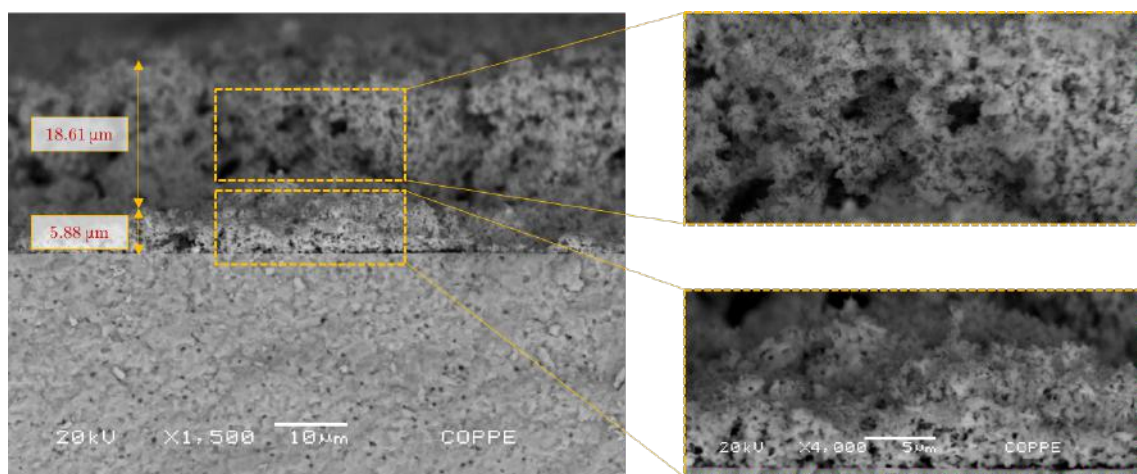
Figure 6.14a shows the anode for the cerium-rich composition in which the buffer layer is approximately $7.5\ \mu\text{m}$ thick whereas the anode layer is $12.9\ \mu\text{m}$ thick. Figure 6.14b show the cross section for the 1:2:1 composition showing thickness of $5.8\ \mu\text{m}$ and $18.6\ \mu\text{m}$ for the buffer layer and anode, respectively. Figure 6.14c presents the microstructure for the copper-rich composition showing layers of 5.8 and $13.4\ \mu\text{m}$ for the buffer layer and anode, respectively. The point EDX results are shown in Figure 6.15 corroborating strongly with the cross section imaging with clear distinction between phases through each layer. For all three anodes the EDX spectra presented by the dot 1 show the elements of the anode in abundance, whilst in dot 2 the metals cobalt and copper are less present. Finally, dot 3 present the electrolyte elements Zr, Sc and Ce, accordingly.

Figures 6.16, 6.17 and 6.18 show the EDX mapping and distributions of phases for the elements zirconium, cerium, cobalt and copper in cerium, cobalt and copper-rich compositions, respectively. Figures 6.16f, 6.17f and 6.18f represent the EDX elements

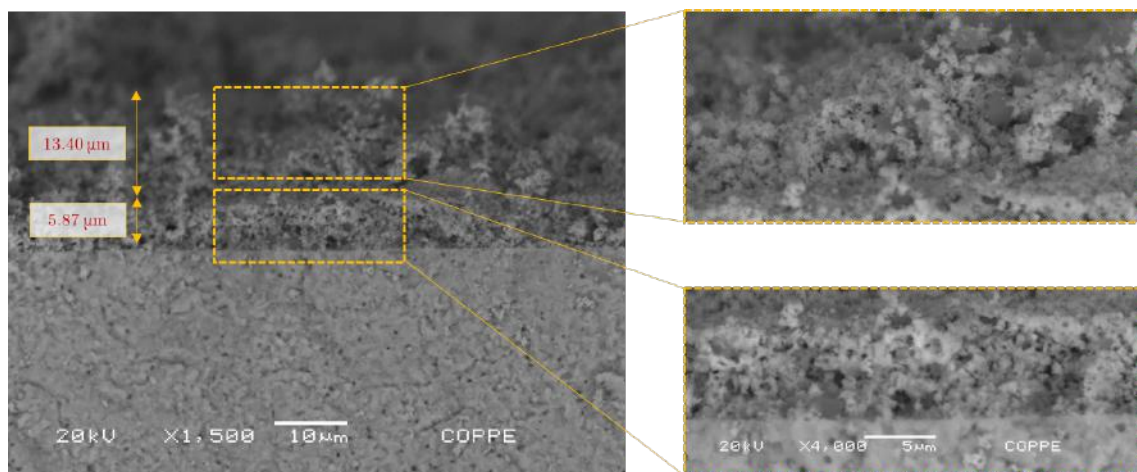
images merged all together to depict phase and pores distribution throughout the cross section of each composition. The images merging was done using the image processing software Metallographica to apply low-pass filters eliminating noise and to attribute colors to each phase. After that, Matlab was used to superpose each image. Furthermore, the porosity of each composition was estimated by image analysis over Figures [6.14a](#), [6.14b](#) and [6.14c](#) as 30.3, 27.8 and 14.5% for cerium-rich, cobalt-rich and copper-rich compositions, respectively. Although cerium and cobalt-rich composition presented similar porosities it has to be pointed out the considerable difference of the copper-rich composition that might be due to coarsening.



(a)

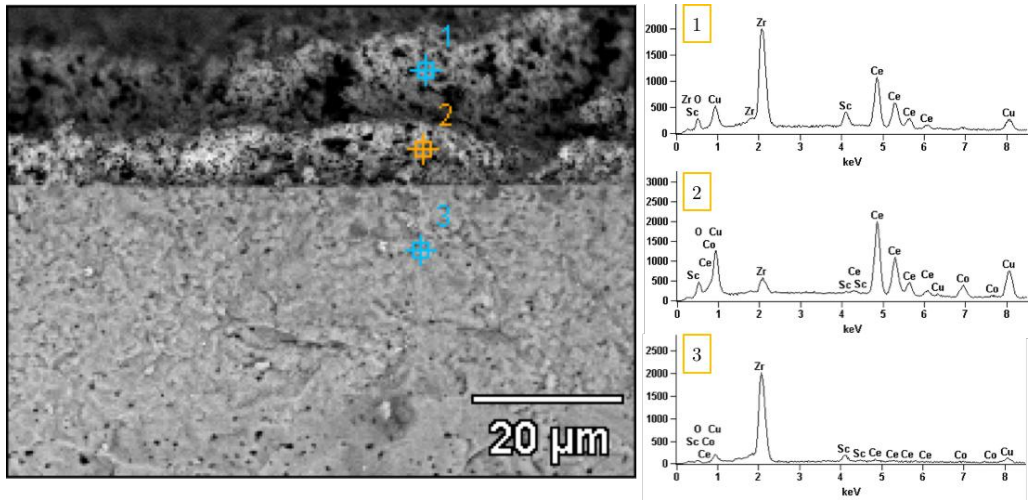


(b)

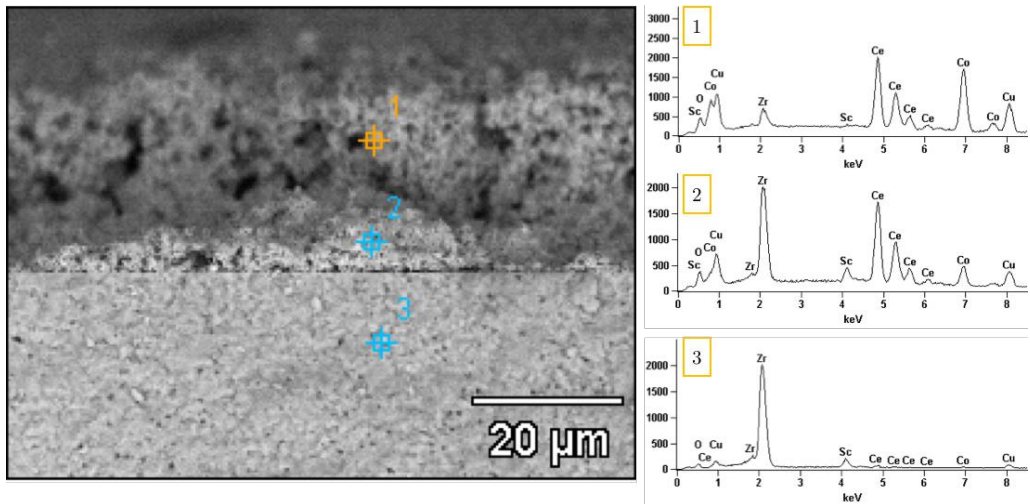


(c)

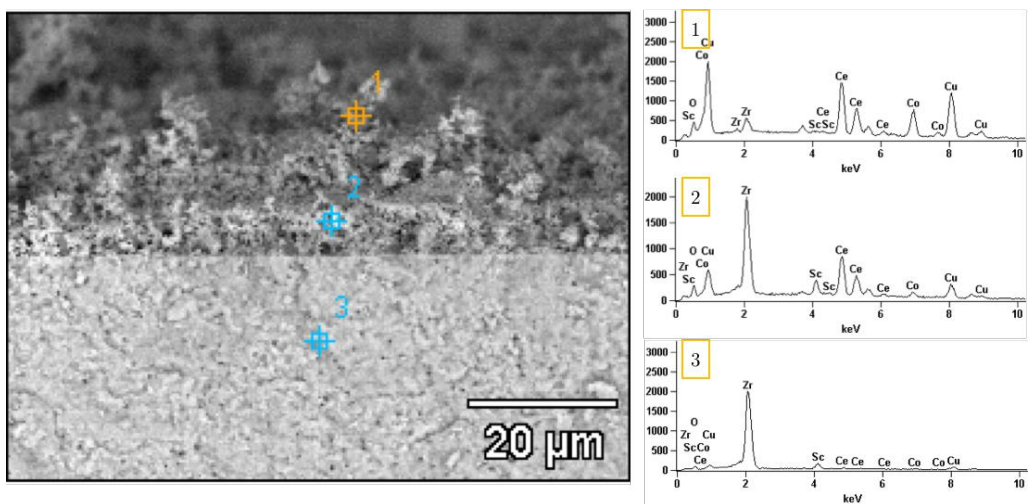
Figure 6.14: SEM imaging over reduced and aged anodes (a) Ce:Co:Cu - 2:1:1, (b) Ce:Co:Cu - 1:2:1 and (c) Ce:Co:Cu - 1:1:2.



(a)



(b)



(c)

Figure 6.15: EDS point composition - identifying the layers for the reduced and aged anodes (a) Ce:Co:Cu - 2:1:1, (b) Ce:Co:Cu - 1:2:1 and (c) Ce:Co:Cu - 1:1:2.

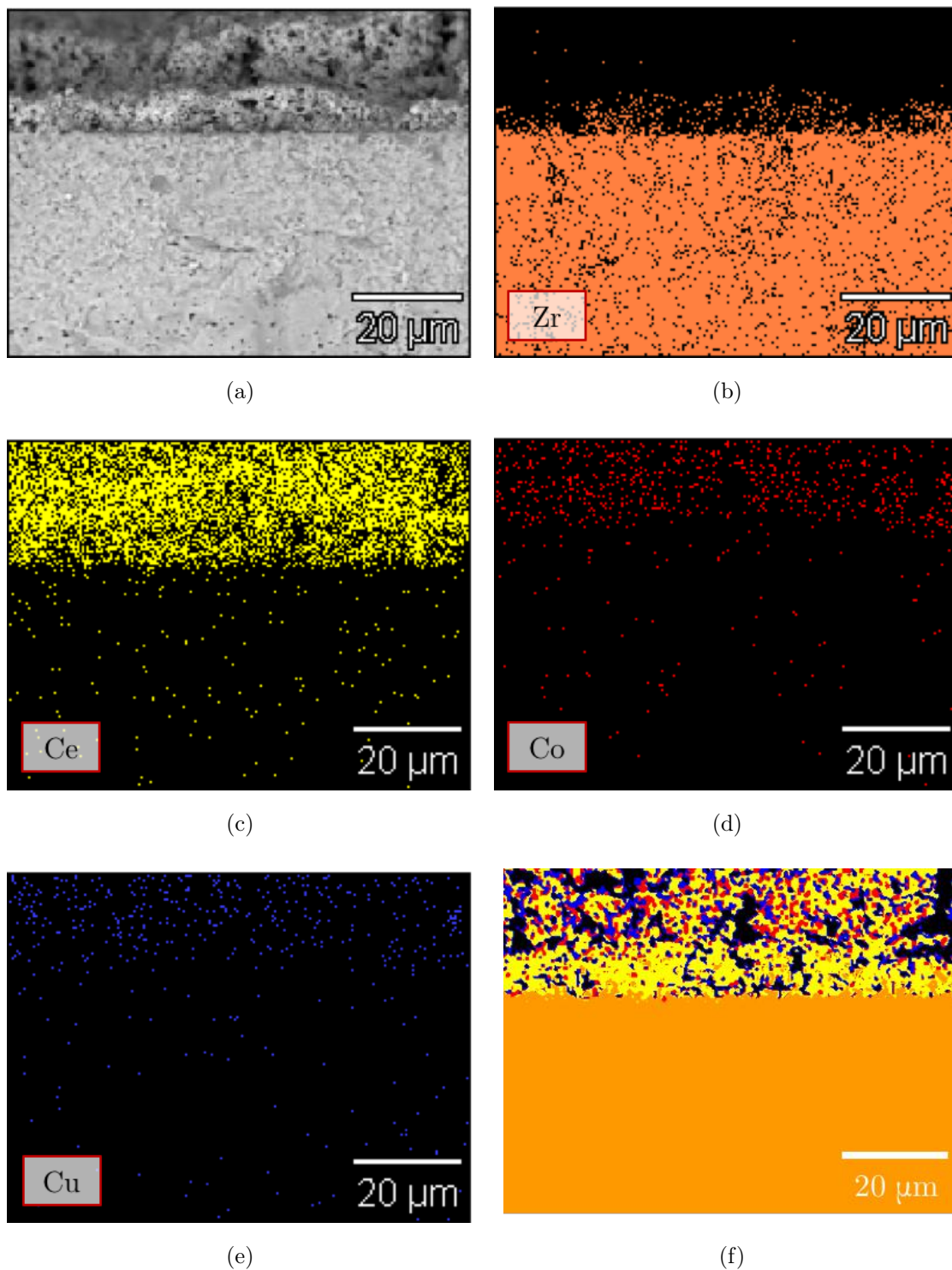


Figure 6.16: EDX mapping over reduced and aged anode cross section - cerium-rich composition. (a) Original field micrographed, (b) zirconium, (c) cerium, (d) cobalt, (e) copper and (f) phases overlap.

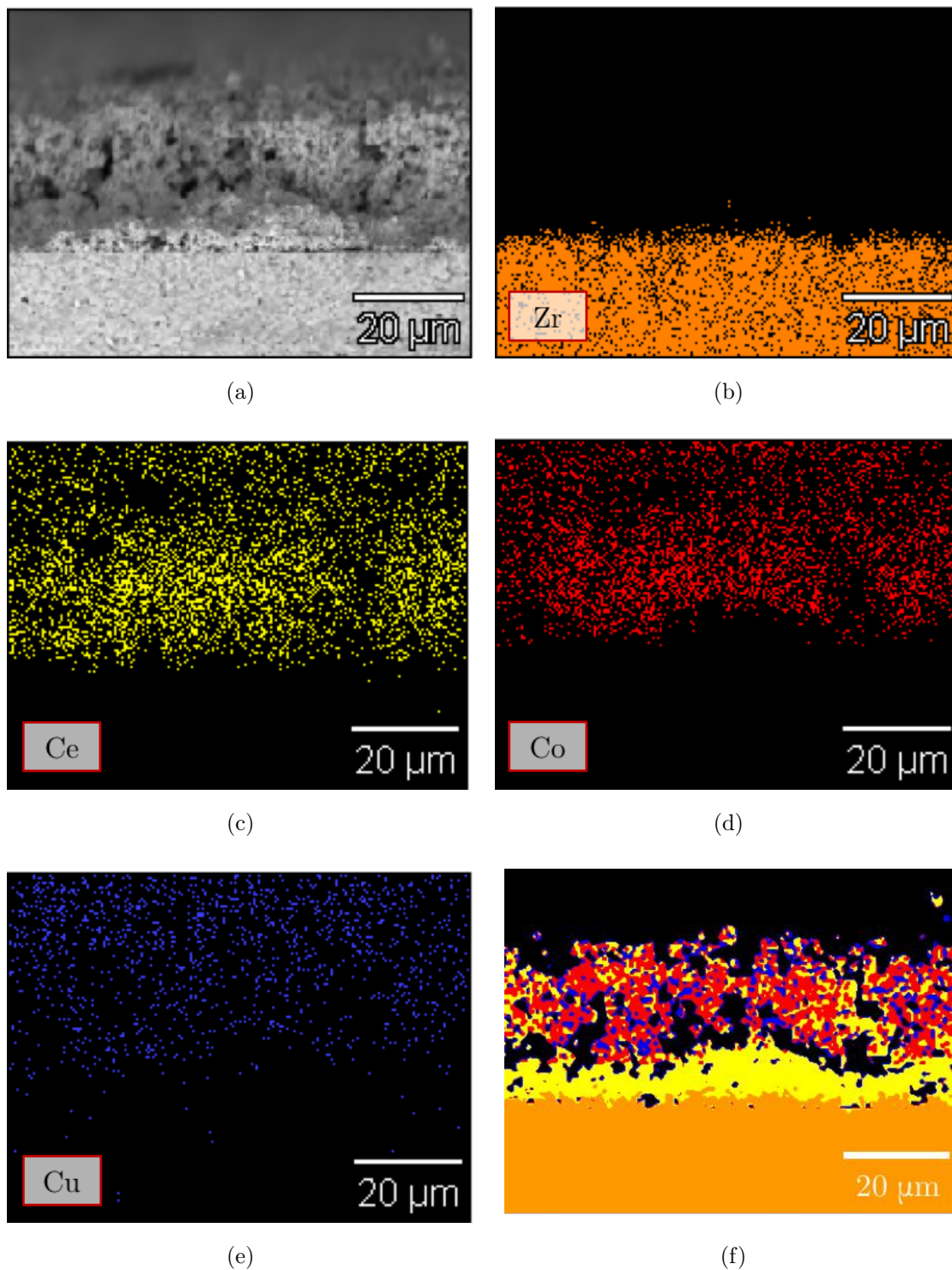


Figure 6.17: EDX mapping over reduced and aged anode cross section - cobalt-rich composition. (a) Original field micrograph, (b) zirconium, (c) cerium, (d) cobalt, (e) copper and (f) phases overlap.

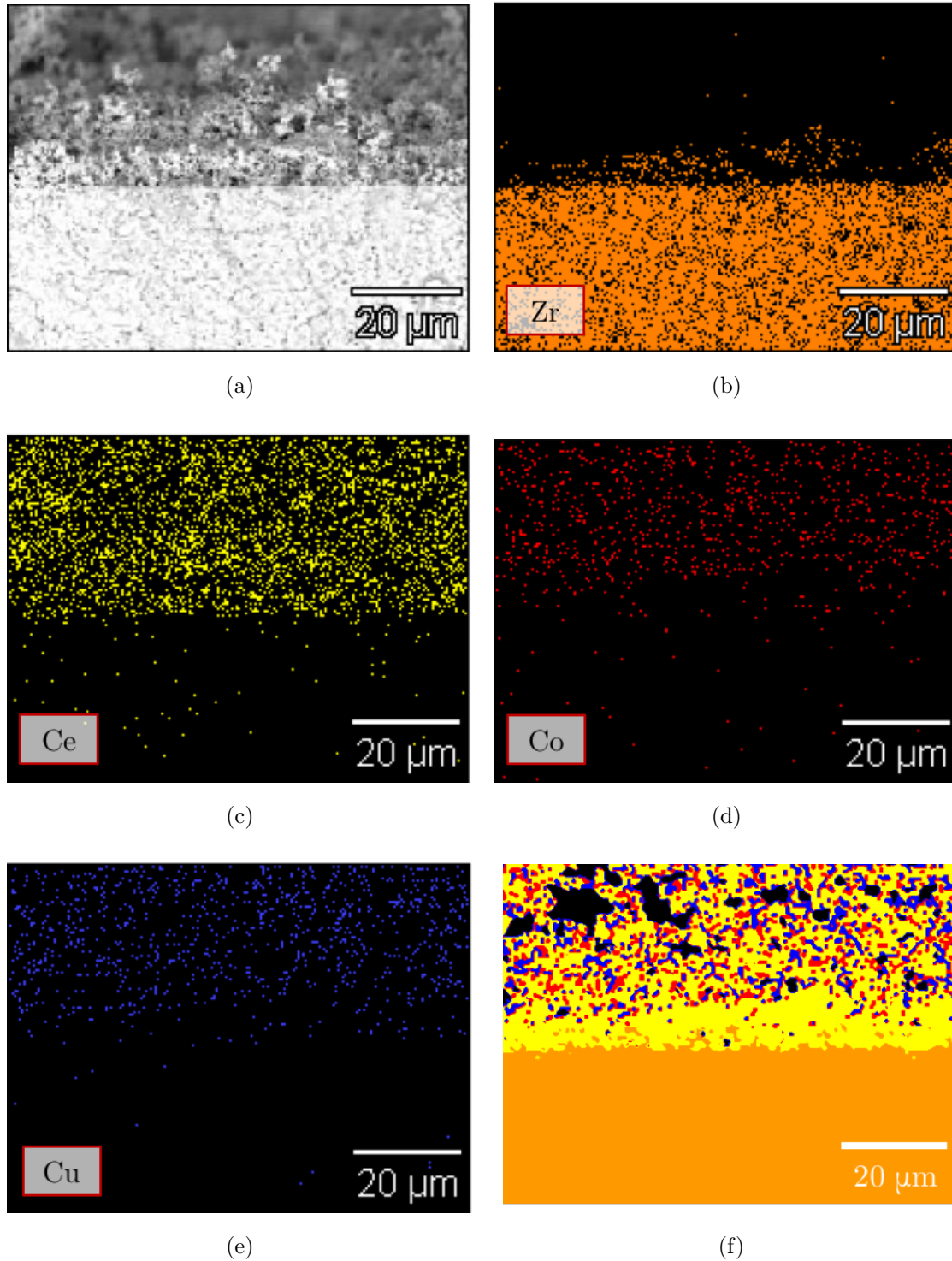


Figure 6.18: EDX mapping over reduced and aged anode cross section - copper-rich composition. (a) Original field micrographed, (b) zirconium, (c) cerium, (d) cobalt, (e) copper and (f) phases overlap.

6.6 Summary of the chapter and conclusions

The OCVs of the tests with hydrogen ranging from 1.00 to 1.15 V suggest that no significant leakage occurred thus showing that the Thermicullit sealing gasket worked properly and without the necessity of high loads when mounting the tubes over one another.

Taking into account the impedance spectra of Figures [6.3b](#), [6.4b](#) and [6.5b](#), the ohmic resistance is almost unaltered for the three compositions varying only when temperature is changed, thus indicating that ohmic contributions are mainly due to the electrolyte effect, which is the same in all cases, and the electrodes ohmic resistance within it can be neglected.

GC analysis gave the idea of which range of temperature is the most effective for each composition to operate, considering that the cases when the reaction path is shifted towards full oxidation present higher efficiency to the system. In this case, it can be said that for the cerium-rich composition, operation at 825°C is the best condition, considering that the CO₂ amount increases as current is applied. The cobalt-rich composition seems to operate better at 800°C since CO₂ amounts are greater at this condition. The same occurs for the copper-rich composition, that showed higher amounts of CO₂ at 800°C.

From the short-term methane tests, it was observed that cobalt seems to play an important catalytic role in the proposed mixture. However, even though performance results with methane were the highest with the cobalt-rich composition, the asymptotic behaviour on the impedance for this composition suggests high concentration effects that might be due to carbon deposition that somehow promoted clogging. Moreover, the increase in OCV for the cobalt-rich composition after methane was used as fuel also can suggest carbon formation [\[273\]](#) since OCV is altered by the reaction products presented in the anode chamber. Nevertheless, Raman results in Figure [6.12](#) do not show evidence of coking on the surface of any tested composition.

Moreover TPO results confirmed that even though no carbon was found by Raman spectroscopy for the operated cells, small amounts of it were impregnating

the anode microstructures and since no long-term test was taken so far, nothing can be said about these deposits being negligible or not. However, it was observed that the amounts of carbon per unit volume were not enough to deplete physically or visually the anode of any composition.

SEM results have shown homogeneous phase distribution throughout the cross section of each composition. The thickness of each anode layer deposited is reproducible at each studied anode. Pores distribution has shown to be higher with the cerium-rich composition and quite similar to the cobalt-rich composition. However, the copper-rich composition presented almost half of porosities, indicating that pore blocking might have occurred by copper phase coarsening.

Chapter 7

The role of cobalt and copper

In order to understand the role of each metal in the ceria-based material whilst operating with hydrogen or methane monometallic compositions were produced. The ceria-cobalt and ceria-copper powder were also synthesised by the amorphous citrate method as explained in Section [4.1](#). However the molar composition was 1:1 both for Ce:Co and Ce:Cu and thus from here onwards named $\text{CeO}_2\text{-Co}_3\text{O}_4$ and $\text{CeO}_2\text{-CuO}$, respectively. For the two monometallic compositions produced, the following amounts of nitrates, water and citric acid that were used are shown in Tables [7.1](#) and [7.2](#).

Table 7.1: Synthesis of precursors $\text{CeO}_2\text{-Co}_3\text{O}_4$.

Ce:Co:Cu - 1:1:0	Nitrates Solution		Citric Acid Solution	
	Salt [g]	DI Water [mL]	Citric Acid [g]	DI Water [mL]
$\text{Ce}(\text{NO}_3)_3 \cdot 6\text{H}_2\text{O}$	5.4536	3.1164	2.6392	1.9844
$\text{Co}(\text{NO}_2)_3 \cdot 6\text{H}_2\text{O}$	3.6552	2.7278	2.6392	1.9844
$\text{Cu}(\text{NO}_3)_2 \cdot 3\text{H}_2\text{O}$	0.0000	0.0000	0.0000	0.0000

Table 7.2: Synthesis precursors $\text{CeO}_2\text{-CuO}$.

Ce:Co:Cu - 1:0:1	Nitrates Solution		Citric Acid Solution	
	Salt [g]	DI Water [mL]	Citric Acid [g]	DI Water [mL]
$\text{Ce}(\text{NO}_3)_3 \cdot 6\text{H}_2\text{O}$	5.3301	3.0458	2.5794	1.9394
$\text{Co}(\text{NO}_2)_3 \cdot 6\text{H}_2\text{O}$	0.0000	0.0000	0.0000	0.0000
$\text{Cu}(\text{NO}_3)_2 \cdot 3\text{H}_2\text{O}$	2.9656	2.1490	2.5794	1.9394

The powders produced were characterised by basic techniques such as X-ray

diffraction and TGA analysis as described in Sections [4.2.1](#) and [4.2.2](#), respectively. The cells were assembled with LSM as cathode and an anode buffer layer as described in Section [4.3](#) and then the $\text{CeO}_2\text{-Co}_3\text{O}_4$ and $\text{CeO}_2\text{-CuO}$ anode inks were deposited over it to compose the full cell and also sintered at 900°C . The scheme of these cell assemblies is depicted in Figure [7.1](#).

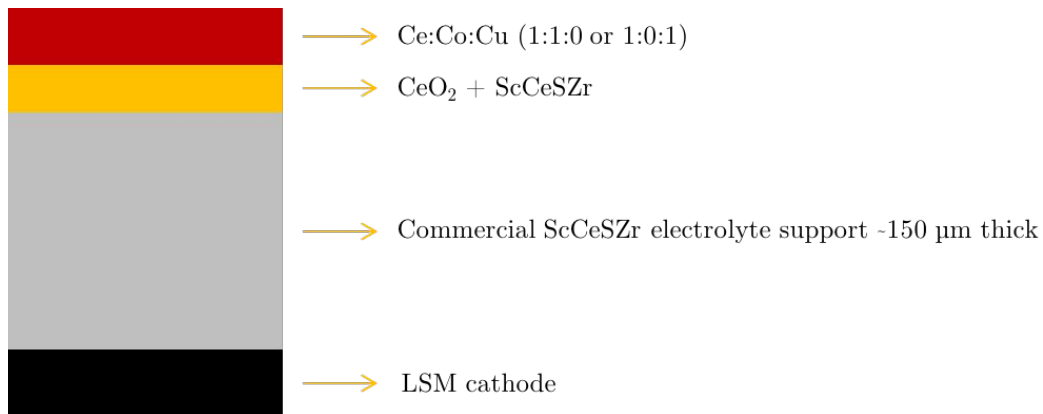


Figure 7.1: Cells assembly scheme - Monometallic compositions.

7.1 X-ray analysis

X-ray patterns are presented in Figure [7.2](#). The phases formed were CeO_2 , Co_3O_4 and CuO after heat treatment at 800°C . It is important to point out that before heat treatment, the 1:0:1 composition had copper oxide on its least oxidised form (Cu_2O) and after treating in air, full oxidation of Copper took place turning it into CuO . The details can be seen inserted in Figure [7.2](#).

7.2 Thermogravimetric analysis

The TGA results are presented in Figure [7.3](#). The losses around 7.58 % in Figure [7.3a](#) from 25 to 450°C represent the volatiles evaporation whereas in Figure [7.3b](#) a gain of mass of around 0.53 % can be observed from 25 to 450°C which is assigned to copper oxidation ($\text{Cu}_2\text{O} \rightarrow \text{CuO}$), which corroborates with X-ray results in Figure [7.2](#). No further significant loss is noted at higher temperatures.

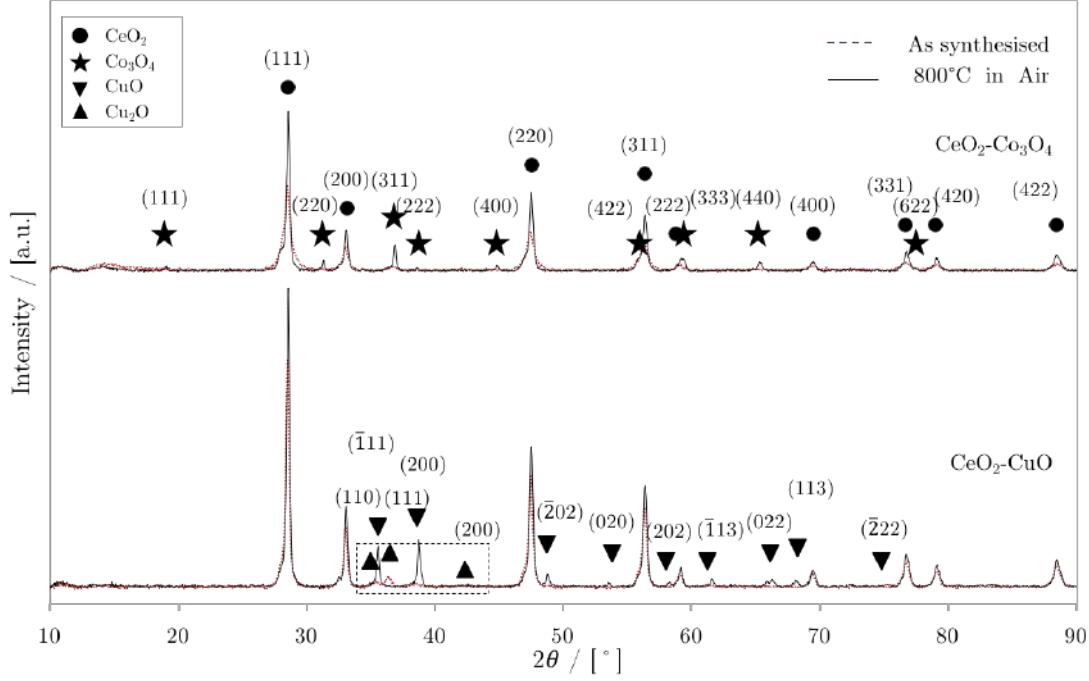


Figure 7.2: X-ray diffractograms for ceria-cobalt and ceria-copper compositions.

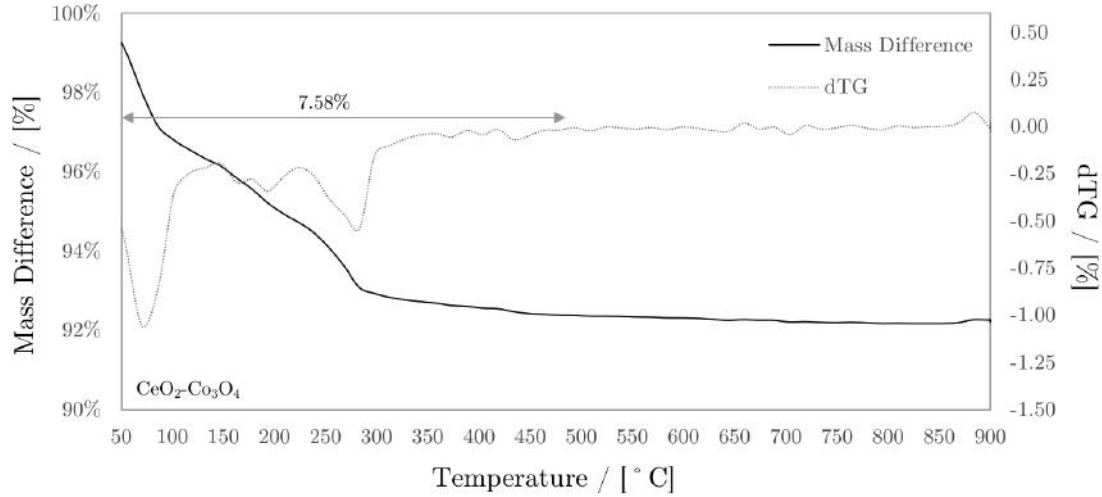
7.3 Electrochemical tests

Results of electrochemical performance and impedance spectra are presented in Figures [7.4a](#), [7.4b](#), [7.5a](#), [7.5b](#), [7.6a](#) and [7.6b](#) for the monometallic compositions.

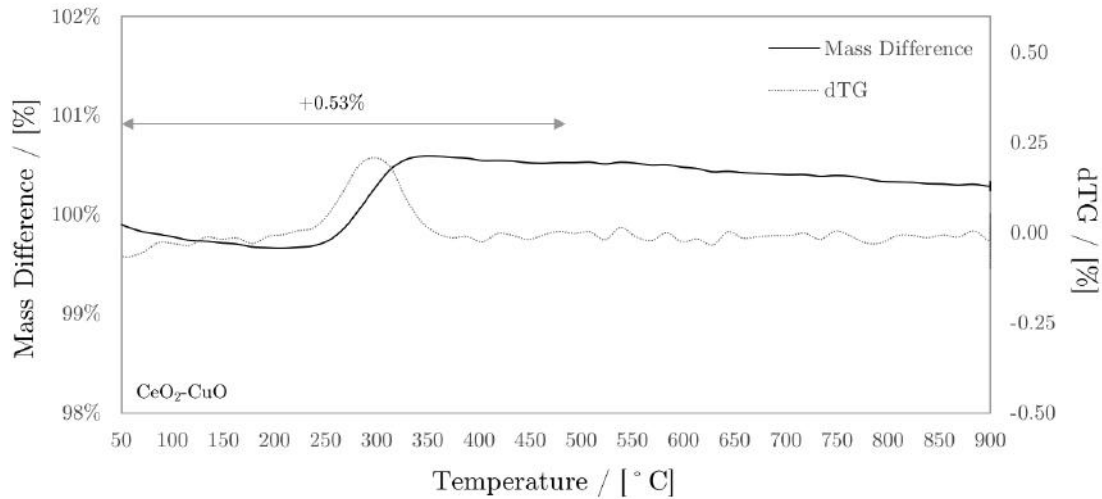
The maximum power densities with hydrogen as fuel for the ceria-cobalt composition were 97, 147 and 247 $\text{mW}\cdot\text{cm}^{-2}$ whereas OCV were 1.12, 1.11 and 1.09 V at 750, 800 and 850°C, respectively as depicted in Figure [7.4a](#). The ohmic resistance was 0.38, 0.24 and 0.18 $\Omega\cdot\text{cm}^2$ whereas total polarisation was 5.09, 3.06 and 1.54 $\Omega\cdot\text{cm}^2$ at 750, 800 and 850°C, respectively.

For the ceria-copper composition operating with hydrogen as fuel the maximum power densities were 40, 71 and 118 $\text{mW}\cdot\text{cm}^{-2}$ and OCV values were 1.15, 1.12 and 1.11 V from 750 to 850°C, respectively as shown in Figure [7.5a](#). For the impedance spectra in Figure [7.5b](#) the ohmic resistances were 0.47, 0.32 and 0.24 $\Omega\cdot\text{cm}^2$ and total polarisations 5.58, 2.55 and 1.80 $\Omega\cdot\text{cm}^2$ at 750, 800 and 850°C, respectively.

The results with methane as fuel shown in Figure [7.6a](#) indicate maximum power densities of 130 and 32 $\text{mW}\cdot\text{cm}^{-2}$ and OCVs of 1.22 and 1.07 V for the ceria-cobalt and ceria-copper compositions, respectively. Regarding ohmic resistances, Figure



(a)



(b)

Figure 7.3: Thermogravimetric analysis for the (a) $\text{CeO}_2\text{Co}_3\text{O}_4$ and (b) CeO_2CuO compositions.

7.6b show 0.19 and $0.24 \Omega \cdot \text{cm}^2$ for $\text{CeO}_2\text{-Co}_3\text{O}_4$ and $\text{CeO}_2\text{-CuO}$ compositions, respectively, whereas for the total polarisation only for ceria-copper composition it was possible to fit a model that converged to 0 at the imaginary axis thus showing $3.78 \Omega \cdot \text{cm}^2$. The spectrum of impedance for the ceria-cobalt anode indicates high polarisation effects at lower frequencies indicating problems with transport, probably due to carbon deposition.

For the parameters of fitted ECMs, refer to Tables **9.8**, **9.9** in the Appendix II.

Yet using the estimative of polarisation resistance for hydrogen as fuel, the Ar-

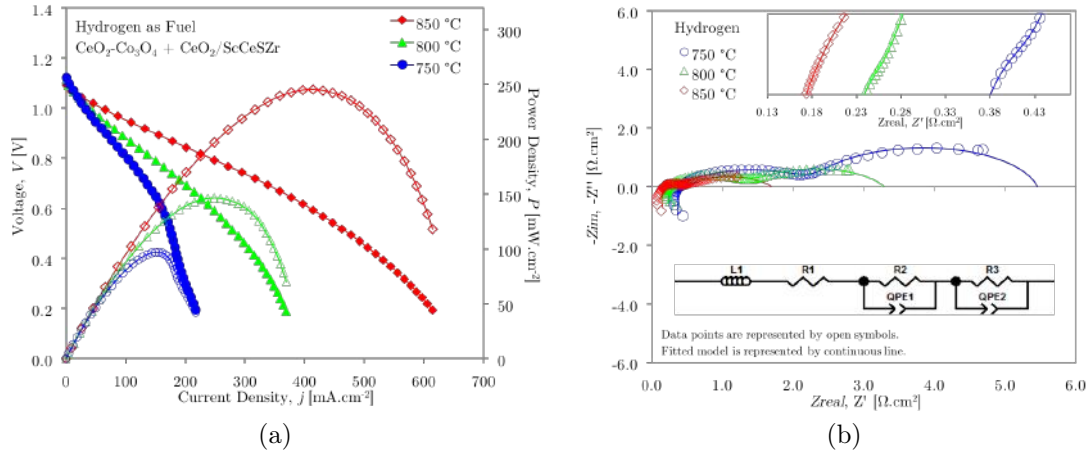


Figure 7.4: Electrochemical performance for $\text{CeO}_2\text{-Co}_3\text{O}_4$ composition from 750 to 850 °C (a) i-V plots and (b) impedance spectroscopy under hydrogen as fuel.

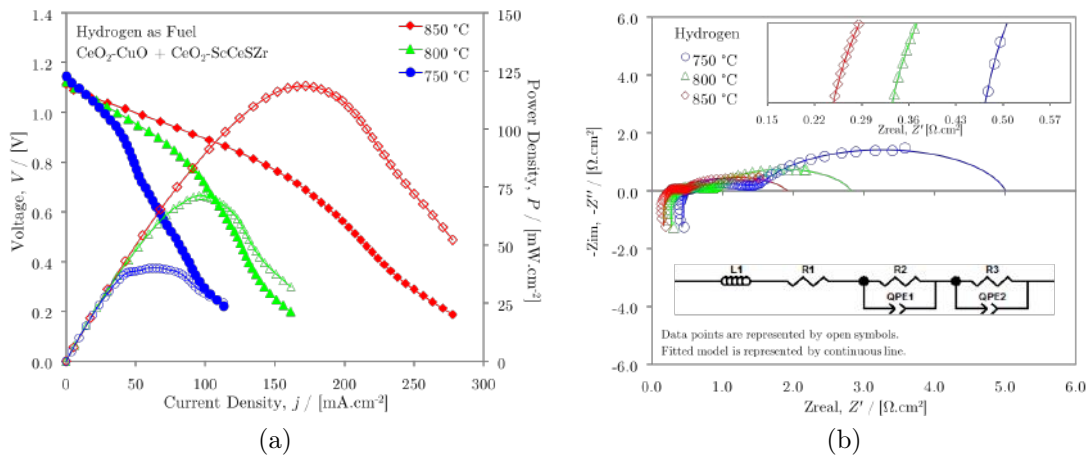


Figure 7.5: Electrochemical performance for the $\text{CeO}_2\text{-CuO}$ composition 750 to 850 °C (a) i-V curve and (b) impedance spectroscopy under hydrogen as fuel.

renius plot is shown in Figure 7.7. The coefficients are presented in Table 7.3 in which can be seen that the slopes are almost the same and larger than those for the bimetallic compositions.

The higher the slope, the higher the temperature needed to activate and make the catalyst work properly. This result shows that the bimetallic compositions tested so far are more effective in terms of anode activity, charge and mass transport phenomena since their activation energies are smaller than for the monometallic compositions.

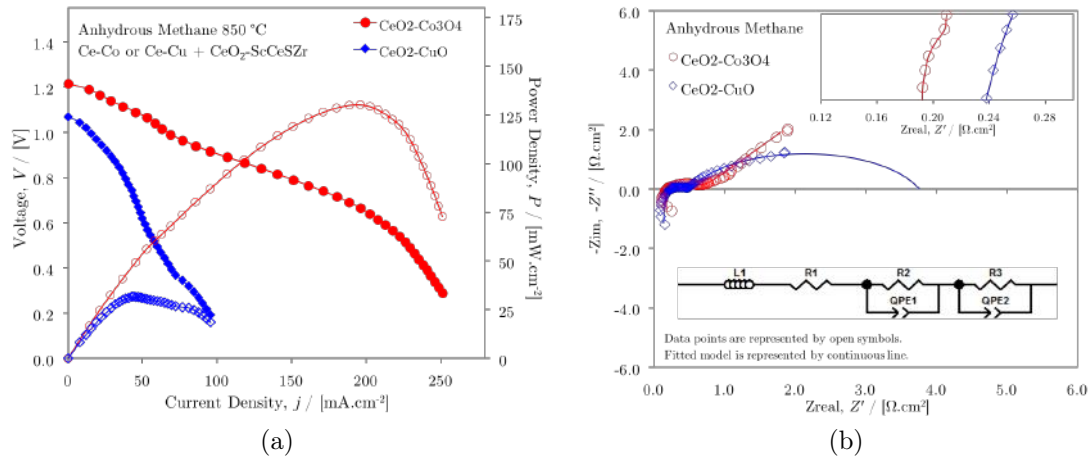


Figure 7.6: Electrochemical performance for CeO₂-Co₃O₄ and CeO₂-CuO compositions at 850°C (a) i-V curve and (b) impedance spectroscopy under direct methane as fuel.

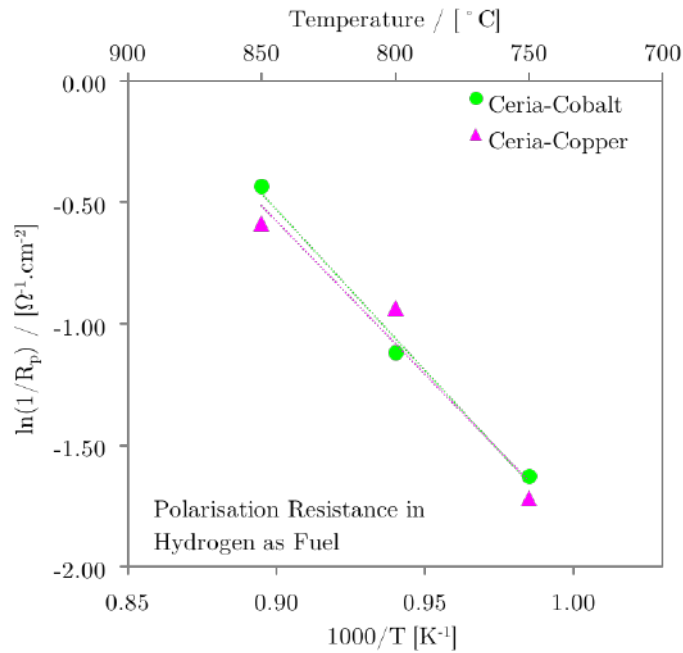


Figure 7.7: Arrhenius plot for total polarisation resistances of monometallic cells in hydrogen as fuel.

7.4 *Post-mortem* characterisation

The Raman spectra for the two monometallic compositions are presented in Figure 7.8. For the CeO₂-Co₃O₄ composition, cobalt oxide is noted at 196, 482, 523, 621 and 691 cm⁻¹ whereas for the CeO₂-CuO composition, copper oxide is seen as CuO at 286 and 347 cm⁻¹ and Cu₂O at 550 cm⁻¹. In both compositions cerium oxide is

Table 7.3: Linear regression for total polarisation - Monometallic compositions.

Composition	Equation	R ²	1/R ₀ [Ω ⁻¹ .cm ⁻²]	-E/R	E [kJ.mol ⁻¹]
Ce:Co:Cu - 1:1:0	-13.693x + 11.720	0.9874	11.720	-13.693	113.84
Ce:Co:Cu - 1:0:1	-13.066x + 11.114	0.9638	11.114	-13.066	108.63

seen at 462 cm⁻¹. Moreover, the CeO₂-Co₃O₄ spectrum shows evidence of carbon deposition over the surface, presented at 1330, 1580 and 2660 cm⁻¹ for the G, D and 2D bands.

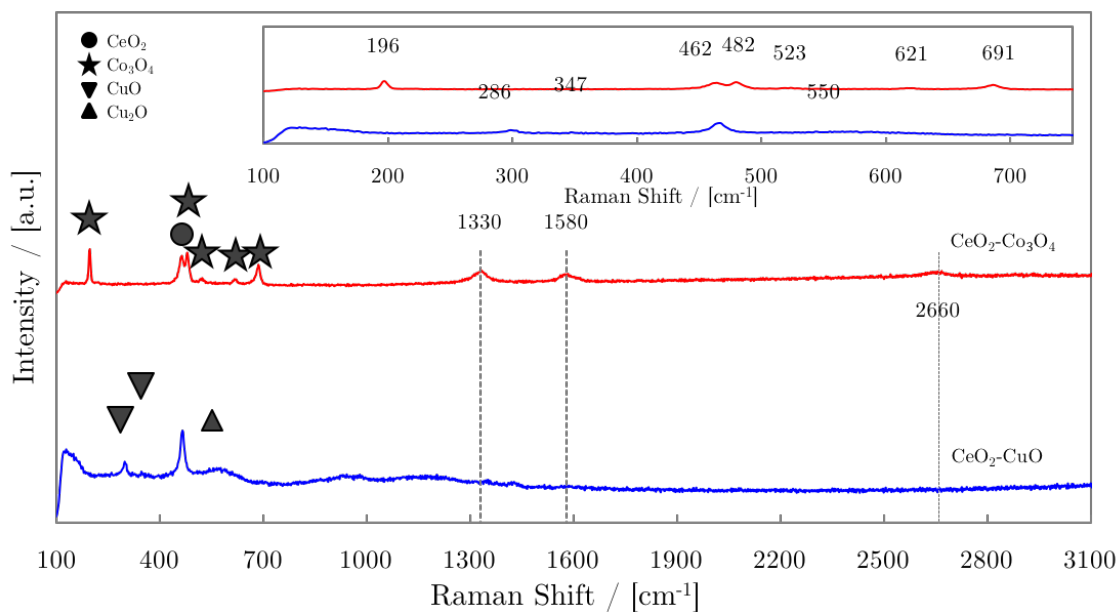


Figure 7.8: Raman spectroscopy for the monometallic compositions.

7.5 Summary of the chapter and conclusions

The aim of this part of the work was to provide valuable information about each metal in monometallic catalyst form and relate it to the effects experienced in the bimetallic compositions. The X-ray results have shown that initially another phase which was the lowest state of copper oxide was present (Cu₂O) in the cerium-copper catalyst, which was oxidised after firing at 800°C in air. Moreover, TGA results corroborated with the aforesaid by showing mass increase in Figure 7.3b. The cerium-cobalt compositions have behaved as expected in that case by forming cerium and cobalt oxides as isolated phases.

Electrochemical tests revealed higher ability of the cerium-cobalt anode to operate with both hydrogen and methane as fuels, whereas cerium-copper has shown to be poorer in performance. However, whilst methane fed, the cerium-cobalt has shown evidences of carbon deposition represented by high impedances at low frequencies of its spectrum shown in Figure [7.6b](#).

The Raman spectra of the *post-mortem* cells revealed evidence of coking on the cerium-cobalt composition whereas nothing was found on the cerium-copper anode. Although the excess of cobalt might shift the decomposition towards coking, this metal seems to play an important role as catalyst whereas copper might be more adequate when the material lacks on electronic conductivity. Another important conclusion is that copper seems to diminish the cobalt activity to retain carbon thus playing an important role on coking prevention.

Chapter 8

Discussions

8.1 Phases formation

The XRD results indicated the formation of CeO_2 , Co_3O_4 and CuO rather than solid solutions. Although solid solutions between CeO_2 and Cu will most likely not occur [279], the phase diagram of CeO_2 - CoO shows that cobalt has a certain solubility into ceria's lattice [280] as can be seen in Figure 8.1a. However, cerium and cobalt oxides are most likely to occur as different phases after oxidation and at room temperature.

Furthermore, the proportion of Ce-Co are 66.7-33.3%, 33.3-66.7% and 50-50% for 2:1:1, 1:2:1 and 1:1:2 compositions respectively whereas for Ce-Cu are 66.7-33.3%, 50-50% and 33.3-66.7%. Yet molar ratios of Co-Cu are 50.0-50.0%, 66.7-33.3% and 33.3-66.7%, respectively.

Nevertheless, taking into account that solubility of Cu into ZrO_2 (which has the same fluorite structure of CeO_2) is low, one might be led to the conclusion that it may behave similarly with CeO_2 [317, 318]. However, at high temperatures, and as metallic phases, compounds might be formed between Ce-Cu (Figure 8.1c) prior to oxidation, and as the material is annealed and CeO_2 begins to form, Cu might precipitate over Ceria's surface and then, finally, after complete oxidation CuO is formed as isolated phase [319-321].

In Figure 8.1a, the black dots represent the three main compositions cerium-rich, cobalt-rich and copper-rich. As can be seen either in operation temperatures

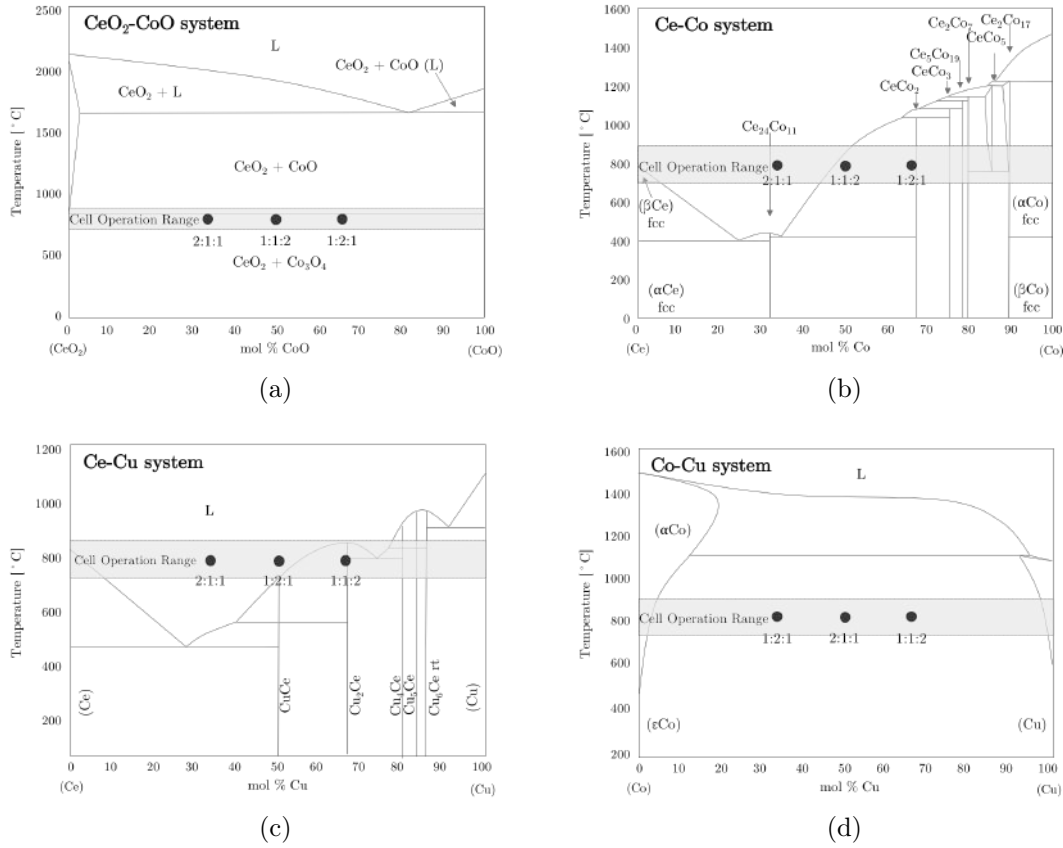


Figure 8.1: Binary phase diagram for (a) $\text{CeO}_2\text{-Co}_3\text{O}_4$ (Adapted from [313]), (b) Ce-Co (Adapted from [314]), (c) Ce-Cu (Adapted from [315]) and (d) Co-Cu (Adapted from [316]).

and room temperatures the oxides are to be formed as separate phases according to thermodynamics. In Figure 8.1b the black dots show that in reducing conditions, metallic phases between Ce-Co might be formed. However, it is known that cerium oxide is prone to surface reducing rather than bulk reducing in most of the cases [284, 285, 288]. Therefore, these Ce-Co phases are most likely to be formed over CeO_2 surface. Yet the same applies to Ce-Cu systems as shown in the phase diagram of Figure 8.1c. On the other hand, considering Co-Cu metallic phases - Figure 8.1d - isolated metallic cobalt and copper are most likely to occur rather than solid solution amongst them.

8.2 Impedance spectroscopy considerations

In Figures [8.2a](#) and [8.2b](#) the Bode diagram is plotted for all three tested compositions fabricated with the buffer layer. In the Bode plot a dark dashed line represented by the minimum values between the cobalt-ceria and copper-ceria (monometallic compositions) impedances can be seen. These minimum values were plotted to serve as a threshold for the bimetallic compositions which have to have lower impedance to be sorted as a better option.

In the Bode plot it is possible to split the contributions from each overpotential source taking into account that some effects are more evident at higher frequencies whereas others are experienced at low frequencies. Therefore, it is known that effects of impedance at frequencies over 20 kHz are associated to ionic transport thus mainly ohmic resistance. Furthermore, responses in a range of frequency of 5 to 0.5 kHz are associated to charge transfer on TPBs and current exchanging. The effects of gas diffusion can be observed in lower ranges such as 100 to 10 Hz whereas gas decomposition or reforming effects can be sensed in even lower frequencies such as 5 to 0.1 Hz [\[322-324\]](#). In addition, the processes occurring at low frequencies such as gas diffusion through the microstructure and channels as well as fuel conversion/reforming can be linked to mass transfer. At higher frequencies, phenomena such as dissociative adsorption of fuel molecules, oxidation and electrochemical reactions on TPB sites, are charge transfer processes [\[322, 323\]](#).

In comparison with the monometallic compositions the bimetallic anodes performed better in most of the cases. In terms of impedance, the ceria-rich composition has shown to be the most suitable for the anode purpose, especially when in low frequencies, characterising that this electrocatalyst is the best to promote hydrogen or methane conversion. Moreover, even though the ceria-electrolyte buffer layer is present, gas reforming ability was also retained, probably due to ceria's high activity for methane reforming [\[325-328\]](#).

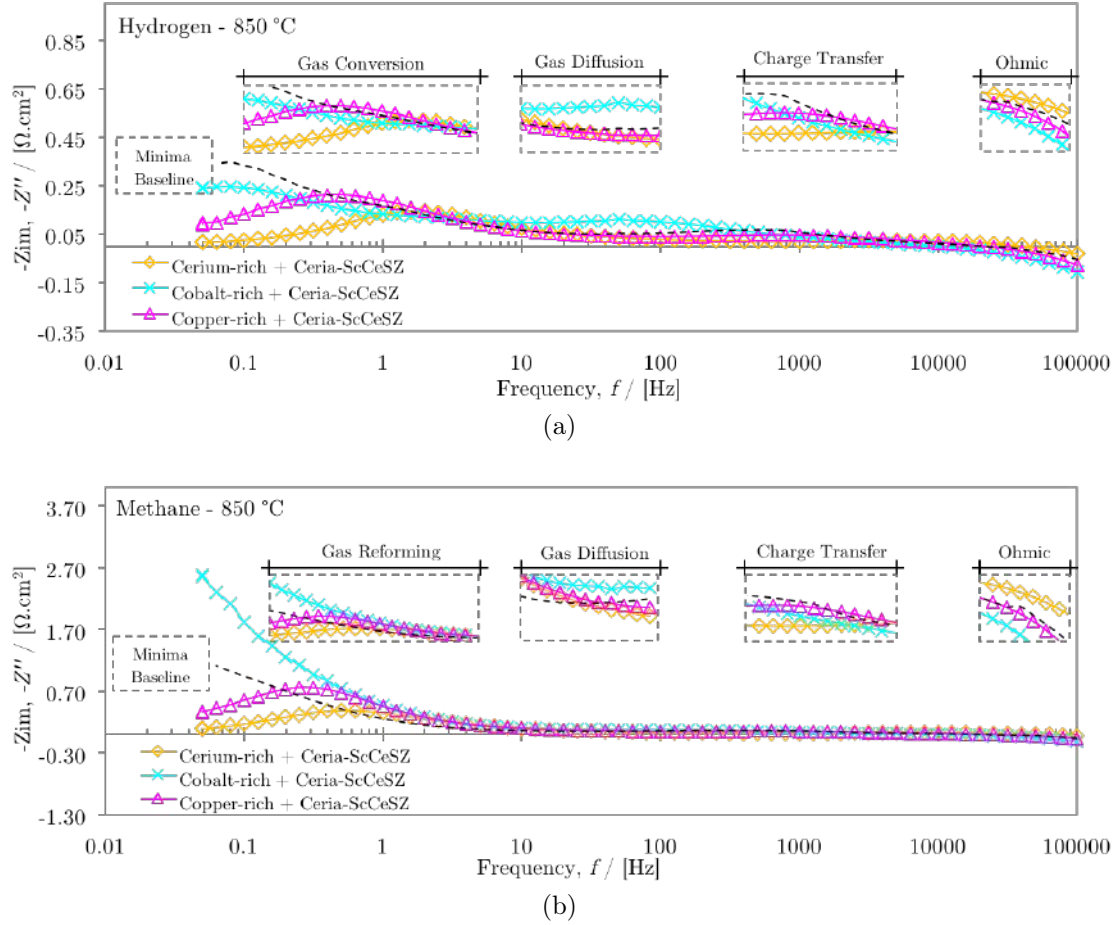


Figure 8.2: Bode diagram of impedance data collected at 850°C with (a) hydrogen and (b) methane as fuel.

8.3 The buffer layer

The phase formation for the $\text{ZrO}_2\text{-CeO}_2$ and $\text{ZrO}_2\text{-CeO}_{1.5}$ can be evaluated in the phase diagrams of Figures 8.3a and 8.3b, respectively obtained from [329-331]. Since 50 % wt. was used for each oxide (CeO_2 and $10\text{Sc}1\text{CeSZr}$) in the mixture, the approximate composition in % mol is marked in each phase diagram as well as its range of operation in case of Figure 8.3a and sintering temperature in Figure 8.3b.

The $\text{ZrO}_2\text{-CeO}_2$ system shows that cubic solid solution might indeed occur as it was observed from the XRD analysis for the buffer layer material in Figure 6.2. Therefore, at high temperatures of operation or sintering, an electric insulating solid solution - $\text{Zr}_{1-x}\text{Ce}_x\text{O}_2$ - could be produced. However, YOKOKAWA *et al.* [242] present the phase diagram calculations and the lattice parameter estimation for the $(\text{Zr}_{1-x}\text{Ce}_x\text{O}_2)_{0.8}(\text{YO}_{1.5})_{0.2}$ system in respect of the amount of CeO_2 in which a

miscibility gap can be observed approximately when “x” is between 0.5 and 0.8, thus indicating the presence of two different phases.

Other work has shown that $\text{CeO}_2\text{-ZrO}_2$ solid solutions demonstrated the ability to catalyse the reaction of carbon oxidation [243]. The incorporation of zirconium cations (Zr^{4+}) into ceria lattice originates a modified solid solution that improves its physicochemical characteristics and has been applied for various reactions such as preferential oxidation of CO [244, 245].

OZAWA *et al.* [246] claim that ceria has an oxygen storage capacity (OSC) that provides oxygen to the system provided with sufficient fuel and absorbs oxygen in lean fuel conditions. However, the OSC of ceria can be increased by the incorporation of Zr^{4+} into ceria lattice and vice-versa which leads to a decrease of cell volume thereby lowering the activation energy for oxide-ion diffusion.

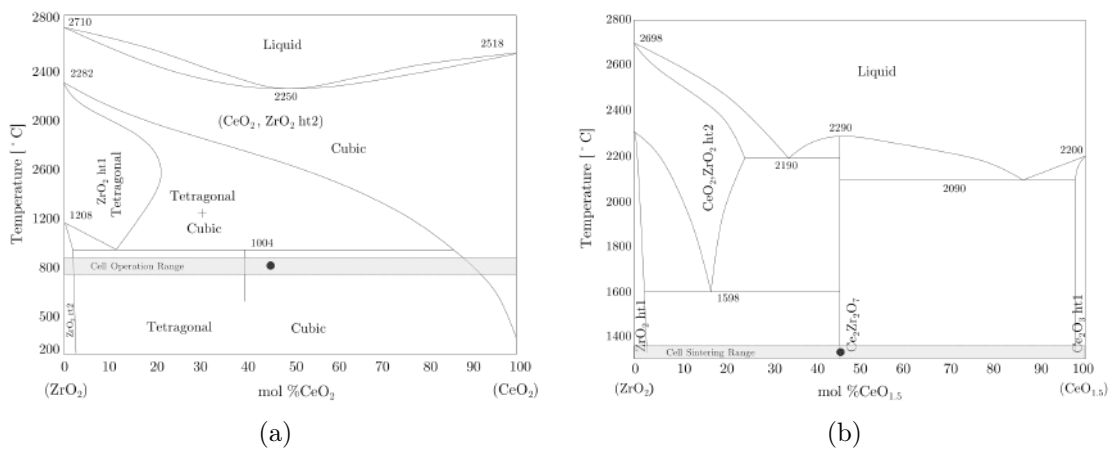


Figure 8.3: Phase diagrams for (a) $\text{ZrO}_2\text{-CeO}_2$ (Adapted from Ref. [329, 330]) and (b) $\text{ZrO}_2\text{-CeO}_{1.5}$ systems (Adapted from Ref. [331])

In Figure 8.4 important results are summarised. In Figure 8.4a, for instance, maximum power densities are higher for cobalt-rich cell showing that, for both hydrogen and methane, the cobalt content enhances the catalytic activity of the cell. Similarly, applying potentiostatic at 0.7 V as a benchmark, cobalt-rich cell was able to drawn more than $600 \text{ mA}\cdot\text{cm}^{-2}$ when methane was being fed, which is a great result for an SOFC. Furthermore, the current densities for the other two compositions were also significant when hydrogen was used whereas for methane

as fuel, current production was poor, which suggest once more the catalytic role of cobalt for methane utilisation. On the other hand, as total polarisation (Figure 8.4d) was significantly higher for cobalt-rich composition this might suggests this composition is prone to carbon deposition. Polarisation effects were sensed due to mass transport limitations since ohmic resistance (Figure 8.4c) do not change significantly between compositions.

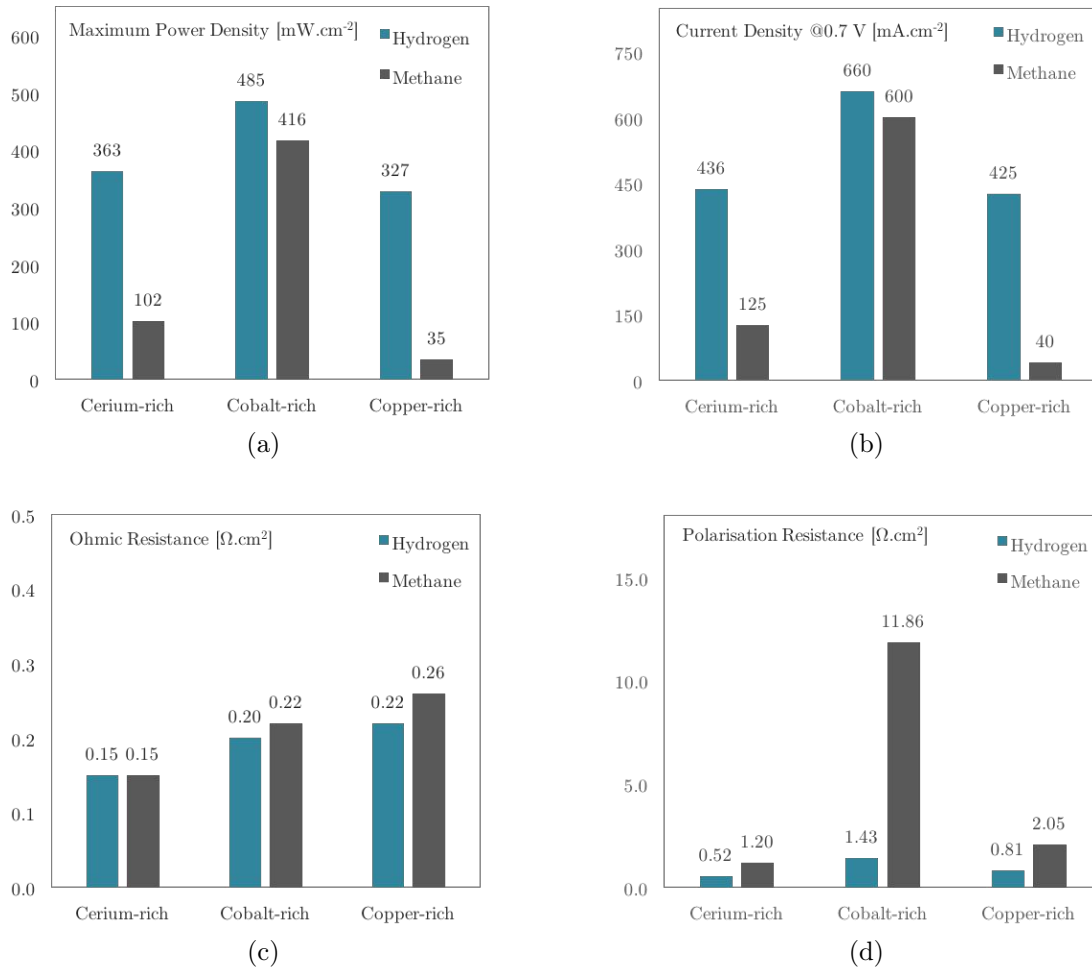


Figure 8.4: Results comparison at 850°C (a) maximum power density, (b) current density at 0.7 V, (c) ohmic resistance and (d) total polarisation for both hydrogen and methane as fuels.

8.4 Catalytic X Electrocatalytic conversion

A test consisting of reducing the cerium-rich powder in methane was performed in order to determine, by Raman spectroscopy, whether carbon deposition took place.

Raman was done firstly over a reference powder which was composed of the natural oxidised condition of the cerium-rich powder and then compared to the reduced powder.

In order to be reduced and aged an aliquot of the electrocatalyst was placed in a quartz tube that served as fixed bed in which methane was flushed at 850°C during 2 hours. After cooling, the reduced material was scanned with the Raman microscope in several spots as explained previously in details in Section [4.5.1](#).

The results are shown in Figure [8.5](#) where the oxides of the reference powder can be seen, and clearly the peaks at 1338, 1580 and 2660 cm^{-1} indicating carbon presence regarding G, D and 2D bands, respectively, over the reduced powder. Therefore it is important to point out that the bimetallic operated cells did not show any evidence of carbon deposition over their Raman spectroscopy which can be revisited in Figure [6.12](#) of Section [6.5](#).

Raman spectroscopy results for the powder reduced in methane suggests that when no electrochemical reaction is involved, methane cracking takes place thus depositing carbon. This result suggests that a similar phenomenon will occur when the cells are kept under OCV operation for long periods. Therefore, for the cells to be properly operated, they should be under charge constantly otherwise cracking will prevail. JIAO *et al.* [332](#) demonstrate that even with a nickel-based cell they were capable of operating under a specific working current suppressing coking.

The results from gas chromatograph evidenced that methane's electrochemical oxidation occurred since the amounts of carbon oxides increased as charge was being applied. The ability of each composition to displace the reaction towards full or partial oxidation was also identified, the former being the most desirable path. For that matter, the cobalt-rich composition showed to be the most promising one not even for its higher power and current densities but also for its ability to promote mainly full methane oxidation at intermediate temperatures such as 775-800°C.

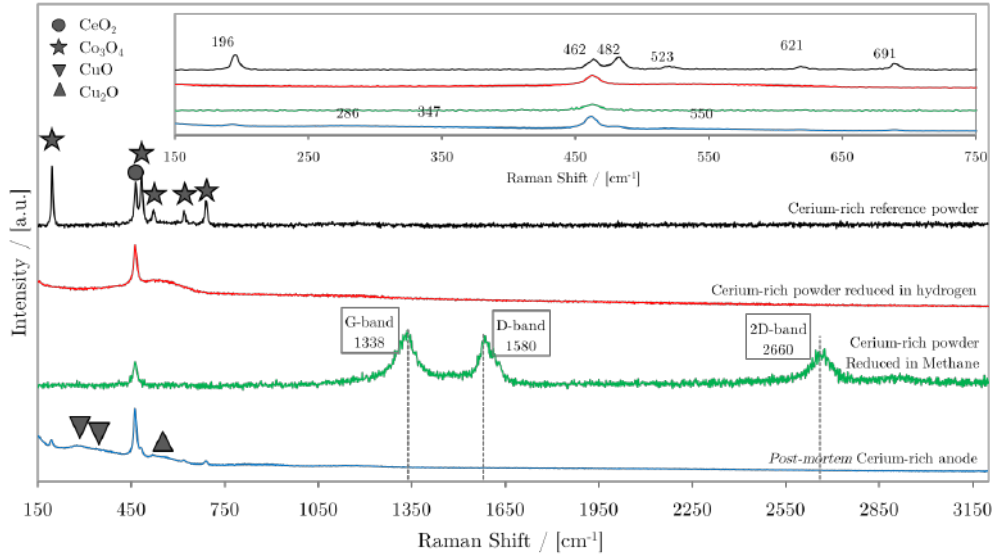


Figure 8.5: Raman spectroscopy and carbon deposition assessed on a reference powder and on a powder reduced with methane for 2 hours at 850°C.

8.5 Carbon deposition considerations

The possible reactions whilst using methane directly as fuel or in reforming processes which have been vastly studied in the literature [105–107, 117–119, 333–339] are listed in Table 8.1. It has to be pointed out that steam reforming (Case 1) will anyway start to take place once steam is produced by the electrochemical reactions (Cases 3 and 4) involving hydrogen. Yet, as carbon dioxide is produced whether by electrochemical oxidation or water-gas shift reaction (Case 7), dry reforming (Case 2) can also occur. In addition, hydrogen and carbon monoxide will be produced and thus used as direct fuels as expected (Cases 5 and 6). Cracking and Boudouard reactions are the paths that are to be avoided since besides their high carbon content no oxygen source are considered for further oxidation and the remaining carbon produced is most likely to stay adsorbed over the catalyst surface.

Referring to Table 8.1, Figure 8.6 shows the position of each possible reaction in the ternary phase diagram for C-O-H from 750 to 1000°C. The phase diagram points out the need of oxygen presence to oxidise the carbon after the reactions with methane. It can be observed that for the reforming cases, the oxygen content whether as steam or carbon dioxide promotes the carbon oxidation and these are

Table 8.1: Possible paths of methane's reaction and its products.

Case#	Reaction Name	Reaction	C [% mol]	O [% mol]	H [% mol]
1	Methane Steam Reforming	$CH_4 + H_2O \rightleftharpoons CO + 3H_2$	12.50%	12.50%	75.00%
2	Methane Dry Reforming	$CH_4 + CO_2 \rightleftharpoons 2CO + 2H_2$	25.00%	25.00%	50.00%
3	Total Electrochemical Oxidation	$CH_4 + 4O^{2-} \rightleftharpoons CO_2 + 2H_2O + 8e^-$	11.11%	44.44%	44.44%
4	Partial Electrochemical Oxidation	$CH_4 + O^{2-} \rightleftharpoons CO + 2H_2 + 2e^-$	16.67%	16.67%	66.67%
5	Hydrogen Electrochemical Oxidation	$H_2 + O^{2-} \rightleftharpoons H_2O + 2e^-$	0.00%	33.33%	66.67%
6	Carbon Monoxide Electrochemical Oxidation	$CO + O^{2-} \rightleftharpoons CO_2 + 2e^-$	33.33%	66.67%	0.00%
7	Water-Gas Shift	$CO + H_2O \rightleftharpoons CO_2 + H_2$	20.00%	40.00%	40.00%
8	Methane Cracking	$CH_4 \rightleftharpoons C + 2H_2$	20.00%	0.00%	80.00%
9	Boudouard Reaction	$2CO \rightleftharpoons C + CO_2$	50.00%	50.00%	0.00%

situated right on the edge for carbon formation for the presented range of temperatures and thus need to have the oxidiser in excess when doing reforming processes. However the electrochemical oxidation reactions (Cases 3 and 4) show to be more suitable to avoid carbon formation whatsoever whereas cracking and Boudouard are the paths that will definitely form carbon (Cases 8 and 9).

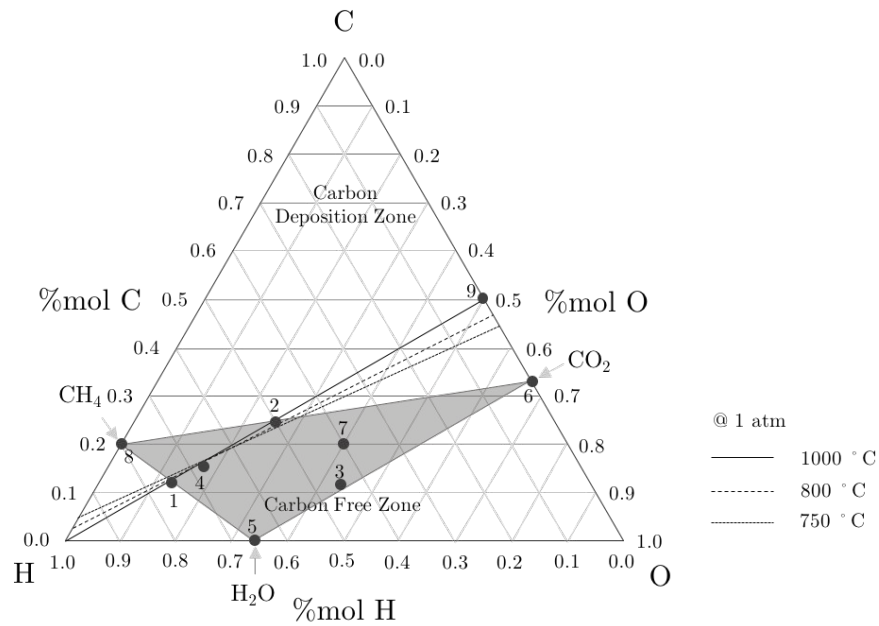


Figure 8.6: C-O-H ternary phase diagram showing the cases listed in Table 8.1.

Work has always been focused to avoid cracking and Boudouard reactions over nickel surfaces since this catalyst absorbs carbon strongly. Hence, ceramic barriers are used whether to promote internal reforming/partial oxidation before nickel layers [340] or even as diffusion barriers that diminish coking [341]. In addition, direct internal reforming is also an alternative. However, there is a penalty in system's efficiency because of the excess of steam or carbon dioxide used [342, 343].

Some work in the literature has shown the influence of reducing technique over cells performance in methane [273-275, 344, 345]. For instance, MALLON and KENDALL [273] show huge differences in cells power densities both in hydrogen and methane as well as carbon deposition when cell was reduced in low or high temperatures. They called “high temperature reducing strategy” when the cell was exposed to hydrogen at 850°C whereas “low temperature reducing strategy” was when the cell was exposed to hydrogen with increasing temperature from room temperature to 850°C. The authors explain that using the former technique, nickel particles became coarse and with low surface area due to the high temperature, thus with high contiguity of the nickel phase which explains the reason for an alike performance on both fuels. On the other hand, whilst reduced from low temperatures as the latter, nickel particles were smaller and more dispersed in the beginning which explains lower performance with hydrogen as fuel whereas when methane was fed carbon deposition increased the connectivity between nickel particles.

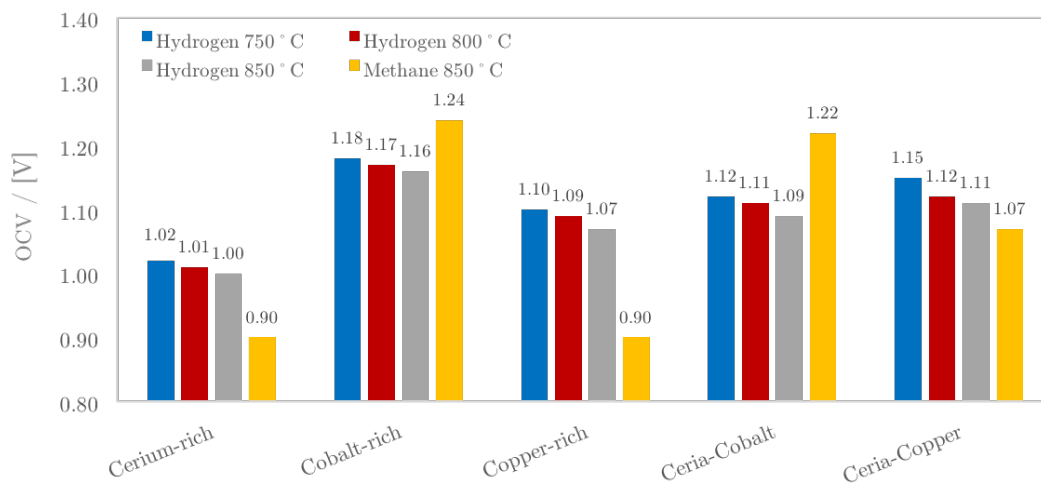


Figure 8.7: OCV for all the compositions tested under hydrogen in several temperatures and methane at 850°C.

Another evidence that might suggest coking is the increase on OCV when operating with methane [273] on both bimetallic cobalt-rich and monometallic cobalt-cerium compositions. This points out that an excess of cobalt might lead to carbon formation thus premature cell degradation. The bar graph in Figure 8.7 depicts the differences of OCVs for all five compositions tested with hydrogen at different

temperatures with methane at 850°C, showing that voltage for cobalt compositions were 1.24 and 1.22 V whereas for the other compositions, OCVs in methane were always lower than in hydrogen as fuel. However, the OCV between 1.0 and 1.2 V for methane direct utilisation is consistent with the literature both for theoretical calculations [346] and experimental reports [347, 348]. In addition, negligible amounts of carbon were spotted from TPO for all three bimetallic compositions.

Some work has been reporting the ability of copper on preventing coking [96-98]. LEE *et al.* [96] has shown that a small addition of copper on a cobalt-based catalyst has decreased carbon deposition from 200% wt. to 5% wt. whilst operating with methane.

Finally the test with the three bimetallic compositions has shown that the cobalt-rich composition is the most promising composition. The monometallic compositions have indicated the importance of copper to avoid coking since monometallic ceria-cobalt has its surface covered with carbon and none of this was experienced over any bimetallic composition. The TPO analysis was the final evidence that no significant carbon had remained on the anode after the operation with methane as fuel. For further conclusions, it may be worth it long-term tests with different duration, followed by TPO after each test (e.g 100, 500, 1000 hours) to confirm that the amount of carbon formed is indeed negligible and it does not increase in time.

8.6 Final considerations

As a final discussion, results from similar works in the literature are summarised and compared to this work in Table 8.2. Results from the work of FUERTE *et al.* [101] are lower than this work both in hydrogen and methane as fuels. Yet, some of their best results with methane are in fact using a H₂+CH₄ mixture rather than pure anhydrous methane.

However, results from LEE *et al.* [102] and LEE *et al.* [103] are whether similar or higher than the present work. Still, it has to be considered that in, their cases, an anode-supported cell was used whereas for the present work an electrolyte-supported

configuration was the case. There are some further work such as microstructure optimisation, cell configuration, cells scaling-up area and so on, which might enhance even more the performance of the cells.

Table 8.2: Results from similar work compared to this work.

Fuel	Temperature	FUERTE <i>et al.</i> [101]	LEE <i>et al.</i> [102]	LEE <i>et al.</i> [103]	This Work
Hydrogen	700°C	—	—	—	300 mW.cm ⁻²
	750°C	93 mW.cm ⁻²	—	—	460 mW.cm ⁻²
	800°C	—	700 mW.cm ⁻²	570 mW.cm ⁻²	560 mW.cm ⁻²
^a Methane	700°C	—	—	100 ^b mW.cm ⁻²	—
	750°C	13 ^a / 76 ^c , mW.cm ⁻²	—	—	—
^b Butane	775°C	—	—	—	160 ^a mW.cm ⁻²
	800°C	—	260 ^a mW.cm ⁻²	360 ^b mW.cm ⁻²	210 ^a mW.cm ⁻²
^c Mixtures H ₂ +CH ₄	825°C	—	—	—	260 ^a mW.cm ⁻²
	850°C	—	—	—	416 ^a mW.cm ⁻²

Chapter 9

Overall Conclusions

A ceria-based anode was successfully developed with the addition of cobalt and copper with the ability to operate with methane with proven resistance to coking.

The electrocatalyst synthesised was produced as isolated oxide phases which was confirmed by Rietveld refinement. In addition, the powder has previously shown its ability to reduce and absorb hydrogen, proved by the temperature-programmed reduction analysis. Moreover, TPR has shown the steps of oxide decomposition in compliance with what is observed in the literature. DC-electrical conductivity has shown that even as oxides the material have shown conductivities as high as 1 S.cm^{-1} . Although DC-conductivity test did not represent *in-operando* condition, further impedance results have shown the ability to operate either with hydrogen or anhydrous methane as fuels.

The development of the buffer layer was the element that brought viability for this anode configuration to operate with performances higher than 500 mA.cm^{-2} both in hydrogen or methane as fuel, enhancing the quality of the anode/electrolyte interface. Results reproducibility was confirmed since tests were run in replicas in different test rigs.

The GC-coupled tests gave straightforward conclusions about the presence of electrochemical oxidation of methane when operating the cells under load. Moreover, from GC analysis, the cobalt-rich was selected as the best material, since its operation at 800°C delivered the highest performance and was more prone to full

oxidation of methane which enhances the overall efficiency of the reaction. The monometallic compositions made the role of each metal very clear showing the catalytic ability of cobalt and the virtue of preventing coking in addition to the role of enhancing electronic conductivity played by copper.

Insights for future work

- To perform long-term tests aiming for stability and coke resistance over time
- To build and test short stacks with the developed material and eventually larger stacks with over 500 W;
- To develop anode-supported cells using a porous electrolyte scaffold impregnated with anode material;
- To perform further optimisation of Ce:Co:Cu molar ratios seeking the best trade-off between coking and catalytic activity;
- To run FIB analysis to help microstructure understanding, especially concerning the distribution of TPBs.

Bibliography

- [1] GUPTA, R. B. *Hydrogen Fuel - Production, Transport, and Storage*. CRC Press, 2009.
- [2] SINGHAL, S. C., KENDALL, K. *High Temperature Solid Oxide Fuel Cells: Fundamentals, Design and Applications*. Elsevier, 2003.
- [3] MIRANDA, P. E. V., DA CUNHA BUSTAMANTE, L. A., CERVEIRA, M. Relatório técnico.
- [4] VERHAERT, I., VERHELST, S., HUISSEUNE, H., POELS, I., JANSSEN, G., MULDER, G., PAEPE, M. D. “Thermal and electrical performance of an alkaline fuel cell.” *Applied Thermal Engineering*, v. 40, pp. 1359–4311, 2012.
- [5] STEINBERGER-WILCKENS, R., LEHNERT, W. *Innovations in Fuel Cell Technologies*. RSC Publishing, 2011.
- [6] BOSE, S., KUILA, T., NGUYEN, T. X. H., KIM, N. H., TAK LAU, K., LEE, J. H. “Polymer membranes for high temperature proton exchange membrane fuel cell: Recent advances and challenges.” *Progress in Polymer Science*, v. 36, pp. 813–843, 2011.
- [7] HIRATA, H., AOKI, T., NAKAJIMA, K. “Liquid phase migration effects on the evaporative and condensational dissipation of phosphoric acid in phosphoric acid fuel cell.” *Journal of Power Sources*, v. 199, pp. 110–116, 2012.
- [8] DICKS, A. L. “Molten carbonate fuel cells.” *Current Opinion in Solid State and Materials Science*, v. 8, n. 5, pp. 379–383, 2004.
- [9] BAUR, E., PREIS, H. “Über Brennstoff-Ketten mit Festleitern.” *Z. Elektrochem*, v. 43, pp. 727–732, 1937.
- [10] NERNST, W. “Über die elektrolytische Leitung fester Körper bei sehr hohen Temperaturen.” *Z. Elektrochem*, v. 6, pp. 41–43, 1899.

- [11] NERNST, W. *Verfahren zur Erzeugung von elektrischem Glühlicht.* - D.R.P 104872. 06-07-1897.
- [12] NERNST, W. *Electrical glow-light.* - US Patent 623811. 25-04-1899.
- [13] EG&G SERVICES PARSONS, I. *Fuel Cells Handbook.* U.S. Department of Energy, Office of Fossil Energy, National Energy Technology Laboratory, 2004.
- [14] WACHSMAN, E. D., SINGHAL, S. C. “Solid oxide fuel cell commercialization, research and challenges.” *American Ceramic Society Bulletin*, v. 89, pp. 22–32, 2010.
- [15] BOVE, R., UBERTINI, S. *Modeling Solid Oxide Fuel Cells.* Springer, 2008.
- [16] BLUM, L., MEULENBERG, W. A., NABIELEK, H., STEINBERGER-WILCKENS, R. “Worldwide SOFC Technology Overview and Benchmark.” *International Journal of Applied Ceramic Technology*, v. 2, pp. 1744–7402, 2005.
- [17] FERGUS, J. W., HUI, R., LI, X., WILKINSON, D. P., ZHANG, J. *Solid Oxide Fuel Cells: Materials Properties and Performance.* Boca Raton: CRC Press; Taylor & Francis Group, 2009.
- [18] FERGUS, J. W. “Electrolytes for solid oxide fuel cells.” *Journal of Power Sources*, v. 162, pp. 30–40, 2006.
- [19] BASU, R. N. *Materials for Solid Oxide Fuel Cells.* New Delhi, India: Anamaya, 2007.
- [20] TAKAHASHI, T., ESAKA, T., IWAHARA, H. “Conduction in Bi₂O₃-based oxide ion conductor under low oxygen pressure. II-Determination of the partial electronic conductivity.” *Journal of Applied Electrochemistry*, v. 7, pp. 303–308, 1977.
- [21] TAKAHASHI, T., ESAKA, T., IWAHARA, H. “Conduction in Bi₂O₃-based oxide ion conductors under low oxygen pressure. I-Current blackening of the Bi₂O₃-Y₂O₃ electrolyte.” *Journal of Applied Electrochemistry*, v. 7, pp. 299–302, 1977.
- [22] ETSELL, T. H., FLENGAS, S. N. “The electrical properties of solid oxide electrolytes.” *Chemical Reviews*, v. 70, pp. 339–376, 1970.
- [23] MINH, N. Q., TAKAHASHI, T. *Science and Technology of Ceramic Fuel Cells.* Elsevier, 1995.

- [24] KRÖGER, F., VINK, H. J. *Solid State Physics*. F. Seitz and D. Turnbull, Academic Press - New York, 1965.
- [25] KILNER, J. A. “Fast oxygen transport in acceptor doped oxides.” *Solid State Ionics*, v. 129, pp. 13–23, 2000.
- [26] MAHATO, N., BANERJEE, A., GUPTA, A., OMAR, S., BALANI, K. “Progress in material selection for solid oxide fuel cell technology: A review.” *Progress in Materials Science*, v. 72, pp. 141–337, 2015.
- [27] YAHIRO, H., EGUCHI, K., ARAI, H. “Electrical properties and reducibilities of ceria-rare earth oxide systems and their applications to solid oxide fuel cells.” *Solid State Ionics*, v. 36, pp. 71–75, 1989.
- [28] GUO, X., WASER, R. “Electrical properties of the grain boundaries of oxygen ion conductors: acceptor-doped zirconia and ceria.” *Progress in Materials Science*, v. 51, pp. 151–210, 2006.
- [29] TULLER, H. L. “Ionic conduction in nanocrystalline materials.” *Solid State Ionics*, v. 131, pp. 131–157, 2000.
- [30] MC, M. C. M., MECARTNEY, M. L. “Grain boundary ionic conductivity of yttrium stabilized zirconia as a function of silica content and grain size.” *Solid State Ionics*, v. 161, pp. 167–179, 2003.
- [31] MONDAL, P., KLEIN, A., JAEGERMANN, W., HAHN, H. “Enhanced specific grain boundary conductivity in nanocrystalline Y_2O_3 -stabilized zirconia.” *Solid State Ionics*, v. 118, pp. 331–339, 1999.
- [32] KHARTON, V. V., MARQUES, F. M. B., ATKINSON, A. “Transport properties of solid oxide electrolyte ceramics: a brief review.” *Solid State Ionics*, v. 174, pp. 135–149, 2004.
- [33] ISHIHARA, T., MATSUDA, H., TAKITA, Y. “Doped $LaGaO_3$ perovskite type oxide as a new oxide ionic conductor.” *Journal of the American Chemistry Society*, v. 116, pp. 3801–3803, 1994.
- [34] FENG, M., GOODENOUGH, J. B. “A superior oxide-ion electrolyte.” *Euro Solid State Inorganic Chemistry*, v. T31, pp. 663–672, 1994.
- [35] FUJII, H., KATAYAMA, Y., SHIMURA, T., IWAHARA, H. “Protonic conduction in perovskite-type oxide ceramics based on $LnScO_3$ ($Ln = La, Nd, Sm$ or Gd) at high temperature.” *Journal of Electroceramics*, v. 2, pp. 119–125, 1989.

- [36] HAYASHI, H., INABA, H., MATSUYAMA, M., LAN, N. G., DOKIYA, M., TAGAWA, H. “Structural consideration on the ionic conductivity of perovskite-type oxides.” *Solid State Ionics*, v. 122, pp. 1–15, 1999.
- [37] NGUYEN, T. L., DOKIYA, M., WANG, S., TAGAWA, H., HASHIMOTO, T. “The effect of oxygen vacancy on the oxide ion mobility in LaAlO₃-based oxides.” *Solid State Ionics*, v. 130, pp. 229–241, 2000.
- [38] ANDERSON, P. S., MARQUES, F. M. B., SINCLAIR, D. C., WEST, A. R. “Ionic and electronic conduction in La_{0.95}Sr_{0.05}GaO_{3+δ}, La_{0.95}Sr_{0.05}AlO_{3+δ} and Y_{0.95}Sr_{0.05}AlO_{3+δ}.” *Solid State Ionics*, v. 118, pp. 229–239, 1999.
- [39] YASUDA, I., OGASAWARA, K., HISHINUMA, M., KAWADA, T., DOKIYA, M. “Oxygen tracer diffusion coefficient of (La, Sr)MnO_{3±δ}.” *Solid State Ionics*, v. 88-86, pp. 1197–1201, 1996.
- [40] NGUYEN, T. L., DOKIYA, M. “Electrical conductivity, thermal expansion and reaction of (La, Sr)(Ga, Mg)O₃ and (La, Sr)AlO₃ system.” *Solid State Ionics*, v. 132, pp. 217–226, 2000.
- [41] CORBEL, G., MESTIRI, S., LACORRE, P. “Physicochemical compatibility of CGO fluorite, LSM and LSCF perovskite electrode materials with La₂Mo₂O₉ fast oxide-ion conductor.” *Solid State Sci*, v. 7, pp. 1216–1249, 2005.
- [42] KAO, W. X., LEE, M. C., CHANG, Y. C., LIN, T. N., WANG, C. H., CHANG, J. C. “Fabrication and evaluation of the electrochemical performance of the anode-supported solid oxide fuel cell with the composite cathode of La_{0.8}Sr_{0.2}MnO₃-Gadolinia-doped ceria oxide/La_{0.8}Sr_{0.2}MnO₃.” *Journal of Power Sources*, v. 195, pp. 6468–6472, 2010.
- [43] SHUYAN, S. L., LÜ, Z., WEI, B., HUANG, X., MIAO, J., CAO, G., ZHU, R., SU, W. “A study of (Ba_{0.5}Sr_{0.5})_{1-x}Sm_xCo_{0.8}Fe_{0.2}O_{3+δ} as a cathode material for IT-SOFCs.” *Journal of Alloys and Compounds*, v. 426, pp. 408–414, 2006.
- [44] VEEN, A. C., REBEILLEAU, M., FARRUSSENG, D., MIRODATOS, C. “Studies on the performance stability of mixed conducting BSCFO membranes in medium temperature oxygen permeation.” *Chemical Communications*, v. 9, pp. 2–16, 2003.
- [45] TEDMON, C. S., SPACIL, J. H. S., MITOFF, S. P. “Cathode Materials and Performance in High-Temperature Zirconia Electrolyte Fuel Cells.” *J. Electrochem. Soc.*, v. 116, pp. 1170–1175, 1970.

- [46] LAU, S. K., SINGHAL, S. C. “Potential electrode/electrolyte interactions in solid oxide fuel cells.” *Corrosion*, v. 85, pp. 1–9, 1985.
- [47] GOODENOUGH, J. B., LONGO, J. M. *Magnetic Oxides and Related Oxides*. Landolt-Bernstein, 1978.
- [48] TOFIELD, B. C., SCOTT, W. R. “Oxidative nonstoichiometry in perovskites, an experimental survey; the defect structure of an oxidized lanthanum manganite by powder neutron diffraction.” *Journal of Solid State Chemistry*, v. 10, pp. 183–194, 1974.
- [49] MIZUSAKI, J., MORI, N., TAKAI, H., YONEMURA, Y., MINAMIUE, H., TAGAWA, H., DOKIYA, M., INABA, H., NARAYA, K., SASAMOTO, T., HASHIMOTO, T. “Oxygen nonstoichiometry and defect equilibrium in the perovskite-type oxides $\text{La}_{1-x}\text{Sr}_x\text{MnO}_{3+\delta}$.” *Solid State Ionics*, v. 129, pp. 163–177, 2000.
- [50] ROOSMALEN, J. A. M. V., CORDFUNKE, E. H. P. “A new defect model to describe the oxygen deficiency in perovskite-type oxides.” *Journal of Solid State Chemistry*, v. 93, pp. 212–219, 1991.
- [51] ROOSMALEN, J. A. M. V., CORDFUNKE, E. H. P. “The Defect Chemistry of $\text{LaMnO}_{3\pm\delta}$: 2. Structural Aspects of $\text{LaMnO}_{3+\delta}$.” *Journal of Solid State Chemistry*, v. 110, pp. 100–105, 1993.
- [52] ROOSMALEN, J. A. M. V., CORDFUNKE, E. H. P. “The Defect Chemistry of $\text{LaMnO}_{3\pm\delta}$: 3. The Density of $(\text{La},\text{A})\text{MnO}_{3+\delta}$ ($\text{A} = \text{Ca}, \text{Sr}, \text{Ba}$).” *Journal of Solid State Chemistry*, v. 110, pp. 106–108, 1993.
- [53] ROOSMALEN, J. A. M. V., CORDFUNKE, E. H. P. “The Defect Chemistry of $\text{LaMnO}_{3\pm\delta}$ 4. Defect Model for $\text{LaMnO}_{3+\delta}$.” *Journal of Solid State Chemistry*, v. 110, pp. 109–112, 1993.
- [54] ROOSMALEN, J. A. M. V., CORDFUNKE, E. H. P. “The Defect Chemistry of $\text{LaMnO}_{3\pm\delta}$ 5. Thermodynamics.” *Journal of Solid State Chemistry*, v. 110, pp. 113–117, 1993.
- [55] SUN, C., HUI, R., ROLLER, J. “Cathode materials for solid oxide fuel cells: a review.” *J Solid State Electrochem*, v. 14, pp. 1125–1144, 2010.
- [56] COLOMER, M. T., STEELE, B. C. H., KILNER, J. A. “Structural and electrochemical properties of the $\text{Sr}_{0.8}\text{Ce}_{0.1}\text{Fe}_{0.7}\text{Co}_{0.3}\text{O}_{3+\delta}$ perovskite as cathode material for ITSOFCs.” *Solid State Ionics*, v. 147, pp. 41–48, 2002.

- [57] STEELE, B. C. H., BAE, J.-M. “Properties of $\text{La}_{0.6}\text{Sr}_{0.4}\text{Co}_{0.2}\text{Fe}_{0.8}\text{O}_{3-x}$ (LSCF) double layer cathodes on gadolinium-doped cerium oxide (CGO) electrolytes: II. Role of oxygen exchange and diffusion.” *Solid State Ionics*, v. 106, pp. 255–261, 1998.
- [58] TROFIMENKO, N. E., ULLMANN, H. “Oxygen stoichiometry and mixed ionic-electronic conductivity of $\text{Sr}_{1-a}\text{Ce}_a\text{Fe}_{1-b}\text{Co}_b\text{O}_{3-x}$ perovskite-type oxides.” *Journal of the European Ceramic Society*, v. 20, pp. 1241–1250, 2000.
- [59] ADLER, S. B. “Mechanism and kinetics of oxygen reduction on porous $\text{La}_{1-x}\text{Sr}_x\text{CoO}_{3-\delta}$ electrodes.” *Solid State Ionics*, v. 111, pp. 125–134, 1998.
- [60] NOWOTNY, J., REKAS, M. “Defect chemistry of $(\text{La,Sr})\text{MnO}_3$.” *Journal of the American Ceramic Society*, v. 81, pp. 67–80, 1998.
- [61] JIANG, S. P. “Development of lanthanum strontium manganite perovskite cathode materials of solid oxide fuel cells: a review.” *Journal of Materials Science*, v. 43, pp. 6799–6833, 2008.
- [62] ALONSO, J. A., MARTINEZ-LOPE, M. J., CASAIS, M., MACMANUS-DRISCOLL, J. L., SILVA, P., COHEN, L. F. “Non-stoichiometry, structural defects and properties of $\text{LaMnO}_{3+\delta}$ with high δ values ($0.11 \leq \delta \leq 0.29$).” *Journal of Material Chemistry*, v. 7, pp. 2139–2144, 1997.
- [63] MITCHELL, J. F., ARGYRIOU, D. N., POTTER, C. D., HINKS, D. G., JORGENSEN, J. D., BADER, S. D. “Structural phase diagram of $\text{La}_{1-x}\text{Sr}_x\text{MnO}_{3+\delta}$: Relationship to magnetic and transport properties.” *Physics Review B*, v. 54, pp. 6172–6183, 1996.
- [64] SOUZA, R. A. D., KILNER, J. A. “Oxygen transport in $\text{La}_{1-x}\text{Sr}_x\text{Mn}_{1-y}\text{Co}_y\text{O}_{3\pm\delta}$ perovskites: Part I. Oxygen tracer diffusion.” *Solid State Ionics*, v. 106, pp. 175–187, 1998.
- [65] JIANG, S. P. “Nanoscale and nano-structured electrodes of solid oxide fuel cells by infiltration: Advances and challenges.” *International Journal of Hydrogen Energy*, v. 37, pp. 449–470, 2012.
- [66] MINH, N. Q. “Ceramic fuel cells.” *Journal of the American Ceramic Society*, v. 76, pp. 563–588, 1993.
- [67] MÖBIUS, H.-H. “On the history of solid electrolyte fuel cells.” *Journal of Solid State Electrochemistry*, v. 1, pp. 2–16, 1997.

- [68] SETOGUCHI, T., OKAMOTO, K., EGUCHI, K., ARAI, H. “Effects of Anode Material and Fuel on Anodic Reaction of Solid Oxide Fuel Cells.” *Journal of the Electrochemical Society*, v. 139, pp. 2875–2880, 1992.
- [69] SUZUKI, M., SASAKI, H., OTOSHI, S., KAJIMURA, A., IPPOMMATSU, M. “High power density solid oxide electrolyte fuel cells using Ru/Y₂O₃ stabilized zirconia cermet anodes.” *Solid State Ionics*, v. 62, pp. 125–130, 1993.
- [70] JIANG, S. P., BADWAL, S. P. S. “Hydrogen Oxidation at the Nickel and Platinum Electrodes on Yttria-Tetragonal Zirconia Electrolyte.” *Journal of the Electrochemical Society*, v. 144, pp. 3777–3784, 1997.
- [71] DE BOER, B., GONZALEZ, M., BOUWMEESTER, H. J. M., VERWEIJ, H. “The effect of the presence of fine YSZ particles on the performance of porous nickel electrodes.” *Solid State Ionics*, v. 127, pp. 269–276, 2000.
- [72] MOGENSEN, M., SKAARUP, S. “Kinetic and geometric aspects of solid oxide fuel cell electrodes.” *Solid State Ionics*, v. 86-88, pp. 1151–1160, 1994.
- [73] JIANG, S. P. “Resistance Measurement in Solid Oxide Fuel Cells.” *Journal of the Electrochemical Society*, v. 148, pp. A887–A897, 2001.
- [74] HOLTAPPELS, P., DE HAART, L. G. J., STIMMING, U. “Reaction of Hydrogen/Water Mixtures on Nickel-Zirconia Cermet Electrodes I. DC Polarization Characteristics.” *Journal of the Electrochemical Society*, v. 146, pp. 1620–1625, 1999.
- [75] BOSSEL, U. G. *Facts and Figures, Final Report on SOFC data*. IEA report, Operating Task II, Swiss Federal Office of Energy, Berne, CH, 1992.
- [76] FEDOTOV, S., KIM, S. H., PITSCH, H. “Anomalous Knudsen diffusion and reactions in disordered porous media.” *Center for Turbulence Research - Annual Research Briefs*, p. 323, 2007.
- [77] KIM, J.-W., VIRKAR, A. V., FUNG, K.-Z., MEHTA, K., SINGHAL, S. C. “Polarization Effects in Intermediate Temperature, Anode-Supported Solid Oxide Fuel Cells.” *Journal of the Electrochemical Society*, v. 146, pp. 69–78, 1999.
- [78] CHAN, S. H., KHOR, K. A., XIA, Z. T. “A complete polarization model of a solid oxide fuel cell and its sensitivity to change of cell component thickness.” *Journal of Power Sources*, v. 93, pp. 130–140, 2000.

- [79] NI, M., LEUNG, M. K., LEUNG, D. Y. “A modeling study on concentration overpotentials of a reversible solid oxide fuel cell.” *Journal of Power Sources*, v. 163, pp. 460–466, 2006.
- [80] COSTAMAGNA, P., SELIMOVICB, A., BORGHIA, M. D., AGNEW, G. “Electrochemical model of the integrated planar solid oxide fuel cell (IP-SOFC).” *Chemical Engineering Journal*, v. 102, pp. 61–69, 2004.
- [81] HAMANN, C. H., HAMNETT, A., VIELSTICH, W. *Electrochemistry*. J. Wiley & Sons - New York, 1998.
- [82] BOCKRIS, J. O., REDDY, A. K. N. *Modern Electrochemistry*. Kluwer Academic-Plenum Press, New York, 1998.
- [83] COSTAMAGNA, P., HONEGGER, K. “Modeling of solid oxide heat exchanger integrated stacks and simulation at high fuel utilization.” *Journal of the Electrochemical Society*, v. 145, pp. 3995–4007, 1998.
- [84] HARDMAN, S., SHIU, E., STEINBERGER-WILCKENS, R. “Changing the fate of Fuel Cell Vehicles: Can lessons be learnt from Tesla Motors?” *International Journal of Hydrogen Energy*, v. 20, pp. 1625–1638, 2015.
- [85] KIM, T., AHN, K., VOHS, J. M., GORTE, R. J. “Deactivation of ceria-based SOFC anodes in methanol.” *Journal of Power Sources*, v. 164, pp. 42–48, 2007.
- [86] ROSSMEISL, J., BESSLER, W. G. “Trends in catalytic activity for SOFC anode materials.” *Solid State Ionics*, v. 178, pp. 1694–1700, 2008.
- [87] MURRAY, E. P., TSAI, T., BARNETT, S. A. “A direct-methane fuel cell with a ceria-based anode.” *Nature*, v. 400, pp. 649–651, 1999.
- [88] YOKOKAWA, H., HORITA, T., SAKAI, N., YAMAJI, K., BRITO, M. E., XIONG, Y. P. “Protons in ceria and their roles in SOFC electrode reactions from thermodynamic and SIMS analyses.” *Solid State Ionics*, v. 174, pp. 205–221, 2004.
- [89] STEELE, B. C. H. “Appraisal of $\text{Ce}_{1-y}\text{Gd}_y\text{O}_{2-y/2}$ electrolytes for IT-SOFC operation at 500 °C.” *solid State Ionics*, v. 129, pp. 95–110, 2000.
- [90] OMAR, S., WACHSMAN, E. D., JONES, J. L., NINO, J. C. “Crystal structure-ionic conductivity relationships in doped ceria systems.” *Journal of the American Ceramic Society*, v. 92, pp. 2674–2681, 2009.

- [91] OMAR, S., WACHSMAN, E. D., NINO, J. C. “A co-doping approach towards enhanced ionic conductivity in fluorite-based electrolytes.” *Solid State Ionics*, v. 177, pp. 3199–3206, 2006.
- [92] OMAR, S., WACHSMAN, E. D., NINO, J. C. “Higher ionic conductive ceria based electrolytes for SOFCs.” *Applied Physics Letter*, v. 91, pp. 144106, 2007.
- [93] VENÂNCIO, S. A., MIRANDA, P. E. V. “Synthesis of $\text{CeAlO}_3/\text{CeO}_2\text{-Al}_2\text{O}_3$ for use as a solid oxide fuel cell functional anode material.” *Ceramics International*, v. 37, pp. 3139–3152, 2011.
- [94] YE, X.-F., WANG, S. R., HU, Q., CHEN, J. Y., WEN, T. L., WEN, Z. Y. “Improvement of Cu-CeO₂ anodes for SOFCs running on ethanol fuels.” *Solid State Ionics*, v. 180, pp. 276–281, 2009.
- [95] YE, X.-F., HUANG, B., WANG, S. R., WANG, Z. R., XIONG, L., WEN, T. L. “Preparation and performance of a Cu-CeO₂-ScSZ composite anode for SOFCs running on ethanol fuel.” *Journal of Power Sources*, v. 164, pp. 203–209, 2007.
- [96] LEE, S.-I., AHN, K., VOHS, J. M., GORTE, R. J. “Cu-Co Bimetallic Anodes for Direct Utilization of Methane in SOFCs.” *Electrochemical Solid-State Letter*, v. 8, pp. A48–A51, 2005.
- [97] LEE, S.-I., VOHS, J. M., GORTE, R. J. “A Study of SOFC Anodes Based on Cu-Ni and Cu-Co Bimetallics in CeO₂ YSZ.” *Journal of the Electrochemical Society*, v. 151, pp. A1319–A1323, 2004.
- [98] FUERTE, A., VALENZUELA, R. X., ESCUDERO, M. J., DAZA, L. “Study of a SOFC with a bimetallic Cu-Co-ceria anode directly fuelled with simulated biogas mixtures.” *International Journal of Hydrogen Energy*, v. 39, pp. 4060–4066, 2014.
- [99] YOO, K. B., PARK, B. H., CHOI, G. M. “Stability and performance of SOFC with SrTiO₃-based anode in CH₄ fuel.” *Solid State Ionics - Proceedings of the 18th International Conference on Solid State Ionics Warsaw, Poland, 3-8 July, 2011*, v. 225, pp. 104–107, 2012.
- [100] ESCUDERO, M. J., DE PARADA, I. G., FUERTE, A., SERRANO, J. L. “Analysis of the electrochemical performance of MoNi-CeO₂ cermet as anode material for solid oxide fuel cell. Part I. H₂, CH₄ and H₂/CH₄ mixtures as fuels.” *Journal of Power Sources*, v. 253, pp. 64–73, 2014.

- [101] FUERTE, A., VALENZUELA, R. X., ESCUDERO, M. J., DAZA, L. “Study of a SOFC with a bimetallic Cu-Co-ceria anode directly fuelled with simulated biogas mixtures.” *International Journal of Hydrogen Energy*, v. 39, pp. 4060–4066, 2014.
- [102] LEE, S.-I., AHN, K., VOHS, J. M., GORTE, R. J. “Cu-Co Bimetallic Anodes for Direct Utilization of Methane in SOFCs.” *Electrochemical Solid-State Letter*, v. 8, pp. A48–A51, 2005.
- [103] LEE, S.-I., VOHS, J. M., GORTE, R. J. “A Study of SOFC Anodes Based on Cu-Ni and Cu-Co Bimetallics in CeO₂YSZ.” *Journal of the Electrochemical Society*, v. 151, pp. A1319–A1323, 2004.
- [104] GROSS, M. D., VOHS, J. M., GORTE, R. J. “A study of thermal stability and methane tolerance of Cu-based SOFC anodes with electrodeposited Co.” *Electrochimica Acta*, v. 52, pp. 1951–1957, 2007.
- [105] ROSTRUP-NIELSEN, J. R. “Catalytic steam reforming.” *Catalysis Science & Technology*, v. 5, pp. 1–117, 1984.
- [106] CLARKE, S. H., DICKS, A. L., POINTON, K., SMITH, T. A., SWANN, A. “Catalytic aspects of the steam reforming of hydrocarbons in internal reforming fuel cells.” *Catalysis Today*, v. 38, pp. 411–423, 1997.
- [107] ARMOR, J. N. “The multiple roles for catalysis in the production of H₂.” *Applied Catalysis A: General*, v. 176, pp. 159–176, 1999.
- [108] JONES, G., JAKOBSEN, J. G., SHIM, S. S., KLEIS, J., ANDERSSON, M. P., ROSSMEISL, J., ABILD-PEDERSEN, F., BLIGAARD, T., HELVEG, S., HINNEMANN, B., ROSTRUP-NIELSEN, J. R., CHORKENDORFF, I., SEHESTED, J., NORSKOV, J. K. “First principles calculations and experimental insight into methane steam reforming over transition metal catalysts.” *Journal of Catalysis*, v. 259, pp. 147–160, 2008.
- [109] LUNSFORD, J. H. “Catalytic conversion of methane to more useful chemicals and fuels: a challenge for the 21st century.” *Catalysis Today*, v. 63, pp. 165–174, 2000.
- [110] CHATTANATHAN, S. A., ADHIKARI, S., ABDOULMOUMINE, N. “A review on current status of hydrogen production from bio-oil.” *Renewable and Sustainable Energy Reviews*, v. 16, pp. 2366–2372, 2012.

- [111] NAVARRO, R. M., SANCHEZ-SANCHEZ, M. C., ALVAREZ-GALVAN, M. C., DEL VALLE, F., FIERRO, J. L. G. “Hydrogen production from renewable sources: biomass and photocatalytic opportunities.” *Energy and Environmental Science*, v. 2, pp. 35–54, 2009.
- [112] YOGESH CHANDRA SHARMA AND, A. K., PRASAD, R., UPADHYAY, S. N. “Ethanol steam reforming for hydrogen production: Latest and effective catalyst modification strategies to minimize carbonaceous deactivation.” *Renewable and Sustainable Energy Reviews*, v. 74, pp. 89–103, 2017.
- [113] KRALEVA, E., POHL, M. M., JÜRGENSEN, A., EHRICH, H. “Hydrogen production by bioethanol partial oxidation over Ni based catalysts.” *Applied Catalysis B*, v. 179, pp. 509–520, 2015.
- [114] DIVINS, N. J., LÓPEZ, E., RODRÍGUEZ, Á., VEGA, D., LLORCA, J. “Bioethanol steam reforming and autothermal reforming in 3- μ m channels coated with RhPd/CeO₂ for hydrogen generation.” *Chemical Engineering and Processing*, v. 64, pp. 31–37, 2013.
- [115] PIREZ, C., FANG, W., CAPRON, M., PAUL, S., JOBIC, H., DUMEIGNIL, F., JALOWIECKI-DUHAMEL, L. “Steam reforming, partial oxidation and oxidative steam reforming for hydrogen production from ethanol over cerium nickel based oxyhydride catalyst.” *Applied Catalysis A: General*, v. 518, pp. 78–86, 2016.
- [116] ZENG, G., LI, Y., OLSBYE, U. “Kinetic and process study of ethanol steam reforming over Ni/Mg(Al)O catalysts: the initial steps.” *Catalysis Today*, v. 259, pp. 312–322, 2016.
- [117] DICKS, A. L. “Advances in catalysts for internal reforming in high temperature fuel cells.” *Journal of Power Sources*, v. 71, pp. 111–122, 1998.
- [118] ZHU, J., ZHANG, D., KING, K. D. “Reforming of CH₄ by partial oxidation: thermodynamic and kinetic analyses.” *Fuel*, v. 80, pp. 899–905, 2001.
- [119] HIEI, Y., ISHIHARA, T., TAKITA, Y. “Partial oxidation of methane for internally reformed solid fuel cell.” *Solid State Ionics*, v. 86-88, pp. 1267–1272, 1996.
- [120] VENÂNCIO, S. A., MIRANDA, P. E. V. “Direct utilization of carbonaceous fuels in multifunctional SOFC anodes for the electrosynthesis of chemicals or the generation of electricity.” *International Journal of Hydrogen Energy*, v. 42, pp. 13927–13938, 2017.

- [121] “AIR LIQUIDE - Gas Encyclopedia.” 26 Nov 2016. Available at: <http://encyclopedia.airliquide.com/encyclopedia.asp>.
- [122] CHEN, T., WANG, W. G., MIAO, H., LI, T., XU, C. “Evaluation of carbon deposition behavior on the nickel/yttrium-stabilized zirconia anode-supported fuel cell fueled with simulated syngas.” *Journal of Power Sources*, v. 196, pp. 2461–2468, 2011.
- [123] PRIMDAHL, S., SØRENSEN, B. F., MOGENSEN, M. “Effect of Nickel Oxide/Yttria-Stabilized Zirconia Anode Precursor Sintering Temperature on the Properties of Solid Oxide Fuel Cells.” *Journal of the American Ceramic Society*, v. 83, pp. 489–494, 2004.
- [124] ROSTRUP-NIELSEN, J. R., HANSEN, J. B., HELVEG, D., CHRISTIANSEN, N., JANNASCH, A.-K. “Sites for catalysis and electrochemistry in solid oxide fuel cell (SOFC) anode.” *Applied Physics A*, v. 85, pp. 427–430, 2006.
- [125] KIHLMAN, J., SUCIPTO, J., KAISALO, N., SIMELL, P., LEHTONEN, J. “Carbon formation in catalytic steam reforming of natural gas with SOFC anode off-gas.” *International Journal of Hydrogen Energy*, v. 40, pp. 1548–1558, 2015.
- [126] KISHIMOTO, H., HORITA, T., YAMAJI, K., XIONG, Y., SAKAI, N., BRITO, M. E. “Feasibility of n-dodecane fuel for solid oxide fuel cell with Ni-ScSZ anode.” *Journal of the Electrochemical Society*, v. 152, pp. A532–5388, 2005.
- [127] STANIFORTH, J., KENDALL, K. “Biogas powering a small tubular solid oxide fuel cell.” *Journal of Power Sources*, v. 71, pp. 275–277, 1998.
- [128] KENDALL, K., FINNERTY, C. M., SAUNDERS, G., CHUNG, J. T. “Effects of dilution on methane entering an SOFC anode.” *Journal of Power Sources*, v. 106, pp. 323–327, 2002.
- [129] SAUNDERS, G. J., PREECE, J., KENDALL, K. “Formulating liquid hydrocarbon fuels for SOFCs.” *Journal of Power Sources*, v. 131, pp. 23–26, 2004.
- [130] GIRONA, K., LAURENCIN, J., FOULETIER, J., LEFEBVRE-JOUD, F. “Carbon deposition in CH₄/CO₂ operated SOFC: Simulation and experimentation studies.” *Journal of Power Sources*, v. 210, pp. 381–391, 2012.

- [131] ZHAN, Z. L., BARNETT, S. A. “An octane-fueled solid oxide fuel cell.” *Science*, v. 308, pp. 844–847, 2005.
- [132] TOEBES, M. L., BITTER, J. H., VAN DILLEN, A. J., DE JONG, K. P. “Impact of the structure and reactivity of nickel particles on the catalytic growth of carbon nanofibers.” *Catalysis Today*, v. 76, pp. 33–42, 2002.
- [133] SASAKI, K., TERAOKA, Y. “Equilibria in fuel cell gases.” *Journal of The Electrochemical Society*, v. 150, pp. A885–A888, 2003.
- [134] KE, K., GUNJI, A., MORI, H., TSUCHIDA, S., TAKAHASHI, H., UKAL, K. “Effect of oxide on carbon deposition behavior of CH₄ fuel on Ni/ScSZ cermet anode in high temperature SOFCs.” *Solid State Ionics*, v. 177, pp. 541–547, 2006.
- [135] HE, H., HILL, J. M. “Carbon deposition on Ni/YSZ composites exposed to humidified methane.” *Applied Catalysis A: General*, v. 317, pp. 284–292, 2007.
- [136] TRIANTAFYLLOPOULOS, N. C., NEOPHYTIDES, S. G. “The nature and binding strength of carbon adspecies formed during the equilibrium dissociative adsorption of CH₄ on Ni-YSZ cermet catalysts.” *Journal of Catalysis*, v. 217, pp. 324–333, 2003.
- [137] GONG, M. Y., LIU, X. B., TREMBLY, J., JOHNSON, C. “Sulfur-tolerant anode materials for solid oxide fuel cell application.” *Journal of Power Sources*, v. 308, pp. 844–847, 2005.
- [138] MCCARTY, J. G., WISE, H. “Thermodynamics of sulfur chemisorption on metals. Alumina-supported nickel.” *The Journal of Chemical Physics*, v. 72, pp. 6332–6337, 1980.
- [139] KUROKAWA, H., SHOLKLAPPER, T. Z., JACOBSON, C. P., JOGHE, L. C. D., VISCO, S. J. “Ceria nanocoating for sulfur tolerant Ni-based anodes of solid oxide fuel cells.” *Electrochemical Solid State*, v. 10, pp. 135–138, 2007.
- [140] NIAKOLAS, D. K. “Sulfur poisoning of Ni-based anodes for Solid Oxide Fuel Cells in H/C-based fuels.” *Applied Catalysis A: General*, v. 486, pp. 123–142, 2014.
- [141] CHENG, Z., WANG, J.-H., CHOI, Y., YANG, L., LINC, M. C., LIU, M. “From Ni-YSZ to sulfur-tolerant anode materials for SOFCs: electrochem-

ical behavior, in situ characterization, modeling, and future perspectives.” *Energy & Environmental Science*, v. 4, pp. 4380–4409, 2011.

- [142] PAPURELLO, D., LANZINI, A., FIORILLI, S., SMEACETTO, F., SINGH, R., SANTARELLI, M. “Sulfur poisoning in Ni-anode solid oxide fuel cells (SOFCs): Deactivation in single cells and a stack.” *Chemical Engineering Journal*, v. 283, pp. 1224–1233, 2016.
- [143] MCCARTY, J. G. “Thermodynamics of sulfur chemisorption on metals. III. Iron and cobalt.” *The Journal of Chemical Physics*, v. 76, pp. 1162–1167, 1982.
- [144] SMITH, T. R., WOOD, A., BIRSS, V. I. “Effect of hydrogen sulfide on the direct internal reforming of methane in solid oxide fuel cells.” *Applied Catalysis A: General*, v. 354, pp. 1–7, 2009.
- [145] WANG, J. H., CHENG, Z., BRÉDAS, J. L., LIU, M. “Electronic and vibrational properties of nickel sulfides from first principles.” *The Journal of Chemical Physics*, v. 2007, pp. 214705–214713, 127.
- [146] VIVET, N., CHUPIN, S., ESTRADE, E., PIQUERO, T., POMMIER, P., ROCHAIS, D., BRUNETON, E. “3D Microstructural characterization of a solid oxide fuel cell anode reconstructed by focused ion beam tomography.” *Journal of Power Sources*, v. 196, pp. 7541–7549, 2011.
- [147] PETERSON, D. R. “Utilization of hydrogen sulfide in an intermediate-temperature ceria-based solid oxide fuel cell.” *Journal of The Electrochemical Society*, v. 145, pp. 1449–1454, 1998.
- [148] SASAKI, K., WATANABE, K., SHIOSAKI, K., SUSUKI, K., TERAOKA, Y. “Multi-Fuel Capability of Solid Oxide Fuel Cells.” *Journal of Electroceramics*, v. 13, pp. 669–675, 2004.
- [149] MATSUZAKI, Y., YASUDA, I. “The poisoning effect of sulfur-containing impurity gas on a SOFC anode: Part I. Dependence on temperature, time, and impurity concentration Original research article.” *Solid State Ionics*, v. 132, pp. 261–269, 2000.
- [150] SASAKI, K., SUSUKI, K., IYOSHI, A., UCHIMURA, M., IMAMURA, N., KUSABA, H., TERAOKA, Y., FUCHINO, H., TSUJIMOTO, K., UCHIDA, Y., JINGO, N. “H₂S Poisoning of Solid Oxide Fuel Cells.” *Journal of Electrochemical Society*, v. 153, pp. A2023–A2029, 2006.

- [151] JENS, F. B., RASMUSSEN, A. H. “The effect of H₂S on the performance of Ni-YSZ anodes in solid oxide fuel cells.” *Journal of Power Sources*, v. 191, pp. 534–541, 2009.
- [152] YOKOKAWA, H., WATANABE, T., UENO, A., HOSHINO, K. “Investigation on Degradation in Long-Term Operations of Four Different Stack/Modules.” *ECS Transactions*, v. 7, pp. 133–140, 2007.
- [153] SASAKI, K., HAGA, K., YOSHIZUMI, T., MINEMATSU, D., YUKI, E., LIU, R., URYU, C., OSHIMA, T., OGURA, T., SHIRATORI, Y., ITO, K., KOYAMA, M., YOKOMOTO, K. “Chemical durability of Solid Oxide Fuel Cells: Influence of impurities on long-term performance.” *Journal of Power Sources*, v. 196, pp. 9130–9140, 2011.
- [154] IWANSCHITZ, B., HOLZER, L., MAI, A., SCHÜTZE, M. “Nickel agglomeration in solid oxide fuel cells: The influence of temperature.” *Solid State Ionics*, v. 211, pp. 69–73, 2012.
- [155] VIVET, N., CHUPIN, S., ESTRADE, E., RICHARD, A., BONNAMY, S., ROCHAIS, D., BRUNETON, E. “Effect of Ni content in SOFC Ni-YSZ cermets: A three-dimensional study by FIB-SEM tomography.” *Journal of Power Sources*, v. 196, pp. 9989–9997, 2011.
- [156] INABA, H., TAGAWA, H. “Ceria-based solid electrolytes.” *Solid State Ionics*, v. 83, pp. 1–16, 1996.
- [157] SHAIKH, S. P. S., MUCHTAR, A., SOMALU, M. R. “A review on the selection of anode materials for solid-oxide fuel cells.” *Renewable & Sustainable Energy Reviews*, v. 51, pp. 1–8, 2015.
- [158] MINH, N. Q. “Solid oxide fuel cell technology-features and applications.” *Solid State Ionics*, v. 174, pp. 271–277, 2004.
- [159] DE BOER, B. *SOFC anodes: hydrogen oxidation at porous nickel and nickel/yttria stabilised zirconia cermet electrodes*. Tese de Doutorado, Twente: University of Twente, 1998.
- [160] MOGENSEN, M., LINDEGAARD, T. “The kinetics of hydrogen oxidation on a Ni/YSZ SOFC electrode at 1000 °C.” In: Singhal S C, Iwahara H, editors. *3rd International symposium on solid oxide fuel cells*. Pennington (NJ), Honolulu (HI, USA): The Electrochemical Society, pp. 484–493, 1993.

- [161] KHAN, M. S., LEE, S.-B., SONG, R.-H., LEE, J.-W., LIM, T.-H., PARK, S.-J. “Fundamental mechanisms involved in the degradation of nickel-yttria stabilized zirconia (Ni-YSZ) anode during solid oxide fuel cells operation: A review.” *Ceramics International*, v. 42, pp. 35–48, 2016.
- [162] IWATA, T. “Characterization of Ni-YSZ anode degradation for substrate-type solid oxide fuel cells.” *Journal of the Electrochemical Society*, v. 143, pp. 1521–1525, 1996.
- [163] SIMWONIS, D. “Nickel coarsening in annealed Ni/8YSZ anode substrates for solid oxide fuel cells.” *Solid State Ionics*, v. 132, pp. 241–251, 2000.
- [164] VASSEN, R., SIMWONIS, D., STÖVER, D. “Modelling of the agglomeration of Ni-particles in anodes of solid oxide fuel cells.” *Journal of Materials Science*, v. 36, pp. 147–151, 2001.
- [165] JIANG, S. P. “Sintering behavior of Ni/Y₂O₃-ZrO₂ cermet electrodes of solid oxide fuel cells.” *Journal of Materials Science*, v. 38, pp. 3775–3782, 2003.
- [166] HAGEN, A., BARFOD, R., HENDRIKSEN, P. V., LIU, Y. L., RAMOUSSE, S. “Degradation of anode supported SOFCs as a function of temperature and current load.” *Journal of The Electrochemical Society*, v. 153, pp. A1165–A1171, 2006.
- [167] HOLZER, L., IWANSCHITZ, B., HOCKER, T., MÜNCHA, B., PRESTAT, M., WIEDENMANN, D., VOGT, U., HOLTAPPELS, P., SFEIR, J., MAI, A., GRAULE, T. “Microstructure degradation of cermet anodes for solid oxide fuel cells: Quantification of nickel grain growth in dry and in humid atmospheres.” *Journal of Power Sources*, v. 196, pp. 1279–1294, 2011.
- [168] NELSON, G. J., GREW, K. N., IZZO, J. R., LOMBARDO, J. J., HARRIS, W. M., FAES, A. “Three-dimensional microstructural changes in the Ni-YSZ solid oxide fuel cell anode during operation.” *Acta Materialia*, v. 60, pp. 3491–3500, 2012.
- [169] YOKOKAWA, H., TU, H., IWANSCHITZ, B., MAI, A. “Fundamental mechanisms limiting solid oxide fuel cell durability.” *Journal of Power Sources*, v. 182, pp. 400–412, 2008.
- [170] THOMANNA, O., PIHLATIE, M., SCHULER, J., O. HIMANEN, J. K. “Method for measuring chromium evaporation from SOFC balance-of-plant components.” *ECS. Transactions*, v. 35, pp. 2609–2616, 2011.

- [171] KATHY, L. *Fuel Cells and Materials, Materials in Energy Conversion, Harvesting and Storage*. John Wiley & Sons, Inc., Hoboken, New Jersey, 2014.
- [172] KHAN, M., SONG, R. H., LEE, S. B., LEE, J. W., LIM, T. H., PARK, S. J. “Effect of GDC interlayer on the degradation of solid oxide fuel cell cathode during accelerated current load cycling.” *International Journal of Hydrogen Energy*, v. 39, pp. 20799–20805, 2014.
- [173] MALZBENDER, J., WESSEL, E., STEINBRECH, R. W. “Reduction and re-oxidation of anodes for solid oxide fuel cells.” *Solid State Ionics*, v. 176, pp. 2201–2203, 2005.
- [174] JIANG, S. P., CHAN, S. H. “A review of anode materials development in solid oxide fuel cells.” *Journal of Materials Science*, v. 39, pp. 4405–4439, 2004.
- [175] JIANG, S. P., CALLUS, P. J., S, S. P., BADWAL. “Fabrication and performance of Ni/3 mol% Y₂O₃-ZrO₂ cermet anodes for solid oxide fuel cells.” *Solid State Ionics*, v. 132, pp. 1–14, 2000.
- [176] PRASAD, D. H., JI, H. I., KIM, H. R., SON, J. W., KIM, B. K., LEE, H. W., LEE, J. H. “Effect of nickel nano-particle sintering on methane reforming activity of Ni-CGO cermet anodes for internal steam reforming SOFCs.” *Applied Catalysis B: Environmental*, v. 101, pp. 531–539, 2011.
- [177] PRASAD, D. H., PARK, S. Y., JI, H., KIM, H. R., SON, J. W., KIM, B. K., LEE, H. W., LEE, J. H. “Effect of steam content on nickel nano-particle sintering and methane reforming activity of Ni-CZO anode cermets for internal reforming SOFCs.” *Applied Catalysis A: General*, v. 411-412, pp. 160–169, 2012.
- [178] WU, X., ZHOU, X., TIAN, Y., KONG, X., ZHANG, J., ZUO, W., YE, X., SUN, K. “Preparation and electrochemical performance of silver impregnated Ni-YSZ anode for solid oxide fuel cell in dry methane.” *Applied Catalysis A: General*, v. 40, pp. 16484–16493, 2015.
- [179] FARRELL, B., LINIC, S. “Direct electrochemical oxidation of ethanol on SOFCs: Improved carbon tolerance of Ni anode by alloying.” *Applied Catalysis B: Environmental*, v. 183, pp. 386–393, 2016.
- [180] PARK, E. W., MOON, H., SOO PARK, M., HYUN, S. H. “Fabrication and characterization of Cu-Ni-YSZ SOFC anodes for direct use of methane via Cu-electroplating.” *International Journal of Hydrogen Energy*, v. 34, pp. 5537–5545, 2009.

- [181] TROSKIALINA, L., DHIR, A., STEINBERGER-WILCKENS, R. “Improved Performance and Durability of Anode Supported SOFC Operating on Biogas.” *ECS Transactions*, v. 68, pp. 2503–2513, 2015.
- [182] NIAKOLAS, D. K., ATHANASIOU, M., DRACOPOULOS, V., TSIAOUSIS, I., BEBELIS, S., NEOPHYTIDES, S. G. “Study of the synergistic interaction between nickel, gold and molybdenum in novel modified NiO/GDC cermets, possible anode materials for CH₄ fueled SOFCs.” *Applied Catalysis A: General*, v. 456, pp. 223–232, 2013.
- [183] NIAKOLAS, D. K., OUWELTJES, J. P., RIETVELD, G., DRACOPOULOS, V., NEOPHYTIDES, S. G. “Au-doped Ni/GDC as a new anode for SOFCs operating under rich CH₄ internal steam reforming.” *International Journal of Hydrogen Energy*, v. 35, pp. 7898–7904, 2010.
- [184] GAVRIELATOS, I., MONTINARO, D., ORFANIDI, A., NEOPHYTIDES, S. G. “Thermogravimetric and Electrocatalytic Study of Carbon Deposition of Ag-doped Ni/YSZ Electrodes under Internal CH₄ Steam Reforming Conditions.” *Fuel Cells*, v. 9, pp. 883–890, 2008.
- [185] GAVRIELATOS, I., DRAKOPOULOS, V., NEOPHYTIDES, S. G. “Carbon tolerant Ni-Au SOFC electrodes operating under internal steam reforming conditions.” *Journal of Catalysis*, v. 259, pp. 75–84, 2008.
- [186] WANG, F.-Y., CHENG, S., WAN, B.-Z. “Porous Ag-CGO cermets as anode materials for IT-SOFC using CO fuel.” *Fuel Cells Bulletin*, v. 2008, pp. 12–18, 2008.
- [187] WANG, F.-Y., CHENG, S., WAN, B.-Z. “Porous Ag-CGO cermets as anode materials for ITSOFC using CO fuel.” *Catalysis Communications*, v. 9, pp. 1595–1599, 2008.
- [188] WU, X., TIAN, Y., ZHANG, J., ZUO, W., KONG, X., WANG, J., SUN, K., ZHOU, X. “Enhanced electrochemical performance and carbon anti-coking ability of solid oxide fuel cells with silver modified nickel-yttrium stabilized zirconia anode by electroless plating.” *Journal of Power Sources*, v. 301, pp. 143–150, 2016.
- [189] BOLDRIN, P., RUIZ-TREJO, E., MERMELSTEIN, J., MENÉNDEZ, J. M. B., REINA, T. R., BRANDON, N. P. “Strategies for Carbon and Sulfur Tolerant Solid Oxide Fuel Cell Materials, Incorporating Lessons from Heterogeneous Catalysis.” *Chemical Reviews*, v. 116, pp. 13633–13684, 2016.

- [190] COSTA-NUNES, O., GORTE, R. J., VOHS, J. M. “Comparison of the performance of Cu-CeO₂-YSZ and Ni-YSZ composite SOFC anodes with H₂, CO and syngas.” *Journal of Power Sources*, v. 141, pp. 241–249, 2005.
- [191] MCINTOSH, S., VOHS, J. M., GORTE, R. J. “An examination of lanthanide additives on the performance of Cu-YSZ cermet anodes.” *Electrochimica Acta*, v. 47, pp. 3815–3821, 2002.
- [192] LU, C., WORRELL, W., VOHS, J., GORTE, R. J. “A comparison of Cu-ceria-SDC and Au-ceria-SDC composites for SOFC anodes.” *Journal of the Electrochemical Society*, v. 150, pp. A13571–1359, 2003.
- [193] SHOLKLAPPER, T. Z., RADMILOVIC, V., JACOBSON, C. P., VISCO, S. J., JONGHE, L. C. D. “Synthesis and Stability of a Nanoparticle-Infiltrated Solid Oxide Fuel Cell Electrode.” *Electrochemical Solid-State Letter*, v. 10, pp. B74–B76, 2007.
- [194] LAI, C.-S., PENG, S.-K., PAN, T.-M., WANG, J.-C., FAN, K.-M. “Work Function Adjustment by Nitrogen Incorporation in HfN x Gate Electrode with Post Metal Annealing Semiconductor Devices, Materials, and Processing.” *Electrochemical Solid-State Letter*, v. 9, pp. A237–A240, 2006.
- [195] AZZOLINI, A., DOWNS, J., SGLAVO, V. M. “Fabrication and co-sintering of thin tubular IT-SOFC with Cu₂O-GDC cermet supporting anode and Li₂O-doped GDC electrolyte.” *Journal of the European Ceramic Society*, v. 35, pp. 2119–2127, 2015.
- [196] HE, B., WANG, Z., ZHAO, L., PAN, X., WU, X., XI, C. “Ti-doped molybdenum-based perovskites as anodes for solid oxide fuel cells.” *Journal of Power Sources*, v. 241, pp. 627–633, 2013.
- [197] SILVA, C. A. *Desenvolvimento de anodo para conversão eletroquímica de metano em hidrocarbonetos C₂ para utilização em pilhas a combustível de óxido sólido*. Tese de Doutorado, Laboratório de Hidrogênio COPPE/UFRJ, 2015.
- [198] SILVA, C. A., MIRANDA, P. E. V. “Synthesis of LaAlO₃ based materials for potential use as methane-fueled solid oxide fuel cell anodes.” *International Journal of Hydrogen Energy*, v. 40, pp. 10002–10015, 2015.
- [199] KIATKITTIPONG, W., TAGAWA, T., GOTO, S., ASSABUMRUNGRAT, S., PRASERTHDAM, P. “Oxidative coupling of methane in the LSM/YSZ/LaAlO SOFC reactor.” *Journal of the Ceramic Society of Japan*, v. 37, pp. 1461–1470, 2004.

- [200] MOE, K. K., TAGAWA, T., GOTO, S. “Preparation of electrode catalyst for SOFC reactor by ultrasonic mist pyrolysis of aqueous solution.” *Journal of the Ceramic Society of Japan*, v. 106, pp. 242–247, 1998.
- [201] MOE, K. K., TAGAWA, T., GOTO, S. “Preparation of electrode catalyst for SOFC reactor by ultrasonic mist pyrolysis.” *Journal of the Ceramic Society of Japan*, v. 106, pp. 754–758, 1998.
- [202] TAGAWA, T., MOE, K. K., HIRAMATSU, T., GOTO, S. “Design of electrode for solid oxide fuel cells reactor.” *Solid State Ionics*, v. 106, pp. 227–235, 1998.
- [203] MARTÍNEZ-CORONADO, R., ALONSO, J. A., AGUADERO, A., FERNÁNDEZ-DÍAZ, M. T. “Optimized energy conversion efficiency in solid-oxide fuel cells implementing $\text{SrMo}_{1-x}\text{Fe}_x\text{O}_{3+\delta}$ perovskites as anodes.” *International Journal of Hydrogen Energy*, v. 39, pp. 4067–4073, 2014.
- [204] MARTÍNEZ-CORONADO, R., ALONSO, J. A., AGUADERO, A., FERNÁNDEZ-DÍAZ, M. T. “New $\text{SrMo}_{1-x}\text{Cr}_x\text{O}_{3+\delta}$ perovskites as anodes in solid-oxide fuel cells.” *International Journal of Hydrogen Energy*, v. 39, pp. 4067–4073, 2014.
- [205] CHAMBERLAND, B. L., DANIELSON, P. S. “Alkaline-earth vanadium (IV) oxides having the AVO_3 composition.” *Journal of Solid State Chemistry*, v. 3, pp. 243–247, 1971.
- [206] KOLOTYGIN, V. A., TSIPIS, E. V., LÜA, M. F., PIVAK, Y. V., YARMOLENKO, S. N., BREDIKHIN, S. I., KHARTON, V. V. “Functional properties of SOFC anode materials based on LaCrO_3 , $\text{La}(\text{Ti},\text{Mn})\text{O}_3$ and $\text{Sr}(\text{Nb},\text{Mn})\text{O}_3$ perovskites: A comparative analysis.” *Solid State Ionics*, v. 251, pp. 28–33, 2013.
- [207] GORTE, R. J., VOHS, J. M. “Nanostructured anodes for solid oxide fuel cells.” *Current Opinion in Colloid & Interface Science*, v. 14, pp. 236–244, 2009.
- [208] GORTE, R. J., KIM, H., VOHS, J. M. “Novel SOFC anodes for the direct electrochemical oxidation of hydrocarbon.” *Journal of Power Sources*, v. 106, pp. 10–15, 2002.
- [209] VENÂNCIO, S. A., GUTIERRES, T. E. F., SARRUF, B. J. M., MIRANDA, P. E. V. “Oxidação direta do etanol no anodo de PaCOS.” *Matéria (Rio de Janeiro)*, v. 13, pp. 560–568, 2008.

- [210] VENÂNCIO, S. A., MIRANDA, P. E. V. “Solid oxide fuel cell anode for the direct utilization of ethanol as fuel.” *Scripta Materialia*, v. 65, pp. 1065–1068, 2011.
- [211] CORALLI, A., DE MIRANDA, H. V., MONTEIRO, C. F. E., DA SILVA, J. F. R., DE MIRANDA, P. E. V. “Mathematical model for the analysis of structure and optimal operational parameters of a solid oxide fuel cell generator.” *Journal of Power Sources*, v. 269, pp. 632–644, 2014.
- [212] TORRES, S. O. A., MESQUITA, A. C., MIRANDA, P. E. V. “Control Strategy for Balance of Plant in Solid Oxide Fuel Cell.” *IEEE - América Latina*, v. 11, pp. 726–736, 2013.
- [213] YOO, K. B., CHOI, G. M. “Performance of La-doped strontium titanate (LST) anode on LaGaO₃-based SOFC.” *Solid State Ionics*, v. 180, pp. 867–871, 2009.
- [214] ZHA, S., TSANG, P., CHENG, Z., LIU, M. “Electrical properties and sulfur tolerance of La_{0.75}Sr_{0.25}Cr_{1-x}Mn_xO₃ under anodic conditions.” *Journal of Solid State Chemistry*, v. 178, pp. 1844–1850, 2005.
- [215] UCHIDA, H., I ARISAKA, S., WATANABE, M. “High performance electrode for medium-temperature solid oxide fuel cells: control of microstructure of La (Sr) CoO₃ cathodes with highly dispersed Pt electrocatalysts.” *Journal of the Electrochemical Society*, v. 149, pp. A13–A18, 2002.
- [216] GIL, V., MOURE, C., TARTAJ, J. “Sinterability microstructures and electrical properties of Ni/Gd-doped ceria cermets used as anode materials for SOFCs.” *Journal of the European Ceramic Society*, v. 27, pp. 4205–4209, 2007.
- [217] E HOU, S., AGUADERO, A., ALONSO, J. A., GOODENOUGH, J. B. “Fe-based perovskites as electrodes for intermediate-temperature solid oxide fuel cells.” *Journal of Power Sources*, v. 196, pp. 5478–5484, 2011.
- [218] WANG, Z., WENG, W., CHENG, K., DU, P., SHEN, G., HAN, G. “Catalytic modification of Ni-Sm-doped ceria anodes with copper for direct utilization of dry methane in low-temperature solid oxide fuel cells.” *Journal of Power Sources*, v. 179, pp. 541–546, 2008.
- [219] PARK, S.-Y., AHN, J. H., JEONG, C.-W., NA, C. W., SONG, R.-H., LEE, J.-H. “Ni-YSZ-supported tubular solid oxide fuel cells with GDC interlayer between YSZ electrolyte and LSCF cathode.” *International Journal of Hydrogen Energy*, v. 39, pp. 12894–12903, 2014.

- [220] SHAIKH, S., BHOGA, S. “Structural and electrical characterization of $\text{Ce}_{1-x}\text{Cu}_x\text{O}_{2-\delta}$ ($x=0.05-0.5$) prepared by combustion technique.” *Integrated Ferroelectrics*, v. 119, pp. 66–73, 2010.
- [221] FUERTE, A., HORNES, A., BERA, P., MARTÍNEZ-ARIAS, A., ESCUDERO, M., DAZA, L. “Study of $\text{Cu-Fe-Ce}_{0.9}\text{Gd}_{0.1}\text{O}_{2-\delta}$ as IT-SOFC anode: catalytic activity, thermal expansion, morphology, electrical conductivity and chemical compatibility.” *ECS Transactions*, v. 25, pp. 2183–2192, 2009.
- [222] ZHU, L., LIU, X., HAN, F., SUN, J., BI, H., WANG, H., YU, S., PEI, L. “ $\text{Ni}_{1-x}\text{Cu}_x$ -SDC anodes for intermediate temperature solid oxide fuel cell.” *Solid State Ionics*, v. 288, pp. 115–119, 2016.
- [223] SHAIKH, S., MOHARIL, S., NAGRARE, B. “A comparative study of copper-cermet anode material synthesized by different technique.” *International Journal of Hydrogen Energy*, v. 37, pp. 6853–6861, 2012.
- [224] ALIOTTA, C., LIOTTA, L., DEGANELLO, F., PAROLA, V. L., MARTORANA, A. “Direct methane oxidation on $\text{La}_{1-x}\text{Sr}_x\text{Cr}_{1-y}\text{Fe}_y\text{O}_{3-\delta}$ perovskite-type oxides as potential anode for intermediate temperature solid oxide fuel cells.” *Applied Catalysis B: Environmental*, v. 180, pp. 424–433, 2016.
- [225] YOON, J. S., LIM, Y.-S., CHOI, B. H., HWANG, H. J. “Catalytic activity of perovskite-type doped $\text{La}_{0.08}\text{Sr}_{0.92}\text{Ti}_{1-x}\text{M}_x\text{O}_{3-\delta}$ ($\text{M} = \text{Mn}, \text{Fe}, \text{and Co}$) oxides for methane oxidation.” *International Journal of Hydrogen Energy*, v. 39, pp. 7955–7962, 2014.
- [226] THAICHAROENSUTCHARITTHAM, S., MEEYOO, V., KITTIYANAN, B., RANGSUNVIGIT, P., RIRKSOMBOON, T. “Catalytic combustion of methane over $\text{NiO/Ce}_{0.75}\text{Zr}_{0.25}\text{O}_2$ catalyst.” *Catalysis Communications*, v. 10, pp. 673–677, 2009.
- [227] KHARTON, V. V., YAREMCHENKO, A. A., VALENTE, A. A., FROLOVA, E. V., IVANOVSKAYA, M. I., FRADE, J. R., MARQUES, F. M. B., ROCHA, J. “Methane oxidation over SOFC anodes with nanocrystalline ceria-based phases.” *Solid State Ionics - Proceedings of the 15th International Conference on Solid State Ionics, Part I*, v. 177, pp. 2179–2183, 2006.
- [228] JI, S., AN, J., JANG, D. Y., JEE, Y., SHIM, J. H., CHA, S. W. “On the reduced electrical conductivity of radio-frequency sputtered doped ceria thin

- film by elevating the substrate temperature.” *Current Applied Physics*, v. 16, pp. 324–328, 2016.
- [229] GIL, V., MOURE, C., TARTAJ, J. “Sinterability, microstructures and electrical properties of Ni/Gd-doped ceria cermets used as anode materials for SOFCs.” *Journal of the European Ceramic Society - Refereed Reports ELECTROCERAMICS X 2006*, v. 2007, pp. 4205–4209, 27.
- [230] LANZINI, A., GUERRA, C., LEONE, P., SANTARELLI, M., SMEACETTO, F., FIORILLI, S., GONDOLINI, A., MERCADELLI, E., SANSON, A., BRANDON, N. P. “Influence of the microstructure on the catalytic properties of SOFC anodes under dry reforming of methane.” *Materials Letters*, v. 164, pp. 312–315, 2016.
- [231] SHEN, Y., LUA, A. C. “Polyol synthesis of nickel-copper based catalysts for hydrogen production by methane decomposition.” *International Journal of Hydrogen Energy*, v. 40, pp. 311–321, 2015.
- [232] GENG, H., YANG, Z., ZHANG, L., RAN, J., CHEN, Y. “Experimental and kinetic study of methane combustion with water over copper catalyst at low-temperature.” *Energy Conversion and Management*, v. 103, pp. 244–250, 2015.
- [233] LIOTTA, L. F., CARLO, G. D., PANTALEO, G., DEGANELLO, G. “Co₃O₄/CeO₂ and Co₃O₄/CeO₂-ZrO₂ composite catalysts for methane combustion: Correlation between morphology reduction properties and catalytic activity.” *Catalysis Communications*, v. 6, pp. 329–336, 2005.
- [234] ASLANNEJAD, H., BARELLI, L., BABAIE, A., BOZORGMEHRI, S. “Effect of air addition to methane on performance stability and coking over NiO-YSZ anodes of SOFC.” *Applied Energy*, v. 177, pp. 179–186, 2016.
- [235] BALDINELLI, A., BARELLI, L., BIDINI, G., MICHELE, A. D., VIVANI, R. “SOFC direct fuelling with high-methane gases: Optimal strategies for fuel dilution and upgrade to avoid quick degradation.” *Energy Conversion and Management*, v. 124, pp. 492–503, 2016.
- [236] SAEBEA, D., AUTHAYANUN, S., PATCHARAVORACHOT, Y., PAENGJUNTUEK, W., ARPORNWICHANO, A. “Use of different renewable fuels in a steam reformer integrated into a solid oxide fuel cell: Theoretical analysis and performance comparison.” *Energy*, v. 51, pp. 305–313, 2013.

- [237] LANZINI, A., LEONE, P., GUERRA, C., SMEACETTO, F., BRANDON, N. P., SANTARELLI, M. “Durability of anode supported Solid Oxides Fuel Cells (SOFC) under direct dry-reforming of methane.” *Chemical Engineering Journal*, v. 220, pp. 254–263, 2013.
- [238] GUERRA, C., LANZINI, A., LEONE, P., SANTARELLI, M., BRANDON, N. P. “Optimization of dry reforming of methane over Ni/YSZ anodes for solid oxide fuel cells.” *Journal of Power Sources*, v. 245, pp. 154–163, 2014.
- [239] SHIRATORI, Y., IJICHI, T., OSHIMA, T., SASAKI, K. “Internal reforming SOFC running on biogas.” *International Journal of Hydrogen Energy*, v. 35, pp. 7905–7912, 2010.
- [240] GÖTSCH, T., SCHACHINGER, T., STÖGER-POLLACH, M., KAINDL, R., PENNER, S. “Carbon tolerance of Ni-Cu and Ni-Cu/YSZ sub- μm sized SOFC thin film model systems.” *Applied Surface Science*, v. 402, pp. 1–11, 2017.
- [241] WOLFBEISSER, A., KOVÁCS, G., KOZLOV, S. M., FÖTTINGER, K., BERNARDI, J., KLÖTZER, B., NEYMAN, K. M., RUPPRECHTER, G. “Surface composition changes of CuNi-ZrO₂ during methane decomposition: An operando NAP-XPS and density functional study.” *Catalysis Today*, v. 238, pp. 134–143, 2017.
- [242] YOKOKAWA, H., SAKAI, N., HORITA, T., YAMAJI, K., XIONG, Y., OTAKE, T., YUGAMI, H., KAWADA, T., MIZUSAKI, J. “Phase Diagram Calculations of ZrO₂-Based Ceramics with an Emphasis on the Reduction/Oxidation Equilibria of Cerium Ions in the ZrO₂-YO_{1.5}-CeO₂-CeO_{1.5} System.” *Journal of Phase Equilibria*, v. 22, pp. 331–338, 2001.
- [243] REDDY, B. M., BHARALI, P., THRIMURTHULU, G., SAIKIA, P., KATTA, L., PARK, S.-E. “Catalytic Efficiency of Ceria-Zirconia and Ceria-Hafnia Nanocomposite Oxides for Soot Oxidation.” *Catalysis Letters*, v. 123, pp. 327–333, 2008.
- [244] REDDY, B. M., BHARALI, P., SAIKIA, P., KHAN, A., LORIDANT, S., MUHLER, M., GRU, W. “Hafnium-Doped Ceria Nanocomposite Oxide as a Novel Redox Additive for Three-Way Catalysts.” *The Journal of Physical Chemistry C - Letters*, v. 111, pp. 1878–1881, 2007.
- [245] MARTINEZ-ARIAS, A., FERNÁNDEZ-GARCIA, M., IGLESIAS-JUEZ, A., HUNGRIA, A. B., ANDERSON, J. A., CONESA, J. C., SORIA, J. “New

- Pd/Ce_xZr_{1-x}O₂/Al₂O₃ three-way catalysts prepared by microemulsion: Part 2. In situ analysis of CO oxidation and NO reduction under stoichiometric CO + NO + O₂.” *Applied Catalysis B: Environmental*, v. 31, pp. 51–60, 2001.
- [246] OZAWA, M., MATUDA, K., SUZUKI, S. “Microstructure and oxygen release properties of catalytic alumina-supported CeO₂-ZrO₂ powders.” *Journal of Alloys and Compounds*, v. 303-304, pp. 56–59, 2000.
- [247] DING, H., TAO, Z., LIU, S., YANG, Y. “A redox-stable direct-methane solid oxide fuel cell (SOFC) with Sr₂FeNb_{0.2}Mo_{0.8}O_{6-δ} double perovskite as anode material.” *Journal of Power Sources*, v. 327, pp. 573–579, 2016.
- [248] WAN, T., ZHU, A., GUO, Y., WANG, C., HUANG, S., CHEN, H., YANG, G., WANG, W., SHAO, Z. “Co-generation of electricity and syngas on proton-conducting solid oxide fuel cell with a perovskite layer as a precursor of a highly efficient reforming catalyst.” *Journal of Power Sources*, v. 348, pp. 9–15, 2017.
- [249] SUNARSO, J., HASHIM, S. S., ZHU, N., ZHOU, W. “Perovskite oxides applications in high temperature oxygen separation, solid oxide fuel cell and membrane reactor: A review.” *Progress in Energy and Combustion Science*, v. 61, pp. 57–77, 2017.
- [250] KONAR, R., MUKHOPADHYAY, J., SHARMA, A. D., BASU, R. N. “Synthesis of Cu-YSZ and Ni-Cu-YSZ cermets by a novel electroless technique for use as solid oxide fuel cell anode: Application potentiality towards fuel flexibility in biogas atmosphere.” *International Journal of Hydrogen Energy*, v. 41, pp. 1151–1160, 2016.
- [251] IDERIS, A., CROISSET, E., PRITZKER, M., AMIN, A. “Direct-methane solid oxide fuel cell (SOFC) with Ni-SDC anode-supported cell.” *International Journal of Hydrogen Energy*, v. In Press, 2017.
- [252] LIU, M., VAN DER KLEIJ, A., VERKOOIJEN, A. H. M., ARAVIND, P. V. “An experimental study of the interaction between tar and SOFCs with Ni/GDC anodes.” *Applied Energy*, v. 108, pp. 149–157, 2013.
- [253] LI, S., PAN, W., WANG, S., MENG, X., JIANG, C., IRVINE, J. T. S. “Electrochemical performance of different carbon fuels on a hybrid direct carbon fuel cell.” *International Journal of Hydrogen Energy*, v. 42, pp. 16279–16287, 2017.

- [254] MADSEN, B. D., BARNETT, S. A. “Effect of fuel composition on the performance of ceramic-based solid oxide fuel cell anodes.” *Solid State Ionics*, v. 176, pp. 2545–2553, 2005.
- [255] MARINA, O. A., CANFIELD, N. L., STEVENSON, J. W. “Thermal, electrical, and electrocatalytical properties of lanthanum-doped strontium titanate.” *Solid State Ionics*, v. 149, pp. 21–28, 2002.
- [256] MUKUNDAN, R., BROSHA, E. L., GARZON, F. H. “Sulfur Tolerant Anodes for SOFCs.” *Electrochemical and Solid-State Letters*, v. 7, pp. A5–A7, 2004.
- [257] CHENG, Z., ZHA, S., AGUILAR, L., WANG, D., WINNICK, J., LIU, M. “A Solid Oxide Fuel Cell Running on H₂S/CH₄ Fuel Mixtures.” *Electrochemical and Solid-State Letters*, v. 9, pp. A31–A33, 2006.
- [258] CASCOS, V., TRONCOSO, L., ALONSO, J. A., FERNANDEZ-DÍAZ, M. T. “Design of new Ga-doped SrMoO₃ perovskites performing as anode materials in SOFC.” *Renewable Energy*, v. 111, pp. 476–483, 2017.
- [259] ZHAO, K., DU, Y. “Calcium-doped ceria materials for anode of solid oxide fuel cells running on methane fuel.” *Journal of Power Sources*, v. 347, pp. 79–85, 2017.
- [260] VENÂNCIO, S. A., MIRANDA, P. E. V. “Synthesis of CeAlO₃/CeO₂-Al₂O₃ for use as a solid oxide fuel cell functional anode material.” *Ceramics International*, v. 37, pp. 3139–3152, 2011.
- [261] KIM, H., VOHS, J. M., GORTE, R. J. “Direct oxidation of sulfur-containing fuels in a solid oxide fuel cell.” *Chemical Communications*, v. 0, pp. 2334–2335, 2001.
- [262] PARK, S., VOHS, J. M., GORTE, R. J. “Direct oxidation of hydrocarbons in a solid-oxide fuel cell.” *Nature*, v. 404, pp. 265–267, 2000.
- [263] SOUSA, A. R. O., ARAUJO, A. J. M., SOUZA, G. S., GRILO, J. P. F., LOUREIRO, F. J. A., FAGG, D. P., MACEDO, D. A. “Electrochemical assessment of one-step Cu-CGO cermets under hydrogen and biogas fuels.” *Materials Letters*, v. 191, pp. 141–144, 2017.
- [264] WASEDA, Y., MATSUBARA, E., SHINODA, K. *X-Ray Diffraction Crystallography: Introduction, Examples and Solved Problems*. Springer, 2011.
- [265] YOUNG, R. A. *The Rietveld method*. Oxford: University Press, 1993.

- [266] RODRIGUEZ-CARVAJAL, J. “Recent advances in magnetic structure determination by neutron powder diffraction.” *Physica B*, v. 192, pp. 55–69, 1993. Available at: <http://www.ill.eu/sites/fullprof>.
- [267] DUVAL, C. *Inorganic thermogravimetric analysis*. Elsevier, 1963.
- [268] JENKINS, R. *X-Ray Fluorescence Spectrometry*. John Wiley & Sons, 1988.
- [269] BECKHOFF, B., KANNGIESSER, B., LANGHOFF, N., WEDELL, R., WOLFF, H. *Handbook of Practical X-Ray Fluorescence Analysis*. Springer, 2006.
- [270] REDHEAD, P. “Thermal desorption of gases.” *Vacuum*, v. 12, pp. 203–211, 1962.
- [271] RAMADAN, A. A., GOULD, R. D., ASHOUR, A. “On the Van der Pauw method of resistivity measurements.” *Thin Solid Films*, v. 239, pp. 272–275, 1994.
- [272] RIETVELD, G., KOIJMANS, C. V., HENDERSON, L. C. A., HALL, M. J., WARNECKE, S. H. P., SCHUMACHER, B. “DC Conductivity Measurements in the Van Der Pauw Geometry.” *IEEE TRANSACTIONS ON INSTRUMENTATION AND MEASUREMENT*, v. 52, pp. 449–453, 2003.
- [273] MALLON, C., KENDALL, K. “Sensitivity of nickel cermet anodes to reduction conditions.” *Journal of Power Sources*, v. 145, pp. 154–160, 2005.
- [274] DHIR, A., KENDALL, K. “Improving Reliability of Microtubular SOFCs for Direct Use on Methane.” *ECS Transactions*, v. 7, pp. 823–828, 2007.
- [275] DHIR, A. *Improved Microtubular Solid Oxide Fuel Cells*. Tese de Doutorado, University of Birmingham, 2008.
- [276] SCHRADER, B. *Infrared and Raman Spectroscopy - Methods and Applications*. VCH, 1995.
- [277] ZHOU, W., WANG, Z. L. *Scanning Microscopy for Nanotechnology - Techniques and Applications*. Springer, 2006.
- [278] PREECE, J. *Oxygenated hydrocarbon fuels for solid oxide fuel cells*. Tese de Doutorado, University of Birmingham, 2005.
- [279] KNAUTH, P., SCHWITZGEBEL, G., TSCHÖPE, A., VILLAIN, S. “Emf Measurements on Nanocrystalline Copper-Doped Ceria.” *Journal of Solid State Chemistry*, v. 140, pp. 295–299, 1998.

- [280] CHEN, M., HALLSTEDT, B., GRUNDY, A. N., GAUCKLER, L. J. “CeO₂-CoO Phase Diagram.” *Journal of the American Ceramic Society*, v. 86, pp. 1567–70, 2003.
- [281] TANG, C.-W., WANG, C.-B., CHIEN, S.-H. “Characterization of cobalt oxides studied by FT-IR, Raman, TPR and TG-MS.” *Thermochimica Acta*, v. 473, pp. 68–73, 2008.
- [282] LIN, H.-Y., CHEN, Y.-W. “The mechanism of reduction of cobalt by hydrogen.” *Materials Chemistry and Physics*, v. 85, pp. 171–175, 2004.
- [283] HUTCHINGS, K. N., WILSON, M., LARSEN, P. A., CUTLER, R. A. “Kinetic and thermodynamic considerations for oxygen absorption/desorption using cobalt oxide.” *Solid State Ionics*, v. 177, pp. 45–51, 2006.
- [284] MARRERO-JEREZ, J., MURUGAN, A., METCALFE, I. S., NÚÑEZ, P. “TPR-TPD-TPO studies on CGO/NiO and CGO/CuO ceramics obtained from freeze-dried precursors.” *Ceramics International*, v. 40, pp. 15175–15182, 2014.
- [285] PINTAR, A., BATISTA, J., HOCEVARZ, S. “TPR, TPO, and TPD examinations of Cu_{0.15}Ce_{0.85}O_{2-y} mixed oxides prepared by co-precipitation, by the sol-gel peroxide route, and by citric acid-assisted synthesis.” *Journal of Colloid and Interface Science*, v. 285, pp. 218–231, 2005.
- [286] KUNDAKOVIC, L., FLYTZANI-STEPHANOPOULOS, M. “Cu- and Ag-Modified Cerium Oxide Catalysts for Methane Oxidation.” *Journal of Catalysis*, v. 179, pp. 203–221, 1998.
- [287] ARNOLDY, P., MOULIJN, J. A. “Temperature-programmed reduction of CoOAl₂O₃ catalysts.” *Journal of Catalysis*, v. 93, pp. 38–54, 1985.
- [288] YAO, H. C., YAO, Y. F. Y. “Ceria in automotive exhaust catalysts: I. Oxygen storage.” *Journal of Catalysis*, v. 86, pp. 254–265, 1984.
- [289] WANG, P., ZHANG, J., BAI, Y., XIAO, H., TIAN, S., XIE, H., YANG, G., TSUBAKI, N., HAN, Y., TAN, Y. “Ternary copper-cobalt-cerium catalyst for the production of ethanol and higher alcohols through CO hydrogenation.” *Applied Catalysis A: General*, v. 514, pp. 14–23, 2016.
- [290] HAYASHI, H., KANO, M., QUAN, C. J., INABA, H., WANG, S., DOKIYA, M., TAGAWA, H. “Thermal expansion of Gd-doped ceria and reduced ceria.” *Solid State Ionics*, v. 132, pp. 227–233, 2000.

- [291] SAMESHIMA, S., KAWAMINAMI, M., HIRATA, Y. “Thermal Expansion of Rare-Earth-Doped Ceria Ceramics.” *Journal of the Ceramic Society of Japan*, v. 110, pp. 597–600, 2002.
- [292] BRABERS, V. A. M., BROEMME, A. D. D. “Low-spin-high-spin transition in the Co_3O_4 spinel.” *Journal of Magnetism and Magnetic Materials*, v. 104–107, pp. 405–406, 1992.
- [293] ROTH, W. L. “The magnetic structure of Co_3O_4 .” *Journal of Physics and Chemistry of Solids*, v. 25, pp. 1–10, 1964.
- [294] KRYNETSKII, I. B., GIZHEVSKII, B. A., NAUMOV, S. V., KOZLOV, E. A. “Size Effect of the Thermal Expansion of Nanostructural Copper Oxide.” *Fizika Tverdogo Tela*, v. 50, pp. 723–725, 2008.
- [295] NATH, S., MANNA, I., JHA, A. K., SHARMA, S. C., PRATIHAR, S. K., MAJUMDAR, J. D. “Thermophysical behavior of thermal sprayed yttria stabilized zirconia based composite coatings.” *Ceramics International*, v. 43, pp. 11204–11217, 2017.
- [296] XU, L., SONG, H., CHOU, L. “Mesoporous nanocrystalline ceria-zirconia solid solutions supported nickel based catalysts for CO_2 reforming of CH_4 .” *International Journal of Hydrogen Energy*, v. 37, pp. 118001–18020, 2012.
- [297] LIU, F., HE, D., LU, J., CHEN, D., LIU, P., YU, J., LIU, J., WAN, G., HE, S., LUO, Y. “A facile and rapid route to synthesize ceria-zirconia nanoparticles with high performance for CH_3SH decomposition.” *Materials Research Bulletin*, v. 93, pp. 150–156, 2017.
- [298] S. SCHMID, R. HAUSBRAND, W. J. “Cobalt oxide thin film low pressure metal-organic chemical vapor deposition.” *Thin Solid Films*, v. 567, pp. 8–13, 2014.
- [299] GÓMEZ, L. E., MÚNERA, J. F., SOLLIER, B. M., MIRÓ, E. E., BOIX, A. V. “Raman in situ characterization of the species present in Co/CeO_2 and Co/ZrO_2 catalysts during the COPrOx reaction.” *International Journal of Hydrogen Energy*, v. 41, pp. 4993–5002, 2016.
- [300] BERENQUER, R., ROSA-TORO, A. L., QUIJADA, C., MORALLÓN, E. “Electrocatalytic oxidation of cyanide on copper-doped cobalt oxide electrodes.” *Applied Catalysis B: Environmental*, v. 207, pp. 286–296, 2017.
- [301] ESCUDERO, M. J., RODRIGO, T., MENDOZA, L., CASSIR, M., DAZA, L. “Porous nickel MCFC cathode coated by potentiostatically deposited

cobalt oxide: I. A structural and morphological study.” *Journal of Power Sources*, v. 140, pp. 81–87, 2005.

- [302] KHANA, A., JIMÉNEZ, C., CHAIX-PLUCHERY, O., ROUSSEL, H., DESCHANVRES, J. L. “In-situ Raman spectroscopy and X-ray diffraction studies of the structural transformations leading to the SrCu₂O₂ phase from strontium-copper oxide thin films deposited by metalorganic chemical vapor deposition.” *Thin Solid Films*, v. 541, pp. 136–141, 2013.
- [303] BALAKRISHNAN, G., RAGHAVAN, C. M., GHOSH, C., DIVAKAR, R., MOHANDAS, E., SONG, J. I., BAE, S. I., KIM, T. G. “X-ray diffraction, Raman and photoluminescence studies of nanocrystalline cerium oxide thin films.” *Ceramics International*, v. 39, pp. 8327–8333, 2013.
- [304] REINA, T. R., IVANOVA, S., LAGUNA, O. H., CENTENO, M. A., ODRIOZOLA, J. A. “WGS and CO-PrOx reactions using gold promoted copper-ceria catalysts: "Bulk CuO CeO₂ vs. CuO CeO₂/Al₂O₃ with low mixed oxide content".” *Applied Catalysis B: Environmental*, v. 197, pp. 62–72, 2016.
- [305] REDDY, B. M., KHAN, A., YAMADA, Y., KOBAYASHI, T., LORIDANT, S., VOLTA, J.-C. “Structural characterization of CeO₂-MO₂ (M = Si⁴⁺, Ti⁴⁺, and Zr⁴⁺) mixed oxides by Raman spectroscopy, x-ray photoelectron spectroscopy, and other techniques.” *Journal of Physical Chemistry B*, v. 107, pp. 11475–11484, 2003.
- [306] JARDIM, E. O., RICO-FRANCÉS, S., COLOMA, F., ANDERSON, J. A., RAMOS-FERNANDEZ, E. V., SILVESTRE-ALBEROA, J., SEPÚLVEDA-ESCRIBANO, A. “Preferential oxidation of CO in excess of H₂ on Pt/CeO₂-Nb₂O₅ catalysts.” *Applied Catalysis A: General*, v. 492, pp. 201–211, 2015.
- [307] LLORCA, J., PISCINA, P. R. D. L., DALMON, J.-A., HOMS, N. “Transformation of Co₃O₄ during ethanol steam-re-forming. Activation process for hydrogen production.” *Chemistry of Materials*, v. 16, pp. 3573–3578, 2004.
- [308] HADJIEV, V. G., ILIEV, M. N., VERGILOV, I. V. “The Raman spectra of Co₃O₄.” *Journal of Physics C: Solid State Physics*, v. 21, pp. L199–L201, 1988.

- [309] XU, J. F., JI, W., SHEN, X., LI, W. S., TANG, S. H., YE, X. R., JIA, D. Z., XIN, X. Q. “Raman Spectra of CuO Nanocrystals.” *Journal of Raman Spectroscopy*, v. 30, pp. 413–415, 1999.
- [310] CHRZANOWSKA, J., IRWIN, J. C. “Raman Spectra from Cupric Oxide.” *Solid State Communications*, v. 70, pp. 11–14, 1989.
- [311] VENÂNCIO, S. A. *Desenvolvimento de Anodo Funcional para a Utilização Direta de Etanol em Pilha a Combustível de Óxido Sólido*. Tese de Doutorado, Laboratório de Hidrogênio COPPE/UFRJ, 2011.
- [312] XIAO, J., XIE, Y., LIU, J., LIU, M. “Deactivation of nickel-based anode in solid oxide fuel cells operated on carbon-containing fuels.” *Journal of Power Sources*, v. 268, pp. 508–516, 2014.
- [313] IVAS, T., GRUNDY, A. N., POVODEN-KARADENIZ, E., GAUCKLERO, L. J. “Phase diagram of CeO₂-CoO for nano-sized powders.” *Calphad*, v. 36, pp. 57–64, 2012.
- [314] OKAMOTO, H. “Cerium-Cobalt Binary Alloy Phase Diagram.” *ASM Alloy Phase Diagrams Center*, v. 2, pp. 1047–1050, 2007.
- [315] ZHUANG, W., QIAO, Z. Y., WEI, S., SHEN, J. “Thermodynamic evaluation of the Cu-R (R: Ce, Pr, Nd, Sm) binary systems.” *Journal of Phase Equilibria*, v. 17, pp. 508–521, 1996.
- [316] NISHIZAWA, T., ISHIDA, K. “The Co-Cu (Cobalt-Copper) system.” *Bulletin of Alloy Phase Diagrams*, v. 5, pp. 161–165, 1984.
- [317] MOSER, W. R. *Advanced Catalysts and Nanostructured Materials*. Elsevier, 1969.
- [318] LEVIN, E. M., ROBBINS, C. R., MCMURDIE, H. E. *Phase Diagrams for Ceramists*. The American Ceramic Society, 1969.
- [319] ABOUKAIS, A., BENNANI, A., AISSI, C. F., GUELTON, M., VEDRINE, J. C. “Microwave frequency behavior of the EPR copper(II) ion pairs spectrum formed in CuCe oxide.” *Chemistry of Materials*, v. 4, pp. 977–979, 1992.
- [320] BECHARA, R., WROBEL, G., AISSI, C. F., GUELTON, M., BONNELLE, J. P., ABOU-KAIS, A. “Preparation and characterization of copper-thorium oxide catalysts. 1. Solid solution of copper(II) in thoria: an ESR study.” *Chemistry of Materials*, v. 2, pp. 518–522, 1990.

- [321] TSCHOPE, A., YING, J. Y., CHIANG, Y.-M. “Processing and structural evolution of nanocrystalline Cu-CeO_{2-x} catalysts.” *Materials Science and Engineering: A*, v. 204, pp. 267–271, 1995.
- [322] RAMOS, T., HJELM, J., MOGENSEN, M. “Towards Quantification of Relations Between Electrode Polarisation and Microstructure.” *Journal of The Electrochemical Society*, v. 158, pp. B814–B824, 2011.
- [323] RAMOS, T., THYDÉN, K., MOGENSEN, M. “Electrochemical Characterisation of Ni/(Sc)YSZ Electrodes.” *ECS Transactions*, v. 28, pp. 123–139, 2010.
- [324] HAGEN, A., JOHNSON, G. B., HJALMARSSON, P. “Electrochemical evaluation of sulfur poisoning in a methane-fuelled solid oxide fuel cell: Effect of current density and sulfur concentration.” *Journal of Power Sources*, v. 272, pp. 776–785, 2014.
- [325] PARK, S., CRACIUN, R., VOHS, J. M., GORTE, R. J. “Direct Oxidation of Hydrocarbons in a Solid Oxide Fuel Cell I. Methane Oxidation.” *Journal of The Electrochemical Society*, v. 146, pp. 3603–3605, 1999.
- [326] PARK, S., GORTE, R. J., VOHS, J. M. “Applications of heterogeneous catalysis in the direct oxidation of hydrocarbons in a solid-oxide fuel cell.” *Applied Catalysis A: General*, v. 200, pp. 55–61, 2000.
- [327] ZHAO, K., KIM, B.-H., DU, Y., XU, Q., AHN, B.-G. “Ceria catalyst for inert-substrate-supported tubular solid oxide fuel cells running on methane fuel.” *Journal of Power Sources*, v. 314, pp. 10–17, 2016.
- [328] KNIBBE, R., WANG, H.-J., BLENNOW, P., THYDÉN, K., ÅSA H. PERS-SON, MIKKELSEN, L., KLEMENSØ, T. “Oxidation in ceria infiltrated metal supported SOFCs - A TEM investigation.” *Journal of Power Sources*, v. 228, pp. 75–82, 2013.
- [329] SOMIYA, S. *Hydrothermal Reactions for Materials Science and Engineering*. Springer, 1989.
- [330] DU, Y., YASHIMA, M., KOURA, T., YOSHIMURA, M. K. M. “Thermodynamic evaluation of the ZrO₂-CeO₂ system.” *Scripta Metallurgica et Materialia*, v. 31, pp. 327–332, 1994.
- [331] HUANG, S., LI, L., VLEUGELS, J., WANG, P., DER BIEST, O. V. “Thermodynamic prediction of the nonstoichiometric phase Zr_{1-z}Ce_zO_{2-x} in the

ZrO₂-CeO_{1.5}-CeO₂ system.” *Journal of the European Ceramic Society*, v. 23, pp. 99–106, 2003.

- [332] JIAO, Y., ZHANG, L., AN, W., ZHOU, W., SHA, Y., SHAO, Z., BAI, J., LI, S.-D. “Controlled deposition and utilization of carbon on Ni-YSZ anodes of SOFCs operating on dry methane.” *Energy*, v. 113, pp. 432–443, 2016.
- [333] GIEZEN, J. C. V., DEN BERG, F. R. V., KLEINEN, J. L., DILLEN, A. J. V., GEUS, J. W. “The effect of water on the activity of supported palladium catalysts in the catalytic combustion of methane.” *Catalysis Today* 47, v. 47, pp. 287–293, 1999.
- [334] GONG, H., CHEN, Z., WANG, M., WU, W., WANG, W. “A study on the feasibility of the catalytic methane oxidation for landfill gas deoxygen treatment.” *Fuel*, v. 120, pp. 179–185, 2014.
- [335] KIM, S. C., CHUN, Y. N. “Experimental study on partial oxidation of methane to produce hydrogen using low-temperature plasma in AC Glidarc discharge.” *International Journal of Energy Research*, v. 32, pp. 1185–1193, 2008.
- [336] YUAN, Q., SUN, C. Y., LIU, B., WANG, X., MA, Z.-W., MA, Q.-L., YANG, L.-Y., CHEN, G.-J., LI, Q.-P., LI, S., ZHANG, K. “Methane recovery from natural gas hydrate in porous sediment using pressurized liquid CO₂.” *Energy Conversion and Management*, v. 67, pp. 257–264, 2013.
- [337] DALAI, A. K., DAVIS, B. H. “Fischer-Tropsch synthesis: a review of water effects on the performances of unsupported and supported Co catalysts.” *Applied Catalysis A: General*, v. 348, pp. 1–15, 2008.
- [338] ZHOU, X., HUANG, H., LIU, H. “Study of partial oxidation reforming of methane to syngas over self-sustained electrochemical promotion catalyst.” *International Journal of Hydrogen Energy*, v. 38, pp. 6391–6396, 2013.
- [339] HUANG, H., ZHOU, X., LIU, H. “A CFD model for partial oxidation of methane over self-sustained electrochemical promotion catalyst.” *International Journal of Hydrogen Energy*, v. 41, pp. 208–218, 2016.
- [340] ZHAN, Z., BARNETT, S. A. “Use of a catalyst layer for propane partial oxidation in solid oxide fuel cells.” *Solid State Ionics*, v. 176, pp. 871–879, 2005.

- [341] LIN, Y., ZHAN, Z., BARNETT, S. A. “Improving the stability of direct-methane solid oxide fuel cells using anode barrier layers.” *Journal of Power Sources*, v. 158, pp. 1313–1316, 2006.
- [342] LIN, Y., ZHAN, Z., LIU, J., BARNETT, S. A. “Direct operation of solid oxide fuel cells with methane fuel.” *Solid State Ionics*, v. 176, pp. 1827–1835, 2005.
- [343] PETERS, R., DAHL, R., KLUTTGEN, U., PALM, C., STOLTEN, D. “Internal reforming of methane in solid oxide fuel cell systems.” *Journal of Power Sources*, v. 106, pp. 238–244, 2002.
- [344] SAUNDERS, G. J., KENDALL, K. “Reactions of hydrocarbons in small tubular SOFCs.” *Journal of Power Sources*, v. 106, pp. 258–263, 2002.
- [345] DHIR, A., KENDALL, K. “Microtubular SOFC anode optimisation for direct use on methane.” *Journal of Power Sources*, v. 181, pp. 297–303, 2008.
- [346] WANG, B., ZHU, J., LIN, Z. “A theoretical framework for multiphysics modeling of methane fueled solid oxide fuel cell and analysis of low steam methane reforming kinetics.” *Applied Energy*, v. 176, pp. 1–11, 2016.
- [347] UKAI, K., MIZUTANI, Y., KUME, Y., YOKOKAWA, O. Y. H., SINGHAL, S. C. *Solid Oxide Fuel Cells, vol. VII*. Electrochemical Society, Pennington, NJ, 2001.
- [348] LIU, J., BARNETT, S. A. “Operation of anode-supported solid oxide fuel cells on methane and natural gas.” *Solid State Ionics*, v. 158, pp. 11–16, 2003.

Appendix I - Materials and Equipments

Table 9.1: List of materials and specifications sorted alphabetically

Reference	Name	Abreviation	Formula	Manufacturer	Comercial Name	Purity
MT-01	Ammonium hydroxide solution 35%	Amonia	NH ₄ OH	Fisher Scientific	—	—
MT-02	Cerium (III) nitrate hexahydrate	—	Ce(NO ₃) ₃ .6H ₂ O	Aldrich	—	99.00%
MT-03	Citric acid monohydrate	—	C ₆ H ₁₀ O ₈	Sigma-Aldrich	—	—
MT-04	Cobalt (III) nitrate hexahydrate	—	Co(NO ₃) ₂ .6H ₂ O	Sigma-Aldrich	—	98.00%
MT-05	Copper (II) nitrate trihydrate	—	Cu(NO ₃) ₂ .3H ₂ O	Sigma-Aldrich	—	99.00%
MT-06	Scandia Ceria Zirconia Electrolyte	ScCeSZ	Patented	Fuel Cell Materials	HIONIC	—
MT-07	Scandia Ceria Zirconia powder	ScCeSZ	Sc _{0.1} Ce _{0.01} Zr _{0.89} O ₂	DKKK	—	—
MT-08	Silver conductive paste - DAD-87	Silver paste	—	Shanghai Inst. of Resin	—	—
MT-09	Silver gauze 80 mesh -	Silver mesh	—	Alfa Aeser	—	—
MT-10	Silver wires 0.25 mm	Silver wires	—	Scientific wire company	—	99.99%
MT-11	Strontium Lanthanum Manganite	LSM	La _{0.8} Sr _{0.2} MnO ₃	Praxair	—	—
MT-12	Terpineol Vehicle	—	—	Fuel Cell Materials	—	—
MT-13	Terpineol Vehicle	—	—	HERAUS	T-100	—

Table 9.2: List of equipments and manufacturer sorted alphabetically

Reference	Name	Manufacturer
EQ-01	Carbolite Furnace	Carbolite
EQ-02	EXAKT Model 50 Three Roll mill	EXAKT
EQ-03	Gas Chromatogrpher GC-2014	Shimadzu
EQ-04	Magnetic Stirrer - IKA RET	IKA
EQ-05	Particle size distribution - Mastersizer 2000	Malvern
EQ-06	pH meter Mettler - Toledo	Toledo
EQ-07	Planetary mill - RETSCH -PM400	RETSCH
EQ-08	Quantachrome ChemBET Pulsar TPR/TPD	Quantachrome
EQ-09	Raman spectroscopy - Renishaw inVia	Renishaw
EQ-10	Screen printing machine	DEK
EQ-11	Screen printing machine - Aurel 900	Aurel
EQ-12	SEM - JEOL JSM-6460LV	JEOL
EQ-13	Solartron	Solartron
EQ-14	Thermogravimetry - NETZSCH TG 209 F1	NETZSCH
EQ-15	Thermometer - IKA ETS-D6	IKA
EQ-16	Vecstar Furnace	Vecstar
EQ-17	X-ray diffractometer Bruker D8	Bruker
EQ-18	X-ray diffractometer Shimadzu 6000	Shimadzu
EQ-19	X-ray fluorescence Spectrometer - Bruker S8 Tiger	Bruker

Table 9.3: Equivalences as metals to oxides for each produced composition.

Parameter [%]	Ce:Co:Cu - 2:1:1	Ce:Co:Cu - 1:2:1	Ce:Co:Cu - 1:1:2	Ce:Co:Cu - 1:1:0	Ce:Co:Cu - 1:0:1
Ce [mol]	50.00%	25.00%	25.00%	50.00%	50.00%
Co [mol]	25.00%	50.00%	25.00%	50.00%	0.00%
Cu [mol]	25.00%	25.00%	50.00%	0.00%	50.00%
Ce [mass]	69.59%	43.58%	42.96%	70.39%	68.80%
Co [mass]	14.63%	36.66%	18.07%	29.61%	0.00%
Cu [mass]	15.78%	19.76%	38.97%	0.00%	31.20%
CeO ₂ [mol]	60.00%	37.50%	30.00%	75.00%	50.00%
Co ₃ O ₄ [mol]	10.00%	25.00%	10.00%	25.00%	0.00%
CuO [mol]	30.00%	37.50%	60.00%	0.00%	50.00%
CeO ₂ [mass]	68.29%	41.76%	41.83%	68.20%	68.39%
Co ₃ O ₄ [mass]	15.92%	38.95%	19.51%	31.80%	0.00%
CuO [mass]	15.78%	19.30%	38.66%	0.00%	31.61%

Appendix II - Impedance Parameters

Table 9.4: Frequencies at imaginary maxima points and real impedance values with hydrogen as fuel at various temperatures.

Maxima	Variables	Cerium-rich			Cobalt-rich			Copper-rich		
		750°C	800°C	850°C	750°C	800°C	850°C	750°C	800°C	850°C
1 st Maximum	Frequency [Hz]	19,953.00	25,119.00	25,119.00	6,309.60	15,849.00	10,000.00	316.23	10,000.00	12,589.00
	Z' [$\Omega \cdot \text{cm}^2$]	0.30	0.21	0.16	0.43	0.24	0.22	0.62	0.29	0.24
2 nd Maximum	Frequency [Hz]	0.79	1.26	2.00	15.85	25.12	31.62	0.20	0.32	0.50
	Z' [$\Omega \cdot \text{cm}^2$]	1.60	0.63	0.42	1.16	0.56	0.44	1.91	1.05	0.69

Table 9.5: Frequencies at imaginary maxima points and real impedance values with methane as fuel at 850 °C.

Maxima	Variables	Cerium-rich	Cobalt-rich	Copper-rich
1 st Maximum	Frequency [Hz]	31,623.00	15,848.93	15,848.93
	Z' [$\Omega\cdot\text{cm}^2$]	0.16	0.22	0.27
2 nd Maximum	Frequency [Hz]	0.50	0.01	0.25
	Z' [$\Omega\cdot\text{cm}^2$]	0.82	6.07	1.41

Table 9.6: ECM parameters for impedance fitted data for the CeCoCu compositions operated with hydrogen.

Circuit Element	Cerium-rich			Cobalt-rich			Copper-rich		
	750°C	800°C	850°C	750°C	800°C	850°C	750°C	800°C	850°C
L1	8.16E-08	7.91E-08	7.68E-08	1.58E-07	1.33E-07	1.54E-07	1.42E-07	1.35E-07	1.25E-07
R1	0.21582	0.13565	0.10633	0.39893	0.22889	0.21422	0.34656	0.25147	0.21853
R2	0.85418	0.53454	0.34902	0.87143	1.50000	0.28714	0.71884	0.33454	0.16666
QPE1-Q	0.20810	0.24786	0.30478	0.00918	5.00000	0.01351	0.00199	0.00471	0.00375
QPE1-n	0.86147	0.84524	0.84126	0.76902	0.35937	0.69796	0.55205	0.49453	0.62396
R3	0.41505	0.23973	0.16606	2.08100	0.48892	1.13900	1.72400	0.90239	0.63875
QPE2-Q	0.00257	0.00352	0.00516	0.15538	0.01778	2.49800	0.42993	0.53765	0.63522
QPE2-n	0.37698	0.33119	0.35961	0.39898	0.65473	0.51898	0.86415	0.85357	0.74245

Table 9.7: ECM parameters for impedance fitted data for the CeCoCu compositions operated with methane at 850 °C.

Circuit Element	Methane as Fuel 850°C		
	Cerium-rich	Cobalt-rich	Copper-rich
L1	6.91E-08	1.52E-07	1.04E-03
R1	0.07508	0.22094	0.25105
R2	0.97566	11.67000	1.84400
QPE1-Q	0.28450	0.40620	0.30190
QPE1-n	0.83612	0.70267	0.87357
R3	0.22454	0.18502	0.20706
QPE2-Q	0.00300	0.00957	0.00515
QPE2-n	0.30375	0.73455	0.59869

Table 9.8: ECM parameters for impedance fitted data for the $\text{CeO}_2\text{-Co}_3\text{O}_4$ and $\text{CeO}_2\text{-CuO}$ compositions operated with hydrogen.

Circuit Element	$\text{CeO}_2\text{-Co}_3\text{O}_4$			$\text{CeO}_2\text{-CuO}$		
	750°C	800°C	850°C	750°C	800°C	850°C
L1	1.53E-07	9.29E-08	1.14E-07	1.99E-07	1.95E-07	1.94E-07
R1	0.36734	0.23348	0.15285	0.41959	0.26754	0.12522
R2	3.10500	1.21200	0.33387	3.42800	0.67289	0.44083
QPE1-Q	0.50243	0.00336	0.00629	0.63866	0.00175	0.00250
QPE1-n	0.88202	0.69348	0.59489	0.86927	0.44478	0.30066
R3	1.98100	1.84300	1.20900	1.15600	1.88200	1.35500
QPE2-Q	0.00183	0.64274	1.83000	0.00096	0.83476	0.88216
QPE2-n	0.64881	0.72455	0.64265	0.49211	0.84072	0.75873

Table 9.9: ECM parameters for impedance fitted data for the $\text{CeO}_2\text{-Co}_3\text{O}_4$ and $\text{CeO}_2\text{-CuO}$ compositions operated with methane at 850°C .

Circuit Element	Methane as Fuel 850°C	
	$\text{CeO}_2\text{-Co}_3\text{O}_4$	$\text{CeO}_2\text{-CuO}$
L1	1.08E-07	1.87E-07
R1	0.17616	1.20E-06
R2	0.52146	0.70083
QPE1-Q	0.00579	0.0017261
QPE1-n	0.62752	0.1829
R3	3.29E+14	3.099
QPE2-Q	0.96919	0.96182
QPE2-n	0.66628	0.81697